Technische Universität München
TUM School of Engineering and Design

TUM

The potential of UVC-irradiation using LEDs as an (*in situ*) biofouling control strategy in reverse osmosis membrane systems

Philipp Julius Sperle

Vollständiger Abdruck der von der TUM School of Engineering and Design der Technischen

Universität München zur Erlangung eines Doktors der Ingenieurwissenschaften (Dr.-Ing.)

genehmigten Dissertation.

Vorsitz: apl. Prof. Dr. rer. nat. habil. Brigitte Helmreich

Prüfer*innen der Dissertation:

1. Prof. Dr.-Ing. Jörg E. Drewes
2. Prof. Dr. Karl Linden
3. Prof. Dr. Johannes S. Vrouwenvelder

Die Dissertation wurde am 29.09.2023 bei der Technischen Universität München

eingereicht und durch die TUM School of Engineering and Design am 04.12.2023

angenommen.

I.   Abstract

Population growth, increased consumption behavior, economic development, and climate change increase stress on the limited freshwater resources on Earth. Groundwater resources are being depleted and the quality of water resources can be impaired by salinization or anthropogenic pollution. Through insufficient sanitation and limited access to safe drinking water, human health can be directly impacted. Additionally, the permanent exposure to micropollutants can have adverse effects on both, the environment and human health.

Pressure-driven membrane filtration, especially reverse osmosis (RO) might play an important role not only in increasing available freshwater resources via desalination but also in removing persistent contaminants. While RO is considered the most economical desalination process, a major challenge remaining is the unacceptable reduction of performance over time caused by biofilm formation, also known as biofouling. While approaches to control biofouling have received tremendous research interest, it remains unavoidable. A chemical free technology for biofouling control represents the ultraviolet (UV) disinfection of the feed stream. UV disinfection itself is a mature and well-researched technology. Several studies successfully applied it for biofouling mitigation, but likely due to the missing residual effect, up-to-date, UV disinfection is not a widely established pre-treatment. As UV disinfection has more effects than the inactivation of cells, the overall aim of this dissertation was to examine the (untouched) potential of UV disinfection for limiting the negative impacts of biofouling.

A promising alternative for UV light generation are UV-light-emitting diodes (UV-LEDs). Through their compact and robust structure, they allow new reactor geometries and a possible *in situ* integration into the pressure vessel of membrane systems. Besides, through their fast start-up times, they allow for pulsed operation.

Within a first study, it was examined, whether already a low fluence is sufficient for biofouling control and if UV pre-treatment is changing the biofilm attributes. A lab-scale membrane test skid with an UV-LED reactor attached in the immediate vicinity to membrane fouling simulators, mimicking an *in situ* integration was built. Accelerated biofouling experiments were conducted using local tap water as feed, supplemented with easily degradable nutrients. When reaching a defined feed channel pressure drop as a surrogate for the degree of biofouling, experiments were terminated and the formed biofilms were analyzed for various parameters including adenosine triphosphate, cell count, extracellular polymeric substances, and bacterial community composition. It could be proven that a low fluence of 2 mJ cm^{-2} was sufficient to significantly delay biofilm formation by more than 15%, likely caused by inactivation of cells, but possibly also by changed adsorption properties or cells suffering from cell cycle arrest. Besides, the biofilms that formed, showed a reduced hydraulic resistance by more than 40%. While the exact mechanisms behind the changed resistance remain unclear, the results

from biofilm analysis indicate that amongst others, a change in microbial community could be the explanation.

As determining the fluence in complex reactors is challenging, in the next section of the dissertation, a new actinometric method was developed to directly quantify the average fluence in UV reactors. To characterize the fluence in reactors commonly biodosimetry is applied. Biodosimetry directly shows the inactivation of the used surrogate organisms, but it is associated with higher costs and might not be practicable for all processes (e.g. for UV based advanced oxidation processes with high fluence). The application of chemical actinometry for flow-through reactors is currently limited to quantifying the light intensity entering the system or at distinct points. Complex reactor geometries and non-parallel irradiation associated with unknown path lengths propose challenges for actinometry, but it was hypothesized that through the usage of different actinometers, the degree of reflections can be determined. Therefore, uridine and KI/KIO$_3$ actinometry were applied using a collimated beam apparatus (CBA), irradiating petri dishes with or without reflective polytetrafluoroethylene (PTFE) layers. In contrast to the optical opaque KI/KIO$_3$ actinometry, uridine was affected by the reflective layers, but the addition of absorbing substances revealed that the unknown path lengths led to errors. In cooperating those results a new uridine actinometry was developed, based on an existing semi-empirical model, solving a set of equations for path length and fluence rate. While the results of the enhanced actinometric procedure could be validated with biodosimetry in the CBA setting (e.g., 2.6-fold fluence rate increase when the complete bottom of the petri dish was lined with PTFE), it cannot replace biodosimetry as it is not giving information about fluence distribution and hydraulic short cuts. Still, it has several possible implications for practice like fluence determination when biodosimetry is too sensitive, fluence determination for non-parallel light, optical model validation, and in combination with biodosimetry, to qualitatively characterize fluence distribution.

Being able to characterize the fluence in a reflecting UV reactor using the developed actinometry, it was investigated whether increasing the fluence rate during pulsed irradiation leads to enhanced disinfection of bacteria. The results of past studies using UVC- and UVB-LEDs in pulsed mode are inconsistent. Past studies either increased the time of irradiation in pulsed mode or the log inactivation was normalized to fluence. To evaluate whether an increased fluence rate during the pulses leads to additional positive effects for disinfection, biodosimetry using MS2 phages and a bacterium species, potentially relevant for biofouling, was performed. When starting biodosimetry in the lab-scale flow-through reactors, it was recognized that there exist various methodical challenges, especially for the used biofilm bacteria. As there exists no standardized procedure for lab-scale bacterial flow-through biodosimetry, a practical procedure was developed including measures against cell protraction, photorepair and adsorption to labware. Within the conducted biodosimetry experiments, no enhanced disinfection for the biofilm bacterium could be proven, even

though the peak fluence rate during pulsed operation was more than one order of magnitude higher than in continuous mode (141 versus 2 mW cm^{-2}).

Even though disinfection efficiency on a fluence basis was not increased in pulsed biodosimetry experiments, effects might vary for biofouling control and a better thermal management for LEDs through pulsation was reported. To test whether pulsed irradiation leads to savings of operational expenditures (OPEX), lab-scale biofouling experiments in continuous and pulsed settings in the range of 1.5 to 61.3 mJ cm^{-2} were performed. Thereby, it could be seen that the delay in biofilm formation relates to fluence but stagnates towards higher values. In general, OPEX could be saved by UV irradiation assuming the energy demand of conventional lamps (e.g., ~18% for 28 mJ cm^{-2} and brackish water RO at 91% UV transmittance and continuous operation), but the optimal fluence might depend on the feed water/application. Pulsed settings on average showed a 20% higher delay than continuous equivalents, but no clear trend in saved OPEX was visible between the modes, neither on a fluence nor on an electrical basis.

To prove whether the positive effects of UV pre-treatment for biofouling control translate to up-scaled applications, UV as an *in situ* pre-treatment was employed using real feed water at pilot-scale. A UV-LED device was successfully integrated into the pressure vessel of a RO system. Applying a low fluence of approximately 1.4 mJ cm^{-2}, a delay of biofilm formation, comparable to continuous dosing of NaOCl was visible (17-22%). In the first cycle, OPEX savings were estimated at ~7%, using analogous calculations as for the lab-scale experiments. However, after a couple of cleanings performed, the hydraulic resistance of the biofilm of the UV line was less well restored, leading to no saved OPEX in comparison to the reference line in a later cycle.

Overall, UV disinfection as a pre-treatment has the potential to save energy and chemicals. Higher fluence might lead to higher savings than observed in the performed pilot-scale experiments and by a combination with advanced cleaning procedures, OPEX savings might be present in the long-term. While UV pretreatment cannot avoid biofouling completely, it can be seen as an additional strategy, contributing to a holistic approach for biofouling mitigation.

II. Zusammenfassung

Bevölkerungswachstum, gestiegene Konsumgewohnheiten, wirtschaftliche Entwicklung und Klimawandel erhöhen die Belastung für die begrenzten Süßwasserressourcen auf der Erde. Die Grundwasserressourcen werden erschöpft und die Wasserqualität kann durch Versalzung oder anthropogene Verschmutzung beeinträchtigt werden. Unzureichende sanitäre Einrichtungen und der eingeschränkte Zugang zu sauberem Trinkwasser können unmittelbare Auswirkungen auf die menschliche Gesundheit haben. Darüber hinaus kann die ständige Exposition gegenüber Mikroschadstoffen negative Auswirkungen sowohl auf die Umwelt als auch auf die menschliche Gesundheit haben.

Die druckbetriebene Membranfiltration, insbesondere die Umkehrosmose (UO), kann nicht nur bei der Erhöhung der verfügbaren Süßwasserressourcen durch Entsalzung, sondern auch bei der Entfernung von persistenten Schadstoffen eine wichtige Rolle spielen. Während UO als das wirtschaftlichste Entsalzungsverfahren gilt, bleibt der inakzeptable Leistungsabfall über die Betriebszeit durch Biofilmbildung, auch bekannt als Biofouling, eine große Herausforderung. Obwohl Ansätze zur Bekämpfung von Biofouling großes Forschungsinteresse erfahren, bleibt es unvermeidlich. Eine chemikalienfreie Technologie zur Biofouling-Kontrolle stellt die Ultraviolett (UV)-Desinfektion des Zulaufs dar. Die UV-Desinfektion selbst ist eine ausgereifte und gut erforschte Technologie. Verschiedene Studien haben sie erfolgreich zur Abschwächung von Biofouling eingesetzt, dennoch ist UV-Desinfektion bis heute keine weit verbreitete Vorbehandlung, wahrscheinlich aufgrund der fehlenden Depotwirkung. Da die UV-Desinfektion mehr Effekte aufweist als die Inaktivierung von Zellen, war es das übergeordnete Ziel dieser Dissertation, das (ungenutzte) Potenzial der UV-Desinfektion zur Begrenzung der negativen Auswirkungen von Biofouling zu erforschen.

Eine vielversprechende Alternative zur UV-Lichterzeugung sind UV-Leuchtdioden (UV-LEDs). Durch ihren kompakten und robusten Aufbau ermöglichen sie neue Reaktorgeometrien und eine mögliche *In-situ*-Integration in den Druckbehälter von Membransystemen. Außerdem ermöglichen sie durch ihre schnellen Anlaufzeiten einen gepulsten Betrieb.

In einer ersten Studie wurde untersucht, ob bereits eine geringe Fluenz für die Biofouling-Kontrolle ausreicht und ob die UV-Vorbehandlung die Biofilm-Attribute verändert. Im Labormaßstab wurde ein Membran-Versuchsstand mit einem UV-LED-Reaktor in unmittelbarer Nähe zu Membranfouling-Simulatoren gebaut, der eine *In-situ*-Integration nachahmt. Beschleunigte Biofouling-Experimente wurden mit lokalem Leitungswasser als Zulauf, ergänzt mit leicht abbaubaren Nährstoffen, durchgeführt. Bei Erreichen eines definierten Druckabfalls im Zulaufkanal als Surrogat für den Biofouling-Grad wurden die Experimente beendet und die gebildeten Biofilme auf verschiedene Parameter wie Adenosintriphosphat, Zellzahl, extrazelluläre Polymersubstanzen und die Zusammensetzung der Bakteriengemeinschaft analysiert. Es konnte nachgewiesen werden, dass eine geringe Fluenz von 2 mJ cm^{-2} ausreicht, um die Biofilmbildung

iv

signifikant um mehr als 15% zu verzögern, wahrscheinlich verursacht durch die Inaktivierung von Zellen, aber möglicherweise auch durch veränderte Adsorptionseigenschaften oder Zellen beeinträchtigt durch einen Zellzyklusstopp. Außerdem zeigten die entstandenen Biofilme einen um mehr als 40% reduzierten hydraulischen Widerstand. Während die genauen Mechanismen hinter dem veränderten Widerstand unklar sind, deuten die Ergebnisse der Biofilmanalyse darauf hin, dass unter anderem eine Veränderung der mikrobiellen Gemeinschaft die Erklärung sein könnte.

Da die Bestimmung der Fluenz in komplexen Reaktoren eine Herausforderung darstellt, wurde im nächsten Teil der Dissertation eine neue aktinometrische Methode entwickelt, mit der die durchschnittliche Fluenz in UV-Reaktoren direkt quantifiziert werden kann. Um die Fluenz in solchen Reaktoren zu charakterisieren, wird üblicherweise Biodosimetrie angewendet. Biodosimetrie zeigt direkt die Inaktivierung der verwendeten Surrogatorganismen, ist aber mit höheren Kosten verbunden und möglicherweise nicht für alle Prozesse praktikabel (z. B. bei UV-basierten weitergehenden Oxidationsverfahren mit hoher Fluenz). Die Anwendung der chemischen Aktinometrie für Durchflussreaktoren beschränkt sich momentan auf die Quantifizierung der Lichtintensität, die in das System eintritt oder an einzelnen Punkten. Komplexe Reaktorgeometrien und nicht-parallele Bestrahlungen, verbunden mit unbekannten Weglängen, stellen Herausforderungen für die Aktinometrie dar. Dennoch wurden in der Dissertation die Hypothese aufgestellt, dass sich durch den Einsatz verschiedener Aktinometer der Grad an Lichtreflektionen in einem Reaktor bestimmen lassen. Daher wurden Uridin- und KI/KIO_3-Aktinometrie an einem kollimierten Strahlapparat (CBA) angewendet, mit welchem Petrischalen mit oder ohne reflektierende Polytetrafluorethylen (PTFE)-Schichten bestrahlt wurden. Im Gegensatz zur optisch opaken KI/KIO_3-Aktinometrie wurde das Uridin von den reflektierenden Schichten beeinflusst, aber die Zugabe von absorbierenden Substanzen zeigte, dass die unbekannten Weglängen zu Fehlern führten. Aufbauend auf diesen Ergebnissen wurde eine neue Uridin-Aktinometrie entwickelt, die auf einem existierenden semi-empirischen Modell basiert und eine Reihe von Gleichungen für Pfadlänge und Fluenzrate löst. Obwohl die Ergebnisse des verbesserten aktinometrischen Verfahrens mit der Biodosimetrie in dem CBA Aufbau validiert werden konnten (z. B. 2,6-facher Anstieg der Fluenzrate, wenn der gesamte Boden der Petrischale mit PTFE ausgekleidet war), kann es die Biodosimetrie nicht ersetzen, da es keine Informationen über die Fluenzverteilung und hydraulische Kurzschlüsse liefert. Dennoch hat es mehrere mögliche Implikationen für die Praxis, wie Fluenzbestimmung, wenn Biodosimetrie zu empfindlich ist, Fluenzbestimmung für nicht-paralleles Licht, Validierung optischer Modelle und in Kombination mit Biodosimetrie, um die Fluenzverteilung qualitativ zu charakterisieren.

Da die Fluenz in einem reflektierenden UV-Reaktor mit der entwickelten Aktinometrie charakterisiert werden konnte, wurde untersucht, ob eine Erhöhung der Fluenzrate bei gepulster Bestrahlung zu einer verbesserten Desinfektion von Bakterien führt. Die Ergebnisse früherer Studien mit UVC- und UVB-LEDs im gepulsten Modus

sind inkonsistent. Frühere Studien erhöhten entweder die Bestrahlungszeit im gepulsten Modus oder die Log-Inaktivierung wurde auf die Fluenz normalisiert. Um zu beurteilen, ob eine erhöhte Fluenzrate während der Pulse zu zusätzlichen positive Effekten für die Desinfektion führt, wurde eine Biodosimetrie mit MS2-Phagen und einer möglicherweise für Biofouling relevanten Bakterienart durchgeführt. Bei Beginn der Biodosimetrie in den Durchflussreaktoren im Labormaßstab, wurde erkannt, dass eine Reihe von methodischen Herausforderungen, insbesondere für die verwendeten Biofilmbakterien, bestehen. Da es kein standardisiertes Verfahren für die bakterielle Durchfluss-Biodosimetrie im Labormaßstab gibt, wurde ein praktikables Verfahren entwickelt, das Maßnahmen gegen die Verschleppung von Zellen, Photoreparatur und Adsorption an Labormaterialien beinhaltet. In den durchgeführten Biodosimetrie-Experimenten konnte keine verbesserte Desinfektion des Biofilmbakteriums nachgewiesen werden, obwohl die Spitzenfluenzrate im gepulsten Betrieb um mehr als eine Größenordnung höher war als im kontinuierlichen Betrieb (141 versus 2 mW cm^{-2}).

Obwohl die Desinfektionseffizienz auf Basis der Fluenz in gepulsten Biodosimetrie-Experimenten nicht erhöht wurde, können sich die Effekte für die Biofouling-Kontrolle unterscheiden und es wurde ein besseres thermisches Management für LEDs durch Pulsation berichtet. Um zu testen, ob die gepulste Bestrahlung zu Einsparungen bei den Betriebskosten (OPEX) führt, wurden Labor-Biofouling-Experimente in kontinuierlichen und gepulsten Einstellungen im Bereich von 1,5 bis 61,3 mJ cm^{-2} durchgeführt. Dabei konnte man sehen, dass die Verzögerung der Biofilmbildung mit der Fluenz zusammenhängt, aber in Richtung höherer Werte stagniert. Unter der Annahme des Energie Verbrauchs herkömmliche Lampen, konnten generell OPEX durch die UV-Bestrahlung eingespart werden, (z. B. ~18% für 28 mJ cm^{-2} und Brackwasser UO bei 91% UV-Transmission und kontinuierlichem Betrieb), aber die optimale Fluenz hängt vom Zulaufwasser/der Anwendung ab. Bei gepulsten Einstellungen war die Verzögerung um durchschnittlich 20% höher als bei den kontinuierlichen Äquivalenten, aber es war kein eindeutiger Trend bei den eingesparten OPEX zwischen den einzelnen Modi zu erkennen, weder auf Fluenz noch auf elektrischer Basis.

Um nachzuweisen, ob sich die positiven Effekte der UV-Vorbehandlung für die Biofouling-Kontrolle auch in hochskalierten Anwendungen niederschlagen, wurde UV als *In-situ*-Vorbehandlung mit realem Zulaufwasser im Pilotmaßstab eingesetzt. Ein UV-LED-Gerät wurde erfolgreich in den Druckbehälter einer UO-Anlage integriert. Bei Anwendung einer geringen Fluenz von ca. 1,4 mJ cm^{-2} zeigte sich eine Verzögerung der Biofilmbildung, vergleichbar mit der kontinuierlichen Dosierung von NaOCl (17-22%). Im ersten Zyklus wurden die OPEX-Einsparungen auf ~7 % geschätzt, wobei Berechnungen entsprechend der Laborexperimenten zugrunde gelegt wurden. Allerdings wurde nach einigen Reinigungen der hydraulische Widerstand des Biofilms der UV-Linie im geringeren Ausmaß wiederhergestellt, so dass im Vergleich zur Referenzlinie keine OPEX in einem späteren Zyklus eingespart wurden.

Insgesamt hat die UV-Desinfektion als Vorbehandlung das Potenzial, Energie und Chemikalien einzusparen. Höhere Fluenzen könnten zu höheren Einsparungen führen als in den durchgeführten Pilotversuchen und durch die Kombination mit fortgeschrittenen Reinigungsverfahren könnten langfristig OPEX-Einsparungen erzielt werden. Während die UV-Vorbehandlung Biofouling nicht vollständig vermeiden kann, kann sie als zusätzliche Strategie gesehen werden, die zu einem ganzheitlichen Ansatz zur Verringerung von Biofouling beiträgt.

III. Acknowledgements

python programming experiences with you. Christoph, our trip in Reno was unforgettable! Thanks a lot for this amazing time and our friendship. Stinsi 😊 thanks a lot for being my fishing mentor!

Thank you very much Karl Linden and Johannes Vrouwenvelder, not only for joining my Ph.D. committee, but also for the time you took in order to provide me with valuable feedback during my research proposal.

Supervising student works was a pleasure and I also learned a lot, I hope together with you. Thanks you so much, Ragini Bal Mahesh (2019), Syed Muhammad Ahsan Gillani (2019) and Karim El Khodary (2020) for your help with the experiments and in the initial phase of my project (Chapter 4). Thank you very much Omar Shehata (2020) for your help with the actinometrical and first biodosimetry experiments initiating the work done in Chapter 5 and Chapter 6. Andi, supervising your Master's Thesis (Mirlach, 2021) was a real pleasure, I really enjoyed all our discussions and the work on the actinometry (Chapter 5). Thanks for the great times we had. Sheh, I hope you enjoyed the time working together as I did. Thank you very much not only for you Study Project and Master's Thesis (Khan, 2022a, 2022b), but also for your help during your time as working student and the night shifts we did in the lab (around 1-8 AM) as the biofilms did not grow as planned. I'm incredibly happy that we could finish this part successfully. Your work was an essential contribution to my dissertation (Chapters 4,6, and 7). Habibia, thank you very much for working with the spiral-wound membrane modules (Chapter 8.1) as part of your Study Project (Sultana, 2022). Besides many thanks to Johanna Braun (2022), Vongvichra Nay (2020), Kapil Tiwari (2022), Philipp Appelmann (2022) and Xuan Quyet Nguyen (2021). Advait Gangal thank you very much for your excellent work on the COMSOL modeling within your Study Project (Gangal, 2023), described in Chapter 12.8.

I'd also like to express my gratitude to Myriam Reif, Wolfgang Schröder, Heidi Mayrhofer and Ursula Wallentis for your help in the Lab. Max Damberger and Hubert Moosrainer, thank you very much for your support on technical works. I really learned a lot from you!

After, my four years at the chair as Ph.D. student, I joint the Xylem family. Uwe Hübner, thank you very much for your great expertise, not losing focus and the enormous help! I'm very glad we can continue our collaboration now at Xylem. I really appreciate working with you. Also my thanks to Jörg Mielcke, Harald Stapel and Achim Ried for supporting me in finishing my dissertation next to the full time job at Xylem. Thanks also to Arthur Teisch for the helpful discussions on LEDs.

Last and most important, I'd like to express my deepest gratitude to all my family and friends for supporting me in good and bad times. Catherine, your support is incredibly and I know I can always rely on you, thanks for everything! Laura not only could I learn a lot from you on actinometry due to your past Study Project (Rehlen, 2017), but without you finishing the Ph.D. would not have been possible. Thank you so

much for understanding my frustrations and bringing me back to earth! Thank you for all the positive energy, remembering me that there is a life next to Ph.D., your encouragement as well as the amazing support and the best time of my life!

IV. Contents

V.   List of figures

VI. List of tables

VII. Abbreviations and acronyms

6-4PPs	6-4 photoproducts
AHLs	Acyl homoserine lactones
AOPs	Advanced oxidation processes
ARGs	Antibiotic-resistance genes
ASVs	Amplicon sequence variants
ATD	Anti-telescoping device
ATP	Adenosine triphosphate
BER	Base extinction repair
BMBF	German Ministry of Education and Research
CA	Cellulose acetate
CBA	Collimated beam apparatus
CFU	Colony forming units
CIP	Cleaning-in-place
CPDs	Cyclobutane–pyrimidine dimers
DA	Damage avoidance
DBNPA	Monochloramine 2,2-dibromo-3-nitrilopropionamide
DDT	Dichlorodiphenyltrichloroethane
DF	Divergence factor
DI	Deionized
DOC	Dissolved organic carbon
EC	Electrical conductivity
EEM	Excitation emission matrix
EM	Empty module
EPS	Extracellular polymeric substances
FCPD	Feed channel pressure drop
GC	Guanine and cytosine content
GO	Graphene oxide
HA	Humic acids sodium salt
HRT	Hydraulic retention time
IC	Interconnector
LEDs	Light-emitting diodes
LHS	Left-hand side
LMH	L m^{-2} h^{-1}
LP	Low-pressure
LRV	Logarithmic reduction/removal value
LVRPA	Local volumetric rate of photon absorption
MF	Microfiltration
MFS	Membrane fouling simulators
MP	Medium-pressure
Na-DDS	Sodium salt of dodecyl sulfate
NaOH	Sodium hydroxide
NER	Nucleotide excision repair
NF	Nanofiltration
OD	Optical density
OPEX	Operational expenses
PAHs	Polycyclic aromatic hydrocarbons

PARAFAC	Parallel factor
PBDEs	Polybrominated diphenylethers
PBS	Phosphate-buffered saline
PERMANOVA	Permutational multivariate analysis of variance using distance matrices
PES	Polyethersulfone
PF	Petri factor
PFAS	Per-and polyfluoroalkyl substances
PFU	Plug forming units
POPs	Persistent organic pollutants
PPA	Permeate port with adaptor
PS	Polysulfone
PTFE	Polytetrafluoroethylene
QC	Quality control
QQ	Quorum quenching
QS	Quorum sensing
RED	Reduction equivalent dose
REF	Reduction equivalent fluence
RF	Reflection factor
RO	Reverse osmosis
ROS	Reactive oxygen species
RTD	Residence time distribution
SMD	Surface mount device
SWM	Spiral-wound membrane
TDC	Total direct cell counts
TFC	Thin film composite
TLS	Translesion synthesis
TMP	Transmembrane pressure
TOC	Total organic carbon
UF	Ultrafiltration
UV	Ultraviolet
UVA	Ultraviolet-A
UVB	Ultraviolet-B
UVC	Ultraviolet-C
UVC-LEDs	Ultraviolet-C-light-emitting diodes
UVT	Ultraviolet transmittance
UV-LEDs	Ultraviolet-light-emitting diodes
WF	Water factor
WPEs	Wall plug efficiencies

1. Introduction

In the first section of this dissertation, a closer look at the state of current water resources concerning quantity and quality will be provided. Based on the different stressors identified, the need for action is derived. Afterward, the state-of-the-art of relevant technologies, i.e., ultraviolet (UV) disinfection and high-pressure membrane filtration, will be defined, necessary background knowledge elucidated, and research hypotheses introduced.

Due to an increasing population, changing consumer behavior, and economic development, global water usage is predicted to increase by 1% per year, while already having increased six times in total since 1920 (UNESCO, 2020). Shiklomanoc (1993) summarized that from the enormous water resources on earth of $1.39 \cdot 10^9$ km³, only ~2.5% are estimated to be available as freshwater, while most of them (~68.7%) are bound as ice or snow. Furthermore, from the overall water, only 0.76% is available to humans as fresh groundwater and 0.007% and 0.0002% as fresh water in lakes and river flows, respectively. Only a small fraction of available groundwater is made from water younger than 50 years, also referred to as modern groundwater (Gleeson et al., 2016; UNESCO, 2022). Sustainable water withdrawal (based on freshwater renewal rates) is limited and depends on regional circumstances (Ritchie and Roser, 2017; UNESCO, 2022). Groundwater represents 25% of all withdrawn freshwater, mainly for agricultural purposes (UNESCO, 2022).

Estimation of global groundwater resources, as well as withdraw and depletion rates is complex and highly uncertain (Bierkens and Wada, 2019). A common estimate of total groundwater resources is 23 million km³, however, more recently determined values are considerably lower (Bierkens and Wada, 2019; Richey et al., 2015). Furthermore, the extractable volumes might be significantly less, as those are also influenced by technical, economic, and quality constrains (Bierkens and Wada, 2019). Aside from fluoride and arsenic contaminations, indeed more than half of groundwater below the land surface is assumed to be saline, especially in deeper domains, next to coastal areas or in shallow depths within arid climates (Bierkens and Wada, 2019; Shiklomanoc, 1993; UNESCO, 2020; van Weert et al., 2009). Estimates for groundwater depletion rates within the last ~20 years are within the range of 92 and 510 km³ y^{-1} (Bierkens and Wada, 2019). Global aquifers which are especially affected by depletion include the North China Plain, California's Central Valley and the High Plains aquifer in the United States, central Mexico, a part of eastern Pakistan and western India, Iran, and the Middle East (Bierkens and Wada, 2019). The urgency of the situation was highlighted by Richey et al. (2015), who estimated that the Northwest Sahara aquifer system might be depleted by 90% within the next 50 years, still calculations are uncertain. Even before the complete exhaustion of groundwater resources, as reviewed by Bierkens and Wada (2019), the adverse effects of groundwater depletion are numerous, including:

- **Land subsidence**, caused by the shrinking of clay and peat layers or the release of pore pressure resulting in a compaction of the water-carrying layers by the weight of the overlying sediments. Land subsidence can, among others, result in damage to infrastructure.
- **Hydrological drought**, e.g., lower stream flows due to less groundwater recharge in dry periods. Lower stream flows can further result in higher stream temperatures and less diluted pollution and pathogens, with negative environmental impacts.
- **Sea-level change**, water volumes shifting from groundwater to sea water, might increase sea water levels, but impacts need further investigation.
- **Groundwater salinization**, especially in coastal areas or regions with a shallow saline aquifer, excessively high pumping rates can lead to mixing with salty groundwater, possibly making a large area around the extraction well unsuitable as potable water for a long period of time.
- **Impact on groundwater-dependent ecosystems**, ecosystems depending on groundwater discharge and proximity of the water table are affected by groundwater depletion, as it can change the streamflow quantity and quality, groundwater levels, and evaporation rates.

Besides, during irrigation, accumulated salts in the soil might be flushed down into the upper aquifer leading to additional salinization (UNESCO, 2022). In addition, pumping groundwater and other human interactions may lead to the release of arsenic and fluoride into aquifers (UNESCO, 2022).

Using data from the years 1996-2005, Mekonnen and Hoekstra (2016) estimated the blue water scarcity, an indication if more water is needed than locally available on a monthly basis and in a 30 x 30 arc min resolution. Here water scarcity was defined as the ratio of blue water footprint (fresh surface and groundwater withdrawn and not returned, including evaporation losses and water in products), over blue water availability (run-off generated within each cell and the upstream cells minus the environmental flow requirements and footprint of upstream cells). Hence, an annual water scarcity > 1 represents unstainable water withdrawls, leading to the depletion of surface or groundwater if transferring of water resources from close areas with water scarcity < 1 is not feasible (UNESCO, 2022). Two-thirds of the world's population were estimated to suffer from sever water scarcity (> 2) for at least one month a year, meaning their water demand is twice as high as the availability (Mekonnen and Hoekstra, 2016).

Aside from groundwater depletion and salinization, water resources can get polluted from varies sources. Concerning human health, deficits in sanitation and safe drinking water are the most direct impact, but also indirect contacts with pathogens or toxic substances, e.g., over the food chain need consideration (Schwarzenbach et al., 2010). According to Schwarzenbach et al. (2010), pollution can be separated according to macro- and micropollutants.

Macropollutants (in the range of mg L^{-1}) thereby contain, among others nutrients, natural organic substances, and salts, which impacts are, e.g., eutrophication, oxygen consumption, and algal blooms (Heisler et al., 2008; Schwarzenbach et al., 2010). If properly collected, nutrient loads of sewage can be well reduced within wastewater treatment plants using conventional technology.

Micropollutants, on the contrary, represent thousands of different natural and artificial pollutants usually present in the range of µg L^{-1} to ng L^{-1} (more than 100,000 chemicals are registered and most of them are in daily use) (Schwarzenbach et al., 2006; 2010). Those contaminants may be harmful to health already at those low concentrations, especially as many pollutants are present simultaneously (Schwarzenbach et al., 2006; 2010). In many parts of the world, wastewater generated by municipalities and industries is not treated sufficiently to remove micropollutants (Schwarzenbach et al., 2010). Furthermore, pesticides form agriculture, oil and gasoline spills, municipal and hazardous waste sides, former military and industrial sites, as well as traffic in general are causing additional pollution (Schwarzenbach et al., 2010). Many micropollutants can also be classified as persistent organic pollutants (POPs) as they are not considerably removed by nature, may be transported over long distances, are bioaccumulative, and are toxic to humans and wildlife (Schwarzenbach et al., 2010). Examples for those compounds are dichlorodiphenyltrichloroethane (DDT), polychlorinated dioxins, dibenzofurans, and polycyclic aromatic hydrocarbons (PAHs), but also more recently recognized chemicals such as polybrominated diphenylethers (PBDEs), and a variety of per-and polyfluoroalkyl substances (PFAS) used in numerous industrial applications, as flame retardants and in consumer products (Kurwadkar et al., 2022; Schwarzenbach et al., 2010; Vonderheide et al., 2008). Especially the latter ones experienced increased research interest in the past years, are found in waters worldwide and are challenging to be destroyed during advanced water treatment (Kurwadkar et al., 2022; Merino et al., 2016; Palma et al., 2022).

Municipal wastewater further represents a main point source for pharmaceuticals and personal care products in the environment (approximately 3,000 different pharmaceuticals are used in Europe, including antibiotics, beta-blockers, painkillers, lipid regulators, contraceptives, antidepressants, etc.) (Schwarzenbach et al., 2010; Ternes et al., 2006). In 2003, the consumption of pharmaceuticals was 79 g cap^{-1} a^{-1} and production of personal care products was estimated with more than 6,000 g cap^{-1} a^{-1} at the beginning of the 1990s in Germany (Ternes et al., 2006). Even though the presence of those substances in the aquatic environment might have been expected, only the development of environmental analytical chemistry allowed the detection of pharmaceuticals in the ng and µg range as occurring in wastewater and aquatic systems (Noguera-Oviedo and Aga, 2016; Schwarzenbach et al., 2010). Pharmaceuticals are only partially removed by sorption and biodegradation in wastewater treatment plants, e.g., < 10% for carbamazepine and > 90% for ibuprofen and often metabolites are formed (Joss et al., 2005; Schwarzenbach et al., 2010). Especially pharmaceuticals found in drinking water are of high concern as the effects

on human health by permanent exposure to low levels are not known (Noguera-Oviedo and Aga, 2016). The ecotoxicity of pharmaceutics and other micropollutants is complex as there is an exposure of mixed substances over long periods (Noguera-Oviedo and Aga, 2016). Additionally, the release of antibiotics to the environment via wastewater is critical as it can accelerate the spread of antibiotic-resistance genes (ARGs) and antibiotic-resistance bacteria (Noguera-Oviedo and Aga, 2016).

In addition to groundwater depletion and pollution, climate change impacts are resulting in increasing stress on available water resources. Climate change has numerous complex impacts on the water cycle. In general, it is assumed that due to global warming, the global water cycle will intensify, especially for atmospheric moisture fluxes as well as for land and ocean surface exchanges (Allan et al., 2020). Overall, a higher temperature will lead to higher evaporation as well as to more intense and an increased number of extreme weather events, like heavy precipitation or droughts (UNESCO, 2020). Nevertheless, in contrast to the clear trend of a rising temperature due to climate change, annual precipitation volumes are more uncertain and trends will vary with location (UNESCO, 2020). More extreme precipitations due to climate change can lead to higher amounts of pollution being flushed into aquifers, e.g., by surface runoff/flooding of poorly stored chemicals and waste, or contamination of groundwater by pathogens from sanitation facilities (Mkandawire, 2008; Olago et al., 2007; UNESCO, 2022; WHO, 2018). Especially in regions with insufficient sanitation and no access to safe drinking water, waterborne pathogens pose a great risk to human health (Schwarzenbach et al., 2010). However, actually the greatest impact of climate change is likely caused by higher groundwater withdrawals to overcome less reliable precipitation and meet an increasing global demand (Taylor et al., 2013; UNESCO, 2022). Furthermore, seawater level rise by melting of ice and thermal expansion of the oceans will increase saltwater intrusions in coastal aquifers, even though this is assumed to be rather small in comparison to the effects if groundwater depletion, assuming a maximal sea level rise of 0.59 m (Ferguson and Gleeson, 2012; UNESCO, 2022).

Overall, due to growing water demand, groundwater depletion, water pollution, and climate change, water stress worldwide is assumed to rise. Non-sustainable groundwater withdrawal was also entitled "a ticking time-bomb for food security" (Bierkens and Wada, 2019). Furthermore, exposure to pathogens and toxic chemicals poses an additional threat (Schwarzenbach et al., 2010). To counteract a global water crisis in future, innovative technologies and research might play a key role.

2. State-of-the-art

A technology playing an essential role for solving the water crisis concerning quantity and quality represents pressure-driven membrane filtration. Applying reverse osmosis (RO) membrane filtration has been seen as the most economic process for desalination since the mid 1990s (van der Bruggen, 2018). Desalination can be used to make the largest global water resources (the oceans (Shiklomanoc, 1993)) available for human use (Darre and Toor, 2018). Besides, desalination can be applied to treat brackish groundwater to make it drinkable (UNESCO, 2022). Furthermore, RO enables the removal of most contaminants or pharmaceuticals, making it an important technology often used in water reclamation and reuse applications (U.S. EPA and CDM Smith, 2017; Warsinger et al., 2018; WHO, 2017). Furthermore, RO membranes also show promising removal of problematic chemicals like PFAS (Merino et al., 2016; Tang et al., 2006). Besides, water from reuse schemes utilizing RO might be used for managed aquifer recharge or direct injection projects as a hydraulic barrier for sea water intrusion (Ortuño et al., 2012; van Houtte and Verbauwhede, 2013). Nevertheless, a major challenge or even the "Achilles heel" (Flemming et al., 1997) of this technology is biofouling, basically a reduction of membrane performance caused by biofilms growing on the membrane and spacer surfaces (Najid et al., 2022; Nguyen et al., 2012; Vrouwenvelder and van der Kooij, 2001). Therefore, the overall aim of this dissertation was to elucidate the potential of using UV disinfection to reduce the negative impacts of biofouling. Within the following chapters, the basics and state-of-the-art of UV disinfection, pressure-driven membrane filtration, membrane (bio)fouling, and current fouling control strategies will be discussed.

2.1. UV disinfection

UV irradiation is an established disinfection procedure being researched for more than a century (Harm, 1980). It has the great advantage of being chemical-free with limited byproduct formation (Harm, 1980; Li et al., 2019b; Liberti et al., 2003; Romero-Martínez et al., 2019). UV irradiation covers the complete wavelength range from 100-400 nm, whereas 100-200 nm are known as vacuum UV, 200-280 nm as ultraviolet-C (UVC), 280-315 nm as ultraviolet-B (UVB) and 315-400 as ultraviolet-A (UVA) (U.S. EPA, 2006). Within UV disinfection the terms irradiance and fluence rate are differentiated. Whereas fluence rate is defined as the radiant power from all sides on an infinitesimal sphere divided by its cross-section area, irradiance only considers power from an upwind direction (Bolton and Stefan, 2002). When there is only irradiation from an upwind direction, irradiance is equal to fluence rate, and fluence is fluence rate multiplied by irradiation time (Bolton and Stefan, 2002). When light passes through an absorbing water matrix, irradiance is reduced. Following Beer-Lambert law, UV transmittance (UVT) [%] can be calculated using equation (2-1) with a being the (decadic) absorption coefficient [cm^{-1}], l the path length in the absorbing medium [cm], and $E(0)$ and $E(l)$

being the incident irradiance or irradiance after path length l [mW cm^{-2}] (Bolton and Cotton, 2022; Braslavsky, 2007; U.S. EPA, 2006).

$$T\,[\%] = 10^{-al} \cdot 100\% = \frac{E(l)}{E(0)} \cdot 100\%$$ (2-1)

2.1.1. Generation of UV light

Several different lamps exist to generate UV light. Probably the most common one is the low-pressure mercury lamp. It has an almost monochromatic spectrum at 253.7 nm, but a minor peak can be found at 184.9 nm, as well as some small emissions at higher wavelengths. Low-pressure lamps have their optimal operating temperature around 40 °C. However, also high-output mercury/Amalgam lamps have been developed, which have higher outputs and are operating around 100°C. If the envelope of such lamps is made from ultrapure quartz, transmitting the 184.9 nm peak, the lamp is also referred to as vacuum UV lamp. Another type of lamp is the so-called medium-pressure mercury lamp. They propose an alternative to low-pressure lamps with higher output, but a broad polychromatic spectrum with higher wavelengths. Furthermore, there are flash lamps (e.g., using xenon) producing high energy pulses of light, but those lamps are associated with low germicidal efficiency and lifetime. Besides, excimer lamps, producing a narrow band of wavelengths, have been developed, but those are still at the research stage. (Bolton and Cotton, 2022)

Aside from the above mentioned lamps, ultraviolet-light-emitting diodes (UV-LEDs) are a newly available option, receiving increasing research interest (Ibrahim et al., 2014; Mondal et al., 2021; Song et al., 2016). LEDs are solid-state semiconductor devices converting direct current into light (Chen et al., 2017). A p-n junction is created by doping a group II and IV element in a group III element (e.g. AlGaN) (Chen et al., 2017). The created bandgap influences the wavelength of light produced (Chen et al., 2017). Typically, the p-n junction is present in a layer-by-layer mode on a transparent sapphire substrate (Chen et al., 2017). UV-LEDs are heat sensitive, especially due to the current low light generation efficiencies (Chen et al., 2017). The LED chip can be housed in different ways (e.g. surface mount device (SMD)), impacting attributes like radiation pattern, optical output, and lifetime (Chen et al., 2017).

In comparison to conventional lamps, UV-LEDs have different characteristics. UV-LEDs have the advantage of not containing mercury, working with low voltages, and fast start-up times with the possibility of turning them on and off with a high frequency (Würtele et al., 2011). Furthermore, their compact and robust design enables novel reactor configurations, and they are available in different wavelengths (Song et al., 2016; Würtele et al., 2011). The UV-LEDs have a Gaussian/bell-shaped emission with a narrow bandwidth of approximately 10 nm and are available in the range of 250-400 nm (Bolton and Cotton, 2022; Chen et al., 2017). Efficiencies and lifetime of UV-LEDs were predicted to rise, as it has been observed with LEDs for visible light (Ibrahim et al., 2014). For visible light LEDs, efficiencies of 80% with lifetimes of 100,000 h are reported

(Koutchma et al., 2019). There have been some improvements since 2014, however, up-to-date (January 2023) this rise has not been observed at the predicted extent. Commercially available UV-LEDs are still limited in efficiency and lifetime. Common ultraviolet-C-light-emitting diodes (UVC-LEDs) have wall plug efficiencies (WPE) between 0.2 and 5% but also WPE of close to 10% have been reported (Compound Semiconductor Magazine, 2012, 2018; Koutchma et al., 2019). Still, the electrical to germicidal efficiency of UVC/UVB-LEDs (0.2-9.5%) is considerable lower than the one of low-pressure lamps with 30-40% (Koutchma et al., 2019). The same holds true for lifetime, with approximately 1,000-10,000 h for UVC/UVB-LEDs and 8,000 to 18,000 h for low-pressure lamps (Koutchma et al., 2019). Reasons for not having seen the increase in efficiency of UV-LEDs are complex and an own field of research. For a summary of the current challenges of UV-LEDs reaching higher efficiencies, the reader is referred to the study of Mondal et al. (2021).

2.1.2. DNA damage, repair processes, and biological effects of UV irradiation

According to Harm (1980), UV irradiation can have several effects on microbiological cells. By the usage of action spectra (comparing the relative disinfection efficiency of incident light vs. wavelength), it was concluded that nucleic acids are the main drivers for inactivation of bacteria and phages, as the action spectra of e.g. *Escherichia coli* resembled absorbance of nucleic acids quite well. Both proteins and nucleic acids show increasing absorbance at lower wavelengths (< 230 nm), however, proteins are showing a local maximum around 280 nm and nucleic acids between 260-265 nm. DNA consists of nucleotide bases, which can be categorized into purine (adenine and guanine) and pyrimidine derivates (cytosine and thymine). The first ones are of minor importance for UV disinfection as their quantum yields for decomposition are one to two orders lower than for pyrimidines (in the range of 10^{-4} mol Einstein^{-1}). As summarized by Harm (1980), photoproducts formed by UV irradiation include:

- Cyclobutane[1]–pyrimidine dimers (CPDs): Cyclobutane-pyrimidine dimers, also known as pyrimidine dimers, represents the most important DNA photoproduct. In total four different pyrimidine dimers can be formed in double-stranded DNA from two adjacent pyrimidine residues; thymine-thymine, thymine-cytosine, cytosine-thymine, and cytosine-cytosine dimers. In double stranded DNA, commonly dimers are configured as cis-syn, whereas for single stranded DNA trans-syn types are also found. At high UV doses, dimer formation and photoreversal of dimers are in equilibrium (50 mJ cm^{-2} for cytosine-cytosine and 200 mJ cm^{-2} for thymine-thymine dimers) (Errol C. Friedberg, 2006).

---

[1] Harm (1980) referred to this photoproduct as cyclobutyle-pyrimidine dimers, however in more recent studies, e.g. Sinha and Häder (2002), the photoproduct is known as cyclobutane-pyrimidine dimers

- Pyrimidine adducts: Similarly, as for CPDs, pyrimidine adducts are dipyrimidines built from neighboring pyrimidine bases in a DNA strand, but they occur at a lower rate in comparison to CPDs (e.g., 1/10 (Harm, 1980) or 25% (Sinha and Häder, 2002)). Commonly the pyrimidine adducts are referred to as 6-4 photoproducts (6-4PPs) (Sinha and Häder, 2002). In contrary to CPDs they might not be degraded by photoenzymatic monomerization, but by irradiation around 315 nm. When irradiated around 315 nm 4-6PPs can be further transformed into Dewar isomers (Errol C. Friedberg, 2006).

- Spore photoproducts: Formed in the absence of water, 5-thyminyl-5,6-dihydrothymine is a lethal dipyrimindine photoproduct in DNA. It is not found in vegetative bacterial cells, but in bacterial spores, e.g. *Bacillus subtilis* spores.

- Pyrimidine hydrates: Hydration causes a loss of the 5,6 double bond, e.g. in cytosine. Nevertheless, not all hydrates are stable at room temperature and biological significance of pyrimidine hydrates is not finally elucidated.

- DNA-protein crosslinks: The rarer crosslinking of DNA and proteins might interfere with DNA replication and cause lethality, but they might become rather important when few dimers are formed or dimers have been efficiently repaired.

- Strand breakage: UV irradiation directly leading to strand breakage is rare in comparison to e.g., CPDs (1/300 to 1/1000). Nevertheless, stand breakage must be repaired to maintain the integrity of the genome (Friedberg, 2003).

- Interstrand crosslinks: Interstrand crosslinks are as rare as strand breaks, but they likely interfere with cell replication.

Aside of direct damage of DNA, reactive oxygen species (ROS) can be generated by UV light (Errol C. Friedberg, 2006; Harm, 1980; He and Häder, 2002; Jager et al., 2017; Sinha and Häder, 2002). ROS, in general, can not only damage DNA but actually all intracellular macromolecules (Errol C. Friedberg, 2006). The effects of ROS for disinfection might become more important for longer wavelengths (Hamamoto et al., 2007; Pousty et al., 2021). For UVA irradiation and solar disinfection, protein and other damages have been reported to be important (Bosshard et al., 2010b; Bosshard et al., 2010a). Nevertheless, in this dissertation, UVA disinfection is not being discussed further.

As described by Harm (1980), the biological effects of DNA damages caused by UV irradiation are divers (Figure 2-1). There might occur damages with and without biological relevance. According to Harm (1980), for UV irradiated microorganisms, lethality/inactivation is referred as the loss of self-reproduction. Furthermore, inactivation/lethal effects of UV irradiation can be caused by functional or replicational damages. As an example, CPDs might not be recognized as the two original pyrimidines during DNA polymerase and synthesis is stopped. Besides, if early functions before nucleic acid replication are impaired, this could also cause lethality. On the other hand, microorganisms can be capable of recovering from DNA damage by repair processes. (Harm, 1980) Furthermore, two pathways of programmed cell death for *E. coli* have been reported, which can be triggered by DNA damage (Erental et al., 2012; 2014).
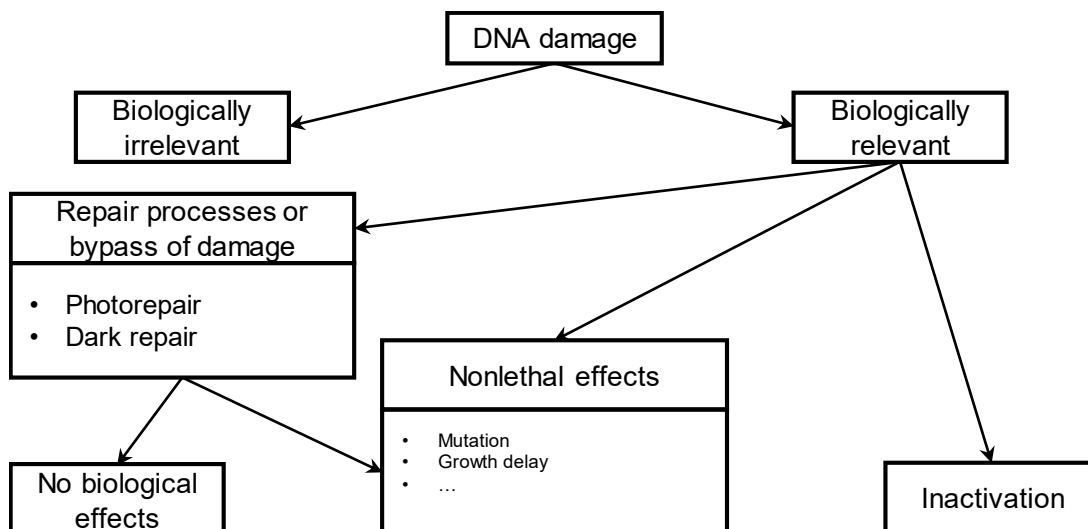
Figure 2-1:   Overview of consequences of DNA damages, adopted from Harm (1980).

Within repair processes, DNA damage might be directly reversed (e.g. photoenzymatic repair/photorepair), the damaged part of DNA is removed and replaced by a resynthesized section (e.g. excision resynthesis repair), or if more than one DNA molecule/strand is present in the cell, undamaged regions of one strand might be replicated and combined with the damaged molecule to form an intact one (recombination/postreplication repair). Within photorepair CPDs or other photorepairable lesions are monomerized by an enzyme. The enzyme first binds to the lesion. Following, light in the range of approximately 310-480 nm photolyzes the formed complex, leaving the repaired DNA and the enzyme. The photoreactivable sector (fraction of UV fluence rendered ineffective by photorepair) in biological systems can be high e.g., 0.9 as in the in vitro *Haemophilus* DNA system, low as 0.25 for phage φX or 0.5-0.7 for wild type *E. coli*. (Harm, 1980) Photorepair of 6-4PPs was reported for e.g., *Drosophila*, silkworm, *Xenopus laevis* but not for *E. coli* (Sinha and Häder, 2002; Thoma, 1999). According to Harm (1980), other repair mechanisms without the need of light can be grouped as dark repair. A major dark repair is the excision(-resynthesis) repair. In general, this repair mechanism includes four steps, the incision (UV endonucelease), followed by excision and resynthesis in either a cut-and-patch or patch-and-cut mode. Thereby complementary DNA strand serves as a template. Finally, the resynthesized nucleotide is rejoined by polynucleotide ligase. In contrast to photorepair, excision-resynthesis repair is less specific to the kind of DNA lesion. (Harm, 1980)

In other studies, the excision repair is divided into two important sub pathways, base extinction repair (BER) and nucleotide excision repair (NER) (Rastogi et al., 2010; Sinha and Häder, 2002). BER, thereby, is important for the repair of base lesions, e.g., caused by ROS, whereas NER can successfully repair DNA lesions like CPDs and 6-4PPs (Chatterjee and Walker, 2017; Rastogi et al., 2010). Additional repair processes found include mismatch repair for mismatched bases, single strand repair for single strand breakages and homologous recombination, as well as non-homologous end joining repair, important for double stand breakages (Chatterjee and Walker, 2017;

Rastogi et al., 2010). Furthermore, direct photoreversal and interstrand crosslink repairs are possible (Chatterjee and Walker, 2017).

Repair mechanisms are not limited to bacterial cells and can occur for viruses by host-cell reactivation, in which the cellular enzymatic repair mechanisms repair damages of phages. Furthermore, when several phages infect a host, multiplicity reactivation by genetic recombination and possibly also functional cooperation can occur. Other phage recoveries include among others marker rescue and Weigle recovery. (Harm, 1980)

The so-called SOS system is activated in bacteria subjected to DNA damage. An SOS response can be initiated by single stranded DNA generated during the DNA replication process with DNA lesions being present. Within the regulation of the SOS system, two proteins are of major importance, LexA and RecA. The SOS response itself is linked to the expression of many genes, including cell division arrest, excision repair, homologous recombination, and translesion DNA replication. Within SOS response, first genes for excision and recombination repair are induced, followed by encoding DNA polymerase II and IV. Besides, cell division might be inhibited to give more time for DNA repair. In case of excessive and not completely repaired DNA damage, translesion synthesis (TLS) can be activated, which is error-prone and can lead to higher mutations (especially for polymerase V), but enables replication and cell survival. TLS together with alternative error-free damage avoidance (DA) pathways are referred to as the DNA damage tolerance pathways. (Maslowska et al., 2019)

In general, observed nonlethal effects by UV irradiation include mutagenesis and a reduced rate of macromolecule synthesis, especially affecting DNA (more than RNA or proteins). Higher fluence was observed to lead to a longer time period of reduced synthesis. Reduced synthesis is likely caused by CPDs. Furthermore, CPDs can lead to shortened messenger RNA with incomplete information. Incomplete RNA can also lead to truncated polypeptide chains. Besides, due to UV damages, longer latent phases in phage multiplication and delay of bacterial cell division have been observed. Furthermore, CPDs at low fluence were suspected to cause filament formation of *E. coli* strains (cells showing elongation, leading to cell length increases of multiple times). (Harm, 1980)

Other indirect effects of UV irradiation include the induction of prophage (Harm, 1980; Landini, 2009). In addition, adenosine triphosphate (ATP) degradation of UV irradiated cells was observed, being faster for medium than for low-pressure UV irradiation (Yang et al., 2020). Reduced ATP levels were also observed for UVA and solar disinfection, along with reduced efflux pump activity, glucose uptake, and membrane potential, up to a loss in membrane integrity (Berney et al., 2006; Bosshard et al., 2010a). In addition, according to Kolappan and Satheesh (2011), surface adhesion, as well as extracellular polymeric substances (EPS) production of bacterial cells were reduced by UV treatment. Whereas protein reduction was only little, carbohydrate composition seemed to have changed. Nevertheless, another study rather suspected the reduced

viable cell count for a reduced cell abundance on surfaces by UV irradiation (Friedman et al., 2016).

The study of Fröls et al. (2008) showed the formation of type IV pili by DNA damage for the archaeon *Sulfolobus solfataricus* and changed cell aggregation depending on fluence. Thereby the highest aggregation was found at 7.5 mJ cm^{-2}. Higher fluence showed less aggregation (20 and 100 mJ cm^{-2}). DNA damage (double strand breakages) might induce this aggregation. Aggregation could not only shield cells from irradiation but might also enable DNA exchange and homologous recombination repair (Ajon et al., 2011; Fröls et al., 2008). UV induced aggregation was also found for some more but not all bacteria strains in the study of Vitzilaiou et al. (2021). Thereby in general, the aggregation led to higher protection against UV. In summary, UV damage can, but must not lead to the inactivation of cells.

2.1.3. Kinetics of UV disinfection

In general, UV disinfection is assumed to follow Bunsen–Roscoe reciprocity law, meaning UV disinfection solely depends on the product of fluence rate and time (fluence). If fluence is constant, the same disinfection results should be achieved for a high fluence rate and short irradiation time as for a lower fluence rate and irradiation over an extended time. Following the one-hit-one-target function, logarithmic survival/logarithmic reduction value (LRV) behaves linearly over fluence (Harm, 1980).

$$\frac{N}{N_0}[-] = e^{-k\,H'} \tag{2-2}$$

$$LRV\,[-] = log_{10}(\frac{N_0}{N}) \tag{2-3}$$

With N being the surviving cells, N_0 being the cell number without irradiation, H' being the applied fluence in mJ cm^{-2}, and k being the inactivation constant for the UV sensitivity of the irradiated cells in cm^2 mJ^{-1}. According to Harm (1980), this relationship is more useful to describe the inactivation of single stranded DNA/RNA viruses, but for other biological systems, it can show a different behavior. Shouldered curves can be observed at low fluence as the inactivation rather follows a multi-hit model or multi-target model or due to more efficient repair processes at lower fluence. Survival of the multi-target model can be calculated using equation (2-4) with n corresponding to the number of targets. The equation can be approximated with n multiplied by the one-hit-one-target curve for lower survivals. An example is shown in Figure 2-2a. (Harm, 1980)

$$\frac{N}{N_0}[-] = 1 - \left(1 - e^{-k\,H'}\right)^n \approx n\,e^{-k\,H'} \tag{2-4}$$

Furthermore, upward concave curves have been descried if multi-components (multiple fractions with different inactivation rates) are present, e.g. this can be observed at T3 phage plated on *E. coli* B and part of the T3 undergoing more host cell reactivation than others. For a simple two compartment model, survival can be calculated using the sum of the one-hit-one-target curves with f_1 and f_2 corresponding to the fractions of

each population. This approach can be extended for more fractions. The behavior of a two component system is depicted in Figure 2-2b. (Harm, 1980)

$$\frac{N}{N_0}[-] = f_1\, e^{-k_1\, H\prime} + f_2\, e^{-k_2\, H\prime} \tag{2-5}$$

On top, tailing effects are observed at higher fluence. Aside from more UV resistant subpopulations being present, they are likely caused by reactor hydraulics, cell aggregates, or other shielding effects (Azimi et al., 2017; Emerick et al., 2000; Kowalski et al., 2020; U.S. EPA, 2006; Würtele et al., 2011).
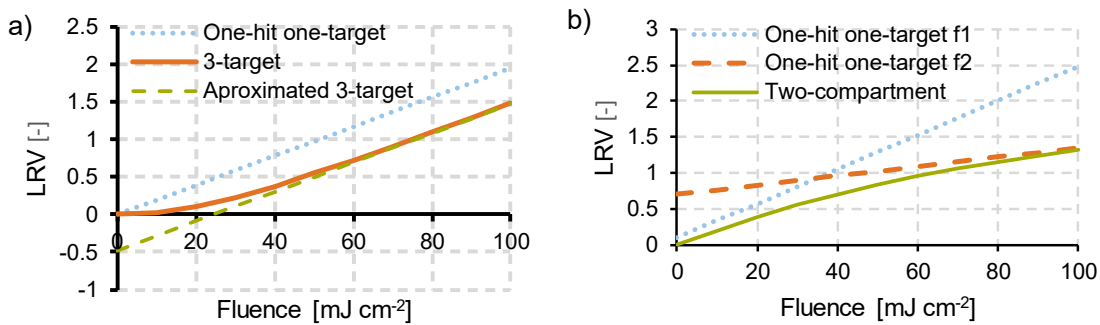
Figure 2-2:   *Exemplary comparison of a) one-hit one-target model to 3-target model and its approximated form and b) two-compartment model to the one-hit one-target models of the two compartments f1 and f2 separated.*

Even though Bunsen–Roscoe reciprocity law is generally accepted, with a higher fluence rate in the range of 0.002 to 0.2 mW cm^{-2} at 254 nm, Sommer et al. (1998) observed enhanced inactivation of *E. coli*. The enhanced inactivation was explained by repair enzymes being more affected under high irradiation. However, in the range of 0.1 to 0.001 mW cm^{-2} at 265 nm, Pousty et al. (2021) observed no deviation form Bunsen-Roscoe law but worse disinfection efficiency at higher wavelengths with increasing fluence rate. A possible explanation for the observed effects was that at higher wavelengths, disinfection by ROS becomes more important, and higher fluence rates lead to higher ROS concentrations with higher ROS-ROS reactions.

An additional effect observed is that with an increased wavelength of irradiation (275 instead of 268 nm), photorepair effects might be reduced, probably as protein damages caused inactivation to a greater extent (Nyangaresi et al., 2019). Interestingly effects were also observed by combining the irradiation of UVC, UVB and UVA in different manors for *E. coli (Song et al., 2019a; Song et al., 2019b)*. Whereas, the combination of UVC and UVB showed simple additive effects and no synergies, the simultaneous combination of UVC/UVB with UVA reduced disinfection performance, likely due to photorepair induced by UVA light (Song et al., 2019b). The same effect was observed when UVA irradiation followed UVC (Song et al., 2019a; Song et al., 2019b). On the contrary, when UVA was used as pre-treatment for UVC irradiation, cell photorepair was reduced, leading to overall increased disinfection efficiency (Song et al., 2019a). This effect seems to be caused by hydroxyl radicals generated by UVA and

is likely fluence dependent with a threshold between 1.7 and 17 mJ cm^{-2} of UVA irradiation (Song et al., 2019a). Those effects were not observed for MS2 virus (Song et al., 2019a; Song et al., 2019b). According to Xiao et al. (2018), however, the positive effect of UVA pre-irradiation was not observed for all tested *E. coli* strains. For one strain also negative impacts by UVA pre-treatment were observed. They linked the positive effects of pre-irradiation not to ROS but rather to reduced dark repair and increased CPD formation. Besides, they linked the observed negative impact of UVA pre-irradiation for one *E. coli* strain to an induction of TLS and hence increased survival.

2.1.4. Characterizing UV flow-through reactors

Characterizing a flow-through UV-reactor is more complex than a standardized, completely mix batch system. Non-parallel light, reflection, and light absorption of the water matrix can lead to a non-uniform fluence rate within a reactor. In addition, the reactor hydraulics can lead to, e.g., streamlines of microorganisms receiving less fluence than others. The resulting fluence distribution is critical for reactor characterization (Sun et al., 2022).

The standard method of characterizing a UV reactor for water disinfection is biodosimetry. Biodosimetry was the first time applied by Qualls and Johnson (1983). According to standardized procedures (NSF/ANSI, 2019; U.S. EPA, 2006), within biodosimetry, a challenge microorganism solution is injected into the system, and the LRV is measured for the desired conditions like flowrate, UVT, and UV intensity. The same microorganism solution is used in a collimated beam apparatus (CBA) test to set up a fluence-response curve. Within the experiments using a CBA, the exact fluence applied to the microorganism suspension can be calculated by using a calibrated radiometer and correction factors accounting for special variations among the used petri dish, UVT, beam divergence, and reflection (Bolton and Linden, 2003). The developed fluence response curve can now be used to calculate the reduction equivalent fluence (REF)/reduction equivalent dose (RED) and inactivation credits (U.S. EPA, 2006). If the target microorganism shows a different sensitivity than the used surrogate, corrections for so call RED bias might be needed (U.S. EPA, 2006). Biodosimetry has the advantage of directly predicting the disinfection capability of a UV reactor (Sun et al., 2022). On the other hand, major drawbacks include limited information about the fluence distribution, elevated costs for cultivation and analysis, different sensitivity of surrogated and target pathogens, as well as potential variability between different laboratories (Sun et al., 2022). Furthermore, for high fluence applications like UV based advanced oxidation processes (AOPs) it might be too sensitive and hence not practical.

Potential alternative methods for reactor characterization are particle dosimetry using dyed microspheres, the model-detector method or reactor modeling (Sun et al., 2022). Modeling of UV reactors has been successful several times (Jenny et al., 2014; Jin et al., 2005; Sun et al., 2022). It has the advantage of not needing an expensive

testing facility and giving information about fluence distribution and optical field, however, complex reactor designs can be challenging, and therefore results should be validated using a different approach like biodosimetry (Sun et al., 2022). Within the dyed microsphere method (also called Lagrangian actinometry), as described by the study of Blatchley et al. (2006), particles in the μm-range are covered with an actinometer. When exposed to UV irradiation, a fluorescent compound is formed on the particle surface. The fluorescence intensity of the particles can be assessed in flow cytometry, and hence the fluence distribution within the reactor is investigated. Even though this method was implemented successfully, background noise through other particles or substances present in the feed water scavenging the fluorescence can cause problems (Blatchley et al., 2008; Sun et al., 2022; Wols et al., 2012). For the model-detector method, a micro fluorescent silica detector is placed *in situ* in the UV reactor and combined with a CFD and optical model, it can achieve real-time fluence monitoring (Li et al., 2011; Li et al., 2017b; Sun et al., 2022)**.** Even though this is the only method allowing real-time and long-term monitoring, positioning of the sensor can be challenging and uniform fouling for the lamp and sleeve are assumed, which needs further investigations (Li et al., 2017b; Sun et al., 2022). All three methods have been validated in up-scaled, real applications (Blatchley et al., 2008; Jenny et al., 2014; Li et al., 2017b), but to the author's knowledge, they are not widely applied or part of industry standards.

Another method to characterize irradiation is actinometry. Actinometry utilizes the photolytic reaction of a chemical with a known quantum yield to estimate the photons absorbed in a defined space per time (Braslavsky, 2007; Kuhn et al., 2004; Rabani et al., 2021). In actinometry experiments, either the decrease of the chemical concentration (e.g., uridine) or the stoichiometric formation of a product (e.g., formation of I_3^- from KI/KIO$_3$) is measured (Rabani et al., 2021). When applying actinometry, the solution should be mixed effectively, and either all photons should be absorbed or there needs to be detailed knowledge about the absorbance (Kuhn et al., 2004; Rabani et al., 2021). In the current state, chemical actinometry is mainly applied for calibrating radiometers or fluence determination under highly controlled conditions (Bolton et al., 2011; Jin et al., 2006; Song et al., 2018; Wang et al., 2017). Its application to characterize flow-through reactors for water treatment is limited. In general, actinometry is a well-suited tool to validate model results at distinct points within a reactor (Jin et al., 2005). In addition, actinometry might be used to estimate the fluence or light intensity entering a system, which can further be used, for instance, in the radiative transfer equation to estimate the local volumetric rate of photon absorption (LVRPA), representing an important parameter in the field of chemical synthesis (Kayahan et al., 2020; Zalazar et al., 2005). Nevertheless, complex reactor geometries, reflections or non-parallel irradiation leading to unknown path lengths of the light traveling through the reactor can cause problems in average fluence determination. Furthermore, especially relevant for reactors used for water disinfection, with actinometry hydraulic shortcuts leading to reduced disinfection performance might not be detected. Currently,

the application of actinometry on its own cannot predict fluence distribution and REF in UV reactors for disinfection (Sun et al., 2022).

2.1.5. Pulsed UV disinfection

Pulsed UV irradiation using xenon flash lamps has already been proven to have beneficial effects for disinfection (Bohrerova et al., 2008; Elmnasser et al., 2007; Krishnamurthy et al., 2010; Wang et al., 2005; Wekhof et al., 2001). The irradiance of the studied flash lamps was in the range of kW cm^{-2}, and it could be shown that the positive effects increased with increasing intensity (Elmnasser et al., 2007; Wekhof et al., 2001). Bohrerova et al. (2008) observed an approximately two times higher efficiency of the pulsed disinfection of *E. coli*, T4, and T7 virus compared to the disinfection using a medium-pressure lamp in continuous mode. Elmnasser et al. (2007) summarized three mechanisms for enhanced disinfection:

- **Photochemical mechanism:** Inactivation which is caused primarily by dimer formation of pyrimidine bases in the DNA of microorganisms due to the UV irradiation (Elmnasser et al., 2007; Giese and Darby, 2000; Mitchell et al., 1992). In comparison to conventional UV disinfection, under pulsed UV disinfection, there seems to be no enzymatic repair mechanisms as the damages are too severe or the DNA repair system and other enzymatic functions itself are inactivated (Dunn et al., 1995; Elmnasser et al., 2007; McDonald et al., 2000; Smith et al., 2002).

- **Photothermal mechanisms:** High UV intensities at doses exceeding 500 mJ cm^{-2} can lead to temporary overheating and bacterial disruption (Elmnasser et al., 2007; Wekhof, 2000). A certain threshold, depending on the irradiated microorganism must be exceeded to achieve the thermal effects (Wekhof et al., 2001). Small steam flows induce membrane disruption as the water content of bacteria is vaporized (Elmnasser et al., 2007; Takeshita, 2003). Wekhof et al. (2001) observed disintegration of spores due to overheated cell content resulting in empty cells as well as severe deformation and rupture. According to Cover et al. (2001) cited by Elmnasser et al. (2007), heat could also contribute to cell death by a loss of protein functions as proteins are heat sensitive.

- **Physical mechanism** (effects on the membrane and cell composition): The destruction of nucleic acids might be accompanied by impacts on the cell's proteins, membrane, and other materials (Elmnasser et al., 2007). Takeshita (2003) found a higher concentration of eluted proteins under pulsed than continuous irradiation regimes. Microorganism cells exhibited structural changes like expanded vacuoles, cell membrane distortion and shrinking, change of the circular shape, cell content leakage, and collapsing of the internal cellular structures (Elmnasser et al., 2007; Krishnamurthy et al., 2010; Takeshita, 2003; Wekhof et al., 2001). Through the constant disturbance caused by the pulses, the

bacterial cells may undergo stress that results in structural damage (Krishnamurthy et al., 2010).

Bohrerova et al. (2008) further postulated that bacteria need to be subjected to damage of a certain degree that leads to inactivation (Labas et al., 2006; Severin et al., 1983). Furthermore, for higher intensities, there could occur a deviation from the time-dose reciprocity (Sommer et al., 1998) and there could be different mechanisms for bacteria and viruses. At high photon fluxes, also multiphoton absorption could play a role (Bolton and Cotton, 2022; Song et al., 2018).

Similarly, as for xenon flash lamps, UV-LEDs offer the possibility of flexible pulsed irradiation. Pulsed UV irradiation ($\leq$ 400 nm) using UV-LEDs was investigated in several studies, but the results are inconsistent (Li et al., 2010; Nyangaresi et al., 2019; Sholtes and Linden, 2019; Song et al., 2018; Tran et al., 2014; Wengraitis et al., 2013; Zou et al., 2019). On the one hand, Li et al. (2010), Tran et al. (2014), Wengraitis et al. (2013), and Zou et al. (2019) could observe beneficial effects of pulsed UV irradiations using UV-LEDs. Excluding the study of Li et al. (2010) using UVA irradiation at 365 nm, the wavelengths applied were ranging from 265 to 285 nm with irradiances between 0.0055 and ~0.1 mW cm^{-2} leading to maximum fluence applied for different pulse regimes in the range of 0.25 to 40-50 mJ cm^{-2}. The study of Li et al. (2010) applied fluence of up to 1,008 mJ cm^{-2} with a fluence rate of 0.28 mW cm^{-2}. Investigated microorganisms in water suspension were *Bacillus atrophaeus globigii* spores and *E. coli* as well as *E. coli* on agar plates and *Candida albicans* or *E. coli* biofilms. Compared to continuous irradiation, the studies showed a 1.8 – 6.3 times higher efficiency (concerning the fluence needed for a certain log-removal for different microorganisms). Whereas Li et al. (2010) observed the best results for 100 Hz and a duty cycle of 75% for the irradiated *E. coli* biofilms, Wengraitis et al. (2013) and Zou et al. (2019) concluded better results for the lowest tested duty cycles (5 and 10%) for *E. coli* on agar plates or in suspension. Wengraitis et al. (2013) noticed that their optimal frequency was 1 Hz, whereas the results of Zou et al. (2019) were independent of frequency.

The suspected mechanisms behind the positive effects were likely photothermal effects similar as described above (Li et al., 2010; Tran et al., 2014), an increased intensity of photons within the pulsation as well as a broader spectrum (Tran et al., 2014), and with increasing fluence severe destructions of the microorganisms are slowing down the repair mechanisms (Zou et al., 2019). Besides, Zou et al. (2019) argued that with higher irradiances microorganisms like *E. coli* could be affected by biological processes on top of the photochemical reactions. This would be similar to the phenomena described by Sommer et al. (1998), but no detailed explanation was given.

On the other hand, Nyangaresi et al. (2019), Sholtes and Linden (2019), and Song et al. (2018) did observe no significantly enhanced inactivation using pulsed UV-LEDs. The (peak) wavelengths applied in those pulsed irradiation studies were ranging from

265 to 282 nm with irradiances between 0.045^2 and 0.568 mW cm^{-2} leading to maximum fluence applied for different pulse regimes in the range of 2.7 to 60 mJ cm^{-2}. Tested microorganisms were *E. coli*, total coliforms in wastewater, *Pseudomonas aeruginosa* and MS2 phage. Investigated duty cycles were 10, 25, 50, 75, and 90% with frequencies of 0.1, 1, 10, 100, 1,000, 5,000, and 10,000 Hz. Hence, the used settings are comparable to the studies reporting an increased inactivation. Whereas Sholtes and Linden (2019) observed some enhanced inactivation after 10 mJ cm^{-2} for investigated bacteria (even tough not significant over the whole fluence range), Song et al. (2018) observed slightly worse disinfection performance for 90 and 75% duty cycle.

Several explanations were given by Nyangaresi et al. (2019), Sholtes and Linden (2019), and Song et al. (2018) for not observing significantly enhanced inactivation. As Xenon flash lamps have nine magnitudes of order higher intensities, Song et al. (2018) stated that a too low energy output could be the reason for neither seeing an effect nor photochemical or photophysical damage. They further argued that the cause for other studies seeing an effect is the different disinfection medium or an error in the fluence determination. They observed differences in the measured and calculated fluence when applying pulsation and hence recommended verifying the fluence using actinometry. Besides, they advised it should be avoided to normalize the log inactivation by UV fluence if a different fluence is applied. Nyangaresi et al. (2019) argued that even though fluence determination could be an issue, Zou et al. (2019) and Song et al. (2018) used the same actinometry. Following this, they opposed that the difference in LED power caused the discrepancies. Nevertheless, to the author's knowledge, it is not clear if Zou et al. (2019) determined the fluence of the LEDs under pulsed settings with the actinometer or only for continuous irradiation. Still, pulsed UV irradiation using LEDs might induce stress and turbulence on the biological processes in the cells, additional to the photochemical reactions with DNA and RNA, but the low power output might not be enough to lead to further inactivation (Song et al., 2018). Song et al. (2018) concluded that rather the high intensity of UV irradiation using flash lamps plays a key role for the increased inactivation than the pulse pattern. As UV-LEDs are continuously improving, they might reach intensities leading to additional disinfection effects (Nyangaresi et al., 2019; Song et al., 2018).

---

[2] Sholtes and Linden (2019) stated 0.045 mW cm^{-2} as lower range, but it is not clear if they used this also for pulsed experiments, as not all LEDs were used for pulsed irradiation. Nyangaresi et al. (2019) and Song et al. (2018) applied irradiances of 0.13-0.28 mW cm^{-2}.

2.2. Pressure-driven membrane filtration

Within (pressure-driven) membrane filtration, the membrane acts as a barrier separating two phases and/or is limiting the transport of various matters between the phases (Chen et al., 2006; Judd and Jefferson, 2003). In this chapter, first basics of membrane filtration will be described, followed by discussing membrane types and typical RO arrangements, as well as recent developments.

2.2.1. Basics of pressure-driven membrane filtration

As described by van der Bruggen et al. (2003), pressure-driven membrane filtration among others, can be differentiated according to pore size, applied pressure or retained chemicals (Table 2-1). Pore sizes are decreasing from microfiltration (MF) over ultrafiltration (UF) and nanofiltration (NF) to RO, which is basically considered as a dense membrane without any pores. While pore size is decreasing, the needed pressure for driving the filtration process increases. Whereas MF and UF mainly reject contaminates larger than pore size through sieving processes, for NF charge effects (like Donnan exclusion) play a role, leading to the rejection of ionic species smaller than the pores. NF membrane surface gets charged through the dissociation of functional groups and adsorption of charged molecules (Suhalim et al., 2022). In general, Donnan exclusion increases with the charge of ions/molecules, leading to higher rejection of divalent ions than monovalent ones for NF, but other non-sieving mechanisms like dielectric exclusion and hydration are of importance, too (Suhalim et al., 2022). Aside from steric exclusion, according to Bellona et al. (2004) long-term rejection of trace organic chemicals in NF filtration can be estimated by using the acid dissociation constant to check if solutes are charged at given pH and therefore electrostatic repulsion occurs.

Table 2-1: *Overview of different categories of membrane filtration, adapted from van der Bruggen et al. (2003)*

Process	Pore size [nm]	Typical pressure [bar]	Rejected species	Separation mechanism
Microfiltration (MF)	100 – 10,000	0.1 - 2	Particles, bacteria	Sieving
Ultrafiltration (UF)	2 - 100	0.1 - 5	All of MF plus viruses and macromolecules	Sieving
Nanofiltration (NF)	0.5 - 2	3 - 20	All UF plus multivalent ions and relatively small organics	Sieving & charge effects
Reverse osmosis (RO)	< 0.5 (dense)	5 - 120	All of NF plus monovalent ions	Solution diffusion

As derived by Lonsdale et al. (1965) for dense RO membranes, water and salt permeation is assumed to follow a solution-diffusion model[3] leading to the following relationship:

$$J_W \ [kg \ m^{-2} \ s^{-1}] = B_W \ (TMP - \Delta\pi) \tag{2-6}$$

where J_W is the water flux (also denoted in $L \ m^{-2} h^{-1}$ (LMH) with the mass of water converted to volume), B_W the water permeability coefficient, TMP the transmembrane pressure, and $\Delta\pi$ the difference in osmotic pressure across the membrane. Please note that compared to the equation by Lonsdale et al. (1965), a change in the sign for flux was done. Whereas osmotic pressure is directly proportional to the concentration of solutes, TMP is the difference between average feed and permeate pressure (Dreszer et al., 2013; Fane et al., 2011). Membrane fluxes and performances are well summarized by Fane et al. (2011), and it is referred to it in the following. According to Darcy's law, J_W can be expressed as

$$J_W \ [kg \ m^{-2} \ s^{-1}] = \frac{TMP - \Delta\pi}{\eta \ R_m} \tag{2-7}$$

with η denoting the dynamic viscosity of water and R_m the hydraulic resistance of water. Salt flow is not depending on TMP but on the concentration difference ΔC between concentrate and permeate as

$$J_s \ [kg \ m^{-2} \ s^{-1}] = B_s \ \Delta C \tag{2-8}$$

with J_s representing the mass salt flux, B_s the solute/salt permeability coefficient. Furthermore, the intrinsic solute rejection can be calculated using equation (2-9) with the solute concentration in the permeate c_p and solute concentration on the membrane surface c_m.

$$R_{int} \ [-] = 1 - \frac{c_p}{c_m} \tag{2-9}$$

Besides, as described by Fane et al. (2011) intrinsic rejection depends on TMP and osmotic pressure (equation(2-10)).

$$R_{int} \ [-] = \left(1 + \frac{B_s}{B_W \ (TMP - \Delta\pi)}\right)^{-1} \tag{2-10}$$

Nevertheless, intrinsic rejection is not observed directly. More commonly, the apparent or system rejections are compared relating c_p to the concentration in bulk c_b or in the feed c_f, as those are influenced by the system recovery and so-called concentration polarization.

---

[3] According to a recent study of Wang et al. (2023b), it was discovered that water flow in RO membranes is actually rather driven by pore flow than solution-diffusion mechanisms, but differences might be more relevant for higher pressures. A better depiction might be achieved over the solution-friction model.

$$R_{app}\ [-] = 1 - \frac{c_p}{c_b} \tag{2-11}$$

$$R_{sys}\ [-] = 1 - \frac{c_p}{c_f} \tag{2-12}$$

Concentration polarization describes an increased solute concentration on the membrane surface by the rejection of the membrane and a boundary layer formed. The effect of concentration polarization on R_{app} can be approximated with equation (2-13) with K being the mass transfer coefficient.

$$R_{app}[-] = \frac{R_{int}}{R_{int} + (1 - R_{int})\ \exp(\frac{J_W}{K})} \tag{2-13}$$

Aside from membrane fouling (Chapter 2.2.4), concentration polarization / in particular the up concertation of salts, is one of the main reasons why RO is generally applied in crossflow filtration mode (van der Bruggen, 2018). In contrast to dead-end filtration, where all of the feed stream is being filtered, in crossflow filtration, water moves parallel to the membrane surface, and only part of the water might be filtered, resulting in a permeate and concentrate stream (Mulder, 1996). K in equation (2-13) hereby is influenced by the crossflow, and in general, concentration polarization has a high impact for large modules with low crossflow and high flux (Fane et al., 2011). The ratio of permeate flow Q_p to feed flow Q_f is also known as recovery Y (Mulder, 1996).

$$Y\ [-] = \frac{Q_p}{Q_f} \tag{2-14}$$

The recovery of a RO membrane system again influences c_b and hence R_{sys} can approximated using equation (2-15) (Fane et al., 2011).

$$R_{sys}\ [-] \cong 1 - \frac{1 - (1 - Y)^{1 - R_{app}}}{Y} \tag{2-15}$$

Overall, a higher applied pressure results in higher water flux, diluted salt flux, and hence higher rejection, but this behavior is limited as at some point concentration polarization becomes significant. Furthermore, a higher recovery leads to lower fluxes and rejections, as it increases the bulk concentration of solutes. Typically, recoveries are limited to 50% for seawater desalination and 80% for water reclamation. In addition, temperature impacts the diffusion coefficient, but usually a larger increase is observed for the solute than for the water flux, leading to an overall reduced rejection. Increased crossflow in general leads to lower concentration polarization and hence higher flux and rejection, but effects are reaching a plateau for higher flows. Finally, with higher solute concentration, osmotic pressure is increased and hence flux reduced. (Bhattacharyya and Williams, 1992; Fane et al., 2011).

2.2.2. Reverse osmosis (RO) membrane types and module configurations

RO membranes are commonly either asymmetric cellulose acetate (CA) or thin film composite (TFC) membranes (Fane et al., 2011; Petersen, 1993). As outlined by

Petersen (1993), asymmetric refers to an anisometric structure, usually a denser surface with a porous sublayer, but both layers are made from the same material. A TFC membrane, on the contrary, consists of several layers made from different materials. Usually, they consist of three layers, typically, a 20-30 μm polysulfone (PS) or polyethersulfone (PES) layer is casted on a 100-200 μm non-woven fabric layer to provide mechanical stability for the active layer (Fane et al., 2011). The active layer, commonly is made from polyamide, sits on top of the supporting layer with a thickness of only ~100 nm and is responsible for most of the membrane's attributes like permeability and rejection (Fane et al., 2011; Petersen, 1993). The asymmetric CA membranes are manufactured by phase-inversion, whereas for TFC membranes, an interfacial polymerization process of aromatic amine monomers is utilized (Fane et al., 2011; Petersen, 1993). Due to carboxylic (–COOH) groups, TFC polyamide layers can be negatively charged at neutral pH (Fane et al., 2011; Tang et al., 2007). Additional coating layers can be used to further modify the attributes of the membrane (Fane et al., 2011; Tang et al., 2007). According to Fane et al. (2011) and Tang et al. (2007), important membrane characteristics are, among others,

- **Hydrophilicity,** measured as contact angle using a goniometer; the more hydrophilic, the higher the water permeability and in general, the lower the fouling propensity.
- **Surface roughness,** measured by atomic force microscopy (Williams, 2015); Usually higher roughness is associated with higher fouling
- **Surface charge,** measured as zeta potential over a range of pH; surface charge impacts the rejection of ions and organic molecules (Bellona et al., 2004; Suhalim et al., 2022), but charge is also linked to fouling propensity.

Overall, CA and TFC membranes show different attributes, as summarized in Table 2-2, but due to higher fluxes and rejections, TFC technology is mainly used in modern membranes (Fane et al., 2011).

Table 2-2:   *Comparison of asymmetric cellulose acetate (CA) and polyamide thin film composite (TFC) membranes according to Fane et al. (2011)*

Attribute	CA	TFC
NaCl rejection [%]	85-98	95-99.9
Permeability	Low	High
Hydrophilicity	Very hydrophilic	Less hydrophilic
Roughness	Smooth	Rough
pH range	4.5-6	3-10, up to 2-11
Resistance to hydrolysis	Low	High
Resistance to biodegradation	Low	Relatively good
Chlorine resistance	< 1ppm	< 0.1 ppm
Max. temperature [°C]	30	45

The produced membranes are employed in membrane elements to optimize packing density, possibility of cleaning and flow distribution. Several different element configurations exist, but for RO, spiral-wound membrane (SWM) elements have evolved as the standard elements for application in the (water) industry. They are combining high packing density (500 - 1,000 $m^2\ m^{-3}$) with good fouling management for waters without solids and moderate energy use, even though they might be more difficult to clean. To construct a SWM element, a permeate spacer (porous matrix, withstanding compressing but enabling water flow) is sandwiched by two membrane layers, which are glued on three sides. Several of such membrane "leaves" are connected with the permeate collection tube (Figure 2-3). Between the leaves, feed spacers (net like structures, enabling tangential cross-flow of water to the membrane surface) are added. The spacers and membrane leaves are wrapped around the collection tube and covered by a rigid housing. To withstand axial pressure drops, caused by the crossflow, anti-telescoping end caps/ anti-telescoping devices are implemented. Standardized diameters of such elements are 2.5, 4, and 8 inch, even though also 16 inch elements have been introduced with a common length of 40 inch. (Fane et al., 2011)
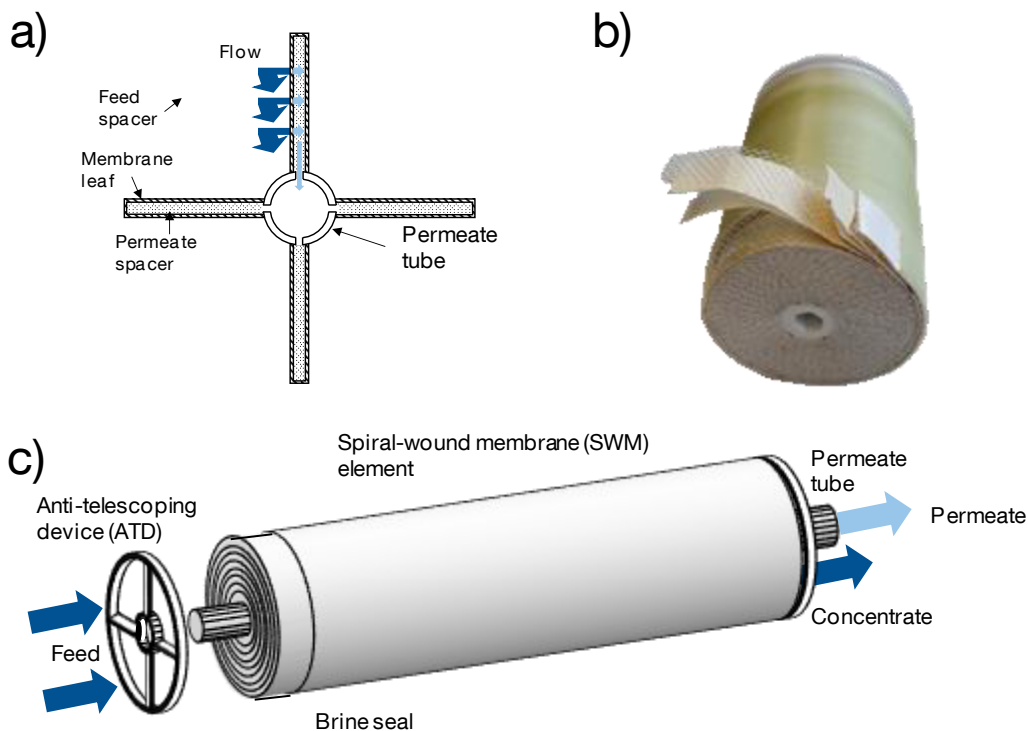
Figure 2-3:   a) Membrane leaves and spacer connected to permeate tube based on Fane et al. (2011); b) photograph of a cut open spiral-wound membrane (SWM) element; c) Schematic of a SWM element adopted from Chong and Fane (2021), Kim et al. (2013) and DuPont (2022a).

2.2.3. Reverse osmosis (RO) system configurations

Up to eight SWM elements can be fitted in series in a pressure vessel and form a RO membrane module (DuPont, 2022a). As shown in Figure 2-4, the permeate collection tubes of the elements are connected over an O-ring connecter, also known as coupler or interconnector. The first and last element can be connected to the permeate port, endcap, and outside piping system via an adaptor. (Bel, 2020; Bhattacharyya et al., 1992; CodeLine, 2009; DuPont, 2022a)

As described by DuPont (2022a), a complete RO membrane system not only consists of the membrane modules, but also pre- and post-treatment steps can be implemented. As further outlined by DuPont (2022a), pre-treatment depends highly on feed water quality. Well water is commonly pre-treated by acidification and/or anti-scalant dose and 5 μm pre-filtration. Surface water pre-treatment usually is more complex including the addition of processes like coagulation/flocculation, clarification, multimedia filtration, chlorination, as well as dechlorination. Overall, also other technologies like MF or UF are possible pre-treatment options. Post-treatment is applied to reach desired water quality and includes hardness adjustment, pH adjustment, and disinfection. For ultrapure water, polishing by electro deionization, ion exchange, and a polishing filter might be added. Furthermore, before discharging the concentrate/brine, it can be sent through an energy recovery device, pressurizing the feed (Fane et al., 2011). Energy recovery devices based on the pressure exchange principle may achieve efficiencies of > 94% (Voutchkov and Semanti, 2008). According to Kim et al. (2019) energy demand for seawater desalinization pre- and post-treatment is estimated with 1 kWh m^{-3}. For the whole RO plant, specific energy demands from < 3 to 6.7 kWh m^{-3} were reported, depending on e.g., feed salinity, pump efficiency, permeate quality, recovery, and energy recovery devices. Seawater desalination was calculated with 2.2 times the costs of the reclamation of secondary wastewater using RO (Côté et al., 2008). This was among others, caused by the seawater desalination running at four times the pressure due to the different feed water quality, higher feed flow (50% instead of 75% recovery) and membrane replacement (Côté et al., 2008).
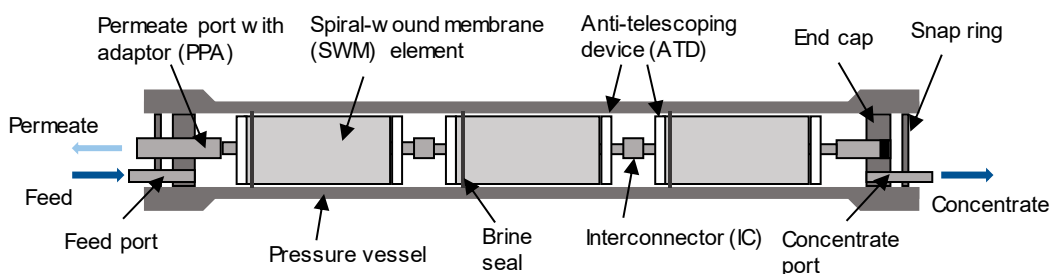
Figure 2-4: *Spiral-wound membrane (SWM) element assembled in a pressure vessel, adopted from DuPont (2022a), Bhattacharyya et al. (1992), Bel (2020), CodeLine (2009) and Kim et al. (2013)*

The membrane system itself consists of several membrane modules, which are elements housed in the pressure vessels, a pump, miscellaneous like instrumentation and spare parts, as well as a cleaning-in-place (CIP) system. The membrane system is typically designed for minimal feed pressure and membrane costs, but maximum permeate quality and recovery. Typically, permeate quality is assured by proper membrane selection, while feed pressure is adapted to reach aimed permeate flux, but considering fouling propensity. Within a module, typical feed channel pressure drop (FCPD), describing the pressure difference between feed and concentrate, usually is around 0.3 - 2 bar, depending on the number of elements, crossflow velocity[4], and temperature. Several modules can be operated in parallel to form a stage. Especially for higher recoveries, several stages in series are applied. Due to the reduced flow by permeate withdraw, later stages employ fewer elements. The ratio of elements used in the different stages is also referred to as the staging ratio, and, e.g., for seawater desalination, a ratio of 3:2 is commonly applied between stage 1 and stage 2. Within the first stage, feed pressure is the highest, whereas osmotic pressure difference is the lowest, which leads to most water being filtered in the first stage. To balance fluxes between the stages, tighter membrane elements might be used in the first stage, permeate back pressure applied or a booster pump used between the stages. To increase the recovery of membrane systems, a recirculation of concentrate can be applied, even though power consumption and salt passage might increase when doing so. Figure 2-5 shows an exemplary tapered two stage system with a staging ratio of 2:1 and a recirculation of concentrate. In contrary to recycling, also part of feed water can bypass the RO if lower permeate quality is sufficient. Finally, the permeate of the RO systems might be treated additionally with RO to archive higher quality, leading to a double pass system. (DuPont, 2022a)
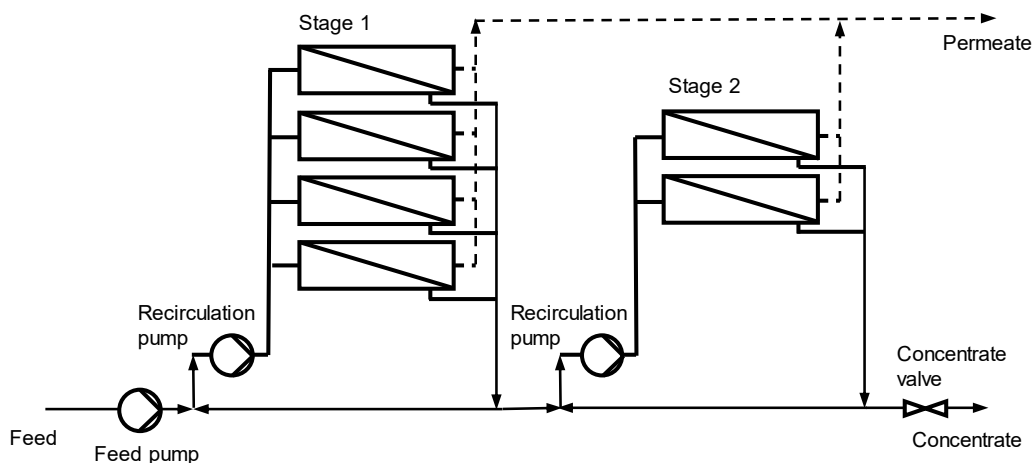
Figure 2-5:   Schematic drawing of a tapered two stage system with recirculation adopted from DuPont (2022a)

---

[4] According to Vrouwenvelder et al. (2009b), typical linear velocities in the lead elements can be around 0.07 to 0.20 m s^{-1}.

2.2.4. Membrane fouling

Membrane fouling (referring to the reduction of membrane performance over time) has been extensively researched over the past years, but is a major drawback of (RO) membrane filtration (Al-Amoudi and Lovitt, 2007; Guo et al., 2012; Jiang et al., 2017; Najid et al., 2022; Vrouwenvelder et al., 2010c). According to Jiang et al. (2017), from 1992 to 2017 more than 3,000 papers have been published addressing membrane fouling and even though current practices are able to reduce fouling, it cannot be completely avoided. A recent study estimated the cost of fouling for several RO systems to 24% of operational expenses (OPEX) (Jafari et al., 2021).

2.2.4.1.   Categories of membrane fouling

Overall, fouling can be separated into four different types, particulate/colloidal fouling, organic fouling, inorganic fouling/scaling, and biofouling (Guo et al., 2012). Particles in size similar to the pores might block the pores directly, whereas the other molecules (especially protein-like substances) might form cake or gel layers on the membrane surface (organic fouling) (Guo et al., 2012; Huang et al., 2008a; Hwang and Hsueh, 2003; Song and Elimelech, 1995; Zhu and Elimelech, 1997). In demineralization and desalination processes, concentration polarization of salts can lead to high salt concentrations on the membrane surface. These high concentration gradients can, amongst others, lead to the precipitation of salts, blocking the membranes, also referred to as inorganic fouling (Guo et al., 2012). Over a longer time period, also the growth of microorganisms on the surface can occur resulting in biofouling (Guo et al., 2012; Ivnitsky et al., 2005). Whereas colloidal fouling and inorganic fouling can be avoided through appropriate pre-treatment or the addition of acids and/or antiscalants, organic and biofouling can always be present (Vrouwenvelder et al., 2009c). Biofouling thereby was identified to be the most severe kind of fouling in many RO systems (Flemming et al., 1997; Najid et al., 2022; Nguyen et al., 2012; Vrouwenvelder and van der Kooij, 2001).

2.2.4.2.   Membrane biofouling und biofilms

Biofouling is defined as an undesired biofilm formation leading to unacceptable operational challenges (Characklis and Marshall, 1990; Vrouwenvelder et al., 2009c). According to Nguyen et al. (2012), problems associated with biofouling include the build-up of a biofilm with low permeability, which leads to an increased TMP needed for water treatment and hence to higher energy consumption. Besides, as Flemming (1997) summarized, the biofilm can lead to areas with no tangential flow increasing concentration polarization. The volume of the formed biofilm is blocking the flow channel in SWM elements, and several studies showed that the build-up of biomass correlates with an increased FCPD (Radu et al., 2010; Vrouwenvelder et al., 2009c; Vrouwenvelder et al., 2009a). Finally, cleaning procedures necessary to maintain membrane performance might impair membrane life span (Flemming et al., 1997), and

(CA) membranes might suffer from biodegradation (Murphy et al., 2001; Nguyen et al., 2012).

Biofilm formation can be categorized into three phases, i) induction phase (adhesion and primary colonization of surfaces by the planktonic cells in water phase), ii) logarithmic growth phase (when the growth of attached microorganism is higher than attachment), and iii) stationary phase (adhesion and cell growth are balanced with detachment and cell senescence) (Flemming, 1997). The dry mass of the biofilm itself usually contains the cells of the microorganisms with ≤ 10%, but the main components are EPS with > 90% (Flemming and Wingender, 2010).

The formed microbial community on high pressure membranes is diverse and amongst others influenced by nutritional levels, temperature, hydrodynamics, pre-treatment, and also by CIP procedures applied (de Vries et al., 2020; Zodrow et al., 2014). Bacteriological orders found in biofilms on high pressure membranes are *Burkholderiales, Pseudomonadales, Rhizobiales, Sphingomonadales,* and *Xanthomonadales* (de Vries et al., 2020). Thereby exemplary genera from the bacterial order are *Sphingomonas from Sphingomonadale* and *Rhodopseudomona* from *Rhizobiales* (Bereschenko et al., 2008; Bereschenko et al., 2010; de Vries et al., 2020; Gutman et al., 2014; Huang et al., 2008b; Pang and Liu, 2007; Sánchez, 2018). Furthermore, the genus of *Pseudomonas and Pseudoxanthomonas* are representatives of the orders of *Pseudomonadales and Xanthomonadales*, respectively (Baker and Dudley, 1998; Bereschenko et al., 2008; Herzberg and Elimelech, 2008; Ridgway et al., 1983; Sánchez, 2018; Tan et al., 2017). Within the order of *Burkholderiales*, the genus of *Polaromonas and Acidovorax* can be found (de Vries et al., 2020; Sánchez, 2018), but also *Aquabacterium,* a genus found in biofilms of drinking water distribution systems in Europe (Kalmbach et al., 1999) might be of relevance. The utilization of P*seudomonas spp.* / *P. aeruginosa* was recently advised as pioneer organisms to research the effectiveness of biofilm control measures in experiments using only a single strain (Curtin et al., 2020). Furthermore, fungi might also be important in RO biofouling (de Vries et al., 2020). Nevertheless, the found microbial community of biofilms and the one of the respective feed waters can differ (de Vries et al., 2020).

The EPS, which was also entitled "the perfect slime" (Flemming, 2017), mainly consists of polysaccharides, proteins, lipids, as well as DNA and is mostly produced by the microorganisms themselves (Flemming et al., 2017; Flemming and Wingender, 2010). It has various functions, e.g., protection, allowing for cell-cell communications, external digestive system, adhesion, sorption of organic compounds, retention of water, and aggregation of bacterial cells (Flemming and Wingender, 2010). Several factors like the microbial community present, shear forces, temperature, nutrients, and cell-cell communication can affect the production and composition of EPS, but exact mechanisms are still not well understood (Flemming, 2017; Flemming and Wingender, 2010; Frederick et al., 2011; Jiang and Liu, 2013). According to Flemming and Wingender (2010), the EPS matrix changes in charge, concentration, cohesion,

architecture and sorption capacity. Furthermore, they reported that different morphology and porosity could be found, with the EPS being smooth, flat, rough, fluffy or filamentous. In addition, by retaining lysed cells and DNA in the matrix it can contribute to horizontal gene transfer (Flemming and Wingender, 2010). The EPS itself is seen as a main driver for the hydraulic resistance of biofilms, whereas microbial cells might rather hinder the back diffusion of salts, resulting in elevated osmotic pressures on the membrane surface (Dreszer et al., 2013; Herzberg and Elimelech, 2007).

2.2.5. Current approaches for biofouling control

In general, biofouling control measures can be differentiated into three categories, **A) apparatus design and operation, B) biomass growth conditions,** and **C) cleaning agents** (Vrouwenvelder et al., 2010c). Each of those categories will be introduced further in the following section, even though some approaches might fit to more than one category. As the research field of biofouling control is broad, here just an overview will be given.

2.2.5.1. Apparatus design and operation

Apparatus design and operation approaches describe modifying membrane and spacer materials so they are less prone to fouling, but also suitable pre-treatment and biomass removal are included (Vrouwenvelder et al., 2010c). Many studies are focusing on membrane modifications, whereas according to Vrouwenvelder et al. (2009a), for SWM elements, biofouling is rather a feed spacer related problem. Siddiqui et al. (2017) observed that the geometrical design of feed spacers not only impacts the pressure drop of virgin feed spacers but also can reduce the feed channel pressure drop of biofouled spacers even though comparable amounts of biomass are present. Bucs et al. (2018) further emphasize the importance of spacer design for biofouling control in future studies. Overall, there exist numerous examples of membrane modifications, but also some that were changing feed spacer properties:

- Chae et al. (2015) embedded graphene oxide (GO) into the polyamide layer of TFC membranes, leading to reduced zeta potential, contact angle, and roughness, depending on the GO content. Besides, they observed increased water permeability, biofouling, and chlorine resistance.
- Yang et al. (2009) coated RO membranes and spacers with nanosilver. Both the coating of spacer and membrane reduced biofouling, but problems during long-term operation were observed, likely due to other foulants blocking the coating. The adaption of the spacer showed even longer lasting antimicrobial effects than for the membranes.
- Tang et al. (2015) added a polydopamine layer on polysulfone membranes, followed by an *in situ* formation of silver nanoparticles, which enhanced both, bacterial anti-adhesive and antimicrobial properties.

- Younas et al. (2016) created a super-hydrophobic PVDF membrane by adhesion of TiO_2 nanoparticles on the surfaces. Results showed lower contact angle and zeta potential with lower hydraulic resistance. Both adhesion and growth of bacteria on the membrane were reduced. In addition, fouled membranes showed enhanced recovery after cleaning.

Even though the studies showed promising results, abiotic fouling might pose a serious challenge to long-term efficiency of modified spacer or membrane surfaces (Flemming, 2020).

In general, an increased linear velocity in SWM elements leads to a higher influence of the biomass on the FCPD increase (Vrouwenvelder et al., 2009b). As biofouling is predominantly occurring in lead elements and the increase of FCPD caused by biomass is depending on flow, a possible option to reduce increased FCPD is to reverse flow direction (from former concentrate to feed side) as flow is reduced over membrane modules in series (Vrouwenvelder et al., 2009b). In laboratory experiments, a reduced overall substrate load as caused by such a switch lead to reduced biomass (Vrouwenvelder et al., 2009b). In practice, more elements in lead position might be used that reduce velocity and substrate load in each module leading to lower biofouling effects (Vrouwenvelder et al., 2009b). On top, as shown by Vrouwenvelder et al. (2010b), enhanced shear conditions in RO and NF systems lead to thin, compact biofilms, whereas reference experiments showed thick an fluffy biofilms. A thin biofilm might be beneficial in short term as impacts on FCPD are less, but the biofilm might be harder to be removed in long-term (Vrouwenvelder et al., 2010b).

Depending on the pre-treatment used, it might also impact the biomass growth conditions, e.g., phosphate or substrate removal. According to Jiang et al. (2017), pre-treatment steps for (bio) fouling control receiving great research interest in the past years included MF and UF, as well as coagulation and flocculation. Especially UF, but also MF might remove biomass and total organic carbon from the system. As an example, in the study of Vrouwenvelder et al. (2009d), UF pre-treatment showed significant effects on fouling, but biofouling of downstream NF could not be avoided completely. Coagulation and flocculation might be useful as they reduce dissolved organic carbon (DOC) (Jiang et al., 2017). Other researched pre-treatment technologies include granular media filtration to reduce DOC but also disinfection processes (Jiang et al., 2017).

Disinfection might represent a mean of biomass removal. The utilization of chlorine is further discussed in Chapter 2.2.5.2, whereas the application of UV irradiation as a chemical free disinfection is further outlined in Chapter 3. Nevertheless, in general, sterilization or complete biomass removal in technical systems might only be achieved by enormous efforts (Flemming et al., 1997). When disinfecting a system so that 99.99% of the microorganisms are removed, there are still enough left that can use nutrients to multiply and lead to biofouling (Flemming et al., 1997).

2.2.5.2. Affecting biomass growth conditions

Associated with changing biomass growth conditions are limiting substrate conditions, creating repetitive stress conditions, biofilm morphology engineering, changing cell adhesion, and biofouling inhibitor usage (Vrouwenvelder et al., 2010c).

Whereas the effects of biomass on FCPD increase depend on the linear velocity in SWM elements, the build-up of biomass seems to depend on substrate load (linear velocity and substrate concentration) (Vrouwenvelder et al., 2009b). Concerning the approach of limiting substrate conditions, Vrouwenvelder et al. (2010a) observed that not only carbon, but also phosphorus could be a limiting factor in some (extensively pre-treated) RO systems. Further, they discussed that in those systems, phosphorous limiting conditions are promising means to control biofouling, but the addition of phosphorus containing anti-scalants might increase biofouling. Nevertheless, phosphorous limiting conditions might be challenging to obtain in practice, especially as phosphate concentrations increase on the membrane surface due to concentration polarization and in general, by membrane rejection (Vrouwenvelder et al., 2010a). Phosphorous limitation might, among others, lead to a changed biofilm removability and adhesion protein production at the bacterial cell walls, but also to changes in the microbial community and EPS production (Javier et al., 2021b). In general, not only phosphorous but also nitrogen limitations affect biofilm composition and EPS (Desmond et al., 2018). Overall, the removal of nutrients can delay biofilm formation but likely cannot completely avoid it (Bucs et al., 2014; Flemming, 2020). Nutrients might not only be provided by the water, but also materials used in the installation might leach them (Flemming, 2020).

Repetitive stress conditions for controlling biofouling can be achieved by, e.g., low and high salt conditions like flushing with permeate to generate an osmotic shock, but also by varying between low and high flow velocities (Vrouwenvelder et al., 2010c).

Biofilm morphology engineering (e.g., through a combination of approaches), aims in reducing the negative impacts of biofouling. An example is to create open, porous structures by e.g., nutrient limitations and limited shear forces, which could generate fingerlike structures that can break and be flushed out of the module (Vrouwenvelder et al., 2010c). Besides, the movement of such filamentous structures might reduce concentration polarization effects (Vrouwenvelder et al., 2010c).

Another emerging field of research for biofouling control involves the interaction with cell-to-cell communication, i.e., quorum sensing (QS), to limit biofilm growth. Basically, bacteria are able to generate QS signals over messenger molecules like acyl homoserine lactones (AHLs) (Solano et al., 2014). QS molecules were found to impact EPS and play important roles in biofilm development/differentiation, but also in biofilm dispersal (Davies et al., 1998; Kampouris et al., 2018; Mukherjee et al., 2018; Solano et al., 2014). Hence, impacting QS was proposed as a biofouling mitigation strategy (Davies et al., 1998; Mukherjee et al., 2018). There are not only bacterial strains

generating messenger molecules but also some that are degrading them (quorum quenching (QQ) strains) (Kampouris et al., 2018). By adding the QQ strain *Lactobacillus* sp. into a membrane bioreactor, Kampouris et al. (2018) found reduced biofouling and EPS while maintaining COD removal. A similar successful application was shown by Iqbal et al. (2018), but this time QQ bacteria were embedded on the surfaces of so called QQ sheets within the membrane bioreactor. On the contrary of QQ, Wood et al. (2016) engineered an *E. coli* strain that limits its own biofilm growth by the expression of QS signals leading to biofilm dispersion. In addition, they adapted the strain to produce NO to further disperse biofilms of *Sphingomonas wittichii* and *P. aeruginosa* and to degrade Epichlorohydrin. In their experiments, the preconditioned membranes with the modified strain could successfully reduce fouling and degrade Epichlorohydrin. Nevertheless, aside from the potential release of the modified strain to the environment, the approach needs validation by experiments under real conditions (Wood et al., 2016). Even though there are many innovative approaches using QS or QQ, the prove of long-term success is still missing (Flemming, 2020), and some of the approaches might not be practical for cross-flow RO systems.

Using free chlorine (continuously dosed) as a biofilm inhibitor/disinfectant is problematic for RO systems, as the membranes can be damaged by it (DuPont, 2022a; Vrouwenvelder et al., 2010c). Instead of free chlorine, monochloramine could be used, however, disinfection byproducts like NDMA, which might be poorly rejected by RO membranes, can be formed (Vrouwenvelder et al., 2010c). In addition, an incorrect dosage of ammonia during the monochloramine formation could lead to free chlorine damaging the membrane (Vrouwenvelder et al., 2010c). Several other chemical biocides are available for the reduction of biofouling (Kucera, 2019). An alternative non-oxidizing biocide is 2,2-dibromo-3-nitrilopropionamide (DBNPA) (Bucs et al., 2018; DuPont, 2022a; Vrouwenvelder et al., 2010c).

2.2.5.3. Advanced cleaning procedures and early warning systems

To remove biofilms from biofouled modules, membrane manufacturers advise the application cleaning agents such as simple sodium hydroxide (NaOH) or NaOH mixed with sodium salt of dodecyl sulfate (Na-DDS) (DuPont, 2022a). Furthermore, membrane modules cleaned from deposits might be sanitized using 0.1% hydrogen peroxide (DuPont, 2022a). Nevertheless, during the cleaning, it is essential to remove the dead biomass as this could otherwise result in fast regrowth, and depending on the used chemical, the membranes might get deteriorated by the CIP itself (Bereschenko et al., 2011; Flemming et al., 2011; Nguyen et al., 2012; Saad, 1992; Vrouwenvelder et al., 2010c). The combination of urea with HCl seemed to outperform the conventional combination of NaOH/HCl cleaning concerning biomass removal and inactivation (Sanawar et al., 2021).

An alternative to using chemical cleaning agents, but also to reduce biofouling in general, could be the usage of bacteriophages. Bhattacharjee et al. (2015) could successfully restore membrane flux of biofouled membranes by a single bacteria

through the application of phages. Ma et al. (2018b) once immobilized T4 phages on a UF membrane operated in dead-end mode and once applied them in the feed of a cross flow system. The phages immobilized on the membrane surfaces could effectively reduce flux decline by *E. coli* biofouling. Spiking the feed with phages in crossflow mode showed higher benefits than when using the membrane with immobilized phages in crossflow, probably as phages were detached/washed away from the membrane. Ma et al. (2018b) further demonstrated that a fouled membrane operated in dead-end mode could be cleaned more efficiently than the control experiment using the phages in the washing solution. Nevertheless, for biofilms consisting of several species, polyvalent phages might be needed (Bhattacharjee et al., 2015), and like with QS approaches, long-term validation in practice is still missing (Flemming, 2020).

Another approach to increase membrane cleanability was to create protective layers on top of the membrane, which can be removed together with the fouling layer by flushing with high salinity feed and then being recovered *in situ* (Son et al., 2018). This approach showed promising results at lab-scale and dead-end filtration but still needs to be validated in practice (Son et al., 2018).

In general, the usage of membrane fouling simulators (MFS) is advised as an early warning system to initiate cleanings in an early biofouling stage to be more effective (Vrouwenvelder et al., 2010c). MFS basically represent a flow channel including the same membrane and spacers with identical flow channel height to mimic the hydrodynamic conditions and fouling behavior of SWM element (Vrouwenvelder et al., 2006). MFS have the advantage of flexible usage, being easy to handle while reducing water, chemical, and membrane area needed with non-destructive fouling observation over a sight window (Vrouwenvelder et al., 2006). Using higher flow velocities in the MFS parallel to the lead elements with sensitive FCPD measurement enhances the early warning, as through higher velocity, the impact of formed biomass increases and the higher substrate load results in a faster biomass build-up (Vrouwenvelder et al., 2011). In addition to early fouling detection, MFS might also be used to optimize inhibitor dosing (Vrouwenvelder et al., 2010c).

According to Vrouwenvelder et al. (2010c), biofouling shall ideally be controlled through a combination of single approaches but without the need of cleaning agents. Unfortunately, this might not be possible at the current state. On top, as the EU regulation 528 2012 aims to limit the harmful effects of biocides (EU, 2012), there currently is a great need for alternative biocide-free (pre-)treatment processes to limit the harmful effects of biofouling.

3. UV disinfection for biofouling control, research significance and hypotheses

An alternative, chemical-free pre-treatment[5] process for biofouling control represents UV disinfection. Probably because it has no residual effect, it is often not considered (Harif et al., 2011). At the time starting the dissertation (December 2018), a couple of studies already tested UV disinfection as a pre-treatment for biofouling control using low- or medium-pressure lamps, with a fluence of 20-400 mJ·cm^{-2} (Harif et al., 2011; Marconnet et al., 2011; Martino et al., 2011; Otaki et al., 1998). In those studies, a delayed build-up of biofilms in NF or RO membrane systems could be demonstrated using river or groundwater as feed in a full-scale application (Harif et al., 2011; Marconnet et al., 2011; Martino et al., 2011). Biofilms that were grown for a defined period of time exhibited a lower cell number, dry weight, as well as a reduced ATP, protein and polysaccharides content (Marconnet et al., 2011). Not only the quantity of biofilm was changed, furthermore, Harif et al. (2011) recognized a lower specific EPS production per biovolume and an altered microbial community composition. More specifically, Harif et al. (2011) reported a less diverse community with *Nitrospirae* and *Bacteroidetes* being reduced. On the contrary, *Parvularcula of the Alphaproteobacteria,* as well as *Betaproteobacteria* and *Chloroflexi* showed an increased abundance in the UV treated biofilm, *Alphaproteobacteria* in general, were not affected. Overall, a reduced viable cell count in the feed stream, changed adhesion properties, and EPS productions, as well as the differences in microbial community, were suspected as possible mechanisms behind the positive effects of UV pre-treatment for biofouling control (Friedman et al., 2016; Harif et al., 2011; Kolappan and Satheesh, 2011; Marconnet et al., 2011). Only the study of Lakretz et al. (2018) observed a reduced membrane flux with UV pre-treatment. Within the progress of the dissertation, a couple of other studies also investigating UV as a pre-treatment for biofouling control have been published (Hu et al., 2023; Wang et al., 2023a; Wu et al., 2021a). Two of these studies confirmed the positive effects of UV (Hu et al., 2023; Wang et al., 2023a), whereas one did not (Wu et al., 2021a). The proposed effects were similar and are further discussed in the introduction of Chapter 7. In summary, the positive effects of UV are conversely discussed and yet detailed mechanisms are not well understood, but the technology could have a great potential to save energy and chemicals for CIPs.

---

[5] There are some studies directly irradiating the surfaces/biofilms, e.g., Rho et al. (2022), but due to the difference in the process, direct irradiation versus pre-treatment, they are not further outlined here.

3.1. Objective 1: Evaluate the potential of continuous UVC irradiation using LEDs as an *in situ* treatment approach for biofouling control in high-pressure membrane applications

Compared to other technologies, e.g., UF, UV was not a commonly applied/researched pre-treatment technology for RO fouling control in the recent past (Harif et al., 2011; Jiang et al., 2017). Even though several reasons for the positive effects of UV pre-treatment have been proposed, currently, it is not clear if the observed changes in the biofilm composition are only linked to a delay of the biofilm formation, as experiments were terminated after a defined period of time (Harif et al., 2011; Marconnet et al., 2011; Martino et al., 2011) rather than a function of biofouling development.

While there exist several lamps for UV light generation (Chapter 2.1.1), it is worth considering and generating as much knowledge as possible with the newly emerging UV-LEDs. If their efficiency and lifetime rise in the future, they might replace conventional mercury containing low-pressure lamps. Additionally, through their compactness, the LEDs might be implemented in the treatment train with spatial proximity to the membranes, ideally integrated inside the pressure vessel of RO membrane systems, allowing easy retrofitting of existing systems without any or only a low spatial footprint. Besides, UV-LEDs are available at different wavelengths. As outlined in Chapter 2.1, UV has several other biological effects than just a simple inactivation of cells, which might vary depending on the applied wavelength. Nevertheless, in the long-term, it is suspected that for the change in biofilm attributes, a change in the microbial community might be a major mechanism.

Furthermore, it is suspected that for successful biofouling control, a lower fluence than for drinking water disinfection is sufficient, as the prime targets are rather less UV resistant bacteria and not viruses (e.g., a reaction rate constant at 254 nm around 0.5 cm^2 mJ^{-1} for *E. coli* and *P. aeruginosa* vs. 0.06 cm^2 mJ^{-1} for MS2 phage (Sholtes and Linden, 2019)). If already a low fluence for biofouling control could be sufficient, this would represent a new market opportunity for LEDs that are currently lacking high power output. Especially for an *in situ* integration of an UV pre-treatment inside the pressure vessel of an RO membrane system, space is limited. Therefore, it is important to clarify if also a low fluence is sufficient for biofouling control. Hence, combining the untouched potential of UV treatment as a chemical free technology for biofouling control with the emerging UVC-LEDs, offering the possibility to directly integrate the UV-treatment into the RO system, the following objective for this study is proposed:

Objective 1: *Evaluate the potential of continuous UVC irradiation using LEDs as an in situ treatment approach for biofouling control in high-pressure membrane applications.*

Within this research objective two hypotheses at lab-scale will be tested, one focusing on the quantification of the delay of biofilm build-up, the other one elucidating the impact of UV on the biofilm structure:

> **Hypothesis 1:** *UV treatment using UVC-LEDs with a fluence lower than 10 mJ cm^{-2} is capable of delaying severe biofouling (FCPD of 67 mbar cm^{-1}) of RO membranes by more than 10%.*
>
> **Hypothesis 2:** *Due to a change of the microbial community structure, UV treatment using UVC-LEDs with a fluence lower than 10 mJ cm^{-2} is resulting in 15% less hydraulic biofilm resistance at a severe biofouling state.*

To evaluate research hypotheses 1 and 2, a lab-scale RO membrane skid was built up using two MFS in parallel. To ensure reproducible results, the skid was fully automated and monitored using a computer added control system and a fully controlled biofouling protocol was established. To mimic biofouling under realistic conditions, local tap water was used as feed, and easily degradable nutrients were added to enhance the biofouling rate, enabling a higher number of experimental repetitions in a reasonable time. FCPD as a surrogate for the degree of biofouling, was monitored online and as soon as a value of 0.8 bar was reached, the biofilms were analyzed for various parameters, including ATP, total cell count, differentiating dead and live cells, proteins, and polysaccharides. To detect changes on the microbial community, 16S rRNA sequencing was performed and data was analyzed using the DADA2 pipeline (Callahan et al., 2016).

3.2. Objective 2: Establish a simple actinometrical method to quantitatively characterize the degree of reflection in UVC-reactors

As reviewed in Chapter 2.1.1, UV-LEDs represent a promising emerging alternative source for UV irradiation. Even though their efficiency might improve in the near future, in their current state, means to increase the fluence within a UV-LED reactor are of great interest. To increase fluence rates, new reactor designs and UV reflecting surfaces are a promising option (Chen et al., 2017; Li et al., 2017c; Mohaghegh Montazeri and Taghipour, 2023). Next to aluminum walls (Sommer et al., 1996), polytetrafluoroethylene (PTFE) (Silva et al., 2010; Weidner et al., 1985; Weidner and Hsia, 1981) could be an interesting material to increase reflections and therefore the path length of the light in novel reactor designs. Even though there were different methods proposed to characterize UV reactors, so far, next to biodosimetry, only modeling approaches are described in the literature to characterize the reflections in UV reactors (Bolton, 2000; Heidarinejad et al., 2020; Sommer et al., 1996). However, the reflection characteristics are important properties of an UV reactor to evaluate the disinfection performance for different UVT of the treated water (Sommer et al., 1996). Besides, e.g., for the application of UV-AOPs, higher fluence might be needed, proposing a challenge for biodosimetry, as the used challenge organisms might be too sensitive.

In the current state, chemical actinometry is limited to radiometer calibration, fluence determination under controlled conditions or at distinct points within a reactor, as well as estimating input power in a system to solve the radiative transfer equations (Bolton et al., 2011; Jin et al., 2005; Jin et al., 2006; Kayahan et al., 2020; Song et al., 2018; Wang et al., 2017; Zalazar et al., 2005). Especially in flow-through reactors, complex reactor designs, and non-parallel irradiation can result in unknown optical path lengths and therefore might be problematic for the application of actinometry. Nevertheless, objective 2 of this dissertation is to show that actinometry, if conducted and interpreted in the right way, can be an effective tool for fluence and path length determination, even in reflective/complex systems. Having a reliable actinometry method could enable fast and cost efficient UV reactor characterization (especially for UV based AOPs) and propose a new means of optical model validation.

Objective 2: Establish a simple actinometrical method to quantitatively characterize the degree of reflection in UVC-reactors.

To successfully develop an actinometrical procedure, a combination of actinometers could be helpful. The theory behind using KI/KIO_3 and uridine actinometry is quite different. For the KI/KIO_3 actinometer, all photons < 290 nm are absorbed and the fluence rate is calculated based on the product formation of I_3^- (Jin et al., 2006; Rahn, 1997). In contrary, uridine actinometry is based on the degradation of the educt uridine and a Taylor series expansion of the Beer-Lambert law, and might only be applied when the absorbance is low (Jin et al., 2006). The comparison of those two actinometers in reflecting UV reactors could provide valuable information. KI/KIO_3 actinometry might indicate the irradiation emitted by a UV source ($E_{0,\,source}$) but is likely not considering photons passing the solution more than once as those are absorbed in the first place. As uridine only absorbs a small quantity of the photons, it could indicate the total fluence rate in the reactor, including photons passing the solution multiple times due to reflections ($E_{0,\,total}$). Following, the ratio of $E_{0,\,source}$ to $E_{0,\,total}$ could be used to characterize the degree of reflection within a reactor. Hence, within research objective 2, hypothesis 3 will be tested:

Hypothesis 3: The ratio of fluence rate determined with uridine and KI/KIO3 actinometry can be used to quantitatively characterize the reflection in UV reactors.

To verify hypothesis 3, controlled actinometry experiments using uridine and KI/KIO_3 actinometer are performed using a collimated beam apparatus (CBA). Thereby a petri dish containing the actinometrical solutions is irradiated with a known energy. To introduce reflections, the bottom of the petri dish was lined with highly diffuse reflective PTFE foil. The results of the proposed actinometry method were validated using biodosimetry.

3.3. Objective 3: Elucidate the effect of fluence rate in pulsed UVC-LED irradiation on disinfection efficiency

One advantage of UVC-LEDs is that they offer the possibility of flexible pulsed irradiation. As reviewed in Chapter 2.1.5, pulsed UV irradiation using UV-LEDs was investigated in several studies, but the results are inconsistent. Some studies observed an enhanced efficiency for pulsed disinfection, whereas others did not. In the studies using pulsed UVC/UVB irradiation for the inactivation of microorganisms (Nyangaresi et al., 2019; Sholtes and Linden, 2019; Song et al., 2018; Tran et al., 2014; Wengraitis et al., 2013; Zou et al., 2019), either the time of pulsed irradiation was extended or the log inactivation normalized to fluence applied[6]. Besides, whereas for continuous irradiation, Sommer et al. (1998) observed a deviation from Bunsen-Roscoe with higher fluence rate leading to higher inactivation, opposite, wavelength dependent effects were observed by Pousty et al. (2021). Overall, it is not clear how pulsed irradiation affects microorganism inactivation at constant overall fluence and increasing the fluence rate (and not irradiation time) by more than one order of magnitude. Hereby, not only effects by sole pulsation, but also fluence rate could affect microbial inactivation in combination. Especially fluence rate in pulsed disinfection was suspected to be of great importance but has not been investigated in detail, yet (Song et al., 2018; Zou et al., 2019). Besides, if conducted in flow-through mode, pulsed disinfection could impact the overall fluence distributing, changing the observer LRV. To close the research gap on possible enhanced disinfection effects of pulsed irradiation with increased but well determined fluence rate in a flow-through system, objective 3 was derived.

Objective 3: Elucidate the effect of fluence rate in pulsed UVC-LED irradiation on disinfection efficiency.

In case pulsed irradiation is able to increase disinfection efficiency, this could be an additional advantage of LEDs counteracting their currently still limited efficiency. Following, within research objective 3, hypothesis 4 will be tested:

Hypothesis 4: With raising fluence rates (in the range of ~1 – 100 mW cm^{-2}), the disinfection efficiency of pulsed UVC-LEDs is increasing significantly by more than 30% for bacteria.

To test whether an increased fluence rate in pulsed UVC irradiation enhances overall disinfection performance, a flow-through UV-reactor was characterized using actinometry. Therefore, the developed actinometric method (objective 2) was adapted for flow-through mode. Besides, a new UV-reactor made from reflective material was utilized to increase the fluence rate up to 100 mW cm^{-2}. As challenge organism, a

---

[6] To the author's knowledge no study could be found that increased the fluence rate while keeping fluence constant in the UVB/UVC range and without the addition of photocatalytic substances. For higher wavelengths the reader is referred to the study of Gillespie et al. (2017).

bacterial species potentially relevant for biofouling was selected. Finally, with the same overall fluence, a continuous setting with a lower fluence rate was compared to a pulsed setting with an increased fluence rate during the pulses. When starting to work on objective 3, it was recognized that in order to perform reliable biodosimetry experiments at lab-scale and flow-through mode, especially with bacteria, several critical aspects need to be considered. In order to provide reliable results, first a method of biodosimetry needed to be developed. Using this biodosimetry method, pulsed and continuous settings were tested.

3.4. Objective 4: Investigate the potential of pulsed UV as an operational strategy for efficient control of biofouling

Even with no improved disinfection of microorganisms, applying pulse regimes can lead to better thermal management of the LEDs with reduced duty cycles (Nyangaresi et al., 2019; Sholtes and Linden, 2019; Song et al., 2018). Hence, this operation might lead to an increased LED efficiency and lifetime, reduced energy costs as well as to less shifted spectra (Nyangaresi et al., 2019; Sholtes and Linden, 2019; Song et al., 2018). For objective 4, possible beneficial effects for the disinfection efficiency of pulsed irradiation shall be combined with better thermal management of the UV-LEDs to optimize the pre-treatment for biofouling control in lab-scale.

Objective 4: Investigate the potential of pulsed UV as an operational strategy for efficient control of biofouling.

It is suspected that actually no additional biological mechanisms will be dominant for the pulsed compared to the continuous pre-treatment. Nevertheless, in the end for a plant operator, overall saved costs and energy are of major importance. Hence, hypothesis 5 focuses on energy efficiency.

Hypothesis 5: Applying pulsed UVC-irradiation as an operational strategy for biofouling control leads to 30% higher energy efficiency compared to continuous irradiation.

To estimate energy savings by (pulsed) UV pre-treatment for biofouling control, a series of experiments with different fluence in the range of 1.5 to 61.3 mJ cm^{-2} were performed. Thereby three settings with a comparable fluence of pulsed and continuous irradiations were compared. Based on the laboratory results, potential operational expenditure (OPEX) savings were estimated considering FCPD and the changed hydraulic resistance of the biofilms. In addition, OPEX were estimated, including savings by a lower number of CIPs needed and extended membrane lifetime. Finally, the effect of UV pre-treatment for biofouling control after CIP was tested in three experiments.

3.5. Objective 5: Validate the effect of *in situ* UV treatment for biofouling control under real feed water conditions in an up-scaled system

Even though (*in situ*) UV pre-treatment using LEDs might delay the biofilm formation and lead to a lower hydraulic biofilm resistance in accelerated biofouling studies, using a defined substrate at lab-scale, it is unclear if this effect translates to real applications. Different water matrixes, temperatures, pressures, and pH conditions might lead to biofilms with varying attributes like EPS content, porosity, and biodiversity. Furthermore, within the lab-scale experiments (objectives 1 and 4), the effects for biofouling control can only be related to a small part of an up-scaled system. Harif et al. (2011), Marconnet et al. (2011), and Martino et al. (2011) successfully tested UV pre-treatment for biofouling control in up-scaled systems using conventional irradiation systems at high fluence. Still, the *in situ* integration of the UVC-LEDs in a membrane pressure vessel, as well as the transferability of the quantified effects for biofouling control (objective 1) and energy efficiency (objective 3) remains unclear. Thus, the final objective of this study focuses on the upscaling of this technology.

Objective 5: Validate the effect of *in situ* UV treatment for biofouling control under real feed water conditions in an up-scaled system.

It is expected that the UV-LEDs can be integrated into the pressure vessel of an up-scaled system and that the effects are transferring to real feed water quality, so we hypothesize:

Hypothesis 6: *In situ* UVC treatment of the feed stream in the pressure vessel of RO membrane systems is reducing the impacts of long-term biofouling under real conditions.

Hypothesis 6 was investigated both, at lab- and pilot-scale. At lab-scale, experiments similar to objective 1 were performed, but instead of dosing easily degradable nutrients, real feed water from a groundwater supply was used. Furthermore, instead of using MFS, SWM elements in point-of-use scale /1.8'' were tested. For the experiments at pilot-scale, first, different possibilities to integrate the UVC-LEDs in the pressure vessel were evaluated. After successfully building a prototype reactor, the long-term effects of *in situ* UVC-irradiation on biofouling control were investigated in a real application. Within this test, three treatment trains (one with UV treatment, one with NaOCl dosing and one reference line), each consisting of a pressure vessel with a 4040 sized module installed, were run in parallel. Both continuous and pulsed UV irradiation were tested with several CIPs done throughout the runtime. Pilot-scale studies were performed in collaboration with UV-EL GmbH & Co. KG (Germany) and Delta Umwelt-Technik GmbH (Germany).

3.6. Dissertation structure

This thesis was prepared as a cumulative dissertation based on a collection of different peer-reviewed publications. The investigations of objectives 1-4 led in total to four peer-reviewed papers with the lead author's major contribution, each representing a standalone chapter in this dissertation. The results of objective 5 are represented in an own chapter, as well, but were not published in a journal. In addition, due to the significance of the developed actinometric procedure, another publication is currently in progress validating the actinometric procedure using an optical model coupled with computational fluid dynamics. Its state is outlined in Chapter 12.8.

Paper 1: "*Reducing the Impacts of Biofouling in RO Membrane Systems through In Situ Low Fluence Irradiation Employing UVC-LEDs*" by Philipp Sperle, Christian Wurzbacher, Jörg E. Drewes and Bertram Skibinski published in *Membranes 10 (12), 2020* is addressing objective 1 (Chapter 3.1) and elucidated research hypotheses 1 and 2. Herein, lab-scale biofouling experiments were conducted to prove the effects of low fluence UV pre-treatment on biofouling control.

Paper 2: *"An actinometric method to characterize performance of reflecting UVC reactors used for water treatment"* by Philipp Sperle, Andreas Mirlach, Karl Linden, Uwe Hübner and Jörg E. Drewes published in *Water Research* 230, 119543 2023, developed a new actinometric procedure and was investigating research objective 2 (Chapter 3.2) while proving hypothesis 3.

Paper 3: *"A practical bacterial biodosimetry procedure to assess performance of lab-scale flow-through ultraviolet water disinfection reactors"* by Philip Sperle, Mohammad S. Khan, Jörg E. Drewes and Christian Wurzbacher, published in *ACS ES&T Water 3 (8), 2130–2139*, 2023, describes a detailed hands-on protocol that was developed to enable reproducible biodosimetry experiments in lab-scale for biofilm bacteria. This protocol was needed to investigate objective 3 (Chapter 3.3) and to test hypothesis 4, whether disinfection efficiency in pulsed UV disinfection with higher fluence rate is increased.

Paper 4: "*Optimizing UVC-disinfection using LEDs as an energy efficient pre-treatment for biofouling control in spiral-wound membrane systems*" by Philipp Sperle, Mohammad S. Khan, Bertram Skibinski, Christian Wurzbacher and Jörg E. Drewes, published in *Desalination* 557, 116589, 2023, is addressing objectives 3 and 4 (Chapter 3.3 and 3.4), while elucidating hypotheses 4 and 5. It compared pulsed to continuous UV disinfection in biodosimetry and biofouling experiments with an additional OPEX calculation.

The structure of the cumulative dissertation is depicted in Figure 3-1, with a link to the respective thesis chapters, objectives, hypotheses, applied processes, and methods, as well as the published papers.

Process | **Methods** | **Objective** | **Hypothesis** | **Paper/Chapter**

Lab-scale | Reverse osmosis (RO) | Continuous UV | Biofouling experiments | Biofilm characterization

Objective 1: Evaluate the potential of continuous UVC irradiation using LEDs as an *in situ* treatment approach for biofouling control in high-pressure membrane applications.

Hypothesis 1: UV treatment using UVC-LEDs with a fluence **lower** than **10 mJ cm^{-2}** is capable of **delaying** severe biofouling (FCPD of 67 mbar cm^{-1}) of RO membranes by **more** than **10%.**

Hypothesis 2: Due to a change of the microbial community structure, UV treatment using UVC-LEDs with a fluence **lower** than **10 mJ cm^{-2}** is resulting in **15% less** hydraulic biofilm **resistance** at a severe biofouling state.

Paper 1 | Chapter 4

Collimated beam apparatus (CBA) | Biodosimetry | Actinometry

Objective 2: Establish a simple actinometrical method to quantitatively characterize the degree of reflection in UVC-reactors.

Hypothesis 3: The **ratio** of **fluence rate** determined with **uridine** and **KI/KIO$_3$ actinometry** can be used to **quantitatively** characterize the **reflection** in UV reactors.

Paper 2 | Chapter 5

Flow-through UV reactor

Objective 3: Elucidate the effect of fluence rate in pulsed UVC-LED irradiation on disinfection efficiency.

Hypothesis 4: With **raising fluence rates** (in the range of **~1 – 100 mW cm^{-2}**), the disinfection efficiency of pulsed UVC-LEDs is increasing significantly by **more** than **30%** for **bacteria**.

Paper 3 | Chapter 6

Lab-scale | Reverse osmosis (RO) | Pilot-scale | Pulsed UV | Biofouling experiments | Cleaning-in-place (CIP)

Objective 4: Investigate the potential of pulsed UV as an operational strategy for efficient control of biofouling.

Hypothesis 5: Applying pulsed UVC-irradiation as an operational strategy for biofouling control leads to **30% higher energy efficiency** compared to continuous irradiation.

Paper 4 | Chapter 7

Objective 5: Validate the effect of *in situ* UV treatment for biofouling control under real feed water conditions in an up-scaled system.

Hypothesis 6: *In situ* **UVC treatment** of the feed stream in the pressure vessel of RO membrane systems **is reducing the impacts of long-term biofouling** under **real conditions**.

Chapter 8

Figure 3-1: *Dissertation structure indicating applied processes and methods, investigated objectives and hypotheses with the link to dissertation chapters and published papers.*

4. Reducing the impacts of biofouling in reverse osmosis (RO) membrane systems through *in situ* low fluence irradiation employing UVC-LEDs

The following chapter shows the results of the investigations related to hypothesis 1 ("*UV treatment using UVC-LEDs with a fluence lower than 10 mJ cm^{-2} is capable of delaying severe biofouling (FCPD of 67 mbar cm^{-1}) of RO membranes by more than 10%*") and 2 ("*Due to a change of the microbial community structure, UV treatment using UVC-LEDs with a fluence lower than 10 mJ cm^{-2} is resulting in 15% less hydraulic biofilm resistance at a severe biofouling state*").

This chapter has been previously published with some editorial changes as follows:

4.1. Abstract

Biofouling is a major concern for numerous reverse osmosis membrane systems. UV pre-treatment of the feed stream showed promising results but is still not an established technology as it does not maintain a residual effect. By conducting accelerated biofouling experiments in this study, it was investigated whether low fluence UV *in situ* treatment of the feed using UVC light-emitting diodes (UVC-LEDs) has a lasting effect on the biofilm. The application of UVC-LEDs for biofouling control is a novel hybrid technology that has not been investigated, yet. It could be shown that a low fluence of 2 mJ·cm^{-2} delays biofilm formation by more than 15% in lab-scale experiments. In addition, biofilms at the same feed channel pressure drop exhibited a more than 40% reduced hydraulic resistance. The delay is probably linked to the inactivation of cells in the feed stream, modified adsorption properties or an induced cell cycle arrest. The altered hydraulic resistance might be caused by a change in the microbial community, as well as reduced adenosine triphosphate levels per cells, possibly impacting quorum sensing and extracellular polymeric substances production. Due to the observed biofilm attributes, low fluence UV-LED *in situ* treatment of the feed stream seems to be a promising technology for biofouling control.

4.2. Introduction

Many regions worldwide suffer from water scarcity (Mekonnen and Hoekstra, 2016; UNESCO). Especially if no conventional water resources are available, water reuse (Drewes and Khan, 2011), brackish groundwater or seawater desalination are viable approaches to provide alternative water supplies (Côté et al., 2005; Dolnicar and Schäfer, 2009; Drewes et al., 2017). In these scenarios, pressure-driven membrane filtration, including nanofiltration (NF) and reverse osmosis (RO), may act as a key process while employing advanced water treatment (Côté et al., 2005; Tomaszewska, 2007). Membranes are an attractive technology as they can reject both organic and inorganic contaminants as well as remove pathogens (Howe et al., 2012). However, fouling, a loss of membrane performance over time, is a significant drawback (Guo et al., 2012; Koros et al., 1996).

For many NF and RO applications, the presence of microorganisms and nutrients in the feed stream, especially biofouling is a major concern (Baker and Dudley, 1998; Flemming et al., 1997; Flemming, 2011, 2020; Vrouwenvelder et al., 2009c). Biofouling is defined as an undesired biofilm formation leading to operational challenges like a higher pressure drop, a reduction in membrane flux, an increased salt passage, and/or a reduced membrane lifetime (Characklis and Marshall, 1990; Flemming et al., 2011; Vrouwenvelder et al., 2009c). The biofilm is built up in three phases: 1) adhesion and attachment of microorganisms, 2) their growth, and 3) a stationary phase (Vrouwenvelder et al., 2009c) (p. 13). Amongst others, the adhesion phase is influenced by the microorganism species, their population density and physiological responses, as well as the concentration and composition of dissolved organic matter in the feed water (Nguyen et al., 2012; Wilbert, 1997).

The biofilm itself consists of microorganisms (usually ≤ 10% of dry mass) and a matrix known as extracellular polymeric substances (EPS) (Flemming and Wingender, 2010). Biofilms forming on membrane surfaces are comprised of a broad microbial community, which composition is influenced by the influent water matrix, degree of pre-treatment, temperature, and membrane type employed (Sánchez, 2018). Furthermore, the biofilm community can change with age (Khan et al., 2013; Sánchez, 2018). Commonly found microorganisms on high pressure membranes include, amongst others, Alphaproteobacteria *(e.g.,* Order/ Family/ Genus of Rhizobiales/ Bradyrhizobiaceae/ *Rhodopseudomonas or* Sphingomonadales/ Sphingomonadaceae/ *Sphingomonas)* (Bereschenko et al., 2008; Bereschenko et al., 2010; de Vries et al., 2020; Gutman et al., 2014; Huang et al., 2008b; Pang and Liu, 2007; Sánchez, 2018), Betaproteobacteria (e.g., Burkholderiales/ Comamonadaceae/ *Hydrogenophaga, Polaromonas and Acidovorax)* (de Vries et al., 2020; Sánchez, 2018), and Gammaproteobacteria (Pseudomonadales/ Pseudomonadaceae/ *Pseudomonas or* Xanthomonadales/ Xanthomonadaceae/ *Pseudoxanthomonas)* (Ayache et al., 2013; Baker and Dudley, 1998; Bereschenko et al., 2008; Bereschenko et al., 2010; Bereschenko et al., 2011; de Vries et al., 2020; Ferrera et al., 2015; Herzberg and

Elimelech, 2008; Khan et al., 2015; Kim et al., 2014; Ridgway et al., 1983; Sánchez, 2018; Tan et al., 2017; Zodrow et al., 2014). Further, de Vries et al. (2020) revealed that the community in the feed water and the corresponding biofilm differs. Microorganisms present in the fouling layer are usually only present in a small relative abundance in the feed. The composition of EPS, representing the 'glue' of the three dimensional architecture of the biofilms, varies depending on microorganisms themselves, shear forces, temperature, and nutrients (Flemming and Wingender, 2010). Aside from keeping the microbial cells together, EPS has several functions allowing intense interactions, cell-cell communication (quorum sensing), the formation of synergistic micro-consortia, adhesion and retaining extracellular enzymes (Flemming and Wingender, 2010). By keeping lysed cells and DNA in the matrix it also enables horizontal gene transfer (Flemming and Wingender, 2010). The EPS biopolymers include proteins, polysaccharides, nucleic acids, lipids and other organic matter fractions like humic substances (Flemming and Wingender, 2010; Wingender et al., 1999). The EPS matrix can vary in its concentration, cohesion, charge, sorption capacity and architecture (Flemming and Wingender, 2010). The morphology can vary in its porosity, as well as being smooth, flat, rough, fluffy or filamentous. Depending on hydrodynamic conditions, nutrient supply, bacterial motility, intercellular communication/quorum sensing, or exopolysaccharides and proteins the biofilm attributes can change (Flemming and Wingender, 2010). Within quorum sensing, N-acyl homoserine lactones (AHLs) molecules are commonly found (Uroz et al., 2009). Dreszer et al. rather linked EPS to the hydraulic resistance of biofilms than to the cells alone (Dreszer et al., 2013). Herzberg and Elimelech (2007) further revealed that (dead) cells are responsible for an increased salt passage by hindering the back diffusion of salts, leading to a higher osmotic pressure difference on the membrane surface, whereas EPS is mainly responsible for an increased hydraulic resistance.

Currently, there are different approaches to mitigate the unwanted effects of biofouling. These include

1. adaption of the equipment, design and operation, like suitable pre-treatment (e.g. ultrafiltration), optimizing hydrodynamic conditions, membrane surface modifications or feed flow reversal,
2. limitation of the biomass growth conditions by limiting essential resources such as carbon or phosphorus, or
3. application of cleaning agents as sodium hydroxide, monochloramine or other biocidal chemicals (Nguyen et al., 2012; Ridgway and Safarik J., 1991), (Vrouwenvelder et al., 2009c) (p. 291).

Each of the biofouling mitigation strategies has its own strengths and weaknesses. Whereas adaption of the equipment, design and operation, as well as the limitation of biomass growth conditions, can delay and reduce the negative impacts of biofouling, applying cleaning agents has its advantage in removing already established biofilms. Nevertheless, for cleanings it is important to remove the dead biomass as this

could otherwise lead to fast regrowth and depending on the used chemical, the membrane might get deteriorated (Bereschenko et al., 2011; Flemming et al., 2011; Nguyen et al., 2012; Saad, 1992; Vrouwenvelder et al., 2010c). According to Vrouwenvelder et al. (2010c), biofouling shall ideally be controlled through a combination of single approaches but without the need of cleaning agents. Unfortunately, this might not possible at the current state. Thus, even though there exist a variety of strategies for biofouling control, through performance losses, higher energy demand, downtimes in production, cleaning chemicals and their disposal, reduced membrane lifespan and other operational problems, biofouling is still associated with high costs (Flemming, 2011). Hence, there still is a great need for alternative, efficient biofouling mitigation strategies.

UV irradiation using mercury vapor lamps is a well-known approach for the inactivation of microorganisms. The inactivation is mainly caused by damages of the DNA through the formation of dimers (Harm, 1980; Hijnen et al., 2006; Soloshenko et al., 2006; Vilhunen et al., 2009). Other secondary effects caused by UV irradiation are direct and indirect damages of the cells' biomolecules by producing reactive oxygen species (ROS) or exiting photosensitizer molecules within or outside the cell (Reed, 2004). Pullertis et al. (2020) investigated the impact of UV disinfection on the microbial community of drinking water and its development during subsequent storage for six days at 7 °C. According to their findings the community after storage changed significantly. The guanine and cytosine (GC) content of bacterial genomes could be an indicator of UV resistance (Pullerits et al., 2020; Reichenberger et al., 2015; Warnecke et al., 2005). Furthermore, gram-positive and spore-forming organisms could be more UV resistant (Mason and Setlow, 1986; McKinney and Pruden, 2012; Pullerits et al., 2020; Riesenman and Nicholson, 2000). Aside from inactivation, in experiments using solar UV and UV-A disinfection, it was reported that adenosine triphosphate (ATP) levels per cell, efflux pump activity, membrane potential, and glucose uptake were reduced (Berney et al., 2006). Matallana-Surget and Wattiez (2013) reviewed that there are several different responses from microorganisms subjected to UV irradiation (DNA damage), including cell cycle arrest, repair pathways, stress responses, damage tolerance, and cell death. In general, (solar) UV radiation can lead to protein damage due to oxidative stress, including amino acid modifications, carbonyl group formation and protein-protein cross-links (Matallana-Surget and Wattiez, 2013).

Taking into account the various effects of UV irradiations on cells, UV disinfection of the feed stream could be a viable strategy to control biofouling. In particular, RO feed water is usually pre-treated to a great extent and hence, it commonly exhibits high UV transmissions, making it ideal for UV disinfection. Studies investigating the potential of UV-disinfection pre-treatment used low or medium-pressure lamps, with fluence between 20-400 mJ·cm^{-2} (Harif et al., 2011; Marconnet et al., 2011; Martino et al., 2011; Otaki et al., 1998). In several studies, it could be demonstrated that the UV-disinfection is delaying the build-up of the biofilm in NF or RO membrane systems using river or groundwater as feed in a full-scale application (Harif et al., 2011; Marconnet et

al., 2011; Martino et al., 2011). Further, biofilms grown during a defined period of time exhibited a lower dry weight, and cell number as well as a reduced ATP, protein and polysaccharides content (Marconnet et al., 2011). In addition, Harif et al. (2011) recognized a lower specific EPS production per biovolume and an altered microbial community composition. In particular, Harif et al. (2011) reported a less diverse community. Especially Alphaproteobactria genus of *Parvularcula* as well as, Betaproteobacteria and Chloroflexi exhibited an increased abundance in the UV treated biofilm. Alphaproteobacteria in general were not affected. On the contrary, Nitrospirae and Bacteroidetes were reduced. The reason for a positive effect for biofouling control could be attributed to a reduced viable cell count in the feed stream, as well as a change in the adhesion properties (Harif et al., 2011; Kolappan and Satheesh, 2011; Marconnet et al., 2011), with the exception of Lakretz et al. (2018), who observed a reduced membrane flux with UV pre-treatment.

So far, UV irradiation as a pre-treatment strategy for high-pressure membrane applications has not been examined in great depth, probably because UV disinfection of the feed stream has no residual effect on the downstream biofilm (Matin et al., 2011; Ridgway and Safarik J., 1991). Yet, it is not clear, if the observed changes in the biofilm, like lower EPS production per biovolume (2011), are only linked to a delay of the biofilm formation, as experiments were frequently terminated after a defined period of time (Harif et al., 2011; Marconnet et al., 2011; Martino et al., 2011) rather than a function of biofouling development.

Moreover, apart from low and medium-pressure lamps, recent developments in the semiconductor sector led to the emerged application of UVC light-emitting diodes (UVC-LEDs) (Song et al., 2016). These LEDs offer the opportunity to explore economically new designs and operations for *in situ* UV treatments as they are compact and robust, potentially more energy efficient with an increased life span, as well as they do not use or potentially release toxic mercury (Song et al., 2016; Würtele et al., 2011). The combination of higher lifetime and energy efficiency with the possibility of new reactor designs are of great interest as this could enable an *in situ* integration of the LEDs into the pressure vessel of RO systems.

This study aims to elucidate the potential of UVC irradiation using the recently developed UV-LEDs as an *in situ* pre-treatment strategy for biofouling control in RO or NF systems (Figure 4-1). In contrary to UV studies carried out previously, we will test if low fluences are sufficient to not only delay the biofilm formation but further lead to a reduced hydraulic resistance of the biofilm while approaching a severe biofouling state. To examine the mechanisms behind a change in hydraulic resistance, the biofilm formed will be analyzed for changes in ATP level, EPS composition, and microbial diversity. We hypothesize that in addition to a delay of the biofilm formation by inactivating microorganisms in the feed stream, the structure of the biofilm is changed with lasting impacts. If the effect of UV treatment is enduring, it would present an environmentally friendly biofouling control strategy, saving chemicals, energy and costs.
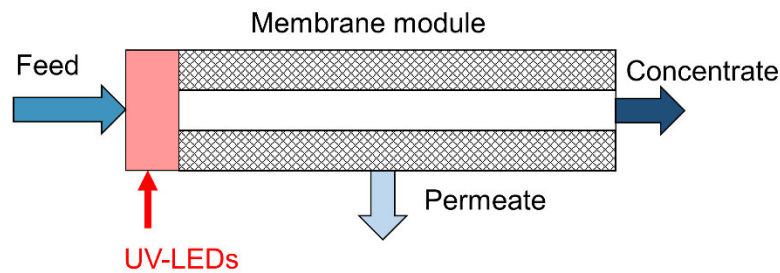
Figure 4-1:   *Schematic application of UV-LEDs for in situ biofouling control.*

4.3. Materials and methods

4.3.1. UV reactor and laboratory skid for biofouling experiments

The flow-through UVC-LED reactor consisted of an LED located directly over a silica glass pipe (7 mm diameter, 50 mm length), covered by an ABS housing. The LED type LEUVA66H70HF00 manufactured by LG Innotek (Seoul, Korea) has its peak wavelength in a range of 270-285 nm (typically 278 nm) with spectrum half width of 10 nm, a view angle of 110° and an optical power of 110 mW (Laser Components GmbH, 2018). An AMPYR LED30W controller (Lighting & Electronics Jena, Jena, Germany) was used to set the driving current, automatically adapting the needed voltage.

To investigate the potential of *in situ* UV pre-treatment for biofouling control, accelerated biofouling experiments employing membrane fouling simulators (MFS) (Vrouwenvelder et al., 2009c) were performed. A low-pressure RO membrane LOW1 (Oltremare, Fano (PU) Italy) was used of which an active membrane area of 2 x 12 cm was employed in a MFS (Figure 4-2). The feed spacer had a height of 20 mil in diamond shape with a porosity of 0.775 and a contact angle of 45°. The UVC-LED reactor was placed in immediate vicinity (< 10 cm) of the MFS, thus mimicking an *in situ* integration in the pressure vessel of an up-scaled system. A "UV-reactor dummy", simply a silica glass pipe with the same dimensions as used in the UV reactor, was attached to the reference train to ensure the same hydraulic retention times in the system. A detailed description of the skid is presented in the supplementary materials Figure S12-1 and Table S12-2 (Sperle et al., 2020b).
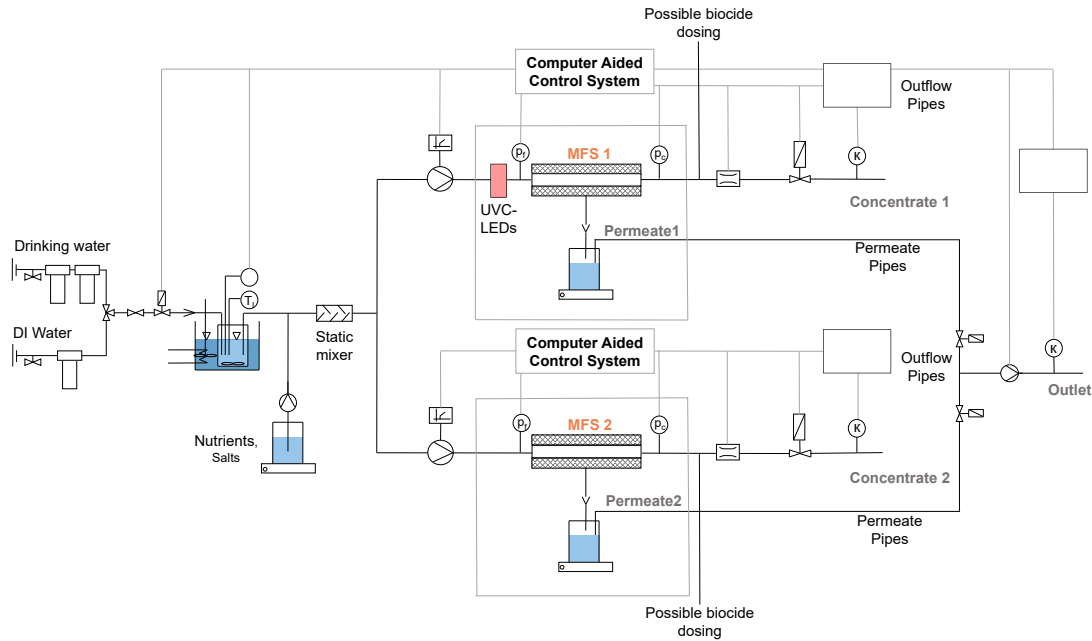
Figure 4-2:   *Schematic drawing of the lab-scale skid for biofouling experiments (further details of the operation are given in the supplementary materials (Sperle et al., 2020b)). MFS: Membrane fouling simulator; DI: Deionized*

4.3.2. Accelerated biofouling experiments

In order to quantify a delay in the biofilm build-up, a certain termination criterion needs to be defined. As neither the cell number within the biofilm nor the total biomass could be monitored online with the available methods, it was decided to take the feed channel pressure drop (FCPD) as a reference value. In previous studies, it was observed that with increasing biomass the FCPD is rising (Radu et al., 2010; Vrouwenvelder et al., 2009c; Vrouwenvelder et al., 2009a). Besides, membrane manufacturers advised taking action against biofouling if a FCPD increase exceeding 15% is observed (Vrouwenvelder et al., 2009c) (p 22). Even though it might not be possible to link the FCPD directly to the biofilm volume, FCPD is a reasonable criterion to quantify the delay of biofilm formation up to a certain degree of biofouling. In preliminary experiments in the 12 cm long MFS, the plateau phase of the FCPD started at values exceeding 1.5 bar. An arbitrary value of 0.8 bar (67 mbar·cm^{-1}) was chosen as the terminating criterion to be still in the exponential FCPD increase and to have a sufficient biofilm volume to monitor changes in the biofilm composition.

For the accelerated biofouling experiments, local tap water (groundwater, treated by aeration and sand filtration) under the addition of easily degradable nutrients 1,000:200:100 µg·L^{-1} of C:N:P (Dreszer et al., 2013) was used as feed. Sodium acetate served as C, sodium nitrate as N and sodium dihydrogen phosphate dihydrate as P source (all supplied by Merck, Darmstadt, Germany) supplemented to the tap water. The workflow for the biofouling experiments consisted of 4 basic steps (see supplementary materials for a detailed description (Sperle et al., 2020b)):

1. Cleaning and sterilization: Membranes were stored at 4 °C in 1% NaHSO$_3$ (Acros Organics, Geel, Belgium) till usage (DuPont, 2020). The cleaning of the system included flushing with 0.1% NaOH (Merck, Darmstadt, Germany) to remove organic matter (DuPont, 2020). Sterilization was done by autoclaving at 121 °C for 20 min or soaking in 0.25% H$_2$O$_2$ solution (Merck, Darmstadt, Germany), analogous to Dow (n.d.), DuPont (2020), Kucera (2019), Li et al. (2019a) and Ling et al. (2017).

2. Reassembling of the skid: After cleaning and sterilization, the skid was reassembled under sterile conditions.

3. Compaction: Before starting each biofouling experiment, a 16 h compaction, using a NaCl solution (Appli Chem, Darmstadt, Germany) was performed and the flux was set to 20 L·m^{-2}·h^{-1} (LMH). Depending on the initial membrane permeability, the feed pressure varied between 3.5 and 6 bar. The crossflow through the MFS is maintained at 4.25 L·h^{-1} resulting in an empty channel velocity of 0.116 m·s^{-1}.

4. Accelerated biofouling phase: Biofouling experiments were performed by using tap water as feed with nutrient dosing to reach the target concentration of 1,000:200:100 µg·L^{-1} of C:N:P (Dreszer et al., 2013). Temperature was maintained at 15 °C and feed pressure (set in compaction) was kept constant. When a FCPD of 0.8 bar was reached, the experiments were terminated.

4.3.3. Biofilm extraction and analysis

After terminating an experiment, the biofilm was extracted under sterile conditions and analyzed for the parameters shown in Table 4-1. Biofilm was extracted by cutting the membrane and spacer in a falcon tube containing 30 mL of 0.1 M NaCl and vortexing for 1 h similar as described by Matar et al. (2016). EPS was extracted by ultrasonic treatment (Han et al., 2013) and centrifugation (Matar et al., 2016). Detailed description is provided in the supplementary materials (Sperle et al., 2020b).

Table 4-1:   Analyzed biofilm parameters representing different biofilm attributes.

Parameter	Biofilm property
TOC/TOC$_{EPS}$	Total organic mass/Total EPS
ATP	Active biomass (Holm-Hansen and Booth, 1966) (Vrouwenvelder et al., 2009c) (p. 26)
Total direct cell counts (TDC)	Dead and living cells
Proteins and polysaccharides	EPS composition
Excitation emission matrix (EEM) (fluorescence spectroscopy)	Differentiation tyrosine- and tryptophan-like proteins
16S rRNA amplicon sequencing	Microbial community composition

4.3.4. Analytical methods

The methods used for analysis are the following:

- Total organic carbon (TOC) was analyzed as non-purgeable organic carbon using the Vario TOC cube analyzer (Elementar Analysensyteme, Langenselbold, Germany) (DIN e.V. (DIN EN 1484:2019-04)). Biofilm samples were diluted 1:50 prior to analysis.

- ATP was measured using the BacTiter-Glow assay (Promega, Walldorf, Germany). The manufacturer's guideline (Promega Corporation, 2016) was followed using flat white 96 multiwell plates (Thermo Scientific, Langenselbold, Germany) and the Tecan Infinite M Plex reader (Männedorf, Switzerland). ATP standards were prepared using adenosine 5'-triphosphat disodium salt (Sigma-Aldrich Chemie, Taufkirchen, Germany). As inner filter effects were observed during ATP analysis, each sample was diluted 1:5, 1:10 and 1:20. The luminescence signal was interpolated to an undiluted state and converted to ATP concentrations with the standard curve.

- Total direct cell counts (TDC) was performed following the procedure of Boulos et al. (1999) using the LIVE/DEAD BacLight kit (Thermo Scientific, Langenselbold, Germany). For filtration, the 0.22 µm black polycarbonate filter manufactured by Piper Filter (Bad Zwischenahn, Germany) were utilized. With this kit, it is possible to differentiate cells with intact and damaged cell membrane (Boulos et al., 1999). Images were taken using the Axioplan 2 imaging employing the Axiocam 503 color camera (Zeiss, Oberkochen, Germany). Cell counting was performed using the Matlab Version (R2018b, Mathworks, Natick, MA, USA) of the CellC software v. 1.2 (Selinummi et al., 2005).

- Protein analysis was done using the modified Lowry protein assay kit (Thermo Scientific, Langenselbold, Germany). Transparent 96 well flat transparent microplates (Greiner Bio-One, Frickenhausen, Germany) were used with the Infinite M Plex reader (Tecan, Männedorf, Switzerland). Protein standard curve was prepared using bovine serum albumin (Thermo Scientific, Waltham, MA, USA).

- Polysaccharides were quantified using the method described by Masuko et al. (2005). Concentrated sulphuric acid was purchased by Merck (Darmstadt, Germany), phenol by Sigma Aldrich (St. Louis, MO, USA). Standards were prepared using D-(+)-glucose (Alfa Aesar by Fisher Scientific, Kandel, Germany). The same multiwell plates and reader as for proteins were utilized.

- Fluorescence spectroscopy was performed using the Aqualog (HORIBA Jobin Yvon, Bensheim, Germany). Two different kinds of samples were analyzed: once the biofilm sample filtered by 0.45 µm (VWR, Radnor, PA, USA) and the EPS sample unfiltered. Both samples were diluted 1:20 to reduce inner filter effects. Instrument settings are summarized in the supplementary materials (Sperle et al.,

2020b). QS high precision cell made of quartz SUPRASIL by Hellma (Müllheim, Germany) was utilized as cuvette.

- For 16S rRNA amplicon sequencing, 1.5 mL of sample was freeze dried, resuspended in 50 µL nuclease-free water (Promega, Walldorf, Germany) and DNA was extracted using the DNeasy PowerSoil kit (Qiagen, Hilden, Germany). The rRNA sequencing was performed by ZIEL - Institute for Food & Health (Freising, Germany) using the primers 341F/806R and a MiSeq Reagent Kit v3 on an Illumina MiSeq benchtop sequencer (Illumina, San Diego, USA). Raw reads were uploaded to the European Nucleotide Archive (ENA) database (PRJEB41202 (ERP124942)).
- Anion and cation analyses were performed according to Standard Methods (DIN e.V. (DIN 38405-9:2011-09); DIN e.V. (DIN 38406-6:1998-07); DIN e.V. (DIN EN ISO 10304-1:2009-07); DIN e.V. (DIN EN ISO 6878:2004-09); DIN e.V. (DIN EN ISO 7980:2000-07)). Feed water characteristics are presented in supplementary materials (Table S12-1) (Sperle et al., 2020b).

4.3.5. Summary of the performed biofouling experiments

To verify the effects of *in situ* UVC treatment of the feed stream for biofouling control, in total eight biofouling experiments were performed. The first seven were performed with the maximum UVC-LED driving current of 360 mA, in the eighth experiment only 180 mA was used. The first experiment could not be stopped on time, so one biofilm analysis (except 16S rRNA sequencing) could not be performed. Experiment 3 had operational problems, thus only the biofilm analysis is available for that run. Experiment 7 was run only with intermittent permeate production (4 days with permeate production for membrane conditioning, then only about 2-3 h per day and finally the last hours during FCPD increase). This approach followed a recommendation by Vrouwenvelder et al. (2009c) (p. 62-63) to clearly depict the effects of biofouling. They did not observe an influence of permeate production on biofouling, but it might reduce the impacts of other kinds of fouling. Still, this setting was only used once, as the aim of the study is to show the effects on fouling as close to real applications as possible. This resulted in six data sets for the membrane performance and biofilm attributes at a driving current of 360 mA. Table 4-2 summarizes the settings of these experiments.

Table 4-2:   *Summary of experimental settings.*

Experiment No.	Line with UV treatment	UV dummy[1]	LED current [mA]	Membrane performance data	Biofilm analysis
1	1	Yes	360	Yes	16S
2	1	Yes	360	Yes	All
3	2	Yes	360	No	All
4	1	No	360	Yes	All
5	2	No	360	Yes	All
6	2	No	360	Yes	All
7	1	No	360	Yes, intermittent permeate production	All
8	1	No	180	Yes	No

[1] Silica glass pipe to ensure same hydraulic retention times in the reference line.

4.3.6. Actinometry

Actinometry using KI/KIO_3 was performed to measure the fluence delivered by the UVC-LED reactor to the water. The protocol was adapted from Rahn (1997), Rahn et al. (2003), Wang et al. (2017), and Zou et al. (2019) and is shown in greater detail in the supplementary materials (Sperle et al., 2020b). A similar but simpler, laboratory-scale skid was set up to perform actinometry experiments. The details are given in the Supplemental Information Figure S12-3 and Table S12-3 (Sperle et al., 2020b), as well. The setup used consisted of a water bath, a pump, a flowmeter, a pressure sensor and a needle valve. To perform the actinometry experiments, a 0.6 M KI (Merck, Darmstadt, Germany), 0.1 M KIO_3 (VWR, Darmstadt, Germany) and 0.01 M $Na_2B4O_7 \cdot 10 H_2O$ (Sigma-Aldrich, Taufkirchen, Germany) solution was prepared (Rahn et al., 2003). The pH of the finished solution was between 9 – 9.2. The solution was adjusted to 23.5 °C in a temperature-controlled water bath, the temperature in the cabinet was set to 15 °C and UVC-LED reactor was turned on for at least 15 min to allow a warm up. Within an actinometry experiment, several flow steps were tested, ranging from approximately 1 to 6 $L \cdot h^{-1}$ leading to hydraulic retention times in the reactor of 0.7 to 6 s. Samples and blank were taken in triplicates and the absorbance at 352 nm was determined using the DR6000 UV-Vis spectrophotometer (HACH, Düsseldorf, Germany).

4.3.7. Data analysis

Outlier analysis for pressure data and calculated permeability (e.g. caused by an emptying of the beaker collecting the permeate) was done based on the interquartile range (Ranga Suri et al., 2019) (p. 14) of a 3 h interval. The detailed procedure is described in the supplementary materials (Sperle et al., 2020b).

Parallel factor (PARAFAC) modeling was performed using the Matlab based drEEM Toolbox V. 0.5.1 (Murphy et al., 2013) available only at http://dreem.openfluor.org/. Components were identified using the OpenFuor database (Murphy et al., 2014). The PARAFAC modeling steps and the model itself are given in the Supplement Information (Sperle et al., 2020b). The model was validated using variance explained, core consistency and split-half analysis (Bro and Kiers, 2003; Murphy et al., 2013; Stedmon and Bro, 2008).

16S rRNA amplicon sequencing data were processed using the R based DADA2 pipeline (V. 3.11) (Callahan et al., 2016) and DECIPHER package 2.16.1 (Wright, 2016). SILVA_SSU_r138_2019 was used as database, available online under: http://www2.decipher.codes/Downloads.html. In case a genus could not be assigned with the Silva database, the gene sequence was identified using BLAST (Altschul et al., 1990; Zhang et al., 2000) available online (https://blast.ncbi.nlm.nih.gov/Blast.cgi) against the INSDC databases (Karsch-Mizrachi et al., 2018). For testing an overall change in the microbial community, microbial counts were rarefied (Heck et al., 1975; Hurlbert, 1971) and compared in a distance based redundancy analysis (Legendre and Anderson, 1999; McArdle and Anderson, 2001) by using the R package vegan 2.5-6 (Oksanen et al., 2019). Dissimilary was calculated by the Bray-Curtis distance. Further, permutational multivariate analysis of variance using distance matrices (PERMANOVA) (Anderson, 2001) using the vegan (Oksanen et al., 2019) package were applied to detect differences in the community. To test for differential abundance of single genera, generated count data were processed using the DESeq2 R package 1.28.1 (Love et al., 2014), applying the "ashr" shrinkage estimator (Stephens, 2017). Corrections for false discovery rates within the calculations was performed according to Benjamini and Hochberg (1995). For Pearson correlation, data were transformed following the Rhea pipeline, applying a centered log- ratio/scaling (Lagkouvardos et al., 2017). Hereby only species present in 30% of the data and correlations with 4 data pairs were considered.

4.4. Results and discussion

4.4.1. Characterization of the UVC-LED reactor

The UVC-LED reactor was characterized three times for the maximum driving current of 360 mA using KI/KIO$_3$ actinometry: before the first experiment with 1.32 mW·cm^{-2}, after the first three experiments with 1.35 mW·cm^{-2}, and after five runs with 1.12 mW·cm^{-2} (mean = 1.26 mW·cm^{-2}). With a hydraulic retention time of approximately 1.6 s at a flow of 4.25 L·h^{-1}, this leads to a fluence of 2 mJ·cm^{-2}. Comparing the fluence to the study of Jarvis et al. (2019), who reported an inactivation rate of 0.171 cm^2·mJ^{-1} for MS2 phages using a 275 nm LED with an irradiance of 4.9 mW·cm^{-2}, this would result in log removal of 0.35. The applied fluence of 2 mJ·cm^{-2} is ten or more times lower compared to the fluences applied for UV disinfection as biofouling control previously reported in literature (Harif et al., 2011; Marconnet et al., 2011; Martino et al., 2011;

Otaki et al., 1998). For a setting of 180 mA, no actinometry was performed. However, reducing the current from 360 to 180 mA, according to the datasheet of the LED (Laser Components GmbH, 2018), would result in approximately 42% of the irradiation power (0.85 mJ·cm^{-2}).

4.4.2. Impact of UVC pre-treatment on the biofilm formation and hydraulic resistance

Seven successful biofouling experiments were performed, six at a fluence of 2 mJ·cm^{-2}, one at 0.85 mJ·cm^{-2}. A representative time series of the FCPD increase and the drop of the relative membrane permeability after compaction for one of the experiments is depicted in Figure 4-3. The other biofouling experiments performed showed similar curves (data not shown). The time for the biofilm growth for biofouling experiments is comparable to times reported in literature (Farhat et al., 2016). The initial increase of permeability is likely to be caused by the storage in $NaHSO_3$ and H_2O_2. This increase is similar as reported by Harif et al. (2011), who linked it to modified surface properties of the membrane as they are sensitive to cleaning agents (Subramani and Hoek, 2010). Nevertheless, no detailed explanation was given. Within the time series of the FCPD increase and permeability decline, a clear distinction between the UV treated and reference line can be seen.
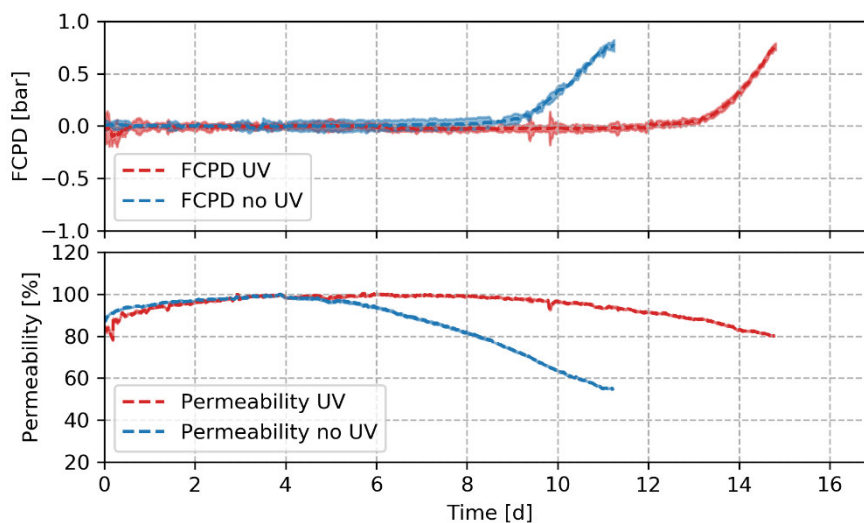
Figure 4-3:   *Representative mean feed channel pressure drop (FCPD) increase and mean relative permeability drop over time with and without UV in situ pre-treatment for one experiment. Shaded areas represent the 95% confidence intervals. Mean value and confidence intervals are calculated for 1.5 h time period.*

In total six sets of experiments using the maximum LED driving current are compared for the delay in biofilm formation and the impact of UV irradiation on the hydraulic resistance (Table 4-3). On average, the membrane filtration experiment with UV pre-treatment reached the FCPD of 0.8 bar 2.0 days later, which equals 16.5% compared to the not treated experiment. The drop in hydraulic resistance of the fouling layer, on average, was 3.4 x10^{13} m^{-1} in the experiments receiving a UV treatment. Thus,

on average, the hydraulic resistance of the fouling layer was reduced by 48.8% in a pairwise comparison. Only in one experiment (experiment 5), no reduced hydraulic resistance was observed, on the contrary, the UV irradiated biofilm exhibited an increase by 18%. The delay in biofilm formation, as well as the change in biofilm resistance, still is significant ($p < 0.05$) for a one tailed non-parametric Wilcoxon signed-rank test. Thus, the UV pre-treatment (2 mJ·cm^{-2}) seems to significantly delay the biofilm formation, as well as reducing the hydraulic resistance of the formed fouling layer in a severe biofouling state.

Table 4-3: Summary of membrane performance for six experiments applying a fluence of 2 mJ·cm^{-2}.

	FCPD delay	FCPD delay	Difference hydraulic resistance	Difference hydraulic resistance
Mean	2.0 d	16.5%	3.4 10^{13} m^{-1}	48.8%
95% confidence-t interval	1.0 d	10.0%	2.7 10^{13} m^{-1}	34.9%
p-value one sided Wilcoxon signed-rank test	0.016[*1]	0.016[*1]	0.031[*2]	0.031[*2]
Wilcoxon test statistic W	21[*1]	21[*1]	1[*2]	1[*2]

[*1] Testing for increase compared to UV; [*2] Testing for reduction compared to UV

For the eighth experiment, the driving current was reduced to 180 mA (0.85 mJ·cm^{-2}) to investigate if there is a certain threshold of UV fluence for a successful biofouling control. Interestingly in experiment #8, no delay in biofilm build-up was observed (time difference 5 h), but the resistance of the UV treated biofilm was only 50% of the control. The fluence of 0.85 mJ·cm^{-2} seems to be not enough for delaying the biofilm formation. Hence it is assumed that the needed fluence for effective biofouling control is up to 2 mJ·cm^{-2} for the given UVC-LED reactor.

In total three mechanism are supposed to explain the observed delayed biofilm build-up due to the *in situ* UV pre-treatment:

1. Reduction of viable bacteria in the feed: UV disinfection using UVC light is a process known for its capability to inactivate microorganisms (Harm, 1980; Hijnen et al., 2006; Soloshenko et al., 2006; Vilhunen et al., 2009). Inactivation was observed in studies investigating the potential of UV pre-treatment for biofouling control (Harif et al., 2011; Marconnet et al., 2011; Otaki et al., 1998). Li et al. (2017a) reported that during UV disinfection of *Escherichia coli*, irradiation using a 278 nm wavelength LED inhibited photoreactivation and dark repair, probably caused by impairment of protein activities.

2. Changed adhesion properties: RO membranes are commonly negatively charged and rather hydrophobic at pH 7 and becoming more hydrophilic with increasing ion concentrations (Hurwitz et al., 2010). During UVA disinfection a depolarization

of the cells' membrane potential was observed (Berney et al., 2006). Similar effects are assumed to happen while using 278 nm UV-LEDs with potential effects on proteins of the cells (Li et al., 2017a). On the one side, a reduction in cell membrane potential would lead to a lower electric repulsion with the membrane which could lead to better adhesion. On the other side, according to Otto and Silhavy (2002), the outer membrane lipoprotein NlpE is required for activation of the CpxR system and a successful attachment of cells to hydrophobic surfaces. In case the NlpE protein of the cell membrane is damaged due to the UV treatment, it could possibly lead to a reduced adhesion. However, the CpxRA system is complex and can be affected by multiple causes (Dorel et al., 2006; Landini, 2009). Whereas Kolappan and Satheesh (2011) observed a reduced attachment of *Alteromonas sp.* cells to hard surfaces due to UV treatment, Friedman et al. (2016) rather linked a reduced viable cell count to a reduced cell abundance on surfaces within their experiments.

3. Cell cycle arrest: Cells experiencing DNA damage might delay or stop the cell cycle to provide more time for DNA repair (Friedberg, 2003; Matallana-Surget and Wattiez, 2013). This delay could further impact the biofilm build-up.

Whereas a change in adhesion properties remains unclear, a reduction of the viable bacteria in the feed and a delay or arrest of the cell cycle seems likely to cause the observed delay in biofouling.

4.4.3. Membrane autopsy and biofilm analysis

Differences in biofilm composition with and without UV treatment were examined by determining the number of live and dead cells as well as ATP and TOC contents in the biofilm at the end of the biofouling experiment (n = 6). The results for the parameters analyzed are summarized in Figure 4-4. Values for ATP, TDC and TOC are comparable to values reported in literature for biofouling (Vrouwenvelder et al., 2009c) (p. 28, 250). The same is true for proteins and polysaccharides (Desmond et al., 2018). On average ATP/TDC values were 3.3 and 4.9×10^{-16} g per cell for UV treated and untreated biofilms, respectively. Those are comparable to the values found in literature (Elhadidy et al., 2017; Velten et al., 2007). ATP/TDC$_{live}$ was found to be 8.5 and 15.6×10^{-16} g per cell for UV pre-treated and untreated biofilms. For the analyzed parameters, one tailed Wilcoxon signed-rank test revealed four significant differences. First, the ATP levels seem to be lower in the UV pre-treated biofilms (p = 0.016, W = 0). Secondly, the cell count for cells with membrane damage, referred to as dead cells is higher without pre-treatment (p = 0.031, W = 1), whereas the cells without cell damage did not seem to differ significantly (p = 0.422, W = 9). TDC in general was reduced (p = 0.047, W = 2). As a consequence, the ATP/TDC ratio was also reduced by more than 30% through the UV treatment (p = 0.031, W = 1). TOC, proteins and polysaccharides were reduced on average, but no statistical significance could be revealed. In summary, all of the measured parameters were reduced by UV treatment at the same degree of biofouling (FCPD = 0.8 bar). The results of the biofilm analyses support the observation of a reduced biofilm resistance.
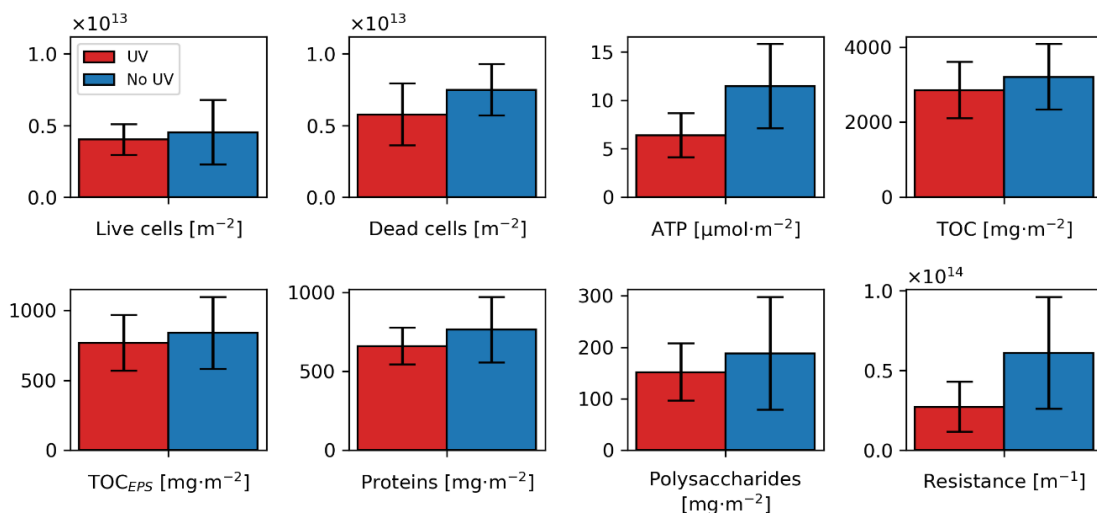
Figure 4-4: *Summary biofilm parameters. Bar plots showing 95% confidence intervals following a t-distribution (n = 6). Biofilm resistance is plotted for biofilms with a conducted biofilm analysis (n = 5).*

4.4.4. Fluorescence spectroscopy and parallel factor (PARAFAC) modeling

A three component PARAFAC model was built from the fluorescence spectroscopy analysis of the biofilm samples. Details are reported in the supplementary materials (Figure S12-4) (Sperle et al., 2020b). According to its emission and excitation spectrum, Component 1 (C1) could be identified as tryptophan-like (protein) (Coble, 1996; Yamashita et al., 2011). Component 2 (C2) could be characterized as tyrosine-like (protein) (Yamashita et al., 2013; Yamashita and Tanoue, 2004) and component 3 (C3) as humic-like of terrestrial origin (Coble, 1996; Painter et al., 2018). For both the filtered and the EPS sample, the maximum fluorescence intensity (F_{max}) was very similar (Figure 4-5). The highest F_{max} values were observed for tryptophan- and tyrosine-like proteins. Nevertheless, it needs to be considered that due to possible differences in the quantum yield of the different components, the calculated F_{max} values cannot be linked directly to a difference in concentration (Baghoth et al., 2011). Still, for none of the modeled components, a significant difference for the UV pre-treated biofilm was revealed. This indicates that the composition of the protein- und humic-like constituents is not changed or at least no change can be monitored with fluorescence spectroscopy. Perhaps, an analysis with LC-OCD as performed in the study of Elhadidy et al. (2017) could reveal differences in the molecular size distribution of the EPS.
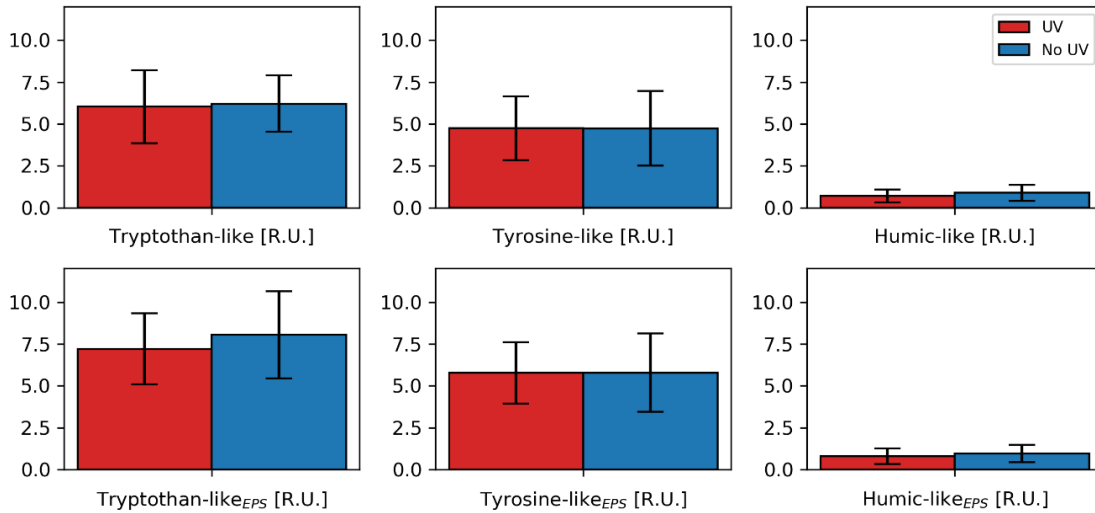
Figure 4-5: *Maximum fluorescence intensity (F_max) for the modeled components. Bar plots with 95% confidence intervals following a t-distribution (n = 6).*

4.4.5. 16S rRNA amplicon sequencing

16S rRNA amplicon sequencing was used to explore the microbial community in the formed biofilms. An overview of the bacteria families present (considering the 40 most dominant amplicon sequence variants (ASVs)) in the treated and not treated samples is given in Figure 4-6. Based on these results, the families Rhodocyclaceae, Pseudomonadaceae, Comamonadaceae and Burkholderiaceae are dominating the microbial community. Especially the abundance of Burkholderiaceae and Pseudomonadacea has been observed frequently on membrane biofilms (de Vries et al., 2020; Sánchez, 2018). For all samples the dominating class is Gammaproteobacteria, but it shall be noted that according to a recent study of Parks et al. (2018), Betaproteobacteria are now reclassified as an order within the class of Gammaproteobacteria (Burkholderiales *(The SILVA ribosomal RNA database project, n. d.))*. A distance-based redundancy analysis differentiating different treatment conditions is presented in the supplementary materials (Figure S12-5) (Sperle et al., 2020b). A distinction between the treated and untreated samples was not significant applying an ANOVA test (p = 0.074, F = 2.122). However, analyzing the variance using PERMANOVA and Bray Curtis distance matrices considering different experimental runs (Adonis ~ treatment + run), a significant difference for the runs (p = 0.006, F = 1.918) and treatment (p = 0.021, F = 2.154) was detected. Overall, the microbial community of the biofilms seems to differ.
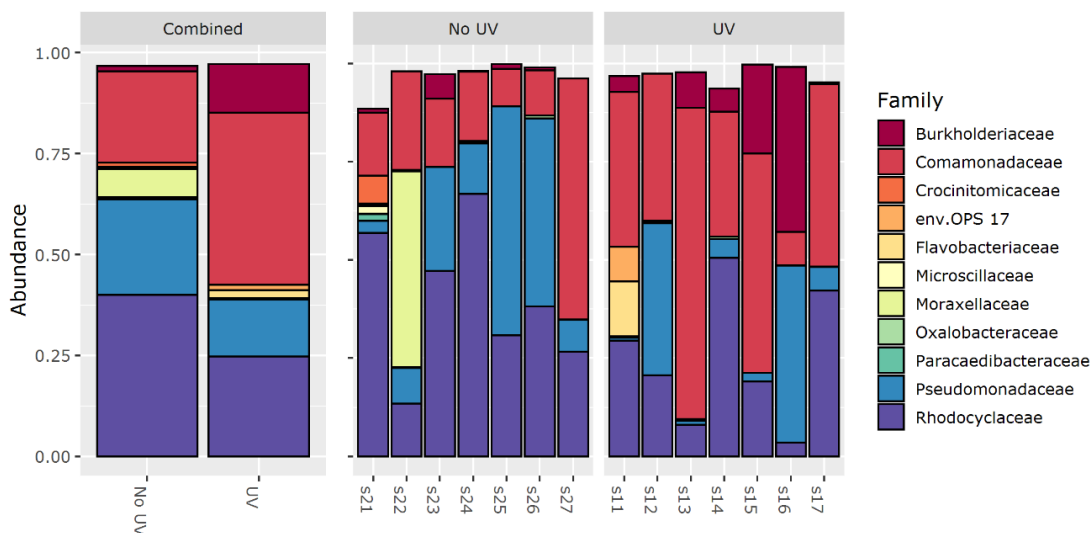
Figure 4-6:   *Overview of the relative abundance of the families identified in the treated and not treated samples. The first number in the sample name represents the treatment condition (2 = untreated, 1 = treated), whereas the second number represents the experimental run. As only the 40 most dominant amplicon sequence variants (ASVs) are plotted an abundance of 1 is not reached completely.*

After investigating the differences in the community composition in general, the DESeq2 analysis was used to determine changes at the ASV level. In total, a difference for five ASVs/species was found (p adjusted < 0.05). Their base mean, log 2 fold change, and adjusted p-value are given in Table 4-4. On the one side *Novosphingobium sp., Acidovorax sp., Sphingomonas sp.* and *Ralstonia sp.* are showing an increased abundance within the UV pre-treated biofilms. On the other side, *Delftia sp.,* if present, seems to be reduced by UV treatment. The differences in abundance could be explained as the genera being rather UV resistant or UV sensitive. This could be caused by a different GC content in the genomes (Pullerits et al., 2020; Reichenberger et al., 2015; Warnecke et al., 2005) or other biological responses to UV light.

Table 4-4:   *Summary of DESeq2 results (the arrows in the last column are indicating an increase or reduced abundance due to the UV irradiation).*

ASV	Family	Genus	Base mean	Log 2 fold change	p Adjusted	Abundance
45	Sphingomonadaceae	*Novosphingobium*	139	25.8	8×10^{-17}	↑
46	Comamonadaceae	*Delftia*	101	-24.8	7×10^{-16}	↓
2	Comamonadaceae	*Acidovorax**	21435	4.0	0.01	↑
60	Sphingomonadaceae	*Sphingomonas*	80	4.5	0.03	↑
4	Burkholderiaceae	*Ralstonia*	5957	3.5	0.03	↑

* identified by BLAST.

4.4.6. Correlation of hydraulic resistance to the main biofilm attributes

To further elucidate the coherences of the hydraulic resistance of the biofilms with the attributes analyzed, a correlation analysis according to Pearson was performed. To illustrate the coherences with the biofilm resistance, correlations with a p value of less than 0.05 and a correlation coefficient larger than 0.5 are summarized in Figure 4-7. A good correlation between TOC, polysaccharides, ATP content normalized to the cells without membrane damage (ATP/TDC$_{live}$) as well as for the humic- and protein-like components was found. Whereas *Sphingopyxis sp.* seem to decrease with hydraulic resistance, the genus of *Aquabacterium sp.* is found in an increased abundance at higher resistances. *Aquabacterium* was found in biofilms of drinking water distribution systems (Kalmbach, 2000) and the study of Gao et al. (2013) recognized an increasing presence of *Aquabacterium* at temperatures of 20 and 10 °C. Nonetheless, to the author's knowledge there are no further information about the EPS production of *Aquabacterium* and its role in increasing hydraulic resistance within biofilms. Nevertheless, parameters showing a correlation with the resistance were not affected significantly by UV treatment. Significant differences were monitored for ATP-levels, TDC and TDC$_{dead}$, as well as for the ATP content normalized to the TDC in total (ATP/TDC). However, ATP/TDC and ATP/TDC$_{live}$ are assumed to be highly correlated (r = 0.797, p = 0.002) and as a difference in ATP/TDC was observed for the treated biofilms, it is assumed that ATP/TDC or ATP/TDC$_{live}$ could indicate the mechanisms behind a changed hydraulic resistance of the biofilms. Further, it should be mentioned that when excluding the analysis of experiment 5, a non-parametric one tailed Mann-Whitney-U-test showed a significant difference for the ATP/TDC$_{live}$ content comparing the treated and the non-treated groups in general (p = 0.018, U = 2). Consequently, it seems that the ATP/TDC$_{live}$ ratio is linked to the resistance and is responsible for the difference observed by UV treatment.
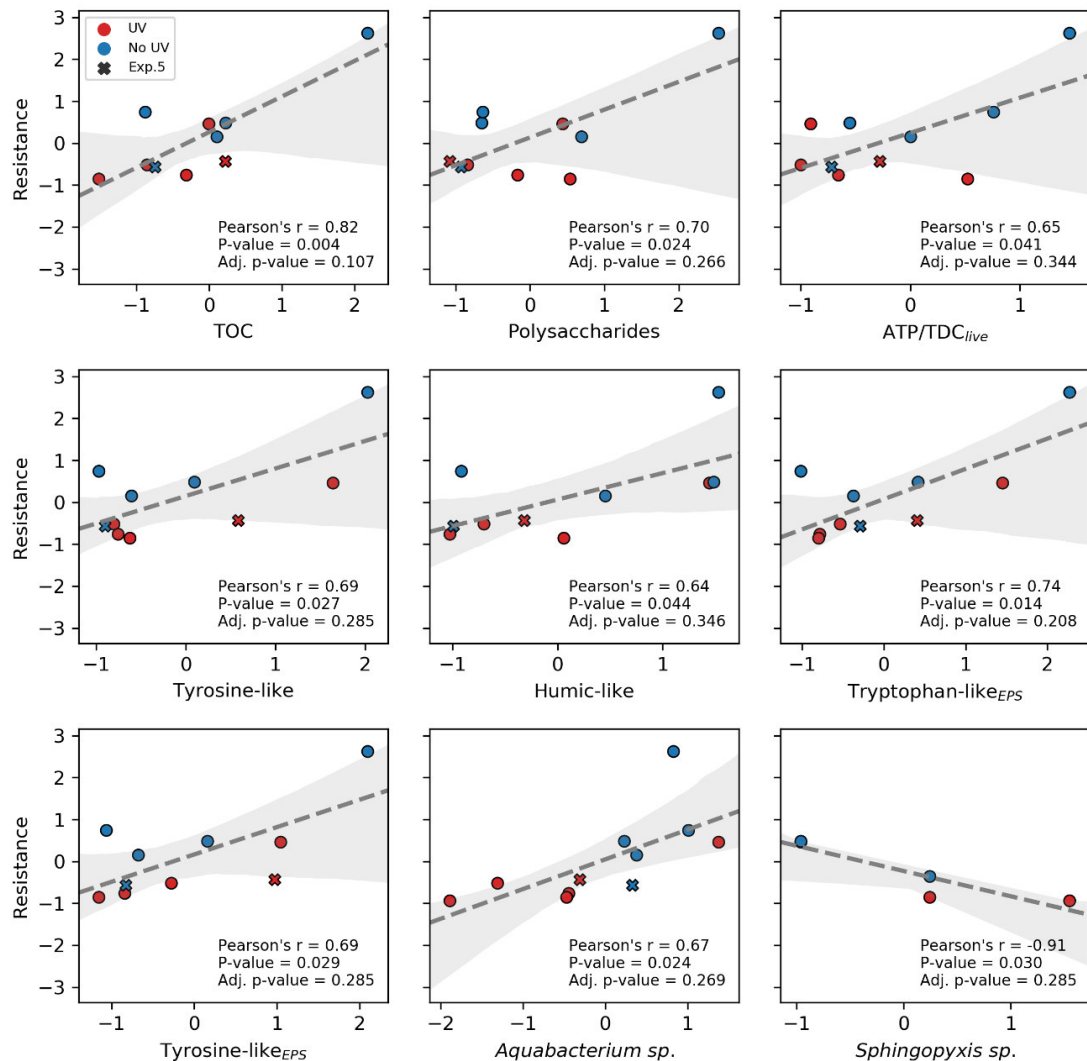
Figure 4-7: *Correlations with biofilm resistance, shaded area representing the 95% confidence intervals. As the values are transformed, no units are depicted on the axis. The x markers in the graphs are representing experiment 5 for which no effect of UV treatment for the resistance could be revealed.*

Even though differences in the biofilm composition and correlations for the resistance were detected, the mechanisms behind the change in biofilm attributes are complex. Some key ideas that could be helpful for future research are discussed in the following:

1. Different quantity in EPS production: As reported in literature (Desmond et al., 2018; Dreszer et al., 2013), polysaccharides and proteins are linked to hydraulic resistance. Even though no significant change for EPS content of treated and untreated biofilms could be revealed, a consistent trend for a reduced average in EPS and TOC quantities for the UV pre-treated biofilm could be seen (11, 8, 14 and 19% for TOC, TOC_{EPS}, Proteins and Polysaccharides, respectively). A significant difference in EPS quantity could probably not be detected due to the low number of replicates (n = 6) or there could exist an interplay among those parameters, making a simple comparison difficult.

2. Changed EPS composition/quality and biofilm morphology due to changed biodiversity: UV pre-treatment seems to alter the microbial community present in biofilms. Interestingly, the genera that showed a significantly differential abundance did not correlate to the biofilm resistance. Furthermore, within the PARAFAC analysis at least no differences for expression of tyrosine- or tryptophan-like proteins was found. Still, a change in the microbial community could lead to different EPS quality (Flemming and Wingender, 2010). A difference in EPS composition could also be polysaccharide related or not be detected with fluorescence measurements.

3. Reduced ATP levels impact quorum sensing or vice versa: ATP/TDC$_{live}$ ratio is correlating to the hydraulic resistance and seems to be changed by the UV treatment. Still the cause for a reduced ATP level and the effects for the biofilm resistance are not clear. Yang et al. (2020) observed an ATP reduction over time for UV irradiated bacteria, especially for medium-pressure UV lamps. Thus, cells irradiated and subsequently adhered to the biofilm could exhibit lower ATP levels. Furthermore, different kind of microorganisms could show different levels of ATP (Ivanova et al., 2006). Jiang and Liu (2013) recognized that if ATP production is limited in aerobic granules, the amount of AHL messenger molecules and EPS is reduced. Vice versa, Zhang et al. (2019) showed in their study that with increasing concentration of quorum sensing molecules (AHLs), ATP levels rose. The reduced ATP levels in the UV treated biofilms could, therefore, indicate less quorum sensing. Additionally, Zhang et al. (2019) observed that ATP needs to be present in a sufficient amount for EPS production. A reduction of quorum sensing could also be caused by an altered microbial community (Ma et al., 2018a; Uroz et al., 2009; Zhang et al., 2019). Not only microorganisms showing increased AHL production could show a changed abundance, but also those quenching AHL signals. According to the review of Uroz et al. (2009), *Delftia acidovorans (Jafra et al., 2006), Ralstonia sp.XJ12B (Lin et al., 2003)* and *Sphingomonas (d'Angelo-Picard et al., 2005)* could degrade or modify AHL signal molecules. Whereas a *Delftia* strain was found with reduced abundance in the UV treated biofilms, a *Ralstonia and Sphingomonas* strain were increased. Unfortunately, in this study, it was beyond the scope to directly elucidate how AHL concentration is affecting ATP levels. Nevertheless, AHL expression might not only impact the quantity of EPS but also correlate to the production of tightly and loosely bound EPS (Ma et al., 2018a). This could possibly affect the resistance of the formed biofilm.

4. Introduction of prophage: Stress conditions like DNA damage are known to lead to prophage induction to biofilms which further can lead to biofilm dispersal or disruption (Landini, 2009; Webb et al., 2003). Biofilm dispersal could not only lead to a delayed build-up but probably also create a more open structure, leading to lower resistance.

In summary, especially the change of microbial community and ATP/TDC$_{live}$ levels (for the same FCPD) are likely to impact the biofilm structure, but could also add

to the delay of biofilm formation. The reasons for reduced ATP/TDC$_{live}$ might be linked to a modified diversity or the effects of the UV treatment itself. Nevertheless, ATP is seen as an indicator for active biomass in general (Holm-Hansen and Booth, 1966) (Vrouwenvelder et al., 2009c) (p. 26).

4.5. Conclusions

Findings of this study reveal that UV pre-treatment using UVC-LEDs in immediate vicinity of RO membrane surfaces is capable of delaying biofouling already at low fluences. Furthermore, at the same degree of biofouling (same FCPD) the hydraulic resistance of the biofilms is reduced. Inactivation of the cells in the feed stream, a change in the adhesion properties and an induced cell cycle arrest are suspected to cause the delay of biofilm formation. Evidence was found that the hydraulic resistance might be affected by a modified microbial diversity, EPS composition, ATP levels per cells and possibly also quorum sensing. Nevertheless, the mechanisms behind the delayed and changed biofilm formation could not be elucidated with certainty. Further research is needed, especially regarding quorum sensing with respect to ATP and microbial community, to provide more insights into the underlying mechanisms. Analysis of the biofilm structure using confocal laser scanning microscopy or optical coherence tomography would be very helpful to further evaluate the observed effects or stated hypotheses. Measurements of hydrophilicity could contribute to a deeper understanding of the changed biofilm resistance or adhesion properties. In addition, it should be investigated if the observed effects translate to full-scale application over multiple cleaning cycles and several membrane modules in series. In conclusion, the results of the study suggest that *in situ* pre-treatment of the feed stream using UVC-LEDs in flexible reactor design (possibly integrating the LEDs in-situ in the pressure vessels) could be a promising environmentally friendly technology for biofouling control in RO and other systems.

Conflicts of Interest: The authors declare no conflict of interest. The funders had no role in the design of the study; in the collection, analyses, or interpretation of data; in the writing of the manuscript, or in the decision to publish the results.

5. An actinometric method to characterize performance of reflecting UVC reactors used for water treatment

The following chapters shows the results of the investigations related to hypothesis 3 (“*The ratio of fluence rate determined with uridine and KI/KIO3 actinometry can be used to quantitatively characterize the reflection in UV reactors*”).

This chapter has been previously published with some editorial changes as follows:

Sperle, P., Mirlach, A., Linden, K., Hübner, U., Drewes, J.E., 2023. An actinometric method to characterize performance of reflecting UVC reactors used for water treatment. Water Research 230, 119543. doi:10.1016/j.watres.2022.119543.

5.1. Abstract

The applicability of chemical actinometry to characterize the fluence in UV reactors with reflections, non-parallel light, and variable water transmittance is limited due to the unknown effective path length or hydraulic shortcuts within the reactor. In this study, the effects of reflection and transmittance on actinometry were examined and a new, optimized and easy method for determining fluence was developed. KI/KIO$_3$ and uridine actinometry experiments were carried out under controlled conditions using a CBA and a completely mixed batch reactor with or without diffuse reflection and compared to biodosimetry results. Whereas optically opaque actinometers such as KI/KIO$_3$ are not directly capable of predicting the fluence of reflecting reactors, the results of uridine actinometry are influenced by reflection and transmission. To precisely predict the fluence rate in UV reactors with uridine, knowledge about the effective optical path length of the light is needed. Here, an existing method to mathematically calculate the optical path length was adopted and optimized for uridine actinometry. Results for average fluence were validated by biodosimetry using MS2 phages under different degrees of reflection and transmission. It could be shown that by modifying the bottom of the reactor with diffusely reflecting polytetrafluoroethylene foil, the fluence rate was increased by a factor of approximately 2.6 and the path length by factor of 2.4. When only half of the bottom was covered with reflective foil, fluence rate increased by a factor of 1.8 and path length by 1.8. Although this new approach cannot replace biodosimetry, to predict the fluence distribution received by microorganisms, it can provide means to characterize more complex reactor designs, validate results of advanced reactor modeling, and quantify fluence for non-parallel irradiation and reflective light, especially for the application of high fluence (e.g., advanced oxidation processes), where biodosimetry may be too sensitive. Further, comparing the fluence obtained with actinometry to the results of biodosimetry might qualitatively indicate hydraulic short cuts or unideal fluence distributions for flow-through reactors.
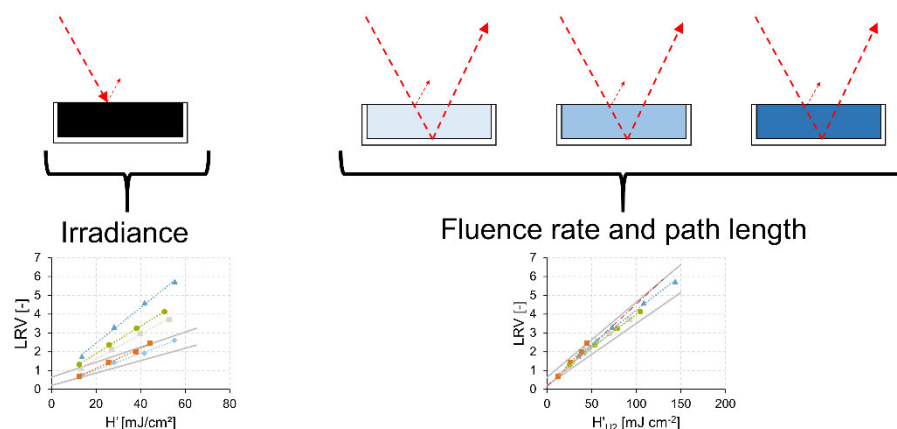
Figure 5-1:   *Graphical abstract Chapter 5.*

5.2. Introduction

Photo-reactors are used for a wide range of applications, ranging from synthesis in the field of chemistry to the treatment of water. Photo-reactors or especially UV reactors are applied in water treatment with the intent of (catalytic) degradation of contaminants, including radical formation in advanced oxidation processes (AOPs) or the inactivation of pathogenic microorganisms. A huge problem in the scale-up of photo-reactors is that just increasing the reactor dimensions can lead to nonuniform light distributions due to the absorption of light (Kayahan et al., 2020). In the design of photo-reactors used in the field of chemical synthesis, the estimation of the local volumetric rate of photon absorption (LVRPA) plays a central role (Kayahan et al., 2020). In contrast to this, in photo-reactors used to degrade organic micropollutants or to inactivate microorganisms, the target might only represent a small fraction of the total absorbance. For these reactors, the most important design parameter is not the LVRPA but rather the fluence H' (representing the radiant energy from all sides on a sphere divided by its area) reaching the target chemical or pathogen (Bolton and Linden, 2003; Bolton and Stefan, 2002; Braslavsky, 2007).

Biodosimetry is the most commonly applied method to characterize the fluence or more precisely, the reduction equivalent fluence (REF) in a UV reactor. For certifying a UV reactor for water disinfection, its disinfection capability needs to be tested using biodosimetry as standard (NSF/ANSI, 2019; U.S. EPA, 2003). In a biodosimetry experiment, the inactivation of a suitable surrogate organism like MS2 phage is measured under the desired conditions (i.e., flow rate, UV transmittance). The measured inactivation is compared to a fluence-response curve (pathogen inactivation expressed as the logarithmic removal value (LRV) as a function of fluence) recorded under controlled conditions, typically a (quasi) collimated beam apparatus (CBA) equipped with a calibrated radiometer (Bolton and Linden, 2003; NSF/ANSI, 2019). Biodosimetry has the advantage that it directly predicts the capability of the reactor to disinfect water (Sun et al., 2022). However, major shortcomings include potential variability between laboratories, differences between the inactivation of the surrogate organism and the target pathogens in real water, limited information about the fluence distribution within the reactor, the elevated costs and the effort for the cultivation and analysis of the microorganisms (Sun et al., 2022). In addition, the high sensitivity of microorganisms to UV irradiation limits the applicability of biodosimetry for processes that employ high UV fluence (e.g., AOPs).

Alternative methods for determining fluence in flowing reactors include modeling of UV reactors, particle dosimetry using dyed microspheres, or the model-detector method (Sun et al., 2022). UV reactor modeling can provide information about the distribution of fluence and the optical field without expensive testing (Jenny et al., 2014; Jin et al., 2005; Sun et al., 2022), but complex reactor designs still need to be validated using a different approach like biodosimetry (Sun et al., 2022). The dyed microsphere method (also called Lagrangian actinometry) covers particles in the micrometer (µm)

range with a fluorescing actinometer on the particle surface that provides a representation of the fluence distribution in the reactor using flow cytometry, background noise and scavenging by other particles or substances may interfere with the fluorescence determination (Blatchley et al., 2008; Sun et al., 2022; Wols et al., 2012). For the model-detector method, a micro fluorescent silica detector can be used *in situ* in the UV reactor together with a CFD and optical model to achieve real-time fluence monitoring (Li et al., 2011; Li et al., 2017b; Sun et al., 2022). Despite the promise of real-time and long-term monitoring, positioning of the sensor can be challenging and uniform fouling for lamp and sleeve are assumed, which needs further investigations (Li et al., 2017b; Sun et al., 2022).

In the field of water treatment, chemical actinometry is mainly applied for calibration of radiometers or fluence determination under highly controlled conditions (Bolton et al., 2011; Jin et al., 2006; Song et al., 2018; Wang et al., 2017). Actinometry uses the photolytic reaction of a chemical with a known quantum yield to estimate the photons absorbed in a defined space per time (Braslavsky, 2007; Kuhn et al., 2004; Rabani et al., 2021). Most actinometers available for liquid phase either measure the decrease of the chemical concentration (e.g., uridine) or the stoichiometric formation of a product (e.g., formation of I_3^- from KI/KIO_3) (Rabani et al., 2021). Within the use of an actinometer either all photons should be absorbed or there needs to be detailed knowledge about the absorbance and the solution should be mixed effectively (Kuhn et al., 2004; Rabani et al., 2021).

The current application of chemical actinometry to characterize flow-through reactors for water treatment is limited. On the one side actinometry is a well-suited tool to validate model results at distinct points within a reactor (Jin et al., 2005) or to estimate the fluence or light intensity entering a system, which can further be used for instance in the radiative transfer equation to estimate the LVRPA (Zalazar et al., 2005). On the other side, complex reactor geometries, reflections or non-parallel irradiation leading to unknown path lengths of the light traveling through the reactor can cause problems in average fluence determination. In addition, hydraulic shortcuts leading to reduced disinfection performance might not be detected using actinometry. Overall, the current state of the art using actinometry alone is unable to predict fluence distribution and REF in UV reactors for disinfection (Sun et al., 2022).

Even though it might not be possible to solve all the challenges of actinometry, the aim of this study was to develop an easy and low-cost actinometrical procedure, which directly estimates the average fluence and effective path length of non-parallel and reflective light within UV reactors used for water treatment. While not replacing biodosimetry for application in water disinfection, the aim was to provide an alternative method for reactor characterization if biodosimetry is not available or too sensitive to fluence (e.g., for AOPs). In addition, the method might be applied to predict the performance of mixed reactors under various UV transmittances (due to estimated path length), identify weaknesses in reactor design, and validate optical reactor models.

5.3. Material and methods

5.3.1. Experimental setup

Uridine and KI/KIO$_3$ actinometry, as well as biodosimetry experiments were conducted under controlled conditions in a CBA as described by Bolton and Linden (2003). The CBA consisted of three low-pressure mercury lamps (UV-fresh A001373, Philips) with a stable output at 254 nm, black collimator tubes of different length (65 cm or 30 cm), and a polystyrene petri dish with a measured inner diameter of 5.3 cm. The petri dish was filled with 0.022 L of sample to reach a water depth of 1 cm and stirred (Variomag micro stirrer with Telemodul 40 C, H+P Labortechnik, Germany) at 190 rpm using a 10 x 3 mm stir bar, covered with polytetrafluoroethylene (PTFE). The irradiance was measured before each experiment and at regular intervals during the experiment with a radiometer (UV-Surface_D, sglux, Germany) calibrated and plane placed at the same height as the water level of the petri dish. It shall be noted that irradiance is referred to as E, whereas fluence rate is abbreviated with E' in this study as used by Bolton and Stefan (2002). A detailed list of symbols and abbreviations is provided in the supplementary information.

To differentiate the fluence rate at the radiometer position and the average fluence within the water sample, correction factors according to Bolton and Linden (2003) were applied when needed. According to the refractive indices of water and air, a reflection factor (RF) of 0.98 was used. For path lengths of less than 5 cm, correction factors for divergence and absorbance can be treated separately, hence equation (5-1) was used for the divergence factor (DF) (Bolton and Linden, 2003).

$$DF\ [-] = \frac{L}{L+l} \tag{5-1}$$

Where L equals the distance of the lamps to the water surface and l the path length perpendicular to the lamp of the cell suspension in cm. Most experiments were conducted with the 65 cm tube and a DF of approximately 0.99 (L = 70 cm, l = 1 cm). Only one uridine experiment utilized the shorter tube of 30 cm (L = 35 cm, DF = 0.97). A petri factor (PF) of approximately 0.99 was determined with both collimator tubes. Equation (5-2) was used to calculate the water factor (WF) (Bolton and Linden, 2003; Morowitz, 1950).

$$WF\ [-] = \frac{1 - 10^{-a^{254} \cdot l_{irr}}}{a^{254} \cdot l_{irr} \cdot \ln(10)} \tag{5-2}$$

Where a^{254} represents the decadic absorption coefficient [cm^{-1}] at the irradiated wavelength (in our case 254 nm) and l_{irr} the path length of the light within the solution [cm].

5.3.2. Experimental procedures

To test the effect of reflection on the fluence rate for actinometry and biodosimetry, the bottom of the petri dish was modified. Apart from the standard case without reflection (R0), either half (R05) or the whole bottom (R1) of the petri dish was lined with a 2 mm thick, highly diffuse reflective PTFE foil (OptoPolymer, Berghof Fluoroplastic Technology GmbH, Germany). The foil showed a reflection of approximately 96% at a wavelength of 254 nm (measured by SphereOptics (2021), Germany) as 8°/Hemispherical spectral reflectance, details are given in the supporting information). Whereas for specular reflection, the angle of incidence is equal to the angle of reflection, for diffuse reflection, as it is occurring with the PTFE foil, light is scattered to all directions (Berghof Fluoroplastic Technology GmbH, n. d; U.S. EPA, 2003). When half of the petri dish was covered with PTFE, the other half was lined with a transparent PVC plate with the same thickness. It should be noted that some reflection might occur on other parts than the PTFE foil like the magnetic stir bar or the side walls of the petri dish.

To test the effect of transmission, the solution (prior to adding MS2 or actinometer) was spiked with 2.62 mg L^{-1} or 5.72 mg L^{-1} of humic acids sodium salt (HA) (Carl Roth, Germany) to reach a transmittance of 85% (T85) and 70% (T70), respectively. If HA was added, the blank absorption of HA was subtracted from the absorbance readings for actinometry calculations but the overall absorbance of the solutions was used for WF corrections in fluence determinations.

In general, uridine actinometries were performed in triplicate, whereas KI/KIO$_3$ actinometry and MS2 biodosimetry were performed in single kinetic experiments at selected, representative settings. Results of actinometry were normalized to radiometer readings to correct for daily variations of lamp behavior. Exposure time for uridine experiments was five times 4 min 36 s and five times 1 min 32 s for KI/KIO$_3$. For actinometry experiments, the fluences were tested in consecutive order. After an UV exposure step, approximately 3.5 mL of solution were transferred to a silica glass cuvette and absorbance was determined. Afterward, the sample volume was transferred back to the petri dish by using a pipette. By weighing the cuvette, it was ensured that the sample was completely transferred (less than 0.04 g of samples remained in the cuvette). For biodosimetry, fluences of 13, 27, 40, and 53 mJ cm^{-2}, measured with the radiometer and corrected as described by NSF/ANSI (2019), were tested in randomized order.

5.3.3. Uridine actinometry

Conventional uridine actinometry experiments (U1) have been conducted analogous as described by Jin et al. (2006) and von Sonntag and Schuchmann (1992). Within a 1 mM phosphate buffer (PBS), a 0.012 mM uridine (AppliChem, Germany) solution was prepared. PBS was prepared from potassium chloride (Merck, Germany), sodium chloride (Carl Roth, Germany), disodium hydrogen phosphate dihydrate (Merck,

Germany), and sodium dihydrogen phosphate (Merck, Germany). The pH of the solution was maintained at 7. The uridine degradation during UV exposure was monitored by measuring the change of absorbance at 262 nm by using an Aqualog (HORIBA Jobin Yvon, Germany). Following the approach of Bolton and Stefan (2002), Jin et al. (2006) and von Sonntag and Schuchmann (1992), the average fluence rate within the actinometer solution, E'$_{U1}$ [mW cm^{-2}], was calculated using equation (5-3).

$$E'_{U1}[mW\ cm^{-2}] = \frac{\ln(A^{262}(0)/A^{262}(t))\cdot U}{2.303\cdot 1000\cdot \varepsilon_U^{254}\cdot \Phi^{254}\cdot t} \qquad (5\text{-}3)$$

Where the term $\frac{\ln(A^{262}(0)/A^{262}(t))}{t}$ represents the slope of the logarithmic absorbance readings at 262 nm plotted over time. Φ^{254} and ε_U^{254} are the quantum yield (0.0185 mol Einstein^{-1}, as will be derived in section 3.2) and the molar absorption coefficient (8,820 M^{-1} cm^{-1}) at 254 nm, respectively. Quantum yield per definition describes the number of events over number of photons absorbed and hence is unitless (Kuhn et al., 2004). For better comprehensibility of derived equations, the unit as stated by Jin et al. (2006) of mol (number of events) Einstein^{-1} (number of photons) will be kept, as it basically renders unitless. ε_U^{254} was determined by multiplying the molar absorption coefficient given by the study of Jin et al. (2006) with the absorbance at 254 nm normalized to the absorbance at 262 nm, measured at three different concentrations, 10,185 M^{-1} cm^{-1} * 0.866 = 8,820 M^{-1} cm^{-1}. UV transmittance of prepared actinometer solution after 1 cm is around 78% and 55% with added HA in highest concentration. U is the photon energy at 254 nm, which was taken as 4.71 · 10^8 mJ Einstein^{-1}. To calculate the fluence rate at the center and surface of the petri dish E'$_{0,U1}$, the average fluence rate E'$_{U1}$ from the actinometer must be corrected with RF, PF, DF, WF (equation (5-4)). Further, it must be kept in mind that equation (5-3) is based on a simplification of a Taylor series expansion and therefore might be problematic for high absorbances/optical path lengths (Bolton and Stefan, 2002; Jin et al., 2006).

$$E'_{0,U1}[mW\ cm^{-2}] = \frac{E'_{U1}}{PF\cdot RF\cdot DF\cdot WF} \qquad (5\text{-}4)$$

5.3.4. KI/KIO$_3$ actinometry

For KI/KIO$_3$ actinometry a 0.6 M KI (Merck, Darmstadt, Germany), 0.1 M KIO$_3$ (VWR, Darmstadt, Germany), and 0.01 M Na$_2$B$_4$O$_7$ · 10 H$_2$O (J.T. Baker, Holland) solution was prepared (pH = 9.25) (Rahn, 1997). Prior to use, the solution temperature was adjusted to 23-24 °C. Generation of I$_3^-$ was monitored by measuring the absorbance at 352 nm using a DR 2800 spectrophotometer (Hach Lange, Germany). The fluence rate at the surface of the actinometer solution was calculated using equation (5-5) based on the studies of Bolton et al. (2011), Jin et al. (2006), Rahn (1997) and Rahn et al. (2003):

$$E'_{KI/KIO_3}[mW\ cm^{-2}] = \frac{(a^{352}(t) - a^{352}(0))\cdot V\cdot U}{\varepsilon^{352}\cdot \Phi^{254}\cdot t\cdot A} \qquad (5\text{-}5)$$

Where $\varepsilon^{352} = $ -, 27,636 M^{-1} cm^{-1} is the molar absorption coefficient of the formed I_3^- (Bolton et al., 2011), U is the photon energy at 254 nm. V = 0.022 L is the sample volume, and A = 22 cm^2 is the surface area of the petri dish. For $\frac{a^{352}(t) - a^{352}(0)}{t}$ the slope of the linear regression of the decadic absorption coefficients measured as cm^{-1} over time was used as in the studies of Sperle et al. (2020a) and Wang et al. (2017). Φ^{254} represents the quantum yield of the actinometer solution at 254 nm of 0.71 mol Einstein^{-1} (Bolton et al., 2011). The temperature of the actinometer solution was tracked during the experiment and the quantum yield was corrected according to Bolton et al. (2011). To calculate the fluence rate at the center of the petri dish, the fluence rate was corrected for RF and PF (Bolton and Stefan, 2002) (equation (5-6)). As the actinometer has an absorption coefficient of > 100 cm^{-1} (Müller et al., 2017), correction for WF and DF is not needed as all photons are absorbed directly at the surface.

$$E'_{0,KI/KIO_3}[mW\ cm^{-2}] = \frac{E'_{KI/KIO_3}}{PF \cdot RF} \tag{5-6}$$

5.3.5. Biodosimetry

To verify the actinometry results for the disinfection efficiency, biodosimetry was performed using MS2 phage (DSM 13767). Phage were plated using the double-agar technique as described in NSF/ANSI (2019) using *E. coli* (DSM 5210) as host strain. To compare the actinometry results for biodosimetry, the normalized fluence rates found with actinometry, were multiplied with the radiometer reading during biodosimetry and corrected for the relevant factors.

5.4. Results and discussion

5.4.1. Effect of transmittance and reflection on chemical actinometry

To facilitate comparison of actinometry results in different experiments, fluence rates at the center and surface of the petri dish (E'$_0$) were determined using equations (5-3)-(5-6) and normalized using radiometer readings from the respective experiment. Results of the KI/KIO$_3$ actinometer were not affected by the degree of reflection with normalized fluence rates of 1.08 (R0), 1.10 (R05), and 1.10 (R1) as expected due to the complete absorbance of photons before the light could penetrate to the reflective parts. Therefore, the KI/KIO$_3$ actinometer results represent the total irradiance/input power to the solution (E$_0$, only considering radiant power from an upwind direction) and not the average fluence rate (E'$_0$). The adjustment of transmittance with 5.72 mg L^{-1} of HA (T70) to the non-reflective case (R0) showed only a negligible influence (normalized fluence rate of 1.06). This is likely caused by the high absorbance of the actinometer (a^{254} > 100 cm^{-1}) in comparison to the one of HA (a^{254} < 1 cm^{-1}), leading to less than 1% of the light being absorbed by the HA and hence not considerably influencing results. Overall, the results fit well with the radiometer reading, with a minor overestimation (1.08

± 0.02). To increase comparability to other studies, the radiometer readings from now on were multiplied with 1.08 as calibration (Bolton et al., 2011).

In comparison to the KI/KIO$_3$ actinometry, the results from uridine exhibit significantly enhanced normalized fluence rates E'$_{0,U1}$ when reflection of the petri dish was increased to 50% and 100% (Figure 5-2). The fluence rates at the surface and center of the petri dish (E'$_{0,U1}$) were calculated from average fluence rates determined by the actinometer (E'$_{U1}$) using equation (5-4). However, whereas E'$_{0,U1}$ in the setting without reflections was comparable for different solution transmittance values (adjusted by addition of HA), decreasing transmittance led to decreased E'$_{0,U1}$ fluence rates in a reflective petri dish. The effect of solution transmittance was corrected for using the WF in equation (5-2) with a path length of 1 cm. The larger deviations for higher reflection scenarios indicate that the effective path length is increased and the WF correction assuming a 1 cm path length is not suitable in those cases.
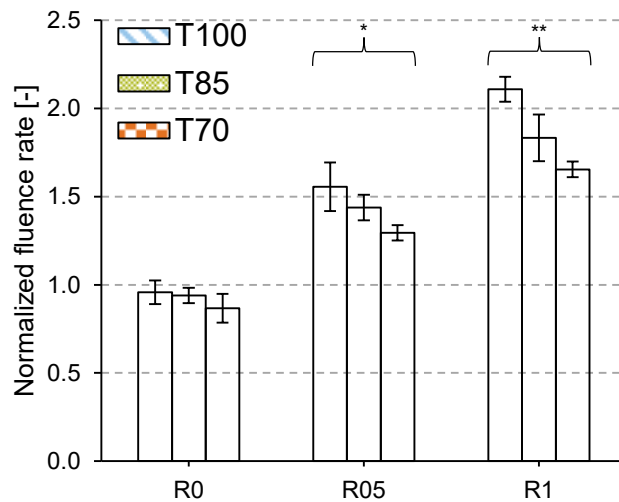
Figure 5-2:   Fluence rates (E'$_{0,U1}$) normalized to the radiometer reading determined with uridine actinometry U1 over different transmittances and reflections, corrected using a path length of 1 cm; * represents p-value < 0.05 and ** p-value< 0.01 using one-way ANOVA; error bars showing standard deviation

To compare the actinometry results with biodosimetry, the incident irradiance radiometer readings from individual biodosimetry experiments were multiplied by irradiation time and the normalized fluence rates from actinometry, as well as corrected for RF, DF, PF, and WF for 1 cm path length to determine the average fluence in the completely mixed water sample. When using the KI/KIO$_3$ actinometer for fluence determination, the measured LRVs for the non-reflective cases (T100-R0 and T70-R0) mostly lie within the quality control (QC) of NSF/ANSI (2019). As soon as reflections are introduced, the measured LRVs are higher than the QC of NSF/ANSI (2019) for the estimated fluence H'$_{KI/KIO3}$ (Figure 5-3a). This demonstrates that fully absorbing actinometers like KI/KIO$_3$ are not suitable to characterize UV reactors with reflections as they are not affected by the effective path lengths of the light. Furthermore, non-parallel light could lead to a similar phenomenon as seen with reflections. Longer

or shorter path lengths of the light traveling through the water body can lead to changed inactivation but might not be detected due to high absorbance. The LRVs of T70-R0 are slightly higher than for T100-R0, but this might be explained by uncertainties of the biodosimetry itself.

Correction of radiometer readings during biodosimetry with normalized fluence rates from uridine actinometry considerably reduced differences between the measured LRVs and the estimated fluence H'$_{U1}$ (Figure 5-3b). As additional reference, the red dotted line (standard case) represents the fitted linear model of LRV vs. the fluence determined using KI/KIO$_3$ for T100-R0 and extrapolated to higher fluences. For experiments with the reflective petri dish, the LRVs from biodosimetry are still slightly higher than QC of NSF55 (NSF/ANSI, 2019) at the estimated fluences with uridine, but already close to the standard case. This effect can be explained by the UV absorbance of the added HA and the actinometer itself. Aside from the simplification using a Taylor series in equation 3, the correction with WF is not adequately addressed. To calculate E'$_{0,U1}$ from the average fluence within the actinometer solution E'$_{U1}$ (equation 4) the changed path length of the light traveling through the medium after introducing reflections is needed.
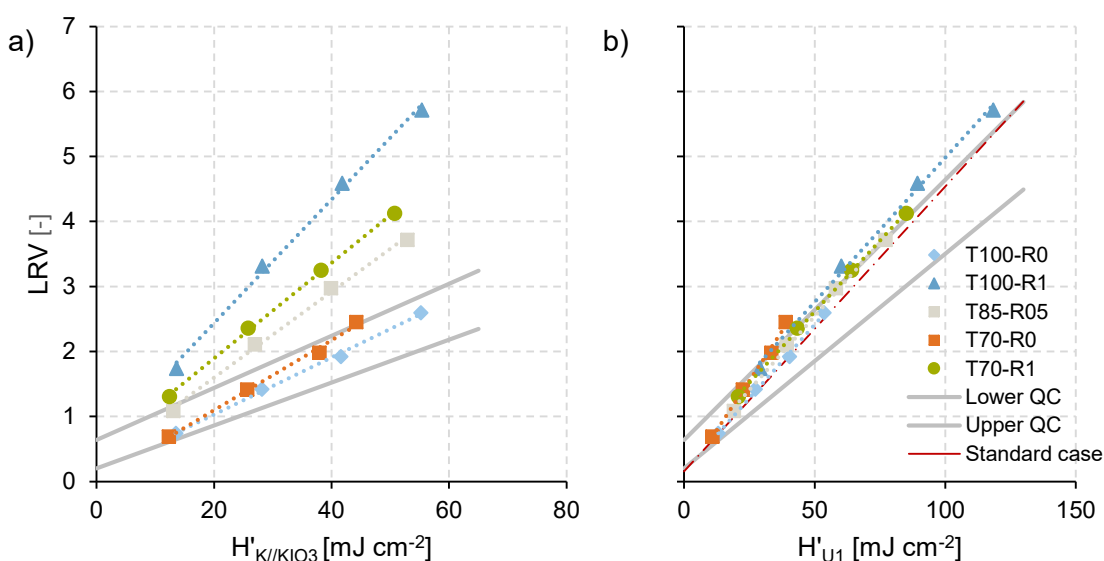
Figure 5-3: *Log removal values (LRV) plotted as a function of fluence values estimated using the KI/KIO$_3$ actinometry H'$_{KI/KIO3}$ (a) and uridine actinometry H'$_{U1}$ (b); grey lines represent the quality control (QC) of MS2 inactivation from the NSF 55 standard (NSF/ANSI, 2019); red dotted line represents fitted linear model of LRV vs. fluence determined with KI/KIO$_3$ for case T100-R0.*

5.4.2. Uridine actinometry correction with effective path length

To determine the effective path length of the light traveling through the solution, an optimized procedure (U2) was developed based on previous studies (Maafi and Maafi, 2013; Maafi and Maafi, 2015; Pousty et al., 2022; Roibu et al., 2018). Uridine experiments with different reflections were repeated with two additional uridine

concentrations ($5 \cdot 0.012$mM = 0.06 mM and $9 \cdot 0.012$ mM = 0.108 mM). The selected concentrations lead to equality distanced a^{254} values of uridine with differences of ~0.42 cm^{-1}. UV transmittances for 1 cm is around 30% for 0.06 and 11% for 0.108 mM solution.

Until recently it was assumed that during the degradation of uridine, no photoproduct with considerable absorbance in germicidal wavelength is formed (Rabani et al., 2021; von Sonntag and Schuchmann, 1992). However, Pousty et al. (2022) observed a photoproduct, absorbing at 254 and 262 nm. As described in their study, the photoproduct can be quantified when irradiating with high enough fluence until no change in absorbance can be detected anymore. As shown in the supplementary information, the found photoproduct exhibits a molar absorption coefficient of ~8% at 254 nm and 6% at 262 nm compared to the one of uridine. To encounter the effect of the formed photoproduct and instead of applying equation (5-3) based on a Taylor series simplification, mathematical analysis followed a semi-empirical model for a unimolecular photodegradation with the formed product showing an absorbance at irradiated and observed wavelength (Maafi and Maafi, 2013; Maafi and Maafi, 2015). Deduction of equation (5-7) and recommendations for calculations are reported in the supplementary information.

$$\frac{ln\left(10^{\left[\left(A^{254}(0)-A^{254}(\infty)\right)\cdot\frac{l_{irr}}{l_{obs}}\right]}-1\right)}{F_H}$$

$$-\frac{ln\left(10^{\left(A^{262}(t)-A^{262}(\infty)\right)\cdot\frac{\varepsilon_U^{254}-\varepsilon_H^{254}}{\varepsilon_U^{262}-\varepsilon_H^{262}}\cdot\frac{l_{irr}}{l_{obs}}}-1\right)}{F_H} \qquad (5\text{-}7)$$

$$= \Phi^{254} \cdot \varepsilon_U^{254} \cdot l_{irr} \cdot \frac{q_0^{254}}{V} \cdot t$$

Constants are equal to the ones described before, A^{262} represents the total absorbance measured with the cuvette at 262 nm at time point t, Φ^{254} is the quantum yield, l_{irr} path length of the light through the solution and ε_U^{254} the molar absorption coefficient of uridine at 254 nm. Furthermore, $A^{254}(t)$ denotes the total absorbance measured in the same cuvette but with irradiation wavelength 254 nm. t = 0 represents starting point of the experiment, t = ∞ represents the time after irradiation when all of uridine was converted to the resulting photoproduct. l_{obs} is the thickness of the measuring cuvette [cm], q_0^{254} is the photon flux at the sample surface [Einstein s^{-1}] and V the reactor volume [L]. In addition, ε_U^{262} = 10,185 M^{-1} cm^{-1}, is the molar absorption coefficient of uridine at 262 nm as shown in the study by Jin et al. (2006). ε_H^{262} and ε_H^{252} are the respective molar absorption coefficients of the photoproduct at the given wavelength and measured as shown in supplementary information. F_H equals to the photokinetic factor at t = ∞ (equation (5-8)). Equation (5-7) equals to the closed form integral of the photoreaction differential equation when the photoproduct shows no absorbances and in general

should work till as long as long $F_H > 1.2$ (Maafi and Maafi, 2015), in our case representing path lengths of ≤ 8.4 cm for 0.108 mM.

$$F_H = \frac{1 - 10^{-\left(A^{254}(\infty) \cdot \frac{l_{irr}}{l_{obs}}\right)}}{A^{254}(\infty) \cdot \frac{l_{irr}}{l_{obs}}} \tag{5-8}$$

As described by Roibu et al. (2018) q_0^{254} can be calculated by plotting the left-hand side (LHS) of equation (5-7) against the time and using the slope of the linear regression (equation (5-9)).

$$q_0^{254}[\,Einstein\ s^{-1}] = \frac{V \cdot slope}{\varepsilon_U^{254} \cdot l_{irr} \cdot \Phi^{254}} \tag{5-9}$$

This determination of photon flux should include corrections for WF and DF to determine the average irradiance. The average irradiance directly below the surface of the water in the petri dish, E_{U2} [mW cm^{-2}], can be calculated from photon flux using the photon energy U and the surface area. In order to get the irradiance at the center and on the water surface as it is measured with the radiometer $E_{0,U2}$ [mW cm^{-2}], the correction of PF and RF need to be considered additionally (equation (5-10) and (5-11)).

$$E_{0,U2}[mW\ cm^{-2}] = \frac{q_0^{254} \cdot U}{A \cdot PF \cdot RF} \tag{5-10}$$

$$E_{0,U2}[mW\ cm^{-2}] = \frac{V \cdot slope \cdot U}{\varepsilon_U^{254} \cdot l_{irr} \cdot \Phi^{254} \cdot A \cdot PF \cdot RF} \tag{5-11}$$

Equation (5-11) was also solved for quantum yield and the quantum yields calculated for the three uridine concentrations for case without reflection and using a l_{irr} = 1 cm. Results are 0.0185 ± 0.0012, 0.0201 ± 0.006 and 0.0208 ± 0.007 mol Einstein^{-1} for the concentrations of 0.012, 0.06 and und 0.108 mM, respectively. Those values are similar to the study of Jin et al. (2006), however, interesting to note is the increase of quantum yield with concentration. This could possibly be caused by reversal of degradation being more prominent at lower concentrations. Such reversal was suspected to cause changes of quantum yield at lower irradiances (Linden and Darby, 1997).

For the determination of the fluence rate at the center and surface of the petri dish, the irradiance from equation (5-11) needs to be transformed to account for the effective volume $V_{eff} = A \cdot l_{irr}$ resulting in equation (5-12). The factor 1,000 is caused by conversion of L to cm³. The newly proposed equation (5-12) allows direct calculation of fluence rate E'$_{0,U2}$ and effective path length l_{irr} (slope of LHS from equation (5-7)). This can be an enormous advantage in complex reactor designs with unknown surface area and volume. As a note, for calculating the average fluence rate in a reactor volume (E'$_{U2}$) rather than the fluence rate at the center and surface of the petri dish, dividing by PF and RF needs to be skipped.

$$E'_{0,U2}[mW\ cm^{-2}] = E_{0,U2} \cdot \frac{V_{eff}}{V} = \frac{slope \cdot U}{\varepsilon_{254} \cdot \Phi^{254} \cdot 1000 \cdot PF \cdot RF} \qquad (5\text{-}12)$$

Analogous to Roibu et al. (2018) the three equations from different uridine concentrations were used to solve the two unknown variables E'$_{0,U2}$ and l_{irr}. Within each case of reflection, the effective path length l_{irr} is assumed to be constant. E'$_{0,U2}$ can be assumed constant for the duration of an experiment or like in our case to encounter small variations, the fluence rate E'$_{0,U2}$ normalized to the radiometer reading was assumed to be constant. The irradiated path lengths in equations (5-7), (5-8) and (5-12) were varied over a range of 0.5 to 5 cm with a step size of 0.01 cm. The effective path length in the water was identified by minimizing standard deviation of normalized E'$_{0,U2}$ for the three uridine concentrations. The behavior of LHS in equation (5-7), as well as the standard deviation of normalized E'$_{0,U2}$ over path length changes during computation is visualized in Figure S12-8 and Figure S12-9 in the supplementary information.

For the three reflective cases, E'$_{0,U2}$ and the average effective light path length are shown in Figure 5-4. E$_{0,U2}$ is also depicted, calculated using equation (5-11) and the found effective path length expressed as l_{irr}. Whereas for R0, effective path lengths is around 1 cm, path lengths for 50% reflection (R05) and 100% reflection (R1) are 1.83 and 2.40 cm, respectively, which implies an increase by roughly a factor of 1.84 for R05 and 2.41 for R1. This high increase can be explained by the diffuse reflection. In the case of a beam perpendicular to the bottom of the petri dish that is being specular reflected, path length would double. In case of diffuse reflection, having a broad range of reflection angles, the path length can more than double, as for instance a light beam at the right side of the petri dish could be reflected by 30° to the left side, traveling a longer distance through the solution. The estimated irradiance at the center and surface of the petri dish, E$_{0,U2}$ shows similar results for the two reflective scenarios, close to the radiometer readings. This further supports the validity of the set-up equation (5-11) as q_0^{254} represents the photons coming from the lamp to the solution (input power). The average increase of E'$_{0,U2}$ between the different reflections is similar as the increase in effective path length (factors of 1.84 and 2.57 for R05 and R1, respectively).
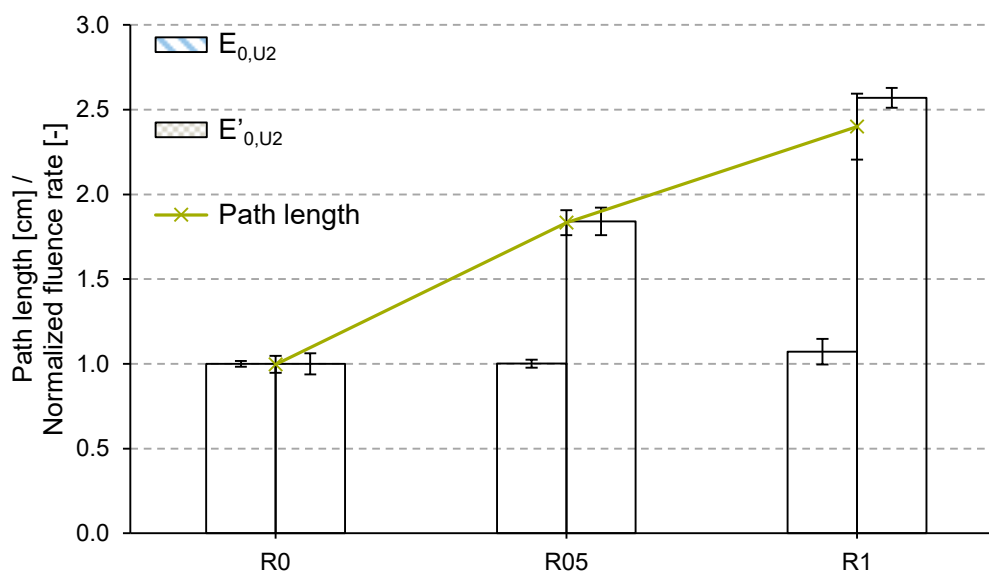
Figure 5-4: *Estimated irradiance $E_{0,U2}$ and fluence rate $E'_{0,U2}$ normalized to the radiometer readings calculated with the optimized uridine procedure, and effective path lengths; error bars showing the standard deviation.*

Experiments in this study were conducted at relatively low irradiance of approximately 0.1 mW cm^{-2} (radiometer readings). Linden and Darby (1997) observed a changed quantum yield of uridine below a fluence rate of 0.4 mW cm^{-2}, which might have been caused by longer exposure time under the heat of the UV lamp leading to a reversing of the degradation. Therefore, the experiments with three different concentrations without reflection were repeated with a shorter collimator tube of 30 cm and an irradiance of approximately 0.5 mW cm^{-2}. Following the same approach as described above, an effective path length of 0.98cm was determined with normalized irradiance $E_{0,U2}$ and fluence rate $E'_{0,U2}$ of 1.12 and 1.10. The results are slightly higher which could indicate higher quantum yields of 0.021, 0.022 and 0.023 mol Einstein^{-1} for the three concentrations 0.012, 0.06 and 0.108 mM. Even though quantum yields in general seemed to be increased, the same trend of higher quantum yield with higher concentration can be seen.

5.4.3. Correction of uridine actinometry for different transmittance and reflection

The estimated effective path lengths were used for WF correction (equation (5-2)-(5-4)) to determine the fluence rate at the center and surface of the petri dish in experiments with different transmittance and reflections (Figure 5-5). Using this correction, no significant differences were found for various transmittances within the three cases of reflection (p-values of one-way ANOVA testing were > 0.28 for all cases). The corrected fluence rates for the reflective cases are slightly higher compared to WF correction with 1 cm and similar to the $E'_{0,U2}$ from experiments with different uridine concentrations. Following this approach, DF correction was not included in equation

(5-3), as its behavior with the diffuse reflections is not known and it was assumed that the DF factor is already included in the calculated average path length. The DF for field reactor applications is not of great importance as the fluence in the water body and not that emitted from the lamp is of interest. Overall, the findings support that the calculated effective path lengths represent the real average path lengths and that $E'_{0,U2}$ indicates the actual average fluence rate in reflecting UV reactors.
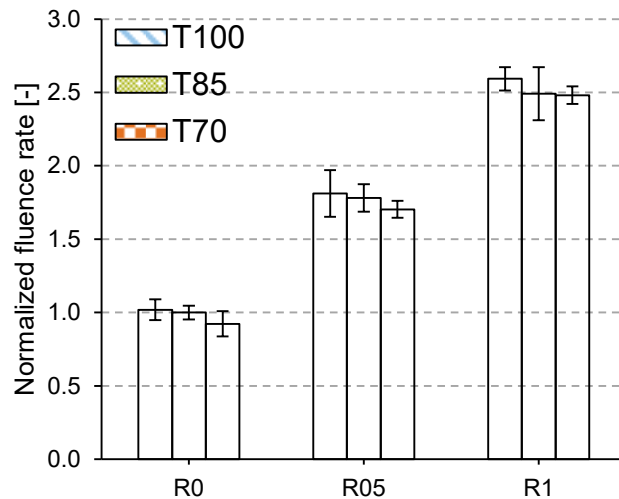
Figure 5-5:   *Fluence rates normalized to the radiometer reading determined with uridine actinometry U1 over different transmittances and reflections, corrected using the estimated effective path lengths; error bars showing standard deviation.*

Average fluence rates in biodosimetry experiments were now determined from normalized $E'_{0,U2}$ values as shown in Figure 5-4, multiplied with the radiometer readings during the biodosimetry and corrected for WF (with the use of l_{irr}), PF and RF. Using the corrected fluence rates, the determined LRVs lie within the QC (Figure 5-6a) and close to the curve of the standard case (linear model of LRV vs. fluence determined with KI/KIO$_3$ for case T100-R0, extrapolated to higher fluences) further confirming validity of the fluence rate adjustments. The correlation of the slope of LRV over irradiation time (k_{MS2}) and the average fluence rate estimated using $E'_{0,U2}$ also confirms the strong similarity of results across different transmittance and reflection scenarios (Figure 5-6b).
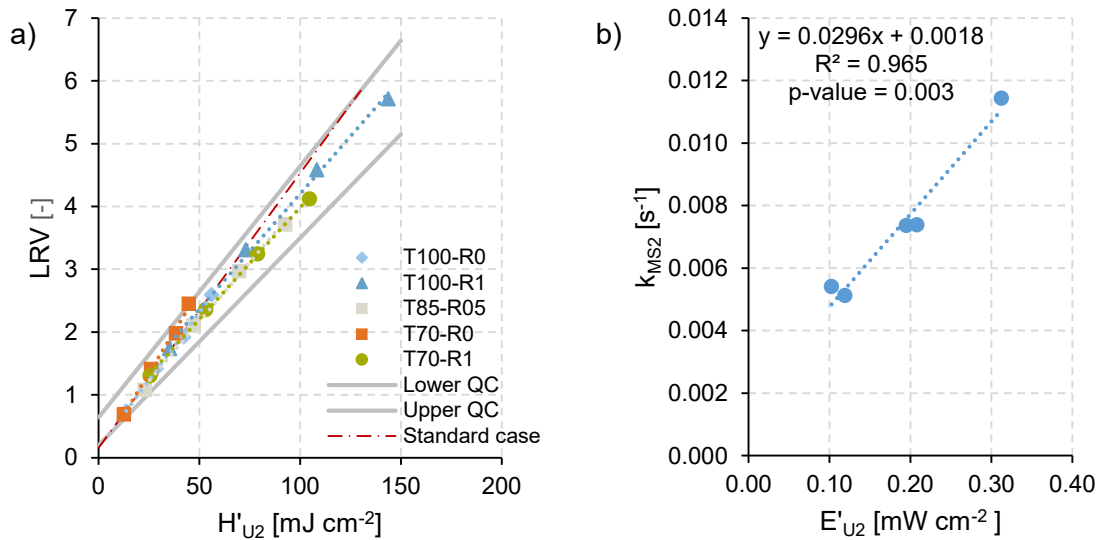
Figure 5-6:   *a) Log removal values (LRV) plotted versus fluence calculated with the optimized uridine procedure H'$_{U2}$; Grey lines representing the quality control (QC) of the NSF 55 (NSF/ANSI, 2019); red dotted line representing fitted linear model of LRV vs. fluence determined with KI/KIO$_3$ for case T100-R0. b) Correlation of fluence rate calculated with the optimized uridine procedure E'$_{0,U2}$; with the slope of MS2 log removal values (LRV) over time (k$_{MS2}$).*

While this new method showed promising results for the evaluated settings, it still needs to be validated for flow-through systems in practice. Several different ways to conduct the actinometry for flow-through systems might be possible, but recirculation of the actinometer solution as described by Zalazar et al. (2005) seems promising. In summary, a simple setup includes the UV reactor, a storage tank with the possibility of sampling, a pump and a heat exchanger. Using this setup, stable temperature, large recirculation rates, sufficient mixing and small conversion per pass, should be ensured. In addition, the volume of the UV reactor should be considerably smaller than the volume of recirculated solution. Under those conditions, irradiation time in equation (5-7) might be estimated by multiplying the recirculation time with the ratio of UV reactor volume to total volume of actinometer solution. The actinometry in recycling mode has been applied by the authors in another study with promising results (Sperle et al., 2023b). For a comprehensive validation of the actinometric method, it is recommended to validate a CFD and optical model with results of biodosimetry and compare the results of average fluence rate with actinometry.

For further improvement, investigation of the optimal uridine concentrations is important. Similarly as described by Roibu et al. (2018), a high absorbance of the light under a specified uridine/actinometer concentration could lead to lower influence of the path length on degradation of the actinometer, as most of the light has already vanished after a short distance, similar to the extreme case of the KI/KIO$_3$ actinometer. This effect might be minimized for instance by ensuring that the highest uridine concentration still shows a transmittance of at least 10% for the average path length. To additionally validate the estimated path lengths, another experiment with a higher water depth was

performed and is shown in the supporting information. Water depth could be well estimated.

When using polychromatic irradiation, coefficients used in the calculation might need to be weighted by the relative spectral output as described by Roibu et al. (2018) and the calculations would be more complex due to the variation of the germicidal action of wavelengths. Additional points to consider are the effects of evaluated temperatures or behavior of the quantum yield at the boarders of uridine absorbance ($\lambda \geq 280$ nm).

Besides, the current study applied a maximum fluence estimated directly with the radiometer ($H'_{0,radio}$) of ~740 mJ cm^{-2}. As AOP processes might be conducted in the range of ~1,000 mJ cm^{-2} (Roback et al., 2021), another run with the 0.012 mM concentration and the long collimator tube was performed. After irradiation with ~2,600 mJ cm^{-2} calculated normalized irradiance $E_{0,U2}$ and fluence rate $E'_{0,U2}$ were 1.10 and 1.11 with a path length of 1 cm. This indicates, that the method should be suitable for AOP processes, but the slight increase might be caused by a change in quantum yield. According to Linden and Darby (1997), quantum yield should not change at irradiances higher than 0.4 mW cm^{-2}, so probably the values derived with the short collimator tube should be applicable for studies with higher intensities. Still it is advised to additionally investigate and validate the behavior of quantum yield at different fluences and fluence rates, coupled with more extreme temperatures and over varying uridine concentrations.

5.4.4. Implications for practice

It was shown that the estimated fluence rate $E'_{0,U2}$ with the estimated path length is a well-suited tool to predict the inactivation of MS2 phage for the diffusely reflected UV irradiation in the CBA setting. For real reactors, however, the actinometry might indicate the average fluence, but as it is not predicting the fluence distribution received by microorganisms it cannot replace biodosimetry for water disinfection. Nevertheless, the proposed actinometry can provide valuable information and has several implications for practice.

5.4.4.1. Simple method to characterize alternative lab-scale UV reactors

Standardized CBA with parallel light and well-defined path length is not accessible for researchers worldwide. In addition, boundary conditions, e.g., the integration into treatment concepts or the need of larger sample volumes, may require the utilization of alternative reactor designs. For a full characterization of such reactors, labor and time intense biodosimetry is required. The new method to determine the effective path length and average fluence rate of the reactor is cost effective, does not require handling of toxic chemicals, and is fast to implement. In addition, biodosimetry might be too sensitive for reactor characterization, e.g. when applying high fluences as

in UV-AOPs. Further, with knowledge about the effective path length of the light, it might be possible to calculate the average fluence rate for different water matrixes and transmittances. Predicting the inactivation performance for the CBA setting worked well, but it must be considered that a correction for WF assumes a completely mixed solution (Bolton and Linden, 2003; Morowitz, 1950), which might not always be the case in real reactors. In lab-scale operation, this limitation might be overcome by recycling the water through the reactor to ensure equal exposure to UV light. However, future experiments are needed to determine required recycling rates and validate the WF correction for the average fluence for flow-through reactors and for reflections with longer path lengths.

5.4.4.2. Fluence determination for non-parallel light sources and reflective reactors

It should be emphasized that it was possible to predict the fluence under diffuse reflection and therefore also non-parallel light. This is extremely helpful for examining the fluence when using light sources such as UV-LEDs, where quasi-collimation might not be achieved due to patterned light output. Non-parallel light can cause problems for radiometer measurements and any increased path length within a reactor could lead to varied disinfection performance. In addition, for a given reactor, the ratio of fluence rate to irradiance could be used to quantitatively estimate the degree of reflection or gain in efficiency due to reflections and path length increases. Furthermore, when reflections are used in an industrial reactor the proposed method might be able to detect if fouling of reflective parts is occurring.

5.4.4.3. Characterization of flow-through reactors by combining actinometry with hydraulic reactor and optical field modeling

The modeling of complex reactor geometries requires validation (Sun et al., 2022). Next to biodosimetry, the proposed method could serve as an alternative for model validation, being easy and fast to implement without expensive testing facilities. Both, average fluence rate as well as the optical path length could be parameters for model comparison. With a validated model the inactivation of microorganisms under different water qualities might be predicted.

5.4.4.4. Qualitatively characterize the fluence distribution in full-scale reactors

Together with the results of biodosimetry, additional information about the reactor performance and possible strategies to enhance future design can be gained. By comparing the fluence estimated with the uridine actinometry using three different uridine concentrations (H'_{U2}), and the measured inactivation of MS2 at a certain fluence/flowrate, it is possible to check if the fluence distribution is behaving similarly as in a CBA. The ratio of REF and average fluence H'_{U2}, can be seen as mixing efficiency (equation (5-13)), a figure of merit for the quality of fluence distribution further described

by Bolton and Cotton (2022) and usually calculated by modeling the reactor. To calculate mixing efficiency a certain fluence ($\eta_{H'}$), a linear model or an interpolation might be used to predict the LRV at a design fluence, if LRV kinetics over several fluences was recorded, but not at the fluence of interest (e.g. predict the LRV at 40 mJ cm^{-2} by an interpolation of the LRV at 30 and 50 mJ cm^{-2}). From this LRV the REF can be calculated using the MS2 inactivation kinetics under standard conditions in a CBA. For wavelengths other than 254 nm, actinometry results might need correction for germicidal efficiency as compared to 254 nm. A $\eta_{H'}$ of ≥ 1 indicates equal or better fluence distribution as in a CBA (likely the best case possible), whereas $\eta_{H'}$ considerably smaller than 1 can indicate hydraulic shortcuts or an unequal fluence distribution occurring in a UV reactor. The investigated settings of reflection and transmittance showed an average η_{40} of 1.02 ± 0.09 at a fluence of 40 mJ cm^{-2}, indicating that in all the experiments the fluence is equally distributed to the phage, as it is suspected as they were performed in a mixed petri dish. Overall, $\eta_{H'}$ can be seen as the efficiency to transfer the light energy within the reactor to the microorganisms. Maximizing $\eta_{H'}$ is a primary goal of engineers designing UV reactors (Bolton and Cotton, 2022). However, it should be noted that changing absorbance of the water might also change $\eta_{H'}$ values in a reactor, as part of the streamlines might receive significantly less irradiation.

$$\eta_{H'} \ [-] = \frac{REF}{H'_{U2}} \tag{5-13}$$

5.5. Conclusion

This study assessed the ability of chemical actinometry to account for effects of reflections and water transmittance in a completely mixed batch reactor under a collimated beam apparatus. The following main conclusions can be drawn:

- Knowledge about the path length of the light is essential, for conventional and the optimized actinometry.
- The developed actinometry demonstrated an easy and fast method to not only quantify irradiance and path length but also by the newly proposed equation (5-12) to accurately calculate average fluence rate in completely mixed batch UVC-reactors used for water treatment, without needing any prior knowledge of surface area or volume.
- The proposed method to predict the average fluence could be validated by biodosimetry using MS2 phage in a CBA setting for different degrees of transmittance and reflection, and can be expected to also apply to non-parallel light sources, such as those emitted by UV-LEDs. Nevertheless, the method needs to be additionally validated in flow-through and industry standard reactors.
- The estimated average fluence rate could provide valuable information for all UV reactors for water treatment but could be especially useful where biodosimetry is too sensitive (e.g., UV-AOP processes). To

enhance results, attributes of uridine should be validated over diverse fluence rate ranges, uridine concentrations and more extreme temperatures.

- The optimized actinometry method is not designed to determine fluence distribution in reactors used for water disinfection but could be used for model validation and a first performance estimation.
- Using the new actinometric method together with biodosimetry, mixing efficiency might be directly calculated without modeling.

Declaration of competing interest: The authors declare that they have no known competing financial interests or personal relationships that could have appeared to influence the work reported in this paper.

6. A practical bacterial biodosimetry procedure to assess performance of lab-scale flow-through UV water disinfection reactors

The following chapters shows the development of a reliable biodosimetry method that provided the basis for the investigations of hypothesis 4 (*"With raising fluence rates (in the range of ~1 – 100 mW cm^{-2}), the disinfection efficiency of pulsed UVC-LEDs is increasing significantly by more than 30% for bacteria"*).

This chapter has been previously published with some editorial changes as follows:

Sperle, P., Khan, M.S., Drewes, J.E., Wurzbacher, C., 2023a. A Practical Bacterial Biodosimetry Procedure to Assess Performance of Lab-Scale Flow-through Ultraviolet Water Disinfection Reactors. *ACS ES&T Water* 3 (8), 2130–2139. doi:10.1021/acsestwater.2c00648.

Author contributions: Philipp Sperle and Christian Wurzbacher conceptualized the research. Philipp Sperle, Christian Wurzbacher and Mohammad S. Khan developed the methodology and validated the study. Formal analysis was done by Philipp Sperle. Investigations and data curation was done by Philipp Sperle and Mohammad S. Khan. Christian Wurzbacher and Jörg E. Drewes were responsible for project supervision, resources and funding acquisition. Philipp Sperle prepared the original draft and visualized the data. Jörg E. Drewes, Christian Wurzbacher and Mohammad S. Khan reviewed and edited the manuscript. Project administration was done by Jörg E. Drewes and Philipp Sperle. The manuscript was written through contribution of all authors. All authors have given approval to the final version of the manuscript.

6.1. Abstract

Biodosimetry can be used to estimate the fluence of a reactor by determining its ability to inactivate a challenge organism. Especially for small-scale flow-through reactors, inconsistent procedures are reported for bacterial cells. This study aims to develop a standardized, simple procedure for bacterial biodosimetry in flow-through UV systems with relevant biofilm-forming bacteria, to evaluate biofouling control by UV. In particular, the challenge organism, the type of experimental setup and the execution of single steps during biodosimetry with bacterial cells can cause largely deviating results. Since previous work was restricted to model organisms, which are not relevant for biofouling, we critically reevaluated all reported steps for the biofilm forming *Aquabacterium citratiphilum* and identified three main factors for biodosimetry reproducibility in flow-through systems: Protractions of cells from controls without UV can heavily impact inactivation efficacy, but can be reduced by ordering samples by decreasing fluence. Further, to avoid photorepair, samples must be processed under red light only. Lastly, biofilm forming bacteria can strongly adsorb on plastic labware, which requires counter measures in form of special labware and the addition of surfactants. Overall, the developed protocol provides a biodosimetry standardization for bacterial cells of flow-through systems, facilitating reproducibility and transferability of results between studies that use bacterial cells as challenge organism.
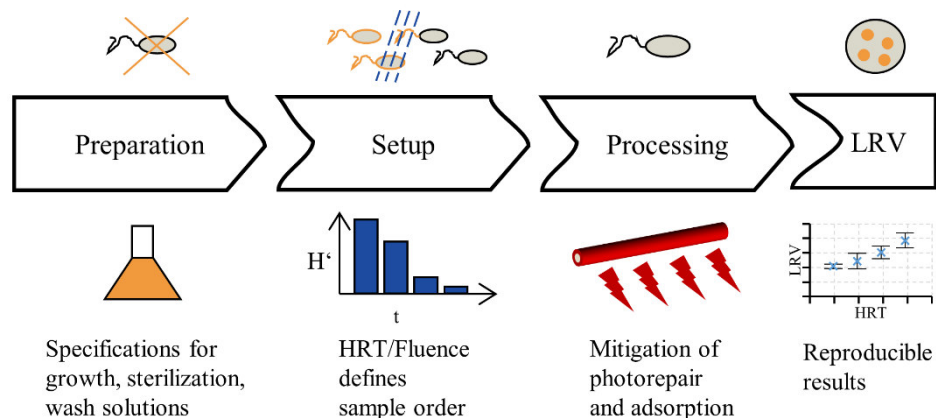
Figure 6-1:   *Graphical abstract Chapter 6.*

6.2. Introduction

Using ultraviolet (UV) light as a disinfection process has been researched for more than 50 years and is a well-established technology (Harm, 1980). UV disinfection has the great advantage of causing limited by-product formation and being chemical-free (Li et al., 2019b; Liberti et al., 2003; Romero-Martínez et al., 2019). In general, UV light can be categorized according to its applied wavelength with UVA covering 315-400 nm, UVB 280-315 nm, and UVC 200-280 nm (U.S. EPA, 2006). Even before unraveling the exact impact of UV light on DNA, it was elucidated that DNA is mainly involved as absorbing material for UV light, leading to the inactivation of microorganisms through the usage of action spectra (comparing the relative efficiency of incident light vs wavelength) (Harm, 1980). Several photoproducts can be induced by UV irradiation, however, cyclobutane-pyrimidine dimers and 6-4 photoproducts are considered to be of main importance for DNA damage (Harm, 1980; Sinha and Häder, 2002). Besides, for longer wavelengths like UVB, the production of reactive oxygen species can play a considerable role in indirect damage to the cells' components, proteins, and DNA (He and Häder, 2002).

Nevertheless, UV-induced damage might not necessarily be lethal and microbial cells might be capable to recover due to dark or photorepair mechanisms by light in the range of 310 to 480 nm (Harm, 1980). The dark repair mechanisms include amongst others nucleotide and base excision repair, but also recombination repair (Chatterjee and Walker, 2017; Harm, 1980; Rastogi et al., 2010). The so- called SOS response can be activated by DNA damage and in addition to inducing repair processes, it can also lead to translesion synthesis possibly bypassing, but not removing DNA damage during replication (Chatterjee and Walker, 2017; Maslowska et al., 2019). All of the above mechanisms can lead to considerably lower disinfection efficiencies (Harm, 1980; Oguma et al., 2002; Xiao et al., 2018).

Even though some studies observed deviations (Pousty et al., 2021; Sommer et al., 1998), UV disinfection is commonly assumed to follow the Bunsen–Roscoe reciprocity law, meaning UV disinfection solely depends on the product of fluence rate and time (fluence) (Harm, 1980; Pousty et al., 2021; U.S. EPA, 2006). Following the one-hit-one-target function, logarithmic survival behaves linearly over fluence (Harm, 1980). However, according to Harm (1980), this inactivation behavior might not be observed over the complete fluence range. More precisely, at a lower fluence/logarithmic reduction value (LRV), curves with shoulders might be observed as the inactivation rather follows a multi-target/multi-hit model or due to repair processes being more efficient at lower fluence. In addition, upward concave curves can be observed if multi-components (multiple fractions with different inactivation rates) are present. At a higher fluence/LRV regions, inactivation curves might show tailing behavior, likely caused by UV resistant subpopulations, reactor hydraulics, cell aggregates or other shielding effects (Azimi et al., 2017; Emerick et al., 2000; Kowalski et al., 2020; U.S. EPA, 2006; Würtele et al., 2011). Regions where shouldered or upward concave/tailing curves are

occurring, might depend on the experimental conditions and the used microorganism solution (Harm, 1980). When fitting a linear model on LRV over fluence, effects of, for instance, repair processes might be seen by a negative y-intercept, whereas upward concave curves result in a positive one (Harm, 1980).

Sources for UV irradiation include low and medium-pressure (LP and MP), and xenon flash lamps (U.S. EPA, 2006). In recent years, UV-LEDs received increasing attention as they have advantages such as not containing mercury, being robust with fast start-up times, and potentially being more energy efficient with a longer lifetime (Würtele et al., 2011). Furthermore, according to Song et al. (2016) they are compact as well as available in different wavelengths and viewing angles which enables new reactor designs and novel applications. Hence, when designing new reactors especially hydrodynamics, radiation distribution, and kinetics require consideration and evaluation (Song et al., 2016). In general, lab-scale systems not only deviate from the scale of application but also new reactor designs or treatment combinations are tested using different organisms for challenge tests. Especially through their compactness (Song et al., 2016), the newly available LEDs allow building of small-scale reactors with variable designs.

There are several methods available to quantify fluence in UV reactors (Sun et al., 2022), but the common method for certifying a new reactor is biodosimetry (NSF/ANSI, 2019; U.S. EPA, 2003; U.S. EPA, 2006). Biodosimetry cannot estimate fluence distribution directly, but it directly measures the inactivation of microorganisms (Sun et al., 2022), being the primary goal in water disinfection. In this paper and according to the U.S. EPA (2003), biodosimetry is referred to as the experimental test during the validation procedure, in which the logarithmic inactivation of a challenge organism is tested under desired flow rates, UV transmittance (UVT), and lamp power combinations. In the next step, the results from the biodosimetry test are compared to a dose-response curve of the same challenge organism solution recorded under controlled conditions using a collimated beam apparatus (CBA), to calculate the reduction equivalent dose (RED) and inactivation credits (Bolton et al., 2015; Bolton and Linden, 2003; U.S. EPA, 2006). In general, the UV disinfection capability of a flow-through reactor might be lower compared to a CBA. Ideally, all microorganisms should receive the same fluence, but for flow-through reactors in practice, this might not be achieved (U.S. EPA, 2006). For reactor validation, commonly used challenge organisms include MS2 phage and endospores of *Bacillus subtilis (Sun et al., 2022; U.S. EPA, 2006)*. For both targets, standardized methods for large-scale and batch reactors (CBA) are available. In contrast, a general standardized procedure for vegetative microbial cells is currently lacking. Microbial cells can have diverse cell wall components with different capabilities for photon absorption through heterogeneous pigments and especially bacterial cells may actively respond to radiation by photorepair mechanisms (Harm, 1980; Sinha and Häder, 2002). If the microorganism used for validation exhibits a different UV sensitivity than the target organism, RED might need correction for so called RED bias (U.S. EPA, 2006). Furthermore, differently applied wavelengths lead to

different disinfection efficiencies, which must be considered for each microorganism (Beck et al., 2015).

As a consequence, a range of different methods for biodosimetry using microbial cells as a challenge organism have been applied to lab-scale reactors (Fitzhenry et al., 2021; Harris et al., 1987; Müller et al., 2017; Nyangaresi et al., 2019; Oguma et al., 2013; Oguma et al., 2016; Romero-Martínez et al., 2019; Sholtes and Linden, 2019; Wang et al., 2021; Wenjun and Wenjun, 2009). However, the parameters for these vary and are not well defined, ranging from flow-through to batch systems with or without recirculation, a range of species in different conditions and feed solutions, varying washing steps and with or without inclusion of photoreactivation of microorganism (Fitzhenry et al., 2021; Harris et al., 1987; Müller et al., 2017; Nyangaresi et al., 2019; Oguma et al., 2013; Oguma et al., 2016; Romero-Martínez et al., 2019; Sholtes and Linden, 2019; Wang et al., 2021; Wenjun and Wenjun, 2009). There are many steps involved in biodosimetry that can be critical, including cultivation, washing, the design of the experiment, and processing of the samples including measures for or against repair mechanisms (Fitzhenry et al., 2021; Harris et al., 1987; Müller et al., 2017; Nyangaresi et al., 2019; Oguma et al., 2013; Oguma et al., 2016; Romero-Martínez et al., 2019; Sholtes and Linden, 2019; Wang et al., 2021; Wenjun and Wenjun, 2009). However, as the methodology is not yet standardized, results may largely differ between studies. Furthermore, most studies focused on nosocomial bacteria or model organism such as *Escherichia coli* (Fitzhenry et al., 2021; Harris et al., 1987; Müller et al., 2017; Nyangaresi et al., 2019; Oguma et al., 2013; Oguma et al., 2016; Romero-Martínez et al., 2019; Sholtes and Linden, 2019; Wang et al., 2021; Wenjun and Wenjun, 2009). *E. coli* might be used as fecal indicator for e.g. drinking and wastewater disinfection. However, applying UV disinfection for other applications like using UV irradiation as pre-treatment for biofouling control in membrane filtration systems (Harif et al., 2011; Sperle et al., 2020a), *E. coli* may not be the ideal model organism. Biofilms often consist of non-infectious, non-model organisms, which to our knowledge have not been used as challenge organisms, yet.

This study aims to provide a standardized biodosimetry protocol for flow-through reactors and to elucidate critical steps that mitigate artifacts exploring new UV treatment designs with bacterial cells (using LEDs or conventional lamps). This is achieved by comparing the existing methods for flow-through UV reactors and the subsequent evaluation of the most important steps resulting in a standardized and reproducible biodosimetry protocol for the non-model organism, *Aquabacterium citratiphilum*, a gram-negative bacterium found typically in drinking water biofilms around Europe (Kalmbach et al., 1999) with potential relevance for biofouling of high-pressure membrane treatment (Sperle et al., 2020a).

6.3. Materials and methods

6.3.1. Testing skid for biodosimetry experiments

The testing skid to perform biodosimetry experiments (Figure 6-2) consisted of a feed container that was continuously stirred with a magnetic stirrer (MR 2000, Heidolph, Germany). Feed was withdrawn using the gear pump (DGS.38PPPV2NN00000, Tuthill Alsip, United States and K21R 63 K2 H, VEM motors Thurm, Germany) and pump speed was regulated using the frequency converter (FUS 037/E2, PETER Electronic GmbH & Co. KG, Germany). The flow was measured using a magnetic-inductive flow meter (MIK-6FC08AC34P, KOBOLD Messring GmbH, Germany). The flow of the pump was controlled over a PI controller implemented in the computer-aided control system. A UV-LED reactor was placed in a temperature cabinet (Innova 4230, New Brunswick Scientific, United States) at 15°C and the reactor was directed in an upright position to avoid any air bubble accumulation. After passing through the LED reactor, the effluent was directed to the waste container, which can be switched with sampling vials. Pipes between the different elements had an inner diameter of 4 mm and were made of black PTFE. Only the last approximately 50 cm were made from a transparent PTFE pipe with an inner diameter of approximately 1 mm to provide more resistance for the water and therefore higher process stability at very low flows. The pipe was covered with aluminum foil to reduce light from the surrounding.
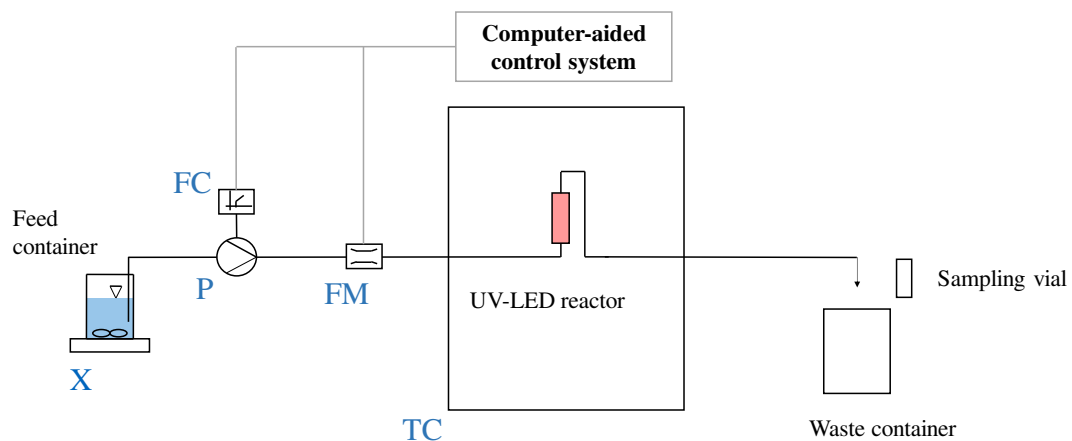
Figure 6-2:   *Schematic of the employed laboratory skid for biodosimetry experiments; X = magnetic stirrer, P = gear pump, FC = frequency converter, FM = flow meter, TC = temperature cabinet.*

Our simplified UV-LED reactor was provided by UV-EL GmbH (Dresden, Germany) and consisted of a reflective PTFE block as housing, which covered the LEDs and the silica glass pipe through which the water was flowing. The silica glass pipe had a total length of 11 cm and an inner diameter of 0.7 cm. UVT of the used silica glass in a planar form and between 265 and 275 nm is around 90% (QSIL GmbH, 2013). The central 6 cm of the 11 cm glass pipe were covered with PTFE and are seen as the reactor volume. Over the LEDs, the LED cooling system, consisting of a metallic cooling body and a fan, was attached to the PTFE block and the LEDs themselves. As LED

module, the 2P2S-S6060 UVC Quad SMD Module (Bolb Inc., United States) consisting of four LEDs with a peak wavelength between 265 to 275 nm was used (Laser Components GmbH, 2019b). A schematic drawing is presented in the supplementary materials (Figure S12-10). The LED was powered using an LED-Pulse-Controller by Leistungselektronik JENA GmbH (Germany). The pulse controller enabled flexible change of the LED output power by adapting the driving current in steps of 8 mA. In general, the higher the driving current, the higher the fluence rate. Whereas fluence rate of the system depends on the driving current of the LEDs, fluence depends on fluence rate multiplied by hydraulic retention time (HRT). The HRT within the experiments was varied by adapting the flowrate within the system and the HRT was calculated by dividing reactor volume through flowrate. HRT was varied in equidistant steps. After switching to a different HRT or irradiation setting, a fixed volume was flushed through the system based on a tracer test to reach a steady state in the outflow.

6.3.2. Tracer test

To characterize the hydraulics and the mean hydraulic retention time within the skid (Figure 6-2), a simple positive step tracer test tracking electrical conductivity (EC) at two flow rates (1.5 and 6.0 L h^{-1}) was performed. For this purpose, the skid was flushed with DI water and then the feed was switched to local tap water. A flow cell with a conductivity meter, attached to the outlet, monitored the outflow EC until it became steady and indifferentiable from the feed averaging across 1 sec time intervals. As EC at the beginning of the experiments was close to 0, the initial EC value was subtracted from the EC readings. Analogous to Levenspiel (2012) the cumulative residence time distribution (RTD) curve F(t) was calculated:

$$F(t) \, [-] = \frac{C\,(t)}{C_{max}\,(t)}$$

(6-1)

Thereby conductivity values were used as a surrogate for total dissolved solids concentration. By differentiating F(t) for time t, the residence time distribution E(t) was obtained (Levenspiel, 2012).

$$E(t) \, [s^{-1}] = \frac{dF(t)}{dt}$$

(6-2)

With knowledge about E(t), mean residence time t$_m$ and variance σ^2 were calculated (Fogler, 2016):

$$t_m \, [s] = \int_0^\infty t \, E(t) dt$$

(6-3)

$$\sigma^2 \, [s^2] = \int_0^\infty (t - t_m)^2 \, E(t) dt$$

(6-4)

Space-time τ was measured by draining the whole system by first running the pump without feed and then flushing the system with pressurized air. The drained water was weighed and τ calculated by dividing the volume of water through flow (Levenspiel,

2012). To compare tracer results to other reactors normalized resident times were calculated based on Fogler (2016).

$$\theta\,[-] = \frac{t}{\tau} \qquad (6\text{-}5)$$

$$E(\theta)[-] = \tau\,E(t) \qquad (6\text{-}6)$$

$$F(\theta)[-] = \int_0^\infty E(\theta)\,d\theta \qquad (6\text{-}7)$$

Recorded cumulative RTDs were further compared to two idealized models, a tank in series and a laminar flow model. The tanks in series model is represented by a number of continuously stirred tank reactors (CSTRs). The number of tanks in series was fitted as described by Fogler (2016).

$$n = \frac{\tau^2}{\sigma^2} \qquad (6\text{-}8)$$

$$E(\theta) = \frac{n\,(n\theta)^{n-1}}{(n-1)!}\,e^{-n\theta} \qquad (6\text{-}9)$$

The laminar flow model was calculated according to Fogler (2016).

$$E(\theta) = \begin{cases} 0, & \theta < 0.5 \\ \dfrac{1}{2\,\theta^3}, & \theta \geq 0.5 \end{cases} \qquad (6\text{-}10)$$

6.3.3. Preparation of Aquabacterium citratiphilum

A. citratiphilum (DSM 11900) was obtained from the Leibniz Institute DSMZ-German Collection of Microorganisms and Cell Cultures GmbH (Germany), grown on suitable agar plates or bouillon with Medium 830a (DSMZ GmbH, 2007, 2012). For the cultivation of *A. citratiphilum* in liquid and establishing a growth curve, a colony grown on an agar plate was transferred into the liquid bouillon in a 250 mL Erlenmeyer flask, which was shaken at 120 rpm at 20°C (Kalmbach et al., 1999). To calibrate a grow curve with absorbance readings at 600 nm (A_{600}) measured with a 1 cm cuvette, the cell suspension was plated and colony forming units (CFU) were counted using a cell density meter WPA CO 8000 (Biochrom, United States) and colony counter BZG 30 (WTW, Germany) (Figure S12-11).

6.3.4. Experimental procedure for conducting biodosimetry

For biodosimetry feed solutions, cells with an A_{600} between 0.24 and 0.54 in exponential growth phase were harvested by a centrifugation step at 5,000 RCF for 10 min at 4°C. The supernatant was withdrawn, and the pellet dissolved in phosphate-buffered saline (PBS), prepared according to NSF/ANSI 55 (NSF/ANSI, 2019). This washing step was repeated three times in total. Based on the growth curve and measured A_{600}, appropriate amount of washed cell suspension was used to reach a final concentration of approximately $5 \cdot 10^6$ CFU mL^{-1} in 2.5 L PBS. For reducing cell

adsorption, PBS was modified with Tween20 (0.002%), when needed. Tween20 was purchased from Sigma-Aldrich, France. After washing, the feed solution should be used immediately to avoid cells from adapting to the new low nutrient conditions (Bucheli-Witschel et al., 2010). For the final three experiments, shown in Figure 6-6, by using the A_{600} of bouillon, cell density of $5.5 \cdot 10^6$ CFU mL^{-1} with a standard deviation of 12% was achieved. Through washing, the decadic absorption coefficient at 273 nm was maintained at 0.043 ± 0.014 cm^{-1}. In general, absorbance should be adapted to the desired value through the addition of additives (U.S. EPA, 2003). In case lower absorbance would be needed, cell number in the feed could be reduced. In this study absorbance was not further changed.

Before starting an experiment, the experimental skid was flushed with DI water, followed by disinfection through recirculating 250 mL of 1% H_2O_2 (Merck, Germany) for 10 minutes, but discarding the first 100 mL to avoid H_2O_2 dilution. Then, the system was primed with 1 L sterile Milli-Q water, followed by 1 L of sterile PBS. During priming, the LED was activated for 10 minutes.

The feed container was connected to the inlet and a waste container was placed below the outlet, where the samples were taken. Samples for different UV irradiation HRTs were taken in triplicates and random order in 15 mL transparent tubes. Blank samples (no UV irradiation) were taken at the same spot, before the first irradiation sample, after the second, and after the last sample. Afterward, samples were diluted serially using PBS to reach 25-250 CFU per plate analogous to NSF/ANSI (2019). 0.1 or 0.15 mL, depending on the expected CFU, was pipetted on room temperature agar plates and spread using a Drigalski spatula made of glass (height 200 mm, width 45 mm and diameter 4 mm) till a resistance between plate and spatula could be felt. Spatula was dipped into 80% ethanol and flamed. Overall, three identical spatulas were used alternately so each spatula had sufficient time to cool down. Plates were inverted and inoculated in dark at 20°C for 7 days. CFU were counted using the BZG 30 (WTW, Germany). The LRV was calculated following equation (6-11):

$$LRV \, [-] = \, log_{10}(\frac{N_0}{N})$$
(6-11)

Whereas N_0 represents the geometrical mean of the unirradiated samples in CFU mL^{-1} and N is the geometrical mean of an irradiated sample at a certain HRT (NSF/ANSI, 2019). Bouillon as well as PBS used for washing and dilution were plated as negative controls.

6.4. Results and discussion

6.4.1. Sterilization of experimental skid and contamination controls

Ensuring proper sterilization at the start of an experiment is critical, and appropriate controls are necessary to ensure a contamination free operation of the biodosimetry. Here, a method using 1% H_2O_2 was chosen, as the solution is easy to handle and compatible with most materials. To test if the sterilization by solely using H_2O_2 is sufficient, a negative control sample was taken during each experiment. The sample was taken during the flushing with sterile PBS and the LED switched off prior to the start of the experiment. Based on these observations, it could be demonstrated that disinfection with 1% H_2O_2 for 10 min is sufficient, as no CFU were found in the negative control samples.

6.4.2. Tracer tests

The appropriate flushing feed volume required to achieve steady-state after changing a setting in a biodosimetry experiment was determined through two tracer tests (Figure 6-3). One tracer test was performed with a constant flow rate of 1.5 L h^{-1}, one with higher flow rate of 6 L h^{-1}. t_m for 1.5 L h^{-1} was 239.2 s and 76.5 s for 6.0 L h^{-1}, respectively. The calculated τ for 1.5 L h^{-1} and 6.0 L h^{-1} were 289.5 and 72.1 s, respectively with a measured reactor volume of 120.3 mL. Whereas for 6.0 L h^{-1} space-time τ and mean residence time t_m were rather comparable, t_m for 1.5 L h^{-1} was smaller than τ, indicating the presence of some dead space (Levenspiel, 2012). Next to the tank in series / CSTR and laminar flow model, to compare the shape of the curves without offset, the F(θ) tm curve of 1.5 L h^{-1} of the tracer experiment was added with $E(\theta) = t_m \cdot E(t)$ and $\theta = \frac{t}{t_m}$. Based on these results, it was decided to flush approximately 0.2 L, representing $\theta \approx 1.7$, in between the different steps to achieve steady state. In addition, it should be noted, that the UV reactor is positioned in the last ~40% of the skid. Hence, the 0.2 L were estimated to be four times the void volume from the UV reactor till effluent.
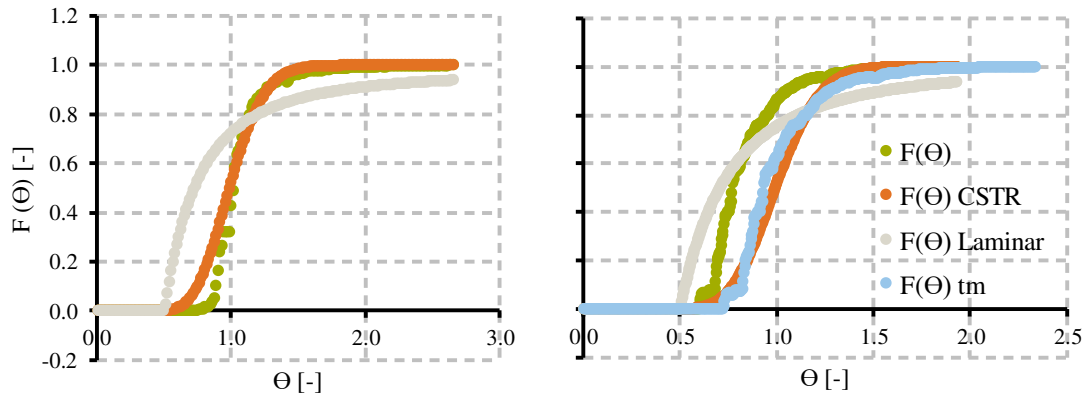
Figure 6-3:   *Fitted cumulative residence time distribution curves for different flow rates 6.0 L h^{-1} (left) and 1.5 L h^{-1} (right); F(Θ) represents the measured cumulative residence time distribution (RTD), F(Θ) CSTR is the tank in series and F(Θ) Laminar the laminar flow model. F(Θ) tm is the measured RTD but shifted using mean residence time t_m instead of space-time τ during normalization.*

6.4.3. Order of flow steps

Based on the tracer test, three biodosimetry experiments with a driving current of 96 mA were performed for flow steps with 2.13, 2.83, 4.25, and 8.50 L h^{-1} resulting in approximately HRTs of 4, 3, 2, and 1 s, respectively (Figure 6-4). The sample order was random, but before the first sample, after sample number two, and after sample four, the blanks without irradiation were taken. Overall, the inactivation seemed not to follow the expected trend of increasing LRV with longer HRT. On average between 300 to 5,900 CFU per mL were detected in the samples of all HRTs, leading to the assumption that higher inactivation should still be possible. The reason for not seeing the expected trend of higher inactivation with higher HRT becomes more obvious when ordering the samples chronologically (ordering them as they were taken instead of increasing HRT) as shown in the supplementary material (Figure S12-12). After taking the blank samples (before samples one and three), the LRV was reduced.
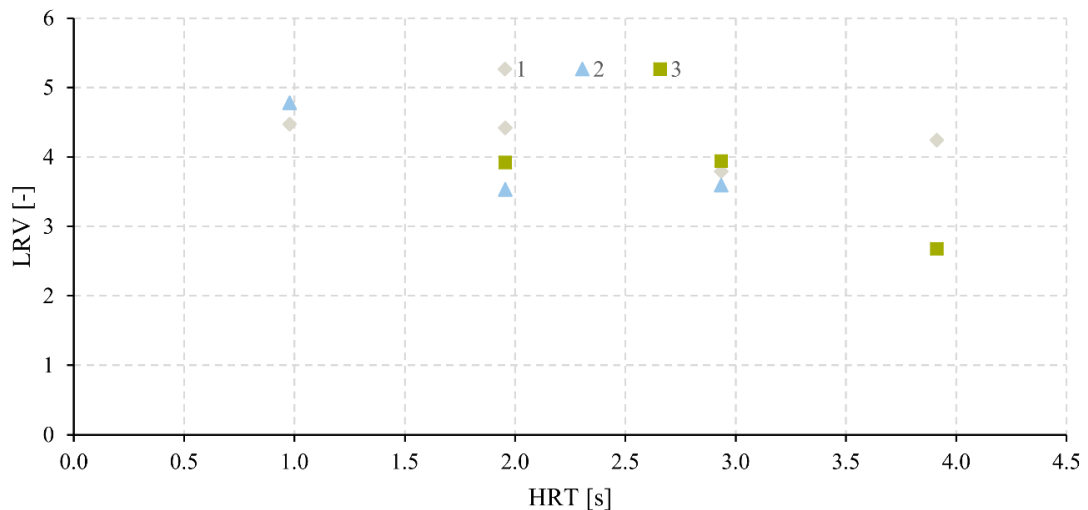
Figure 6-4: *Logarithmic reduction values (LRVs) based on biodosimetry using A. citratiphilum with a driving current of 96 mA over hydraulic retention time (HRT); the numbers 1, 2 and 3 are referring to the repetitions of the experiment.*

The reason for these inconsistencies in LRVs can be found when taking a closer look at the residence time distributions (Figure 6-3). Two models were fitted to the tracer curves to compare the results to ideal reactors. The cumulative residence time distribution curve for the 6.0 L h^{-1} seems to fit with the CSTR model. On the contrary, when looking at the curves of 1.5 L h^{-1}, considerable differences can be seen. First, in comparison to the CSTRs, the curve is shifted to a smaller θ. As discussed this was also seen as $t_m < \tau$, leading to the assumption of dead spaces present (Levenspiel, 2012). Taking a closer look on the curve F(θ) tm, a long tail out was present for $\theta > 1.5$, however, as the used tracer was limited in precision with a maximal detectable change of 1 µS cm^{-1} for the conductivity sensor, the long tailing cannot be analyzed in more detail. The microbiological solution itself may serve as a step tracer to further resolve the long tail. Thereby, the system could be first filled with microbial solution and then flushed with sterile DI water to check which volume is needed to flush to have no CFU measurable anymore.

For the biodosimetry, the long tail can influence the inactivation of microorganisms: to confirm a LRV of 4 after a blank without UV reliably (with an error < one percent), the system needs to be flushed until an F(t) of 0.999999 is reached. Depending on the shape of the tail, this could increase the volume of microorganism solution to be flushed to unpractical volumes. As an extreme example, the laminar flow model is considered with F(θ) = (1- 1/(4 θ^2)) for $\theta > 0.5$ (Fogler, 2016). θ required to reach 0.999 is 15.8 whereas for 0.9999 it is 50. So basically, for pure laminar flow, 50 times of the void volume flushing with sterile solution would be needed to reduce microbial count in the effluent from 10^6 to 100 CFU mL^{-1}.

One solution to reduce the void volume caused by the long tail of the residence time distribution is to reorder the flow steps, starting with the highest UV irradiation and

ending with the samples without UV. Assuming that due to flushing 0.1% of cells are still present in the samples of the next step, when running samples according to increasing cell numbers, the error is negligible. On the contrary, protracting 0.1% of cells from the blank to the next sample can have tremendous effects as it limits the measurable LRV to $\log_{10} (1/0.001) = 3$. To confirm these assumptions, an experiment with a reduced driving current/fluence rate (24 instead of 96 mA) and with the new order of flow steps was performed. Thereby only an HRT of 1 s yielded in countable colonies in the sample. This leads to the assumption that the counts as shown in Figure 6-4 were only caused by the long tail of the residence time distribution. In the following, the new order was maintained and the driving current was further reduced to 16 mA. In addition, flow steps were changed to 1.06, 1.42, 2.13 and 4.25 L h^{-1} resulting in approximately 8, 6, 4, and 2 s HRT. The results of one representative experiment are shown in Figure 6-5. Here the expected trend of increased inactivation with rising HRT became noticeable even though in the step of 8 s less than 25 CFU were present and therefore results were not considered.

On top of the discussed effects of long tails, adsorption-desorption effects could further influence the results. To avoid errors, it is therefore necessary to take the samples from the highest LRV/fluence in decreasing order. This strategy stands in accordance with NSF/ANSI 55 (NSF/ANSI, 2019) stating that the UV experiment needs to be executed before the sample without UV disinfection. Alternatively, for experimental skids described in the U.S. EPA guidelines (U.S. EPA, 2003) influent samples are taken from a separate sampling point before the UV reactor, which can avoid protraction. However, taking an influent sample before the reactor might not be practical in the combination of treatments and does not reduce errors between different UV steps.
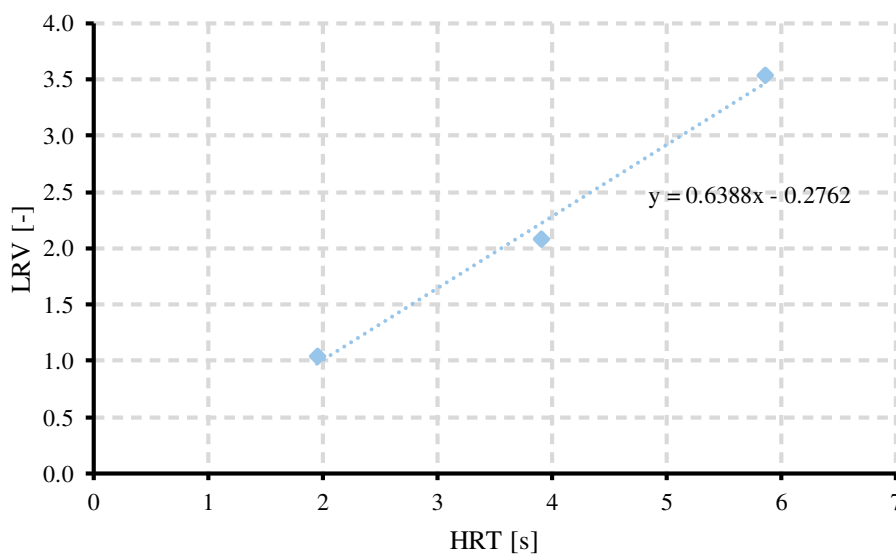
Figure 6-5:   Biodosimetry experiment with a driving current of 16 mA and samples ordered with decreasing fluence.

6.4.4. (Photo)repair and adhesion to plastic labware

Despite the improvement of results with the enhanced order of flow steps, it was recognized that samples sometimes showed inconsistencies between serial dilutions. This effect was especially present for undiluted samples and dilution 10^{-1}. As an example, for an undiluted plated sample 253 CFU could be counted, whereas there were only 5 CFU present in the 10^{-1} dilution. For this inconsistency, two possible reasons were suspected and tested: photoreactivation through photorepair, and adsorption to plastic labware.

6.4.4.1. Repair processes

Exposure to near UV light (310 – 480 nm) can lead to photorepair of damaged DNA (Harm, 1980; Oguma et al., 2002). When Oguma et al. (2002) irradiated 254 nm UV treated samples of *E. coli* with fluorescent tubes with 18 W (0.1 mW cm^{-2} at sample surface for 360 nm) for 3 h, they observed recovery from approximately 3 LRV to 0.9 LRV. The sterile working bench used in this study was equipped with two 36 W fluorescent tubes. As processing of all samples usually took considerably longer than 1 h, photorepair during sample preparation might be significant, as photorepair was suspected to be rather limited by time than by irradiance (Harm, 1980; Oguma et al., 2002).

The photorepair effect might be further increased as samples were taken in transparent 15 mL tubes, while 1.5 mL tubes were used for serial dilutions. The 15 mL tubes are suspected to provide a larger surface and probably also higher transmittance for visible light (Figure S12-13). This could lead to discrepancies between the CFU in undiluted and diluted samples. To reduce the effects of photorepair, the undiluted samples were taken in 1.5 mL tubes and stored on ice in the dark until the cell spreading process was conducted. The laboratory itself was darkened and commercially available red filters were installed in the sterile working bench (the only source of light in the lab). Even though the effects of photorepair are well known, methodological details are often missing (Table 6-1). To avoid artifacts of photorepair, this is however important information that has to be reported accordingly.

When comparing results with the red filter installed (Figure 6-6) to the previous outcome (Figure 6-5), LRVs are increased approximately by 1, which is likely attributed to controlled photorepair. Moreover, a shoulder (negative intercept), typical for repair processes, was observed when the red-light filters were not used in the experiments. This is not the case anymore.

Another explanation on why inconsistent CFU between dilutions could be observed might be caused by homologous recombination repair. Higher number of cells could lead to higher recombination repair similarly as it can occur in cell aggregates (Ajon et al., 2011; Fröls et al., 2008). Nevertheless, testing this hypothesis is beyond the scope of this study.

6.4.4.2. Adsorption to plastic labware

In addition to the optimized sample processing method and the installation of the red filters, the adsorption on plastic labware was examined, as it was previously shown that this may influence results (Richter et al., 2021). Therefore, instead of standard Eppendorf tubes, different low-binding protein or low-binding DNA tubes were used together with low retention tips for pipetting. Similarly as in the study of Richter et al. (2021), differences between different brands of low binding tubes were found. As an example, for one tube, there were 22 CFU observed at a dilution of 10^{-1} whereas 206 CFU were counted for another tube. Although some artifacts remained with all tested tubes, testing different suppliers can improve inconsistencies in the CFU dilution series. Overall, Richter et al. (2021) observed a correlation of phage adsorption to plastic labware based on hydrophobicity. More specific, they observed a threshold of 95° wetting angle below which tubes were marked as safe for adsorption. Tween20, a common surfactant reducing protein adsorption, was found to reduce the wetting angle when used as a coating (Pan et al., 2015; Richter et al., 2021; Smith et al., 1978) and seems therefore promising in reducing bacterial adsorption as well. Following the recommendations of Richter et al. (2021), 0.02 mL Tween20 were added per L PBS in the feed solution, the solution for dissolving washed *A. citratiphilum* pellets, and in the PBS used for dilutions.

Additionally, we considered a 95% confidence interval threshold that will mark and exclude samples with adsorption artifacts automatically. Basic cell counts N for each sample are assumed to follow a Poisson distribution, but it is not clear if cell counts after an inactivation experiment still follow Poisson distribution (Koyama et al., 2016). Nevertheless, confidence intervals for Poisson distribution were calculated based on the Chi-square distribution X_x^2 as following (Garwood, 1936; Sahai and Khurshid, 1993; Ulm, 1990):

$$\mu_{lower} = \frac{X_{2N,0.025}^2}{2} \tag{6-12}$$

$$\mu_{upper} = \frac{X_{2(N+1),0.975}^2}{2} \tag{6-13}$$

Hence if $10 \cdot \mu_{upper}$ of dilution $10^{-x} > \mu_{lower}$ of dilution $10^{-(x-1)}$, the condition was fulfilled. This provides a possible, objective and easily implementable quality control step for biodosimetry experiments. As an example, the inconsistency of 5 CFU counted at 10^{-1} and 253 CFU at 10^0 would be detected. $10 \cdot \mu_{upper}$ for dilution 10^{-1} would equal 117, whereas μ_{lower} of dilution 10^0 is 223 and following $10 \cdot \mu_{upper}$ is smaller than μ_{lower}.

Following the improved procedure inconsistencies between dilution steps could not always be avoided, but were reduced. Results of the improved method can be seen Figure 6-6. Hereby flow rates were additionally adapted to 1.7, 2.13, 2.83, and 4.25 L h^{-1} leading to HRTs of approximately 5, 4, 3, and 2 s. It is noteworthy that for one

experiment less than 25 colonies were counted at the 5 s HRT step potentially leading to a higher deviation of the replicates.

To test if Tween20 in the feed and UV irradiation has additional disinfection effects on the cells, two HRTs were tested without Tween20 added to the feed. As those results fall within the standard deviation of the test with Tween20 in the feed, it is therefore assumed, that Tween20 for the used setting has no significant effect on the inactivation of *A. citratiphilum*. Nevertheless, this could change depending on the irradiation source and tested microorganism. Tween20 was found to serve as food source for *A. citratiphilum* (Kalmbach et al., 1999) and therefore no toxic effects of Tween20 in the used concentration alone can be assumed.
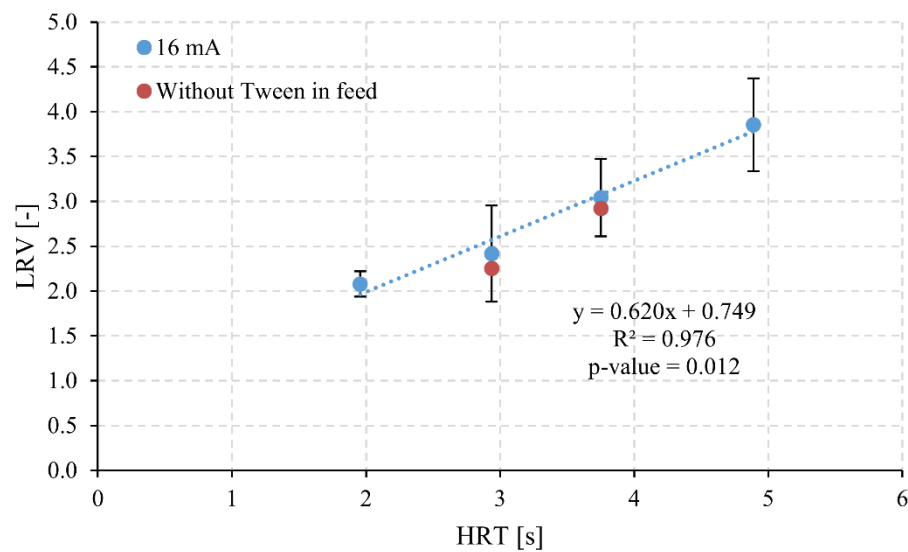
Figure 6-6: *Final biodosimetry results at 16 mA driving current with and without Tween20 added to the feed.*

6.4.5. Final procedure

Within the past years, a variety of biodosimetry studies were conducted at pilot- and lab-scale for flow-through reactors using bacteria as challenge organisms. Our literature search (August, 2022) on bacterial biodosimetry experiments of flow-through reactors resulted in ten studies (excluding experiments with spores; including two studies for batch operation) that shared some steps of a biodosimetry experiment (as washing steps, cultivation and processing of samples). Overall, the different studies investigated revealed major differences and no standardization across many of the experimental parameters (like growth phase, cell washing, processing samples in the dark or triggering photorepair; Table 6-1). Within the studies, *E. coli* has been used as the most common challenge organism (in 10/10 studies) but some studies employed other strains that are important for human health like *Staphylococcus aureus* (Fitzhenry et al., 2021). As UV disinfection has been researched for a long time and there are countless studies in the literature, however, bacterial species other than *E. coli* or non-relevant to human health are not commonly investigated. Experiments were run with

both, exponential and stationary phase cultures (Oguma et al., 2013; Sholtes and Linden, 2019). Sometimes just growth conditions, but no direct information about growth phase is given (Fitzhenry et al., 2021; Wang et al., 2021). Sensitivity of microorganisms to UV light might not only change with type of growth phase but also with the specific growth rate (Bucheli-Witschel et al., 2010). Moreover, it should be noted that some studies used reactors in single pass mode whereas others used recirculation. By direct comparison of those two settings, differences were identified (Romero-Martínez et al., 2019). Finally, whereas some studies gave details on sample processing, the information provided is often incomplete. Overall, this led to the conclusion that there is no standardized protocol for biodosimetry performed in lab-scale flow-through systems. Therefore, we developed a robust, reproducible procedure for the relevant biofilm forming bacterium *A. citratiphilum* considering key operational parameters that were previously not consistently used or recorded based on our literature research (i.e., sterilization of the skid, importance of the hydraulic characteristics of the used system, or the order of flow steps, photorepair and sample processing).

Considering the above-discussed points, our proposed standardized protocol is presented in details in the supplementary material (section 12.5.6). Preparations include the simple tracer test, sterilization procedure, cultivation, setting-up the growth curve and washing of *A. citratiphilum*, as well as preparing feed solution for experiments. The experimental part describes taking the negative control samples, order of flow steps, sampling procedure and controls necessary. Finally, processing of samples is defined including measures against photorepair and checking for adsorption on labware.

6.5. Conclusion

While biodosimetry with phages of batch systems is a highly standardized procedure, bacterial based biodosimetry protocols are not yet standardized, in particular for flow-through systems. Differences of methodology can be seen in the preparation of bacterial solutions, including the growth phase and washing. The experiment itself varies between single pass and recirculation experiments and the order of flow steps is commonly not addressed. The processing of samples varies from avoiding to triggering photorepair or no information given at all. Within this study, it was shown that the reactor hydraulics and possible long tails can heavily impact the results. To avoid and minimize those errors, it is recommended to take the samples descending with fluence. While processing of the samples possible photorepair and adsorption of cells to labware was observed. Even though, photorepair was not intended in the first place, environmental light might have influenced results during processing of the samples. Hence, it is recommended to work only under red light to limit opportunities for photorepair to occur. Installing red light filter covers for fluorescent tubes might be an easy solution for sterile working benches. Concerning adsorption to plastic labware, an objective criterion was presented, adsorption was reduced by the usage of low-

binding tubes and Tween20, as well as Tween20 check for adverse effects conducted. Finally, a hands-on protocol for using *A. citratiphilum* was proposed including a simple tracer test, sterilization of the skid, and the other critical points related to the order of sampling, photorepair and reducing cell adsorption. The complete protocol can be found in section 12.5.6 of the supporting information. The proposed method is reproducible and effectively avoids artifacts. Considering the critical points during biodosimetry for microbial cells greatly increases reproducibility and transferability of results between studies.

Table 6-1: Overview on the methodology of selected studies, B = batch, F= flow-through, S = stationary, E = exponential, R= recirculation, SP= single pass, D = dark, P = photorepair, na = information not available

#	Study	Mode	Irradiations source	Species	Phase	Number of washing	Recirculation or single pass	Processing
1	Oguma et al., 2013	B & F	LED	*E. coli*	S	2	R	D & P
2	Harris et al., 1987	B	LP	*E. coli, Streptococcus faecalis*	na	1	-	D & P
3	Oguma et al., 2016	F	LED	*E. coli*	S	2	SP	Same as 1 / na
4	Wenjun and Wenjun, 2009	F	LP	*E. coli,* and total bacteria count	S	na	SP	na
5	Wang et al., 2021	F	LED	*E. coli*	na	na	SP	na
6	Fitzhenry et al., 2021	F	LP and Xenon flash	*E. coli, S. aureus, Listeria innocua*	na	na	SP	D & P
7	Müller et al., 2017	F	LP	*E. coli*	na	1-3	R	na
8	Romero-Martínez et al.,	F	LP	*E. coli, Enterococcus sp.*	na	2 or none	R & SP	na
9	Sholtes and Linden, 2019	B	LED	*E. coli, Pseudomonas aeruginosa*	E	3 and sonication	-	D
10	Nyangaresi et al., 2019	B	LED	*E. coli*	E	2	-	D&P
11	This study	F	LED	*A. citratiphilum*	E	3	SP	D

Notes: The authors declare no competing financial interest.

7. Optimizing UVC-disinfection using LEDs as an energy efficient pre-treatment for biofouling control in spiral-wound membrane systems

The following chapters shows the results of the investigations related to hypotheses 4 ("*With raising fluence rates (in the range of ~1 – 100 mW cm⁻²), the disinfection efficiency of pulsed UVC-LEDs is increasing significantly by more than 30% for bacteria*") and 5 ("*Applying pulsed UVC-irradiation as an operational strategy for biofouling control leads to 30% higher energy efficiency compared to continuous irradiation*").

This chapter has been previously published with some editorial changes as follows:

7.1. Abstract

Biofouling remains a major challenge for reverse osmosis (RO) systems. Pulsed ultraviolet (UV) pre-treatment has been proposed as a mitigation strategy for biofouling control of RO membranes. This study investigated whether increasing fluence rate during pulsed UV disinfection leads to enhanced inactivation. Further, UV irradiation from 1.5 to 61.3 mJ cm^{-2} was tested for optimal biofouling control. Therefore, an UVC-LED reactor was characterized by successfully adapting an actinometry method for flow-through mode. The inactivation of microorganisms was compared in flow-through biodosimetry experiments in pulsed and continuous irradiation. Finally, several settings were applied as pre-treatment in lab-scale biofouling experiments, and membrane performance and biofilm removability elucidated. Whereas no enhanced inactivation was observed during biodosimetry experiments, pulsed UV disinfection resulted in an average of 20.6% increased delay of biofilm formation. On the contrary, for pulsed UV disinfection, the biofilm hydraulic resistance seemed higher than continuous equivalents, but not significantly. Overall, savings of operational expenditures per fluence applied was highest around 4 mJ cm^{-2}. UV pre-treated biofilms showed no enhanced removability, but delay in biofilm formation was noticeable in two of three experiments. In case the effects translate to up-scaled applications over several cleanings, UV pre-treatment for biofouling control is an interesting option.
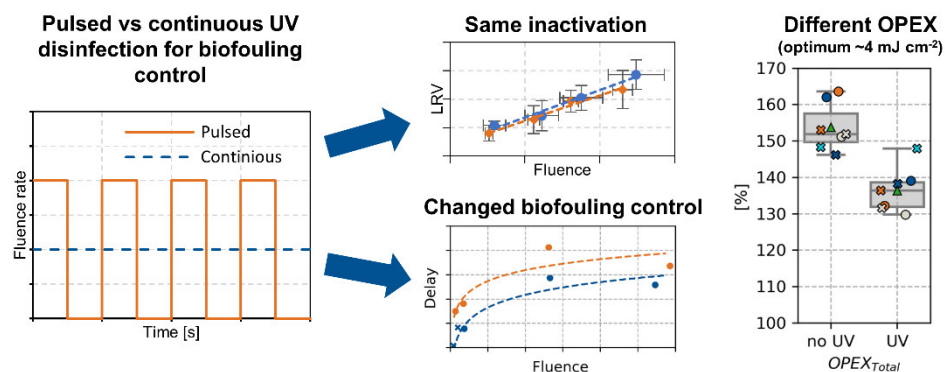
Figure 7-1:   Graphical abstract Chapter 7.

7.2. Introduction

Among the different kinds of fouling, biofouling has been characterized as the most severe kind of fouling in many reverse osmosis (RO) membrane systems for water purification (Flemming et al., 1997; Najid et al., 2022; Nguyen et al., 2012; Vrouwenvelder and van der Kooij, 2001). Biofouling is defined as an undesired biofilm formation leading to 'unacceptable' operational challenges (Characklis and Marshall, 1990; Vrouwenvelder et al., 2009c). As reported by Nguyen et al. (2012), problems associated with biofouling include the formation of a low permeable biofilm, which leads to a higher transmembrane pressure (TMP) and thus to higher energy consumption. Furthermore, several studies showed that for spiral-wound membrane modules the accumulation of biomass correlates with an increased feed channel pressure drop (FCPD) (Radu et al., 2010; Vrouwenvelder et al., 2009c; Vrouwenvelder et al., 2009a). In addition, concentration polarization can occur in areas with no tangential flow caused by the biofilm and the cleaning procedures, necessary to maintain membrane performance, might reduce membrane lifetime (Flemming, 1997).

The dry mass of the biofilm usually consists of extracellular polymeric substances (EPS) (> 90%) and the cells of the microorganisms (Flemming and Wingender, 2010). The microbial community formed on the membranes is diverse and might be affected among others by nutritional, temperature and hydrodynamic conditions, as well as by the applied pre-treatment and cleaning-in-place (CIP) procedures (de Vries et al., 2020; Zodrow et al., 2014). The composition and production of EPS by microorganisms might depend on several factors like the microorganisms' identity, shear forces, temperature, nutrients, and cell-cell communication, but the exact mechanisms are still not well understood (Flemming, 2017; Flemming and Wingender, 2010; Frederick et al., 2011; Jiang and Liu, 2013). While EPS was determined as the primary driver for hydraulic resistance of the biofilm, microbial cells might hinder back diffusion of salts, leading to elevated osmotic pressure on the membrane surface (Dreszer et al., 2013; Herzberg and Elimelech, 2007).

Several pre-treatment technologies are investigated to reduce (bio)fouling, which include micro- and ultrafiltration, coagulation and flocculation, granular media filtration and disinfection processes (Jiang et al., 2017). Furthermore, as the EU regulation 528/2012 aims to limit the harmful effects of biocides (EU, 2012), there currently is a need to develop alternative biocide-free pre-treatment processes. A chemical-free disinfection technique for biofouling control represents ultraviolet (UV) disinfection. It is often not considered, probably because it has no residual effect (Harif et al., 2011). UV irradiation is an established disinfection procedure, not only being chemical-free but also having limited byproduct formation (Harm, 1980; Li et al., 2019b; Liberti et al., 2003; Romero-Martínez et al., 2019). UV disinfection is effective against most bacteria, viruses and protozoa, easy to operate with low capital and operational costs (Bolton and Cotton, 2022). On the contrary, low UV transmittance is a challenge for successful inactivation and especially if viruses need to be inactivated, higher UV

fluences might be needed (Bolton and Cotton, 2022). Another challenge of UV disinfection is associated with tailing effects in the inactivation occurring at higher fluence (Azimi et al., 2017; Emerick et al., 2000; Harm, 1980; Kowalski et al., 2020; U.S. EPA, 2006). This tailing might be caused for instance by particles/cell aggregates shielding cells from irradiation or by sub-populations of the microorganism being more UV resistant (Azimi et al., 2017; Emerick et al., 2000; Harm, 1980; Kowalski et al., 2020; U.S. EPA, 2006). UV light can be categorized into UVA (315-400 nm), UVB (280-315 nm), and UVC (200-280 nm) wavelength ranges (U.S. EPA, 2006). In general, UV disinfection is assumed to follow Bunsen–Roscoe reciprocity law, meaning UV disinfection solely depends on the product of fluence rate and time (fluence) (Harm, 1980; Pousty et al., 2021). Sommer et al. (1998), however, observed enhanced inactivation of *Escherichia coli* with a higher fluence rate in the range of 0.002 to 0.2 mW cm^{-2} at 254 nm. On the contrary, Pousty et al. (2021) observed no deviation form Bunsen-Roscoe law in the range of 0.1 to 0.001 mW cm^{-2} at 265 nm. They even observed worse disinfection performance with increasing fluence rates and wavelengths. This was explained as inactivation at higher wavelengths was also caused by reactive oxygen species (ROS). At higher fluence rates more ROS-ROS reactions might occur, leading to overall decreased inactivation (Pousty et al., 2021).

Aside from low- and medium-pressure vapor lamps, in recent years UV-LEDs have been developed as an alternative UVC irradiation source (Mondal et al., 2021; Song et al., 2016). Similarly as for visible light LEDs, the efficiency of UV-LEDs was predicted to increase (Ibrahim et al., 2014). However, currently LEDs are still lacking efficiency in comparison to low-pressure vapor lamps (Koutchma et al., 2019). Some advantages of LEDs include that they contain no mercury, they are available in different wavelengths, as well as they are compact and robust in design allowing new reactor configurations (Beck et al., 2015; Song et al., 2016; Würtele et al., 2011). Another feature of LEDs is that they allow for pulsed irradiation (Song et al., 2016; Würtele et al., 2011). To compare the inactivation efficiency of pulsed irradiation to a continuous mode of operation at the same fluence, either the fluence rate during the pulses or the irradiation time can be increased. Several studies so far investigated the effect of pulsed UVC/UVB irradiation on the inactivation of microorganisms (Nyangaresi et al., 2019; Sholtes and Linden, 2019; Song et al., 2018; Tran et al., 2014; Wengraitis et al., 2013; Zou et al., 2019). In these studies, either the time of pulsed irradiation was extended or the log removal normalized to fluence applied. Several studies observed considerably enhanced inactivation while applying pulsed irradiation (Tran et al., 2014; Wengraitis et al., 2013; Zou et al., 2019), whereas others did not (Nyangaresi et al., 2019; Sholtes and Linden, 2019; Song et al., 2018). Some of the proposed reasons for observing an increased efficiency during pulsed irradiation were adopted from pulsed disinfection using xenon flash lamps or non-specified biological effects (Song et al., 2018; Tran et al., 2014; Wengraitis et al., 2013; Zou et al., 2019). However, no definitive explanation could be given, especially as the light power of the LEDs is considerably lower than the one of xenon flash lamps (Song et al., 2018; Tran et al., 2014; Wengraitis et al., 2013;

Zou et al., 2019). Song et al. (2018) proposed that artifacts in the calculated fluence could be the reason for the positive effects. They further recommended not to normalize log inactivation by fluence when a considerably different fluence was applied. Whereas for continuous irradiation Sommer et al. (1998) observed a deviation from Bunsen-Roscoe with higher fluence rate leading to higher inactivation, Pousty et al. (2021) observed the opposite. The deviation might be wavelength dependent (Pousty et al., 2021), but overall it is not clear how pulsed irradiation affects microorganism inactivation at constant overall fluence, but increasing the fluence rate (and not irradiation time) by more than one order of magnitude.

UV pre-treatment as biofouling control for membrane processes was investigated in a couple of studies with fluence varying from 0.85 to 400 mJ cm^{-2} and with various feed water from lab- to full-scale set-ups (Harif et al., 2011; Hu et al., 2023; Lakretz et al., 2018; Marconnet et al., 2011; Otaki et al., 1998; Sperle et al., 2020a; Wang et al., 2023a; Wu et al., 2021a). Nevertheless, in comparison to other technologies, e.g. ultrafiltration, UV was not a commonly applied/researched pre-treatment technology for RO fouling control in the recent past (Harif et al., 2011; Jiang et al., 2017). Some of the studies (Harif et al., 2011; Marconnet et al., 2011; Sperle et al., 2020a) observed a delay of biofouling in RO/nanofiltration systems due to UV pre-treatment and a higher flux/permeability. Overall, these studies reported reduced EPS as well as lower ATP/active biomass on the membranes. As reasons for the delay, inactivation of the incoming cells, changed adsorption properties of the cells, or cells suffering from cell cycle arrest were proposed (Harif et al., 2011; Marconnet et al., 2011; Otaki et al., 1998; Sperle et al., 2020a). Through the UV pre-treatment, the microbial community was suspected to change, which was hypothesized to impact the formed EPS and further the permeability of the formed biofilms (Harif et al., 2011; Sperle et al., 2020a). Furthermore, Wang et al. (2023a) suspected that less EPS in biofilms is formed due to an inhibition of functional genes by the UV pre-treatment. Positive impacts of UV pre-treatment on biofouling control might also be influenced by changed quorum sensing or the introduction of prophage, but this could not be proven, yet (Sperle et al., 2020a). On the contrary, other studies observed higher fouling due to UV pre-treatment (Lakretz et al., 2018; Wu et al., 2021a). Wu et al. (2021a) reported increased biofouling to a change in microbial diversity, as well, but this time species present might yield a higher EPS production. Overall, effects of UV irradiation on biofouling control are conversely discussed and it is not clear, how observed effects correlate with the applied fluence. Furthermore, it needs to be elucidated what the benefits regarding overall energy efficiency and operational expenditures (OPEX) are.

The current study aims to validate the effects of UV pre-treatment for biofouling control in RO systems and to optimize the pre-treatment for energy efficiency, testing different fluence and pulsed irradiation. It shall be clarified, if the increased fluence rate during pulsed irradiation enhances the inactivation efficiency of bacteria and viruses. Furthermore, we hypothesize that applying pulsed UVC-irradiation as an operational strategy for biofouling control leads to higher energy efficiency compared to continuous

irradiation. Therefore, a UVC-LED reactor was characterized by adapting an actinometric method for flow-through reactors to enable detailed fluence characterization. In the next step, it was checked if increasing the peak fluence rate by approximately two orders of magnitudes during pulsed UVC irradiation can improve the effects for disinfection of two indicator organisms. Chosen indicator organisms are MS2 phage and *Aquabacterium citratiphilum,* a bacterium found in drinking water biofilms potentially also relevant for biofouling (Kalmbach et al., 1999; Sperle et al., 2020a). In comparison to the studies so far, the experimental approach of this study is different, as for UVC irradiation, the fluence rate is adapted and not the irradiation time. Comparable settings of pulsed and continuous irradiation were further tested in lab-scale biofouling studies and membrane performance parameters were monitored. Based on the experimental results OPEX were estimated and compared for the different pulsed and continuous settings to identify the optimal irradiation setting for biofouling control. Finally, biofilm removability was tested in CIP experiments.

7.3. Materials and methods

7.3.1. UVC-LED reactor

The LED reactor was supplied by UV-EL GmbH (Germany) and used for biodosimetry, actinometry and biofouling experiments. It consisted of a 2P2S-S6060 UVC Quad SMD 275 nm Module (Bolb Inc., United States) sitting over a silica glass pipe through which the water was flowing. A metal cooling body with a fan was attached to the backside of the LEDs. As housing, reflective polytetrafluoroethylene (PTFE) was used to increase the fluence rate within the reactor. On the opposite of the LEDs, a calibrated spectrophotometer (HR 4000, Ocean Optics/Ocean Insight, Netherlands) was connected with a cosine corrector (CCSA2, Thorlabs, Germany) via a silica-core solarization-resistant optical fiber patch cable (QP450-1-XSR) to measure the emission spectrum of the LEDs. The spectrum recorded for the LED is depicted in the supplementary information with the peak wavelength at 273 nm (Figure S12-14). LEDs were powered by a LED-Pulse-Controller (Leistungselektronik Jena, Germany). The LED-Pulse-Controller itself was powered with a 24 V supply. The controller allowed flexible pulsation of the LEDs and adaption of the driving current in steps of 8 mA (16-400 mA used in this study). As a triggering source, the FG250D function generator (H-Tronic, Germany) was set to 10 Hz in TTL mode. The duty cycle during pulsation was adapted by changing the pulse lengths between 500 and 22,000 µs representing a range of 0.5 to 22% duty cycles. A photograph showing the reactor from two perspectives and attached to a membrane fouling simulator (MFS) is depicted in the supporting information (Figure S12-15).

7.3.2. Experimental set-up for actinometry and biosimetry experiments

For biosimetry and actinometry, a similar system as for biofouling experiments was set up (Figure 7-2). It consisted of a feed bottle placed over a magnetic stirrer (Heidolph MR 2000, Germany). Water was withdrawn using a frequency-regulated gear pump (DGS.38PPPV2NN00000, Tuthill Alsip, United States and K21R 63 K2 H, VEM motors Thurm, Germany). To control the flow, a magnetic inductive flow meter (MIK-6FC08AC34P, Kobold Messring GmbH, Germany) was utilized. The LED reactor was placed in an upright position at 15 °C in the temperature cabinet. For actinometry, the flow was recirculated to the feed bottle. For biosimetry experiments, the outflow was directed to a waste container (no recirculation) with the prior possibility of sampling. Before and after a biosimetry experiment, the skid was disinfected by recirculating 250 mL of 1% H_2O_2 (Merck, Germany) for 10 min.
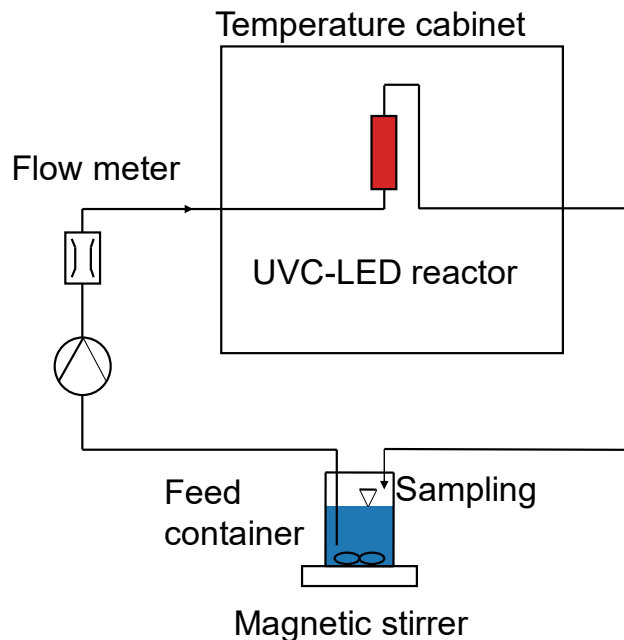
Figure 7-2:   *Schematic of the laboratory skid used for actinometry and biosimetry experiments.*

7.3.3. Actinometry

For estimating the fluence rate within the UVC-LED reactor, uridine actinometry according to Sperle et al. (2023c) was performed. First, for effective path length (l_{irr}) determination, three differently concentrated uridine solutions (AppliChem, Germany) were prepared in a 1 mM phosphate buffer saline (PBS) at pH 7. Uridine concentrations used were 0.012 mM 0.06 mM and 0.108 mM. Within the calculation, path length was varied between 0.5 and 5 cm in steps of 0.01 cm. Effective path length was found when the standard deviation of the calculated fluence rate for the three concentrations was lowest (Roibu et al., 2018; Sperle et al., 2023c). After path length determination, only the 0.012 mM concentration was used to determine fluence at a certain setting.

For actinometry, several steps were adapted to successfully transfer the method used from a batch reactor to a flow-through system. First, the whole skid for actinometry was drained from any water and connected to pressurized air to remove most of the remaining water. Next, a fixed volume (0.2-0.5 L, depending on the investigated setting to limit sampling times to practical ranges) of actinometry solution was connected as feed, and the actinometry solution was recirculated at 10 L h^{-1}. In total, five samples were taken after regular time steps. Before taking a sample, the system was recirculated for 4 min with the LEDs switched off to bring the system to a steady state. Samples were directly taken in the cuvette used for absorbance measurements and after the measurement, the sample was returned to the reactor before reactivating the LEDs again. Although we did not expect temperature to influence uridine degradation (Rabani et al., 2021), during an experiment, the temperature was checked regularly to confirm a constant temperature (approximately range of deviation $\pm$ 3 °C). Overall, through the rather large recirculation, small conversion per pass, mixing in the feed bottle, and volume solution (V_T) being $>>$ volume reactor (V_R), all conditions according to Zalazar (2005) should be met rendering the reaction rate of uridine ($R_{uridine}$) according to equation (7-1). Here, $C_{uridine}$ represents the concentration of uridine at time t.

$$R_{uridine} = \frac{V_T}{V_R} \frac{dC_{uridine}(t)}{dt} \qquad (7\text{-}1)$$

Complete mixing within the reactor could not be guaranteed, but probably due to the low conversion per pass this did not considerably influence the results, as it was tested with a changed flow rate, as will be shown in Chapter 7.4. Hence as shown by Sperle et al. (2023c) calculation for actinometry was modified by the ratio of V_T and V_R so that equation (7-2) can be derived.

$$\frac{ln\left(10^{\left[\left(A^{irr}(0)-A^{irr}(\infty)\right)\cdot\frac{l_{irr}}{l_{obs}}\right]}-1\right)}{F_H}$$
$$-\frac{ln\left(10^{\left(A^{262}(t)-A^{262}(\infty)\right)\cdot\frac{\varepsilon_U^{irr}-\varepsilon_H^{irr}}{\varepsilon_U^{262}-\varepsilon_H^{262}}\cdot\frac{l_{irr}}{l_{obs}}}-1\right)}{F_H}$$
$$= \Phi^{irr} \cdot \varepsilon_U^{irr} \cdot l_{irr} \cdot \frac{q_0^{irr}}{V_R} \cdot t \cdot \frac{V_R}{V_T} \qquad (7\text{-}2)$$

$$F_H = \frac{1-10^{-\left(A^{irr}(\infty)\cdot\frac{l_{irr}}{l_{obs}}\right)}}{A^{irr}(\infty)\cdot\frac{l_{irr}}{l_{obs}}} \qquad (7\text{-}3)$$

Please note that V_R is not crossed out to enable the direct comparison of the equations derived by Sperle et al. (2023c). When plotting the left-hand side of Equation (7-2) over $V_R/V_T \cdot$ t, the slope was used to calculate fluence rate E′as

$$E'[mW\ cm^{-2}] = \frac{slope \cdot U^{irr}}{\varepsilon_U^{irr} \cdot \Phi^{irr} \cdot 1000} \tag{7-4}$$

Hereby, $A^{irr}(0)$, $A^{irr}(\infty)$, $A^{262}(t)$ and $A^{262}(\infty)$ are the absorbance readings at 262 nm and the irradiated wavelength as measured in a cuvette at time 0 and t. ∞ represents the time of irradiation, when only the photoproduct of uridine is present. As done by Sperle et al. (2023c), $A^{irr}(0)$ and $A^{irr}(\infty)$, can be calculated from the absorbances at 262 nm by using the molar absorption coefficients. Absorbance was measured by using an Aqualog (HORIBA Jobin Yvon, Germany) and a 1 cm silica glass cuvette. l_{obs} represents the thickness of the cuvette used for measuring absorbance at 262 nm. Φ^{irr} equals the quantum yield at the irradiated wavelength for the used uridine concentration. Quantum yields of the different concentrations and at the irradiated wavelength are not known with certainty and need further investigations, but due to the higher irradiance of the reactor, 0.021, 0.022 and 0.023 mol Einstein^{-1} for the three concentrations 0.012, 0.06 and 0.108 mM were used. To compare different irradiation settings (and not absolute values) this should be sufficient. $q_{0,irr}$ is equal to the photon flux at the sample surface in Einstein s^{-1}. ε_U^{262} and ε_H^{262} represents the molar absorption coefficients of uridine and its photoproduct at 262 nm with 10,185 M^{-1} cm^{-1} and 625 M^{-1} cm^{-1} (Jin et al., 2006; Sperle et al., 2023c). ε_U^{irr}, ε_H^{irr} and U^{irr} represent the molar absorption coefficient of uridine and its photoproduct in M^{-1} cm^{-1} as well as the average photon energy in mJ Einstein^{-1} (weighted to the spectrum of the LED). The LED spectrum was normalized to the maximum peak (E'$_{rel}$ (λ)). Spectrum was measured from wavelength $\lambda_0 = 250.18$ nm to $\lambda_{181} = 298.46$ nm. By using the trapezoidal rule, a weighting of the spectrum (g(λ_i)) was performed. Details on g(λ_i), as well as on the calculation of ε_U^{irr}, ε_H^{irr} and U^{irr} are given in the supplementary information.

7.3.4. Biodosimetry using MS2 phage

Biodosimetry using MS2 phage (DSM 13767) was performed by varying the flow rates through the reactor and hence the hydraulic retention time (HRT). Flow steps were taken in ascending order with the blank sample being last as described by Sperle et al. (2023a). Germicidal fluence at a certain flow step was calculated as H'$_{germicidal}$ = E' · HRT · GF$_{irr}$ (germicidal factor). GF$_{irr}$ was calculated by using g (λ) and GF (λ) as provided by Beck et al. (2015). Details are shown in the supplementary information. MS2 samples were taken in standard Eppendorf vials and analyzed using the double-agar technique as described in NSF/ANSI 55 (NSF/ANSI, 2019) using *E. coli* (DSM 5210) as the host strain. PBS for feed solution and dilutions was prepared according to NSF/ANSI 55 (NSF/ANSI, 2019). An appropriate amount of phage stock solution was inoculated to yield approximately 6.5 · 10^5 plug forming units (PFU) per mL. Biodosimetry was performed in triplicates for each setting. Further, for each flow step and blank, three samples were taken.

7.3.5. Biodosimetry using *Aquabacterium citratiphilum*

Agar plates for *A. citratiphilum* were prepared according to medium 830a (DSMZ GmbH, 2007, 2012). To prepare the biodosimetry feed solution, a single, one-week-old colony of *A. citratiphilum* was inoculated in 80 mL of bouillon in a 250 mL sterile Erlenmeyer flask (Sperle et al., 2023a). The bouillon was prepared according to medium 830a but in double concentration and without agar. The solution was inoculated at 20 °C and 120 rpm for approximately 48 h and cell growth was monitored using optical density (OD) at 600 nm, using the cell density meter CO 8000 (Biochrom, United States). When sufficient cell density was reached, but still being in the exponential growth phase, the bacterial solution was washed three times using PBS (prepared according to NSF/ANSI 55 (2019)). Therefore, the solution was thrice centrifuged at 5,000 RCF for 10 min at 4°C, supernatant withdrawn, cell pellet suspended in PBS, and vortexed. According to the measured OD, an appropriate volume of washed solution was inoculated in 2.5 L of PBS to reach a cell concentration of approximately $5.2 \cdot 10^6$ colony forming units (CFU) per mL.

Similar to MS2 phage, biodosimetry using *A. citratiphilum* was done by varying flow rates through the reactor. The detailed procedure for biodosimetry of *A. citratiphilum* can be found elsewhere (Sperle et al., 2023a). In short, between the flow rates, sufficient volume was flushed and samples were taken in descending order with fluence. Fluence was determined as fluence rate multiplied with HRT. To reduce photorepair mechanisms, samples were processed in a red-light only laboratory environment. Processing included preparing 10-fold dilutions and spreading 0.1 or 0.15 mL samples on an agar plate using a glass-made Drigalski spatula. To minimize any adsorption effects on plastic lab ware, low binding Eppendorf tubes and low retention tips were used for sampling and processing. Besides, 0.02 mL Tween20 (Sigma-Aldrich, France) was added per L PBS feed solution, as well as in the solution for dissolving the washed *A. citratiphilum* pellets, and in the PBS, used for dilutions to further reduce possible adsorption (Richter et al., 2021). Biodosimetries were performed in triplicates.

7.3.6. Experimental set-up for biofouling experiments and biofouling protocol

The utilized skid, feed water quality, MFS, RO membrane and biofouling protocol are described in detail in (Sperle et al., 2020a). Used feed water was local tap water (groundwater, treated by aeration and sand filtration). Analysis of the tap water from the study of Sperle et al. (2020a) was completed with values for the decadic absorption coefficient at 273 nm and additional total organic carbon measurements. Results are shown in the supplementary materials (Table S12-4). For this study, the same laboratory skid was used, solely an option for dosing CIP stock solution before the high-pressure pumps was added. A simplified sketch of the system is shown in Figure S12-16. Overall, with the utilized system, accelerated biofouling was triggered while monitoring the increase of FCPD as a surrogate for biofouling. At the same time membrane flux and

overall permeability was recorded. Calculations for FCPD, permeability, and biofilm resistance are done analogous to the study of Sperle et al. (2020a) and Dreszer et al. (2013). Permeability is calculated as flux divided by TMP. Relative permeability is the permeability divided by the (maximum) permeability in the initial phase of the experiment, leading to comparable relative permeabilities of UV and reference line before starting permeability reduction by fouling. Total hydraulic resistance is calculated as inverse of permeability divided by dynamic viscosity. Hydraulic resistance of the biofilm is determined as membrane hydraulic resistance subtracted from the system hydraulic resistance. The difference in resistance in this study is calculated as (1-(resistance biofilm with UV/resistance biofilm no UV))·100. In every experiment the line receiving the UV treatment was operated in parallel to a reference line without UV treatment. Each biofouling experiment consisted of the following four basic steps:

1) **Cleaning and sterilization** (using autoclavation or by H_2O_2)
2) **Reassembling of the skid** (under sterile conditions)
3) **Compaction** (16 h with 5.25 mmol·L^{-1} NaCl solution to set a flux of 20 L m^{-2} h^{-1})
4) **Accelerated biofouling phase** (Starting point of the experiment, using tap water supplemented with nutrients, keeping constant pressure till reaching a FCPD of 0.8 bar as a surrogate for the degree of biofouling)

For three experiments, a CIP was conducted after reaching a FCPD of 0.8 bar. Subsequently, biofilm was re-grown till reaching the aimed FCPD again. A simple CIP procedure was established and adopted from (DuPont, 2022a; Jafari et al., 2020; Javier et al., 2021a). When the desired FCPD was reached, the flow of the line and nutrient dosing was stopped, as well as the needle valve fully opened. For five minutes, the flow was doubled to remove coarse biofilm parts. Next, the flow was restored to 4.25 L h^{-1} and NaOH was dosed to reach a final concentration of 0.1% for 15 min (replacing the recirculation step). Next, the flow was stopped and the system was soaked for 1 h. The final step consisted of flushing with 8.5 L h^{-1} for 30 min with tap water, before continuing with normal operation.

7.3.7. Optimization of the UV pre-treatment and estimation of operational expenditures (OPEX)

In order to optimize the UV pre-treatment for biofouling control, actinometry was used to find settings for the LED-reactor that cover the fluence range of up to 60 mJ cm^{-2} with at least three intermediate points. In addition, three pairs of pulsed and continuous settings with comparable fluence were searched. To check for positive effects of pulsed irradiation on inactivation, a setting with similar fluence for pulsed and continuous irradiation for the two challenge organisms was tested in biodosimetry experiments. Next, biofouling experiments over the whole fluence range for pulsed and continuous irradiation were performed and OPEX compared.

As both, delay and change in biofilm resistance are important parameters to judge the potential to control fouling effects, OPEX based on power consumption were calculated. Therefore, the average TMP needed to achieve a design flux of 20 L m⁻² h⁻¹ was calculated using the mean resistances of the membranes over all runs and the mean biofilm resistance throughout each experiment.

$$TMP\ [bar] = \frac{J_{design}}{\frac{1}{\left(R_{avg\_biofilm} + R_{membrane}\right)\eta} \cdot 3.6 \cdot 10^{11}} \tag{7-5}$$

Where J_{design} represents the aimed flux of 20 L m⁻² h⁻¹ and η the dynamic viscosity of water at 15 °C. $3.6 \cdot 10^{11}$ is the factor needed to convert from pressure from Pa in bar and flux from L m⁻² h⁻¹ in m³ m⁻² s⁻¹. $R_{membrane}$ represents the average membrane resistance found during all experiments in m⁻¹. $R_{avg\_biofilm}$ represents the average resistance of the biofilm over the course of the experiment calculated as

$$R_{avg\_biofilm}[m^{-1}] = \frac{\int_0^T R_{biofilm}\,(t)dt}{T} \tag{7-6}$$

With T being the total experimental runtime. To calculate the feed pressure (P_{feed}) needed to run the system at the design flux, also FCPD must be considered as

$$P_{Feed}[bar] = TMP + \frac{FCPD_{avg}}{2} \tag{7-7}$$

Average FCPD was calculated analogously to average resistance with

$$FCPD_{avg}[bar] = \frac{\int_0^T FCPD\,(t)dt}{T} \tag{7-8}$$

As only a short membrane sheet was used, the initial FCPD was close to 0 and therefore neglected. With knowledge about P_{Feed}, power for pumping P and associated costs ($OPEX_{FCPD\&Perm}$) were calculated as

$$P[W] = \frac{Q\,P_{feed}}{36\,\eta_{Pump}} \tag{7-9}$$

$$OPEX_{FCPD\&Perm}[€\,y^{-1}] = \frac{P}{1000} \cdot 8760 \cdot C_e \tag{7-10}$$

With the factor of 36 resulting from the conversion of bar in Pa and L h⁻¹ in m³ s⁻¹. η_{Pump} is the efficiency of a pump, which was assumed with 0.82 (La Torre, 2008). C_e represents the assumed costs of energy (0.32 € kWh⁻¹) and 8,760 are the hours of runtime per year. For a better comparison, results are normalized to $OPEX_{no\,fouling}$ without fouling effects, based on a calculation with FCPD$_{avg}$ and R$_{avg\_biofilm}$ being zero.

The calculated OPEX only represents the effects of membrane permeability and FCPD but they are not taking into account the saved costs due to a reduced number of CIPs and therefore also extended membrane lifetime. To incorporate those, the average needed OPEX for fouling of all reference lines was calculated by subtracting the OPEX needed without fouling. According to the study by Jafari et al. (2021), fouling costs due

to FCPD and reduction in permeability only represent 28% of the total fouling cost for the studied RO systems. Based on this OPEX for CIP and membrane replacement was calculated as

$$\text{OPEX}_{CIP\&membrane}[\euro\, y^{-1}] = (OPEX_{FCPD\&Perm} - OPEX_{no\,fouling}) \cdot \frac{0.72}{0.28} \quad (7\text{-}11)$$

Those costs were added to $OPEX_{FCPD\&Perm}$ of all reference lines to get OPEX$_{Total}$. For UV-treated lines, equivalent power for CIP and membranes was reduced by the factor of

$$\text{F}_{CIP\&membrane}[-] = \frac{1}{(100 + D)/100} \quad (7\text{-}12)$$

With D being the delay in%. As an example, a delay of 100% would lead to half of the costs for CIP and membrane replacement. Finally, the power demand of the LEDs including pulse controller was measured using a commercially available power meter (PM 231 E DE 3655, Brennenstuhl, Germany) at the socket for the pulse controller.

7.4. Results and discussion

7.4.1. Actinometry

The transfer of uridine actinometry for path length determination and direct fluence rate calculation from batch to flow-through reactors as described in Chapter 7.3.3 was done the first time in this study. Actinometry was performed four times using three different uridine concentrations for path length determination at the setting of 96 mA continuous irradiation. The estimated path length is 2.04 ± 0.05 cm. With an average molar absorption coefficient of 6,448.7 M^{-1} cm^{-1} and concentrations of 0.012, 0.06, and 0.108 mM, this leads to transmittances of the light of 69.5, 16.2, and 3.8%, respectively. It should be noted that the highest concentration is close to complete absorbance. Hence, the analysis was also done three times with an additional changed concentration of 0.036 mM. This leads to three concentrations of 0.012, 0.036, and 0.06 mM, respectively. Quantum yield for 0.036 mM was interpolated with 0.0215. The path length estimated in three replicates is 2.31 ± 0.17 cm. Comparing the two estimated path lengths with a two-sided t-test showed a significant difference between them (p-value = 0.025, df = 5, t-statistic = -3.166). The adopted concentrations result in transmittances of 66.2, 29.0, and 12.7% for the estimated path length. Hence, the path length of 2.31 cm with higher transmittance was taken for further calculations as recommended by Sperle et al. (2023c).

With the determined path length, in total four continuous settings with varying driving current and four pulsed settings at 400 mA and 10 Hz frequency but varying duty cycles were analyzed. An overview of the different analyzed settings is given in Table 7-1. The settings, 16 mA continuous and pulsed with a duty cycle of 1.4%, 48 mA continuous and pulsed with a duty cycle of 9.3% as well as for 96 mA and pulsed with

a duty cycle of 22%, resulted in comparable fluence rates (two-sided t-test, p-value = 0.404, 0.814 and 0.064, df =5, 4, and 7; t-statistic = 0.911, 0.252 and -2.194). These pairs of settings were later used to compare differences in pulsed and continuous irradiation during the biofouling experiments. Pulsed settings will only be referred to with their duty cycle and continuous settings only according to their driving current. Overall, for driving currents and duty cycles, the fluence rate behaved linearly over the investigated range. Results are documented in the supplementary information (Figure S12-17). To test the influence on conversion per pass and also mixing in the reactor, an additional experiment with a flowrate of 4.25 L h^{-1} and the 96 mA setting was performed, resulting in a comparable fluence rate of 28.93 mW cm^{-2}.

Table 7-1:   Summary actinometry results.

Driving current [mA]	Frequency [Hz]	Duty cycle [%]	Fluence rate [mW cm^{-2}]	Number of tests
16	-	100	2.02 ± 0.24	3
48	-	100	14.36 ± 0.78	3
96	-	100	29.24 ± 1.23	5
400	-	100	141.26 ± 3.48	3
400	10	0.5	0.76 ± 0.09	3
400	10	1.4	1.90 ± 0.09	4
400	10	9.3	14.16 ± 1.15	3
400	10	22	31.27 ± 1.56	4

7.4.2. Biodosimetry using MS2 phage

Next to actinometry, biodosimetry using MS2 phage was performed to first investigate whether there are differences between pulsed and continuous irradiation on biological entities and second to compare reduction equivalent fluence, incorporating possible hydrodynamic effects and the fluence distribution. Results of biodosimetry for 96 mA continuous irradiation and the equivalent pulsed setting (22% duty cycle) are shown in Figure 7-3. Grey lines are representing the quality control for a collimated beam apparatus according to NSF/ANSI 55 (NSF/ANSI, 2019). First, comparing the slopes and intercepts of the single experiments with each other of pulsed vs. continuous irradiation no significant differences were found (p-value = 0.056 and 0.273, df = 4 and 4; t-statistic = 2.658 and -1.271). Second, it can be seen that the inactivation is lower at higher fluence than the quality controls of NSF/ANSI 55 for a collimated beam apparatus (CBA) (NSF/ANSI, 2019). This can be explained as fluid within the reactor is not mixed but is suspected to rather have a laminar pipe flow profile. Hence, not all phages might receive the same fluence, leading to worse fluence distribution than for a CBA. Interpolating the logarithmic reduction value (LRV) of pulsed and continuous to a germicidal fluence of 40 mJ cm^{-2} leads to a LRV of approximately 1.5 for both cases. Comparing the LRV to fluence in the standard CBA case of Sperle et al. (2023c) leads

to a reduction equivalent fluence of approximately 31 mJ cm^{-2} and therefore to a mixing efficiency of 0.77.
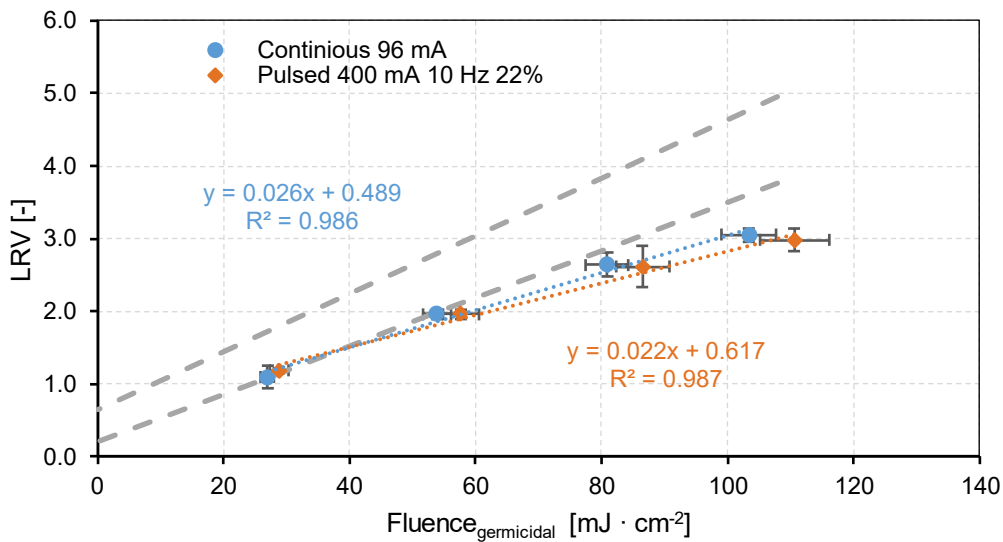
Figure 7-3:   Results of MS2 phage biodosimetry, error bars representing standard deviation; Grey lines representing the quality control for a collimated beam apparatus (CBA) according to NSF/ANSI 55 (NSF/ANSI, 2019)

7.4.3. Biodosimetry using *Aquabacterium citratiphilum*

A. citratiphilum was used as a surrogate to investigate if pulsed irradiation with increased UV fluence rate during the pulses leads to a higher inactivation than continuous irradiation at a lower fluence rate. The reasons of choosing *A. citratiphilum* as surrogate for biodosimetry with the link to biofouling control is further explained in the supplementary information (Kalmbach et al., 1999; NCBI, n. d; Sperle et al., 2020a; Sun et al., 2021; Zhang et al., 2000). As the investigated bacterium was rather sensitive to UV light, the low-fluence rate settings of 16 mA continuous vs. a 1.4% duty cycle were tested. Please note that the inactivation results for continuous irradiation at 16 mA have been shown already in the study deriving the biodosimetry procedure and for the highest fluence setting, in one experiments, < 25 colonies were counted (Sperle et al., 2023a). *A. citratiphilum* inactivation behaved similarly over the tested fluence range for pulsed and continuous mode (Figure 7-4). Further, a two-sided t-test for comparing the slopes and intercepts of the single runs between pulsed and continuous irradiation showed no significant differences (p-value 0.679 and 0.921, df = 4 and 4; t-statistic = 0.445 and -0.105), confirming the results of MS2. These results are in accordance with the findings of Song et al. (2018) who linked observed enhanced inactivation during pulsed irradiation to changed overall fluence during the pulses. As here fluence was precisely determined using actinometry, no differences were observed. In addition, with a wavelength of 273 nm, the high intensity of light should lead to equal/slightly worse results as described in the study of Pousty (2021). Higher intensities could lead to higher concentrations of ROS, which might result in more ROS-ROS reactions, reducing their disinfection capability (Pousty et al., 2021). Nevertheless, the pulsed irradiation might

118

limit the negative effects of ROS-ROS reaction on the inactivation results or the influence of ROS inactivation in general might be only slightly present at 273 nm. Overall, not incorporating hydrodynamic effects, *A. citratiphilum* shows lower resistance to UV than *E. coli* at comparable wavelength and fluence rate (< 1.5 LRV at 8 mJ cm^{-2} at 275 nm (Pousty et al. 2021)).
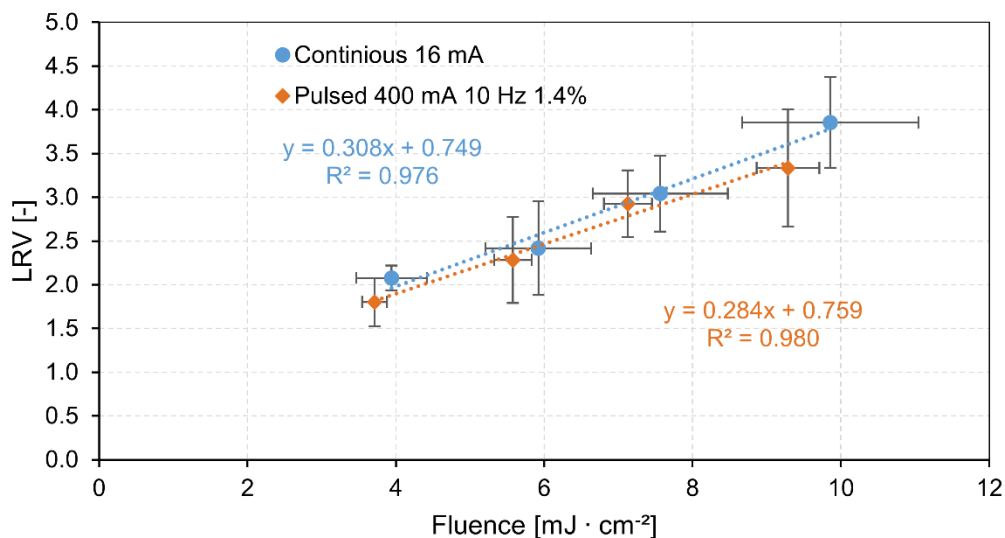
Figure 7-4:   *Results of Aquabacterium citratiphilum biodosimetry, error bars representing standard deviation. Continuous irradiation setting at 16 mA as shown by Sperle et al. (2023a).*

7.4.4. Impacts of pulsed and continuous UV pre-treatment on biofouling delay and hydraulic biofilm resistance

To optimize the UVC pre-treatment, biofouling experiments were conducted with seven different UV irradiation settings; three in continuous irradiation mode (16, 48, and 96 mA) and four in pulsed mode with duty cycles of 0.5, 1.4, 9.3, and 22%, as determined by the actinometry (Table 7-1). The overall investigated fluence was in the range of 1.5 to 61.3 mJ cm^{-1}. A representative result of a biofouling experiment including CIP (development of FCPD and relative permeability of the 16 mA run) is shown in Figure 7-5.
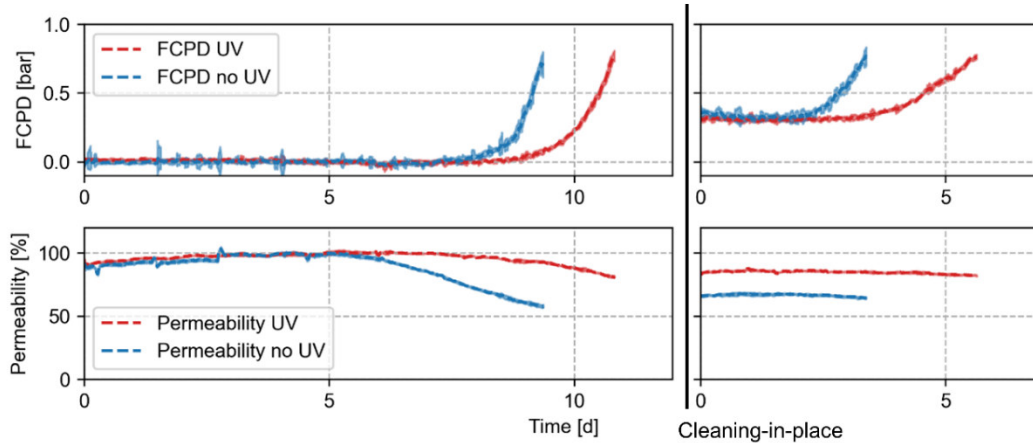
Figure 7-5:   *Representative development of feed channel pressure drop (FCPD) and relative permeability over time and after cleaning-in-place (CIP) for the experiment of continuous irradiation at 16 mA; Left before CIP, right after CIP; Shaded areas represent standard deviation.*

When looking at the delay in FCPD increase caused by continuous irradiation as pre-treatment of all experiments, it can be seen that there is a trend between fluence and delay, but it shows a tailing behavior or is approaching a fixed value at higher fluence (Figure 7-6). A log-linear model was found to describe data well. The added data from the study of Sperle et al. (2020a) fit well with the other data points even though different methods for fluence determination were used. Besides, the wavelength in that study was slightly higher (278 nm). Taking a look at the delay of the pulsed irradiation, the same trend of an increased delay with fluence, but stagnating at higher values can be observed (Figure 7-6). When comparing pulsed to continuous irradiation using a two-sided paired t-test, pulsed irradiation seems to lead to a significantly higher delay in biofilm formation of 20.6 ± 4.6% for the three compared pairs of fluence investigated (p-value 0.016, df = 2, t-statistic = -7.798).

When comparing the difference in resistance over fluence, a different phenomenon can be seen. For continuous irradiation, the resistance of the biofilm seems to be always lower for the UV pre-treatment and rather constant over the fluence range. For continuous irradiation both a linear and a log-linear model did not describe the data well ($R^2 < 0.1$) and hence the difference in resistance is assumed to not depend on fluence. For pulsed irradiation on the contrary, there seems to be a trend of increased difference in resistance with increasing fluence (log-linear model). Nevertheless, values are lower than for continuous irradiation even though not significantly when comparing the differences using a two-sided paired t-test (p-value 0.154, df = 2, t-statistic = 2.241) for the three pairs of 16 mA and 1.4%, 48 mA and 9.3% as well as 96 mA and 22%.
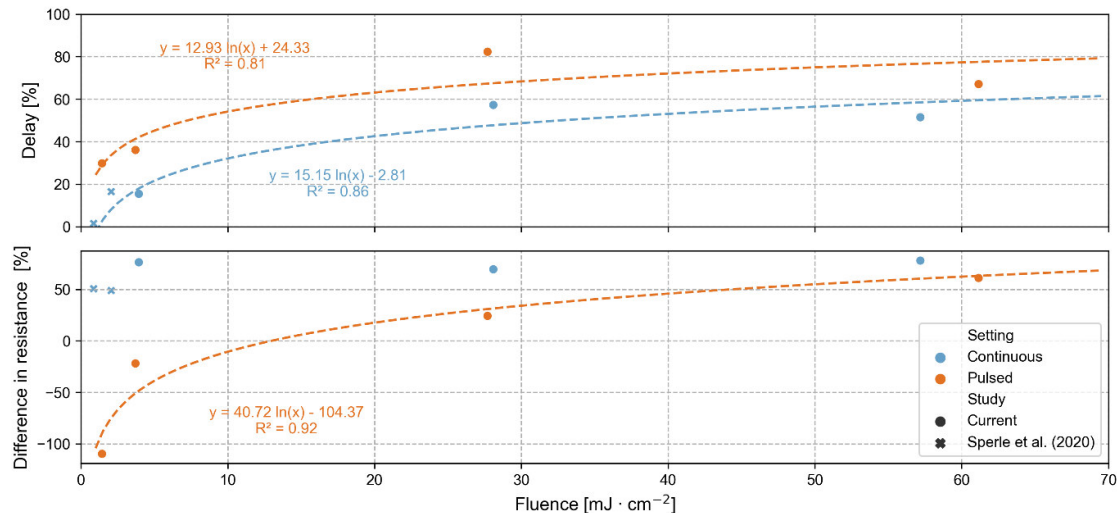
Figure 7-6:   *Results of biofouling experiments in comparison with results of the study of Sperle et al. (2020a); Colors according to continuous or pulsed irradiation; Markers depending on the study, current or Sperle et al. (2020a); Log-linear models exclude the data from (2020a); Dashed lines depict the fitted log-linear model.*

Overall, the increased delay with increased fluence might be linked to a higher inactivation at higher fluence. The tailing of delay at higher fluence can similarly be found for the inactivation of microorganisms and might relate to it. When extrapolating the LRV for the recorded biodosimetry of *A. citratiphilum*, a fluence of 25 mJ cm^{-2} would already lead to a LRV > 8. At that high LRV, all planktonic microorganisms might be inactivated and only those might survive that are shielded from the light e.g. due to the presence of cell clusters or other aggregates (Azimi et al., 2017; Emerick et al., 2000; Kowalski et al., 2020). The presence of aggregates or other clusters leading to shielding effects could also explain the increased delay in inactivation while applying pulsed irradiation. We hypothesize that the higher fluence rate during the pulses (in our case up to 141.3 mW m^{-2} at 400 mA in comparison to 2.0 mW cm^{-2} at 16 mA) might be able to penetrate further in cell clusters and others leading to additional inactivation. This is supported by the study of Vitzilaiou et al. (2021) who also suspected that lower intensities at longer times might reduce the inactivation of cell aggregates. Further, when biofilms are irradiated directly, biofilm control depends rather on a function of light intensity than on total fluence (Torkzadeh et al., 2021; Torkzadeh and Cates, 2021). For future studies, it is recommended to test the effect of fluence rate on the inactivation of cell aggregates to clarify potential effects. In general, it seems reasonable that already high effects of disinfection can be found at fluence leading to relatively low LRVs. As an example, a LRV of 1 removes 90% of the microorganisms, whereas an LRV of 2 would only lead to additional 9% removal (in total 99%).

A possible reason for an altered hydraulic resistance of the biofilms, Sperle et al. (2020a) and Wu et al. (2021a) proposed is that the UV pre-treatment resulted in a change in the microbial community. As an example, gram-positive or bacteria with higher GC content in the 16S rRNA gene region might be more resistant to UV disinfection

(McKinney and Pruden, 2012; Pullerits et al., 2020). Pulsed irradiation might again impact the microbial community in comparison to continuous irradiation. The additional penetration of light into cell clusters during high power pulses might lead to a similar inactivation of clusters as for single cells. Hence, for pulsed irradiation, the protection of cell clusters might be less beneficial, leading to a more equal selection of surviving bacteria than for continuous irradiation. This hypothesis again needs further testing which was beyond the scope of the current study. Wu et al. (2021a), in general, recognized less permeable biofilms due to UV pre-treatment, but it must be considered, that they used a different water matrix, membrane bioreactor effluent from a wastewater treatment plant, and after irradiation, treated feed water had time to regrow between 0 and 24 h. According to Lakretz and Mamane (2010), such post-treatment incubation time might reduce or mitigate the inhibitory effects of UV treatment on biofilm formation.

7.4.5. Estimation of operational expenditures (OPEX) and optimal UV pre-treatment

Results for different OPEX are depicted in Figure 7-7. When looking just at OPEX including FCPD and permeability, continuous irradiation seems to perform better than pulsed. This can be explained by continuous irradiations showing a lower resistance of formed biofilms. The pulsed irradiation with a 9.3% duty cycle seems to perform slightly worse than the reference line even though it showed lower resistance of the formed biofilm at the end and a considerable delay in biofilm formation. This can be explained by a constant permeability drop that occurred over time. Through the long delay of finally reaching 0.8 bar pressure drop, the system was running for quite some time with reduced permeability leading to reduced performance on average. Overall, $OPEX_{FCPD\&Perm}$ savings due to the UV pre-treatment seem to be rather little, but higher for continuous irradiation than for pulsed one (max. 11% for 96 mA compared to the mean reference).

When comparing the effects of the UV pre-treatment to total OPEX, the benefits of UV are more pronounced. Overall, with increasing fluence, an increased saving potential of OPEX is observed. In comparison to the average costs of all reference lines (mean no UV), a setting of 96 mA continuous operation shows a saving of approximately 24.0%, followed by a pulsed setting of 22% duty cycle with 22.2% savings. The third highest savings are achieved by a setting of 48 mA continuous operation with 21.5%. Overall, continuous irradiation seems to still save slightly more OPEX than pulsed operation.
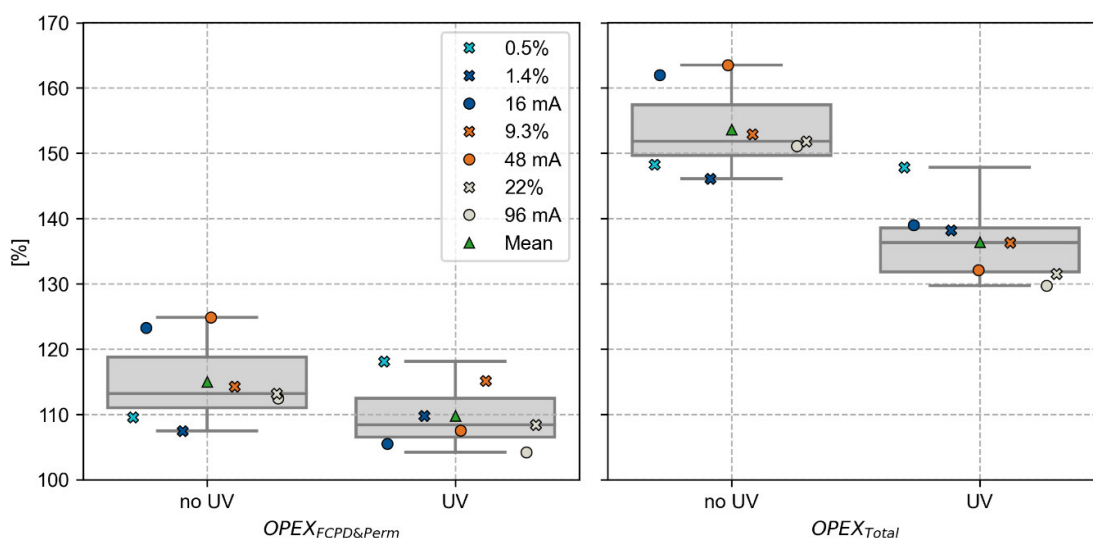
Figure 7-7:   *Comparison of operational expenditures (OPEX) only considering FCPD and permeability as well as OPEX total over for the different UV settings; The OPEX labeled no UV refer to the OPEX of the reference lines which operated in parallel to the line receiving the UV treatment; Green triangle indicating the mean of OPEX, circular markers continuous irradiation, crosses pulsed irradiation; OPEX are normalized to the average OPEX without fouling.*

At the current state, the UV-LED pre-treatment could not be compared to OPEX, as neither the electricity supply of the LEDs, nor the laboratory UV reactor were optimized. Using the electricity demand for the LED in the current state/setup, none of the scenarios would save OPEX. The measured power demand at the socket for the pulse controller ranged between 1.0 and 3.7 W (Table 7-2), whereas pumping power for the average reference case without fouling is approximately 0.7 W for ~4.7 bar. Nevertheless, this likely will change with the usage of commercially available UV reactors. According to Schmalwieser et al. (2017), the median energy demand to disinfect water using low-pressure lamps with 40 mJ cm^{-2} for a UV transmittance of ~98% per cm is 9 Wh m^{-3} and increases to 17 Wh m^{-3} for ~91% transmittance. As a comparison, Kim et al. (2019) reported energy demands for a complete (seawater) RO plant between < 3 to 6.7 kWh m^{-3}, including pre-treatment and post-treatment of approximately 1 kWh m^{-3}. Energy demand for brackish water RO might be considerably lower, e.g. 0.44 kWh m^{-3} with 85% recovery instead of 2.12 kWh m^{-3} with 50% recovery for seawater, excluding pre- and post-treatment (Shrivastava et al., 2015). For a cost comparison, RO recovery needs to be considered, as the UV pre-treatment must be applied to the complete feed and not only the permeate stream. Using the data of Shrivastava et al. (2015) and Schmalwieser et al. (2017), the energy demand of 40 mJ cm^{-2} UV disinfection with 98% and 91% UV transmission in comparison to RO desalination, might account for ~1-2% for seawater and ~2-5% for brackish water. In case the savings of ~22-23% for 40 mJ cm^{-2} (Table 7-2) should transfer to real applications, UV pre-treatment could be an interesting option for biofouling control. Adding a UV reactor prior to RO might also be an easy option for retrofitting. Anyway,

transferring cost of commercial UV disinfection to the laboratory set up, it would lead to 0.04 W representing approximately 6% of OPEX without fouling. In general, the saltier the water, the less significant might be the energy demand of the UV pre-treatment in comparison to the desalination process itself.

To investigate the optimal fluence for biofouling control, saved OPEX will be once normalized to the applied fluence (Table 7-2) and once OPEX saving are exemplary compared to the energy demand of the UV disinfection for different fluence. The order of highest efficiency per applied fluence is 1.4%, 0.5%, 16 mA, 48 mA, 9.3%, 96 mA, and 22%. Thereby, the 1.4%, relative to 16 mA setting, shows 12% higher OPEX savings per applied fluence. Nevertheless, there could no enhanced efficiency be detected by using a two-sided paired t-test for savings per fluence and the pairs of continuous and pulsed irradiation (p-value 0.698, df = 2, t-statistic = -0.448). Overall, it seems that effects for biofouling control only increase little over the applied fluence. For the investigated settings, the highest efficiency per fluence of the UV pre-treatment occurred around 4 mJ cm^{-2}. However, the results might not directly transfer to other systems and further validation is needed in up-scaled systems and with energetically optimized reactors. For full-scale seawater desalination systems, the typical fluence of drinking water disinfection (40 mJ cm^{-2}) or higher could be optimal as the energy demand of UV disinfection in comparison to the desalination process itself might be rather low. For brackish water RO, fluences between 4 and 40 mJ cm^{-2} might become favorable, too. As an example, the energy demand according to Shrivastava et al. (2015) and Schmalwieser et al. (2017) is taken and the effects of continuous UV irradiation are considered to translate directly to up-scaled applications, as well as to a wavelength of 254 nm. Furthermore, in this example the energy demand for 28 mJ cm^{-2} is assumed linear to 40 mJ cm^{-2}. Hence, for 91% transmittance, the energy demand of UV disinfection would be ~3.1% in comparison to the energy for brackish water desalination, while saving ~21.5% of OPEX. The same calculation for 57 mJ cm^{-2} would lead to an energy demand of 6.5% with ~24% savings. For 4 mJ cm^{-2} the energy demand would be < 1% with 14.7% savings. For those three investigated settings, using brackish water and a 91% transmittance, the fluence around 28 mJ cm^{-2} might be optimal. Nevertheless, this calculation is just an example and it must be kept in mind that saved OPEX are based on laboratory accelerated biofouling studies with a rather high biofilm growth potential. Results might differ for real desalination plants, especial when using seawater. Besides, investment costs and other OPEX than energy (e.g. lamp replacement) were neglected.

Table 7-2:   *Summary of total operational expenditures (OPEX) saving compared to the mean OPEX of the reference lines.*

Setting	16 mA	48 mA	96 mA	0.50%	1.40%	9.30%	22%
Power LED [W]	1.30	2.35	3.65	1.00	1.10	2.00	3.50
Savings OPEX$_{Total}$ [%]	14.68	21.54	23.99	5.81	15.48	17.33	22.16
Fluence [mJ cm^{-2}]	3.94	28.10	57.19	1.50	3.71	27.70	61.16
Savings per fluence [% cm^2 J^{-1}]	3.72	0.77	0.42	3.88	4.17	0.63	0.36

The successful implementation of UV irradiation as a pre-treatment from lab- to full- scale might depend on various factors. In general, energy demand of UV treatment is lower in waters with higher UV transmittance (Schmalwieser et al., 2017). Particle free water should be provided, e.g. by means of cartridge filtration to reduce shielding effects during UV treatment, but also to protect the membranes. For most applications using RO membranes, the direct feed water should have a high UV transmittance and be free of particles anyway. As discussed, the energy demand of UV relative to the desalination process depends on salinity. Furthermore, it is hypothesized that three main factors concerning the feed water matrix are important: the number of bacteria/microorganisms, the nutrient load and the microbial community. In case a higher number of bacteria is present in the feed, this might lead to enhanced effects of the UV pre-treatment by disinfection. On the contrary, a higher nutrient load might lead to faster growth of bacteria already being attached to the membranes and spacers and therefore this could reduce the effects of UV pre-treatment. The performed laboratory experiments might actually depict less favorable conditions for the UV pre-treatment, as easily degradable nutrients were added to enhance cell growth. Depending on the microbial community present in the feed, efficiency of UV pre-treatment for biofouling control might change. If the community present has a higher UV resistance, UV dose might need to be increased. Besides depending on the community present, UV pre-treatment might lead to positive effects concerning permeability. The effects of permeability might become less relevant in practice, as in this study only a small membrane sheet was used. As biofouling tends to occur in lead rather than tail-end elements, effects on permeability might be bigger in this study than they might occur in practice or at full-scale applications. Nevertheless, those influencing factors need further validation and testing the pre-treatment at larger scale with different feed waters over different fluence settings is advised for future research.

7.4.6. Biofilm cleanability

In total three CIPs were conducted, for biofouling runs with 16 mA continuous and 9.3 and 22% pulsed operational settings. Effects of CIP were compared according to the reduction in FCPD and delay of build-up to FCPD of 0.8 bar after the cleaning. The drop in FCPD was 0.56 ± 0.09 bar for the UV-treated lines and 0.51 ± 0.09 bar for the reference lines. Comparing the reduction with a paired t-test showed no significant difference (p-value = 0.369, df = 2, t-statistic = 1.151) for the biofilm removability due to UV pre-treatment. Comparing the delay after CIP for the 16 mA experiment, UV treated line was still delayed by 167% in comparison to the reference line. For the pulsed 22% duty cycle experiment, delay was 15%. Only for the experiment with the pulsed setting of 9.3% no delay due to UV pre-treatment was observed after CIP. Here the build-up of biofilm was 3% faster than in the reference line. Overall, results showed a delay after CIP in two out of three cases, but hence it was not significant (paired t-test p-value = 0.319, df = 2, t-statistic = -1.316). The delay in biofilm formation after CIP should be investigated in future studies. UV pre-treatment might still impact biofilm growth after CIP as it impacts the biofilm build-up caused by cells in the feed stream. It might not impact the growth of the attached biofilm directly but maybe a changed microbial community affected by UV treatment could lead to different regrowth behavior. Also, UV treatment in combination with a CIP procedure that sanitizes the membranes seems promising. For successful technology transfer, the presence of the UV-induced delay after CIP needs to be validated, as this is strongly impacting OPEX saved as it was discussed in Chapter 7.4.5. In general, for future studies it would be interesting to test the fouling behavior after multiple cleaning cycles using different CIP protocols.

7.5. Conclusion

Within this study, several different driving currents and pulsed settings were characterized by actinometry. With the same HRT in the reactor, settings with higher fluence rate during the pulses were compared to continuous irradiation with lower fluence rate but the same total fluence. Both, biodosimetry using MS2 phage or a biofilm bacterium, did not show changed inactivation due to the pulses. Applying the UV irradiation as a pre-treatment for biofouling control, several interesting observations were made:

- Delay of biofilm formation is increasing with fluence but seems to approach a steady value for higher fluence, similar as tailing in UV disinfection.
- Pulsed irradiations had a higher delay at the same fluence.
- Biofilm of continuous pre-treatment showed lower resistance than reference lines and the difference in resistance was rather independent of fluence.
- Differences in biofilm hydraulic resistance increased with fluence for pulsed irradiation.

- OPEX savings by changed resistance and FCPD are rather low.
- OPEX savings of biofouling delay increase when including estimated OPEX of CIP and membrane replacements.
- Overall, lower fluence (~4 mJ cm^{-2}) settings in pulsed and continuous mode showed the greatest biofouling control efficiency per fluence applied. Nevertheless, this needs further approval on a bigger scale and might be impacted by feed water.
- Efficiency of 1.4% pulsed irradiation was 12% higher, relative to the comparable continuous setting. For the other settings continuous irradiation outperformed pulsed irradiation.
- In case the savings of OPEX transfer to real applications and over multiple CIP cycles, UV pre-treatment could be an interesting option (also for retrofitting), as energy demand of UV disinfection is rather low compared to the one of desalination.

Declaration of competing interest: The authors declare that they have no known competing financial interests or personal relationships that could have appeared to influence the work reported in this paper.

8. Validation of the effects of *in situ* UV treatment for biofouling control under real feed water conditions in an up-scaled system

The following chapter present the results of the investigations related to hypothesis 6 ("*In situ UVC treatment of the feed stream in the pressure vessel of RO membrane systems is reducing the impacts of long-term biofouling under real conditions.*").

The investigations on the effect of (*in situ*) UV pre-treatment under real conditions were done in two settings, once using well water and three household-size membrane modules in series and once using a 4040 RO module at pilot-scale.

8.1. Applying UV pre-treatment using 1.8" membrane elements

Author contributions: Experiments, data generation, analysis and validation were performed by Philip Sperle together with Habiba Sultana as part of her Study Project (Sultana, 2022). The used laboratory skid was modified but originally constructed by Martin Larasser (2017).

8.1.1. Laboratory skid and experimental procedure

As all biofouling experiments described in Chapters 4 and 7 were performed with the supplement of easily degradable nutrients, further experiments are needed under more realistic conditions. Therefore, biofouling experiments were performed using three TFM 50 elements (GE Osmontics Desal, United States) in series with a local well water supply without adding any nutrients. Well water analysis is summarized in Table 8-1. Further information for analytical procedures can be found in Chapter 4. The used SWM membrane elements had a diameter of 4.55 cm and a total length of 29.85 cm. Each membrane element had an active membrane area of 2,268 cm² (21 cm x 108 cm) and the spacer height was measured as 17.72 mil. The membranes were designed for a nominal permeate production of 50 GPD (0.16 L min⁻¹).

The benchtop skid used for the experiments is depicted in Figure 8-1. Well water was used as feed and filtered once through a 100 µm cartridge filter (1035870, Putsch GmbH & Co. KG), as well as filtered twice at 10 µm (F20 housing, 10 PE filter, MTS & APIC Filter GmbH & Co.KG, Germany). In a mixed feed tank, the water temperature was controlled using a heat exchanger. At the outlet of the tank, a small sieve with 0.5 mm was installed for additional protection of the downstream membranes. Water was withdrawn using a pump (M03EKSGSFSHA, Wanner Engineering, Inc., United States). A level sensor in the tank ensured pump protection. After the pump, the electrical conductivity of the feed was analyzed (GZ-19500-46, Cole-Parmer). An analogous and a digital flowmeter (MIM-1205HG4C3T0, KOBOLD Messring GmbH, Germany) were used to monitor the feed flow. The digital flow meter was also used to record the system temperature. After the flowmeter, only for the experiment using UV pre-treatment, a point-of-use sized commercial UV-LED reactor was mounted (PAQ-06C-450-T00-

128

1142-S1000, AquiSense Technologies, United States). According to the datasheet, the UV-LED reactor should achieve a fluence of approximately 15 mJ cm^{-2} at a flow of 3.2 L min^{-1} and a UVT of ≥ 90% (AquiSense Technologies, 2022). The power demand of the LED unit was measured with 5.7 W using a commercially available power meter (PM 231 E DE 3655, Brennenstuhl, Germany). After the UV reactor, the membrane feed pressure was monitored by an analogous, as well as with a digital pressure sensor (SML-10, ADZ NAGANO GmbH, Germany). After that, the TFM 50 membrane elements were connected in series, each element placed in its own housing. After each element, analogous pressure sensors were installed. Only after the last element, another digital pressure sensor was used to monitor concentrate pressure online (SML-10, ADZ NAGANO GmbH, Germany). Finally, after a needle valve to set the system pressure, an analogous flowmeter was used to determine concentrate flow before the concentrate was discharged. Permeate of each element could be sampled individually over three-way valves. The combined permeate stream was analyzed for electrical conductivity (GZ-19500-45, Cole-Parmer) before being collected in the permeate collection tank. Water height and hence permeate flow were measured through a pressure sensor (SEN-3276 B146, KOBOLD Messring GmbH, Germany). A magnetic valve was controlled by the computer aided control system to discharge the permeate tank when filled. Before each experiment, the whole skid, except for the feed tank and membrane elements, was cleaned by two CIP procedures adopted from Judd (2010), one using 0.5% NaOCl, followed by 0.2% $C_6H_8O_7$ for 2 h each. The feed tank was sterilized by whipping with surfactant (Bode Bacillol, Paul Hartmann AG, Germany) and new membrane modules were used in each run. FCPD was normalized by subtracting the starting value (average of day 2). The average of day 2 was approximately 1.2 bar for both experiments. Permeability was calculated as temperature corrected flux for 25°C (using the temperature correction factor as described by DuPont (2022b)) divided by TMP. Permeability was normalized to the starting point (average of day 2). FCPD and permeability were calculated as daily averages with their standard deviations.
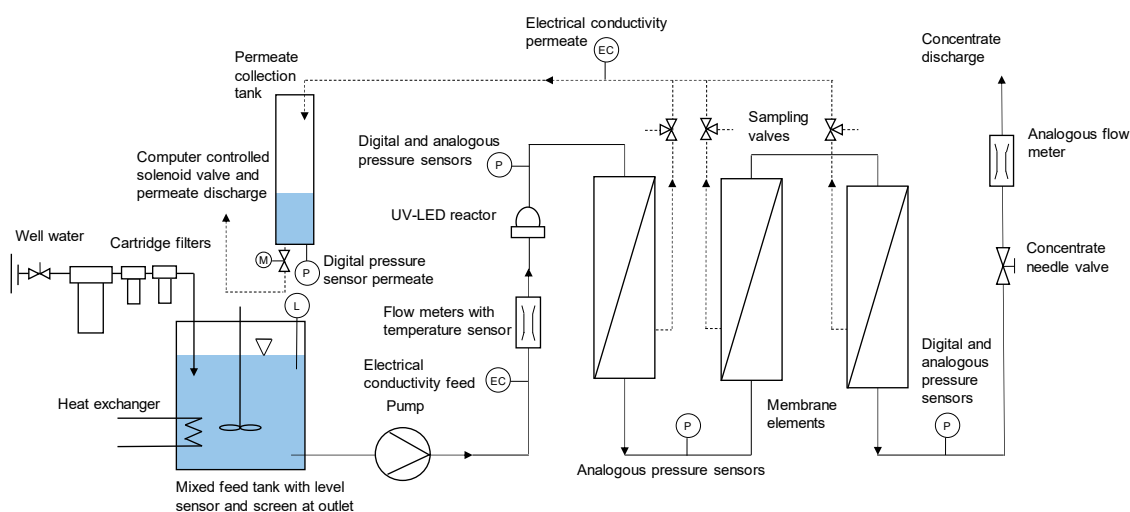
Figure 8-1:   *Simplified schematic of the laboratory skid for biofouling experiments using well water.*

8.1.2. Results laboratory biofouling experiments

Using the benchtop laboratory skid, a biofouling experiment without and one with UV pre-treatment was performed (Figure 8-2). Average temperature for the experiment without UV was 19.3 ± 0.8 °C, for the run with UV, it was 19.7 ± 1.3 °C. The average recovery for the experiment without UV was 9.8% ± 1.3%, for the experiment with UV it was 10.1% ± 1.0%.

During the experiments, a few operational problems occurred. For the run without UV, data recording of the first few hours did not work. Between approximately days 27 till 60, a decrease in permeability was measured. However, as it turned out, this was an artifact caused by the solenoidal valve below the permeate collection tank not closing completely. After replacing the valve on day 60, permeability was restored to approximately 100%. During the run with UV, the system was shut down between days 10 and 11, leading to approximately one day without operation and data. Furthermore, for days 11, 12 and 13 no data for permeability could be recorded as the pressure sensor in the permeate collection tank needed to be repaired. Besides, the huge standard deviation in FCPD between approximately day 31 and 37 was caused by the pre-filters being blocked and hence, the feed pump stopped several times as the water level in the feed tank was too low. Nevertheless, it can be seen that for the experiment without UV, an increase of FCPD (max. at day 87 with 0.37 bar ≙ 30% increase relative to the start) and hence biofouling occurred around day 60. Permeability did not decrease due to biofouling. For the run with UV pre-treatment, no biofouling at all was observed, therefore after day 126 of continuous operation, the UV-LED reactor was turned off. After 100 days of additional operation still no biofouling could be monitored.

After the experiments, a couple of visual observations could be made. When opening the first membrane module in series for the experiment without UV, a fouling layer, probably consisting of biofilm, was only observed in the first centimeters, in an area, where the membrane envelopes were glued and hence not representing an active membrane area (Figure 8-3a). Besides, when removing the effluent pipe from the feed tank, a fouling layer (likely biofilm) was observed for the run with UV (Figure 8-3b). Unfortunately, no picture of a potential biofilm formed in the pipes for the experiment without UV is available.
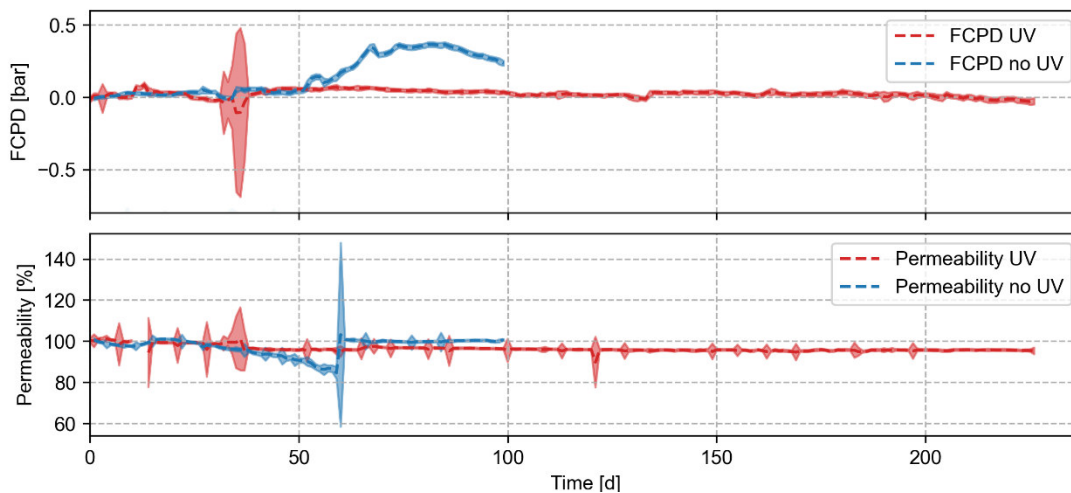
Figure 8-2: Results laboratory biofouling experiments using well water and 3 1.8'' spiral-wound membrane (SWM) elements. Shaded areas represent standard deviation.

a)
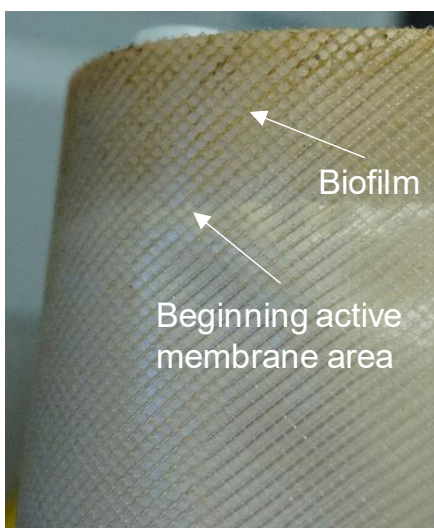
b)

Figure 8-3: a) Biofilm first membrane element in series, experiment without UV pre-treatment; b) Feed pipe after the experiment with UV pre-treatment.

8.2. Applying *in situ* UV pre-treatment at pilot-scale

Author contributions: Investigations within this chapter were performed in collaboration with Delta Umwelt-Technik GmbH (Delta) and UV-EL GmbH & Co. KG (UV-EL). Thereby, the planning of the integration of the UV-EL system within the pressure vessels of an RO membrane system was done by Philipp Sperle (TUM), Bertram Skibinski (TUM), Jörg E. Drewes (TUM), and Andreas Meyer (UV-EL). Andreas Meyer (UV-EL) was responsible for the construction of the UV-LED system, whereas the integration in the pressure vessel was done by Philipp Sperle (TUM) and Hubert Moosrainer (TUM), as well as by Andrea Müller (Delta) and Isidro Oviedo (Delta). Philipp Sperle (TUM) and Andreas Mirlach (TUM) characterized the UV-LED system. Planning of the RO membrane system at pilot-scale was done by Philipp Sperle (TUM), Bertram Skibinski (TUM), and Jörg E. Drewes (TUM), as well as by Andrea Müller (Delta) and Isidro Oviedo (Delta). The membrane system was operated by Andrea Müller (Delta) and Isidro Oviedo (Delta). Data analysis was done by Philipp Sperle (TUM) and Andrea Müller (Delta).

8.2.1. Pilot site and feed water quality

For experiments at pilot-scale, groundwater close to Christuskirche (Firlstraße, 12459 Berlin, Germany) was used and the skid was operated in the immediate vicinity of Christuskirche (Figure 8-4). The used groundwater was analyzed for various parameters, summarized and compared to tap water used for laboratory experiments as shown by Sperle et al. (2020a) and Sperle et al. (2023b), supplemented with values for dissolved organic carbon (DOC), absorption/attenuation coefficient at 254 nm, ATP and bromide, in Table 8-1. Further information for analysis procedures can be found in Chapter 4/ Sperle et al. (2020a).
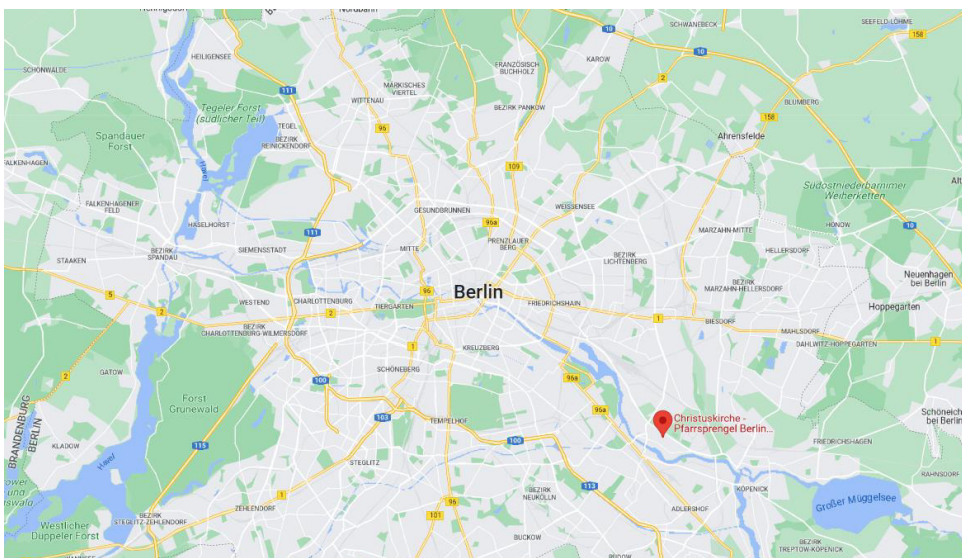
Figure 8-4:   *Location of the pilot skid (Google LLC, n.d.).*

Table 8-1: *Feed water analysis tap water Garching as shown by Sperle et al. (2020a) and Sperle et al. (2023b) supplemented with values for dissolved organic carbon (DOC), absorption coefficient at 254 nm and 273 nm, ATP and Br, as well as analysis results for well water Garching and groundwater Berlin Christuskirche.*

Parameter	Tap water Garching	Well water Garching	Berlin-Christuskirche
TOC [mg L^{-1}]	1.0 ± 0.7	1.2 ± 0.4	4.5
DOC [mg L^{-1}]	1.0 ± 0.3	1.2 ± 0.4	4.2
NO$_3$-N [mg L^{-1}]	0.3[1] ± 0.2	5.0 ± 2.7	0.8
PO$_4$-P [mg L^{-1}]	(< 0.05) [1]	(< 0.05) [1]	0.2
pH [-]	7.6 ± 0.3	7.3	7.4
Absorption coefficient at 254 nm [cm^{-1}]	0.007 ± 0.002	0.022	0.089
Absorption coefficient at 273 nm [cm^{-1}]	0.006 ± 0.001	0.017	0.069 [2]
Electrical conductivity [µS cm^{-1}]	573 ± 25	691 ± 18	818
ATP [mM]	2.5	No data	3.0
Total direct cell count [1 mL^{-1}]	4.2 x10^4 ± 1.5 x10^4	2.3 x10^4 [3]	No data
Ca [mg L^{-1}]	60.8 ± 3.2	79.5 ± 15.0	126.0
Cl [mg L^{-1}]	14.1 ± 2.7	23.0 ± 5.8	60.3
F [mg L^{-1}]	0.1 ± 0.0	0.1 ± 0.0	0.5
Fe [µg L^{-1}]	26.8 ± 16.2	28.5 ± 17.0	32.9
K [mg L^{-1}]	1.0 ± 0.0	2.5 ± 1.2	13.2
Cu [µg L^{-1}]	18.8 ± 2.2	26.4 ± 17.1	5.8
Mg [mg L^{-1}]	23.8 ± 0.6	20.9 ± 2.7	12.5
Mn [µg/ L^{-1}]	(< 5)[1]	(< 5)[1]	687
Na [mg L^{-1}]	31.7 ± 0.8	22.6 ± 6.2	61.6
SO$_4$ [mg L^{-1}]	38.4 ± 5.1	32.0 ± 6.4	178.0
Br [mg L^{-1}]	(< 0,05)[1]	(< 0,05)[1]	0.1

[1] Lower than limit of detection; [2] actually at 272 nm, [3] cells counted with Cell Counter plugin of ImageJ (version 1.52a, National Institutes of Health, USA)

8.2.2. Utilized pilot-scale membrane skid

The build membrane system consisted of three 4040 XLE membrane elements (DuPont, United States) in parallel (Figure 8-5). After a pre-filtration, the high-pressure pump, and a pressure sensor, the feed stream was split into three parallel trains. Each train consisted of a pressure vessel big enough to house two 4040 SWM RO elements. After the pressure vessels, concentrate pressure was measured and the flow was controlled over concentrate valves. One train was equipped with the developed *in situ*

UV-LED system (Chapter 8.2.3), one was equipped with a biocide dosing system (0.1 ppm NaOCl) and one served as a reference. For CIP, room temperature water was acidified to pH 2.5 using a mixture of $NaHSO_4$, H_2SO_4 and H_3PO_4. This solution was recirculated for 15 min followed by 15 min soaking time and again 15 min of recirculation. Next, the system was flushed with water and again flushed with water acidified using $C_6H_8O_7$.
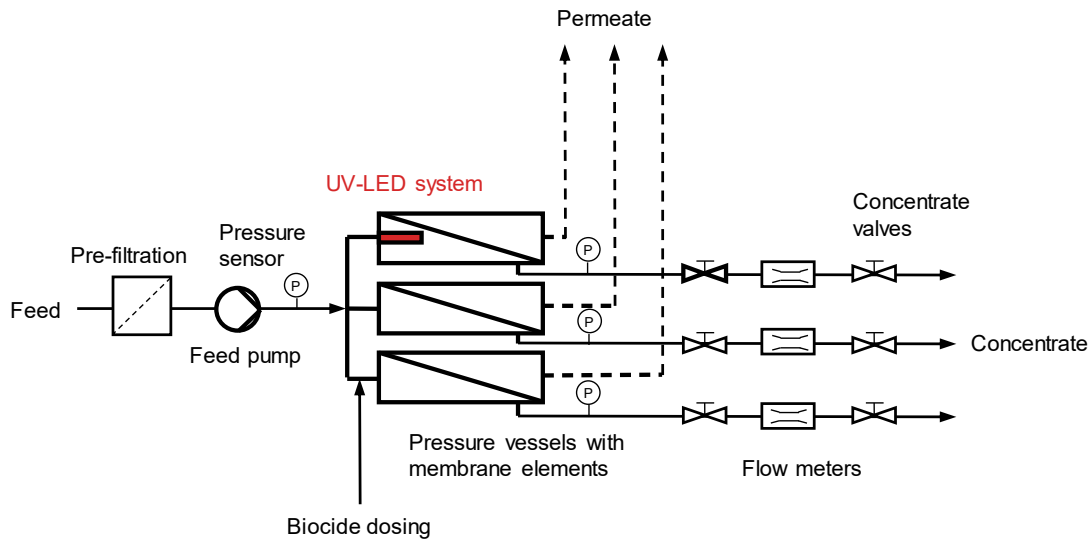
Figure 8-5:   Schematic of the skid used for pilot-scale experiments.

8.2.3. Development, characterization and integration of the *in situ* pilot-scale UV-LED system

Based on typical components of pressure vessels of RO membrane systems (Figure 2-4, Chapter 2.2.2), several possibilities to integrate UVC-LED irradiation *in situ* were investigated (Figure 8-6). Those include modifications of the permeate port with adaptor (PPA), anti-telescoping device (ATD), and interconnector (IC), as well as an empty module (EM). Assuming an outer diameter of 31.8 mm of the PPA, ATD, and IC and 19.0 mm for the empty module with an outer diameter of the pressure vessel of 100 mm for a 4040 module and lengths of 36, 13, 47, and 1016 mm for the PPA, ATD, IC and EM respectively, with a feed flow of roughly 1 m^3 h^{-1}, this leads to HRTs of 0.9, 0.3, 1.2 and 27.7 s. Please note that the assumed dimensions are just approximated and might vary in practice. Considering the calculated HRTs, it can be seen that except for the EM, HRTs are low, so a high power in a small space would be needed to achieve an appropriate fluence. Following the most promising option to integrate the LEDs and ensure a reasonable fluence is to remove a SWM element from the pressure vessel and modify the permeate collection tube in the EM configuration. As biofouling is especially prone in the lead elements (Vrouwenvelder et al., 2009c), the UV-LED system should be put in the first position and be combined with the PPA. Probably the length of half an EM is enough. The electricity connection of the LEDs could, in this case, be connected over the PPA through the endcap.
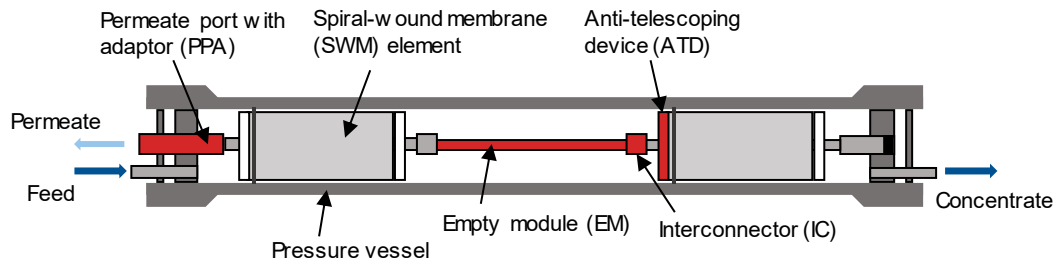
Figure 8-6:   *Possible locations of UV-LEDs inside a pressure vessel.*

Together with UV-EL, a UV-LED system was designed, replacing the permeate port and the first membrane element in a pressure vessel. A photograph of the system, integrated into the pressure vessel end cap, is shown in Figure 8-7. It consists of a square aluminum profile, on which seven LEDs on all four sides were placed (in total 28 LEDs). As LEDs, CUD7GF1B by Seoul Viosys (Korea) with a peak wavelength 275 nm and optical power flux of 11.5 mW at 150 mA (Seoul Viosys, 2017) were utilized. The aluminum profile was placed in a silica glass immersion tube (outer diameter 2.3 cm) that was integrated in and sealed with the pressure vessel end cap. Hence, 18 cm of the aluminum carrier was immersed in the pressure vessel. At the end of the aluminum profile outside of the pressure vessel a fan was attached to provide airflow cooling the LEDs. In general, the UV-LED system was constructed by Bilberry Ltd. (Poland). To enable pulsed irradiation, a PCU 510 time relay (F&F Filipowski sp. j., Poland) was implemented in the electrical cabinet. The time relay did not allow to increase fluence rate during pulsation, but a frequency of 0.83 Hz with a duty cycle of 50% could be achieved.

Figure 8-7:   *The designed UV-LED system for the in situ UV pre-treatment.*

To characterize the UV-LED system, KI/KIO$_3$ actinometry was performed, analogous as described in Chapter 4.3.6/ Sperle et al. (2020a). Therefore, the system was placed in an upright position and the silica glass tube was immersed in a stirred beaker containing 218 mL of actinometer solution (Figure 8-8a). Temperature was maintained at 24 °C and 6 samples were taken spanning an irradiation time of 181 s. As surface area, the outside of the silica glass tube over a length of 18 cm was used and the fluence rate was quantified with 0.72 mW cm^{-2}. The total UV power emitted was estimated with 95 mW. As it was later recognized, the UV-LED actinometer might not have been able to completely absorb the irradiation of LEDs as the wavelength of the used LEDs was on the edge of the absorption spectrum of KI/KIO$_3$ (Figure 8-8b). The

absorbance spectrum of KI/KIO$_3$ was measured 1/100 diluted, then corrected with the dilution factor and transmittance calculated. Assuming the path length as the distance between the silica glass pipe and the inner diameter of the beaker with 0.7 cm in the actinometer solution (as there is no collimated light, this is just an estimate) and averaging the transmittance on the LED spectrum, 21% of the light might not be absorbed and hence the actual value might be a bit higher, ~0.91 mW cm^{-2} and ~119 mW. Per LED this would represent a 4 mW. Even considering a UVT of 90% for the silica glass pipe (QSIL GmbH, 2013), this value is less than the maximum possible output of the LED used. The lower observed optical power might, among others, be explained by one or a sum of the following reasons:

1. Not each LED is supplied with 150 mA; The detailed configuration of LEDs (serial and parallel LEDs) as well as the overall current are not known.
2. Aging of the LEDs for preliminary tests.
3. Error of quantum yield estimation based on the used linear model (Sperle et al., 2020a; Wang et al., 2017; Zou et al., 2019).
4. Even though the beaker was mixed, due to the local high fluence rates above the LEDs the formed I$_3$ might compete for light absorbance, creating a saturation/inner filter effect (Bolton et al., 2011). Besides, without the UV system inserted in the beaker, a clear swirl by mixing was observed, but it is not clear how effective the mixing was after inserting the UV-LED device.

Nevertheless, the quantified value of 0.91 mW cm^{-2} will be further utilized.
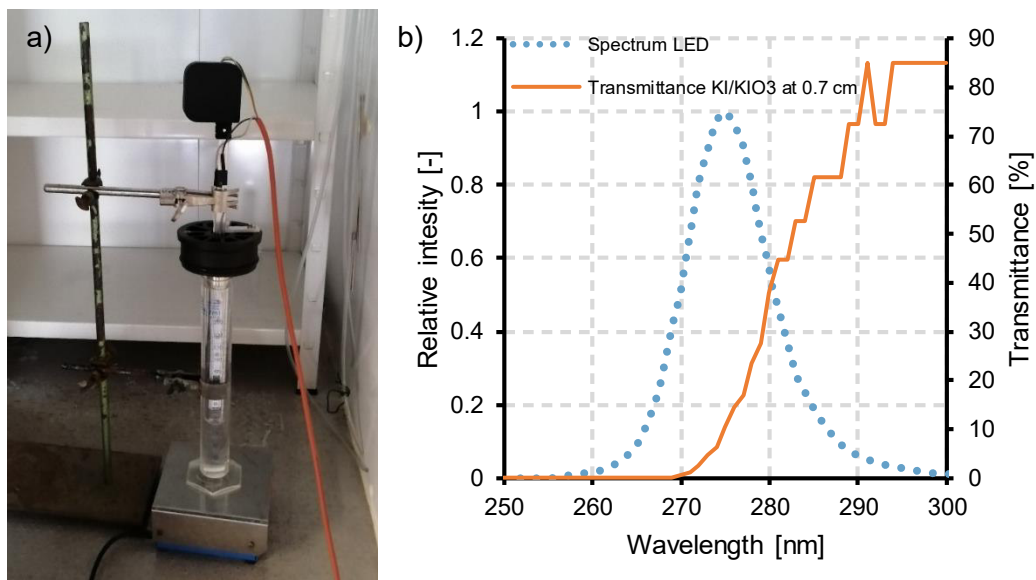
Figure 8-8:   *a) Actinometry set-up to characterize the pilot-scale UV-LED system; b) Spectrum of LEDs according to the datasheet (Seoul Viosys, 2017) and transmittance through the actinometry solution with 0.7 cm path length at designated point of the LED spectrum.*

Within the pressure vessels of the pilot skid, instead of two, only one membrane module was placed (Figure 8-9). In the train equipped with the UV-LED system, the permeate tube was sealed and fixed at the end of the UV-LED system. For the other trains (reference and biocide train) a dummy element was placed. Besides, for the pressure vessel housing the UV system, the reactor wall was lined with 2 mm thick reflective PTFE foil (OptoPolymer, Berghof Fluoroplastic Technology GmbH, Germany).
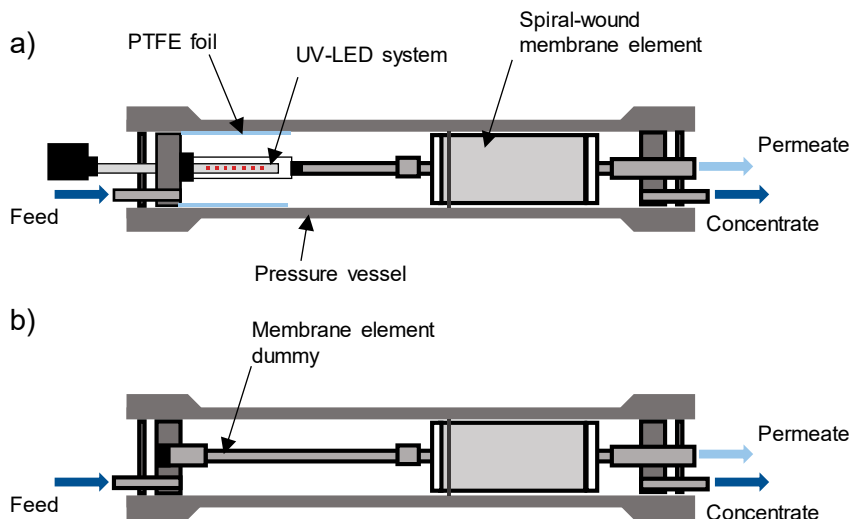
Figure 8-9:   a) Integration of the UV-LED system in the pressure vessel; b) Integration of a dummy element in the pressure vessel.

8.2.4. Results of the pilot-scale biofouling experiments

The pilot skid was run for approximately 98 days and the core process data is depicted in Figure 8-10. The temperature, on average, was 7.9 °C with a standard deviation of ± 1.6 °C. Between each experimental run (0-4), a CIP was performed. Each of these runs shown in a column in Figure 8-10 and will also be referred to as cycles. Within the first five days of operation, a considerable increase of FCPD was observed. This was not linked to biofouling, but was probably caused by inorganic or particle fouling due to insufficient pre-treatment. Therefore, the skid was upgraded with a deironing-filter and a CIP was performed. The gray background color in the diagrams indicates experimental phases with pulsed irradiation (cycle 2 and 3), even though during the first pulsed experiment, for the first ten days, continuous irradiation was still applied (cycle 2). After seven days of operation in cycle 2, the feed pump was again changed. Besides, within the operation of cycle 3, due to holidays, the skid was stopped after three days of operation for three days. The average recovery for the line with UV was 18.9% ± 1.2%, 17.6% ± 1.5% for the line receiving the biocide and 16.7% ± 1.5% for the reference line. FCPD was calculated as the pressure difference of concentrate and feed pressure, as well as subtracting the value recorded after five days in column 1. On this day also a new feed pump was installed. The value for pressure difference for the three lines was 0.33 bar on average. Hence a FCPD of 0.5 is equal to approximately 150%. Unfortunately, the feed flow for the three lines was not equal. To encounter for this variation, FCPD2 was calculated by dividing FCPD through the squared flow. FCPD3 was calculated by subtracting the second value of FCPD2 in each run showing the relative increase after a CIP. Resistance of the membrane without fouling was $6.2 \pm 0.4 \cdot 10^{13}$ m^{-1}.
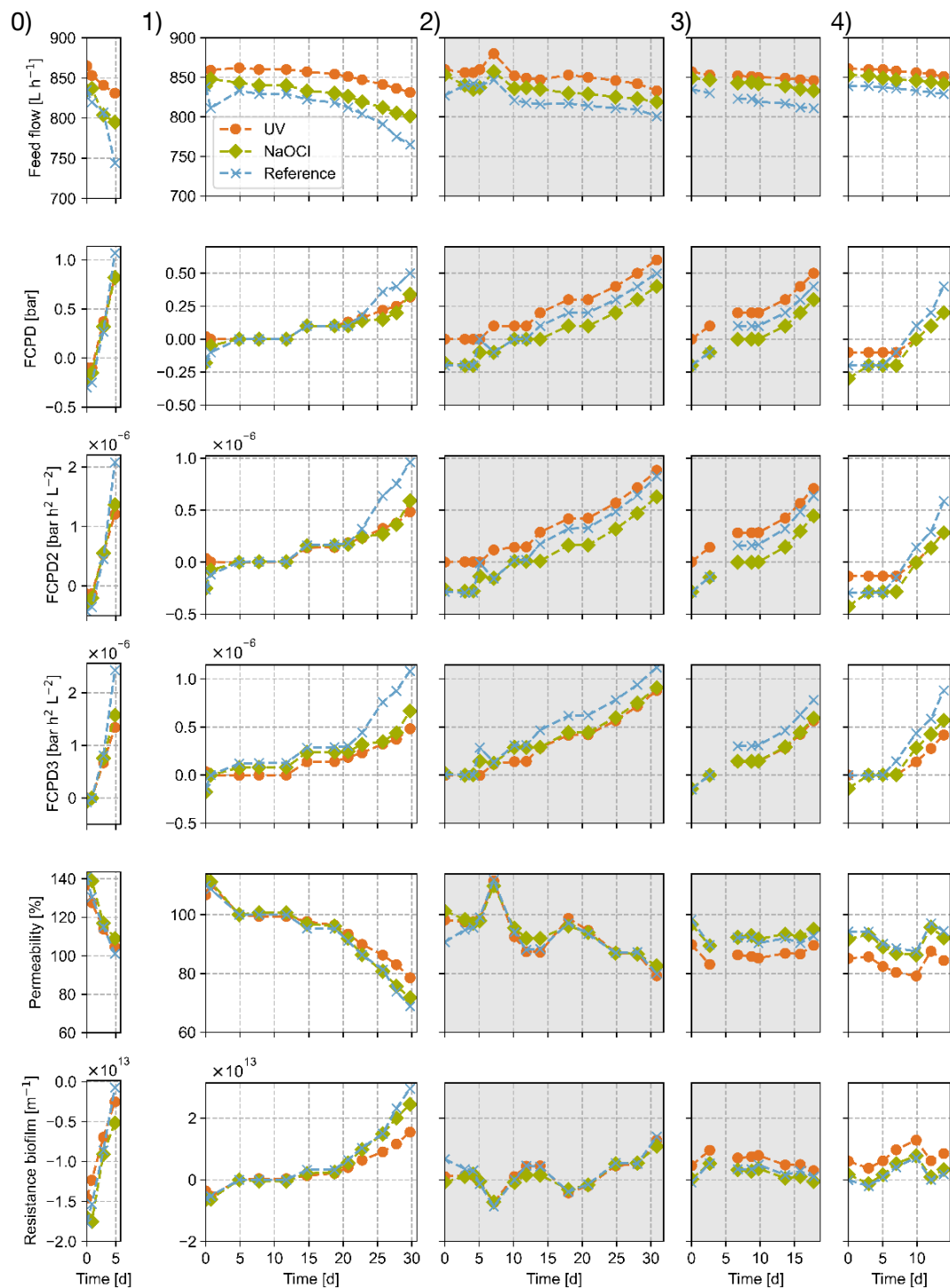
Figure 8-10:   *Summary pilot process data; Cleaning-in-place (CIP) was performed between the data shown in each diagram column. The grey background color indicates pulsed UV irradiation. Feed channel pressure drop (FCPD) was calculated as the pressure difference of concentrate and feed pressure, subtracting the value recorded after five days in column 1. FCPD2 was calculated by dividing FCPD through the squared feed flow. FCPD3 was calculated by subtracting the second value of FCPD2 in each column.*

9. Overall discussion and future research needs

The high research interest in membrane fouling in general (Jiang et al., 2017) and biofouling representing the most severe kind of fouling in numerous applications (Flemming et al., 1997; Najid et al., 2022; Nguyen et al., 2012; Vrouwenvelder and van der Kooij, 2001) stress the importance to progress in the development of fouling mitigation strategies. A chemical free, mature technology for biofouling control that has received less research interest (Harif et al., 2011) and is rarely used in full-scale applications is UV disinfection.

This study aimed to investigate the potential of using the emerging UVC-LEDs as an (*in situ*) pre-treatment technology for biofouling control. As UV-LEDs are an emerging technology, their application was preferred over conventional lamps. Besides, they enable new reactor designs (Song et al., 2016; Würtele et al., 2011). Overall, incorporating the advantages of LEDs, LEDs could be implemented in the treatment train with spatial proximity to the membranes, ideally integrated inside the pressure vessel of RO membrane systems, allowing for easy retrofitting of existing systems.

In Chapter 4, first a proof of concept at lab-scale was conducted to investigate if already a low fluence is sufficient for biofouling control. Besides, it was examined whether applying UV pre-treatment creates positive side effects as a reduced hydraulic resistance of the formed biofilms caused by a changed microbial community.

While working with flow-through UVC-LED reactors, it was recognized that aside from biodosimetry, easy experimental procedures for fluence determination are lacking. When applying a very high fluence, biodosimetry might be not practicable or when testing e.g., if pulsed UV irradiation has additional positive effects for inactivation, the usage of a biological indicator for fluence quantification might not be suitable. As actinometry at the current state was rather limited to fluence determination under fully controlled conditions or radiometer calibration (Bolton et al., 2011; Jin et al., 2006; Song et al., 2018; Wang et al., 2017), in Chapter 5, a novel actinometry method was developed allowing direct fluence determination in reflecting UV reactors with non-parallel irradiation patterns.

In addition, when conducting biodosimetry experiments at lab-scale using biofilm forming bacteria, it was recognized that there are many pitfalls that have to be avoided to generate reproducible and transferable results. Hence, in Chapter 6, a biodosimetry method for challenging bacteria species was developed, considering, e.g. protraction of cells between samples and adsorption to labware.

After having all necessary methods available, a detailed study was conducted at lab-scale (Chapter 7) to check whether pulsed UV disinfection (same fluence but increased fluence rate during the pulses) leads to enhanced inactivation of bacteria. Following, the effects of UV disinfection for biofouling control were studied over a broad fluence range to find the optimal fluence for biofouling control. Thereby, OPEX were calculated and recommendations for full-scale implementations for sea- and brackish

water desalination systems were given. Besides, biofilm removability during CIP was checked.

Finally, to enable a technology transfer form laboratory to more realistic applications, experiments with real feed water were conducted, a UV-LED device for *in situ* integration into the pressure vessel of an RO membrane system was designed and constructed, and effects were tested over several CIP cycles in pulsed and continuous mode (Chapter 8).

9.1. UV disinfection using LEDs, an effective method for biofouling control at low fluence

The first objective of this dissertation was to "*Evaluate the potential of continuous UVC irradiation using LEDs as an in situ treatment approach for biofouling control in high-pressure membrane applications*". Within this objective, hypothesis 1 was to tested if "*UV treatment using UVC-LEDs with a fluence lower than 10 mJ cm^{-2} is capable of delaying severe biofouling (FCPD of 67 mbar cm^{-1}) of RO membranes by more than 10%*". As UV-LEDs are still limited in power output and as for an *in situ* integration of an UV pre-treatment inside the pressure vessel of an RO membrane system, space is limited, it is important to clarify if also a low fluence is sufficient for biofouling control.

The built UV-LED reactor, consisting of a single LED (Chapter 4), was characterized using KI/KIO$_3$ actinometry with a fluence of 2 mJ cm^{-2}. This is only 1/20 of 40 mJ cm^{-2}, the common reduction equivalent fluence (REF) for UV disinfection devices (e.g. DIN 19294-1:2020-08 (DIN e.V., 2020) or class A systems NSF/ANSI 55 (NSF/ANSI, 2019)). Nevertheless, for this fluence determination, three points need to be considered.

1) The fluence determined with actinometry is not incorporating the fluence distribution (Sun et al., 2022). Hence the actual REF might be even lower.
2) The estimated fluence is not taking into account the reduction of fluence by absorbance. However, as the absorbance of the feed water is quite low (Table 8-1 and Table S12-4) this effect might be negligible.
3) As shown in Chapter 5, the path length of the light traveling through the reactor is of great importance in actinometry. Furthermore, as it was shown, KI/KIO$_3$ might not be able to detect fluence rate increase due to reflections or non-parallel irradiation. Within the calculation, the reactor volume and the cross-section area of the silica glass pipe were utilized. Hence, actinometry might only depict irradiance but not fluence rate. The actual fluence rate might be higher. Nevertheless, as the quantified effects align well to the model build in Chapter 7.4.4, it is assumed that the quantified fluence is roughly correct and below 10 mJ cm^{-2}.

Overall, within the six repetitions of biofouling experiments, a significant delay of 2 days and hence 16.5% on average were detected at a sever biofouling state. For one experiment with the reduced LED diving current (0.85 mJ cm^{-2}) on the contrary no considerably delay was observed (5 h difference). Overall, this leads to **the acceptance of hypothesis 1**, as with a fluence of less than 10 mJ cm^{-2} at a peak wavelength around 278 nm, the delay of biofilm formation was more than 10%.

Hypothesis 1	✓ **Accepted**

The suspected mechanisms for the observed delay (as discussed in Chapter 4.4.2 (Sperle et al., 2020a)) were a reduction of viable bacteria in the feed, changed adsorption properties, and cell cycle arrest. As the reduction of viable cells caused by UV disinfection is common knowledge, but as the effects of UV disinfection are more than only inactivation of cells (see Chapter 2.1.2 for a detailed review), all three mechanisms are likely to occur. Nevertheless, the impact of, e.g., changed cell absorption and cell cycle arrest in comparison to the inactivation of the cells are not clear.

While there was not only a delay of biofilm formation observed, in the six experimental repetitions, also a significant difference of 48% in the hydraulic resistance of the formed biofilms was observed. For the difference in hydraulic resistance, four explanations were given (for detailed a description, please refer to Chapter 4.4.6), in short:

1) **Different quantity in EPS production:** EPS is known to correlate with hydraulic resistance (Desmond et al., 2018; Dreszer et al., 2013). At the same FCPD, a different quantity in EPS could explain a difference in hydraulic resistance.

2) **Changed EPS composition/quality:** The composition of EPS can vary and a different microbial community might express EPS with a different quality (Flemming and Wingender, 2010), leading to the changed hydraulic resistance of the biofilm.

3) **Reduced ATP levels impact QS or vice versa**: QS might be impacted by the microbial community (Ma et al., 2018a; Uroz et al., 2009; Zhang et al., 2019). Besides, UV irradiation might lead to a reduced ATP level per cell (Yang et al., 2020), which was found to impact QS and EPS production or the other way around (Jiang and Liu, 2013; Ma et al., 2018a; Zhang et al., 2019).

4) **Introduction of prophage:** It is well known that DNA damage, as caused by UV irradiation, might lead to prophage, which again might lead to biofilm dispersal or disruption (Landini, 2009; Webb et al., 2003). This again could be linked with a more open structure of the formed biofilm.

Within the biofilm analysis, significant differences only for ATP, TDC, TDC$_{dead}$ and ATP/TDC were found. For EPS components, a reduced trend, but no significant

differences were found. Besides, the microbial community seemed to differ between the UV pre-treated and reference biofilms. When correlating the analysis results with the resistances of the biofilms, correlations for some EPS components, TOC, ATP/TDC$_{live,}$ and humic-like substances, as well as for the appearance of *Aquabacterium* sp. and *Sphingopyxis* sp. were observed.

Overall, this leads to the partially acceptance of hypothesis 2 "*Due to a change of the microbial community structure, UV treatment using UVC-LEDs with a fluence lower than 10 mJ cm^{-2} is resulting in 15% less hydraulic biofilm resistance at a severe biofouling state*". At a fluence of less than 10 mJ cm^{-2}, the hydraulic biofilm resistance seemed to be more than 15% reduced. However, it must be kept in mind that with the calculation of hydraulic resistance from the permeability, effects of increased concentration polarization due to e.g., microbial cells and increased hydraulic resistance by EPS (Dreszer et al., 2013; Herzberg and Elimelech, 2007), might be grouped. The significantly changed ATP and ATP/TDC levels could indicate that changed ATP levels might be involved in the difference in resistance found. Besides, even though no significant difference in EPS components was proven, differences could still have caused the change in resistance. Perhaps with better analytical methods or a higher number of replicates, a significant difference might be detected. The only analysis that investigated the quality of EPS was the PARAFAC modeling and here no differences were detected. Nevertheless, with the PARAFAC modeling, only tryptophan- and tyrosine-like proteins might be differentiated, and other changes in EPS quality are not captured. For the introduction of prophage, no biofilm analysis could be performed. The change in microbial community might impact the quality and quantity of EPS as well as QS (Flemming, 2017; Flemming and Wingender, 2010; Frederick et al., 2011; Jiang and Liu, 2013; Ma et al., 2018a; Uroz et al., 2009; Zhang et al., 2019) and seems likely to relate to the change in resistance. A changed microbial community (with impacts on biofilm resistance through changed EPS production) was also proposed by other studies that already have been published or were published during the time of writing the dissertation (Harif et al., 2011; Wang et al., 2023a; Wu et al., 2021a). In those studies, however, biofouling experiments were terminated after a fixed period of time and not at the same "degree" of biofouling. Therefore, also a change of community due to a different stage of biofilm development might be present. The study in Chapter 4 was the only study comparing the biofilm composition at the same FCPD. To conclude, a change in the microbial community seems likely to impact the biofilm resistance (depending on the community in a positive (Sperle et al., 2020a) or negative (Wu et al., 2021a) way), but as also other mechanisms might be relevant, **hypothesis 2 was only partially accepted**.

> **Hypothesis 2**   **(✓) Partially accepted**

9.2. An improved uridine actinometry as an easy and fast method for fluence determination in reflecting UV reactors

The second objective of this dissertation was to "*Establish a simple actinometrical method to quantitatively characterize the degree of reflection in UVC-reactors*". Within this objective, hypothesis 3 should be examined, "*The ratio of fluence rate determined with uridine and KI/KIO₃ actinometry can be used to quantitatively characterize the reflection in UV reactors*". Again due to the currently limited power of UV-LEDs (Koutchma et al., 2019), increasing reactor efficiency and fluence rate is of great interest. Thereby means of reactor design or reflection might be an option (Chen et al., 2017; Li et al., 2017c; Mohaghegh Montazeri and Taghipour, 2023).

In clean water, increasing the light path can lead to an enormously increased efficiency. In the following, two examples will be compared, once an increase of path lengths by reflections and once through a well-designed positioning of the lamps (for ease of comparison, a UV light source with parallel beams is assumed). As shown in example 1 of Figure 9-1, due to the specular reflection, the path length would double. In example 2, the path length might even more than double by changing the beam direction. However, the enhancement of fluence rate increase by higher path lengths is limited in water with low UVT. For example, it is assumed that the path length in Figure 9-1, 1a) would be 8 cm and hence in 1b) 16 cm. For simplification, reflection on the water surface, divergence, and absorbance losses other than in the water body are not considered. If the water had a UVT of 98%, the reflected beam in 1b) entering the water after reflection would still have 85% of its original energy. If UVT would be 85%, the reflected light beam would only carry 27% of its original energy. Please note that this discussion and the effects of path length increase and UVT are assumed common knowledge and therefore no citation is given, but e.g., the behavior of reactor disinfection for a collimated beam UV-LED reactor is also described by Mohaghegh Montazeri and Taghipour (2023). Other examples are found in those studies, Li et al. (2017c) and Sommer et al. (1996). Another limitation for reflective UV reactors that should be mentioned at this point is that the new DIN 19294-1:2020-08 (DIN e.V., 2020) is not allowing reflective materials in UV reactors if increased disinfection performance by reflections cannot be monitored. This is reasonable, as fouling of reflective layers can lead to a reduced reactor performance, and if this is not detected, the UV reactor might insufficiently disinfect the water without any notice. The challenge of fouling of reflective materials was already pointed out by Sommer et al. (1996).
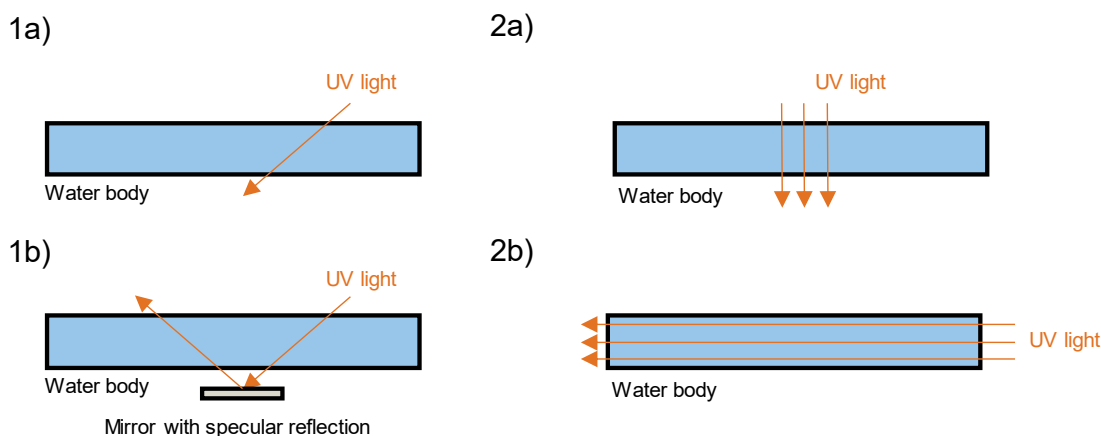
Figure 9-1:   *Schematic comparison of means to increase path length of the light through reactor design; 1) Reflection; 2)Positioning of the lamp.*

As was shown in Chapter 5, for KI/KIO$_3$ actinometry, due to the high absorbance of the actinometer solution at 254 nm, all photons are absorbed immediately (a$_{254}$ > 100 cm^{-1} (Müller et al., 2017)). For an absorption coefficient of 100 cm^{-1} already within 0.1 mm, 90% of the light would have vanished. Hence, it is reasonable that for the calculation of KI/KIO$_3$ actinometry (equation (5-5)) path length is not considered. Rather the energy absorbed is calculated for the actinometer volume and divided by the irradiated surface area. Overall, KI/KIO$_3$ actinometry was found effective in calculating the irradiance at the water surface, but it was not able to quantify the fluence rate under reflective conditions, as the results of biodosimetry showed.

The conventional uridine actinometry (U1) is usually conducted at a lower absorbance of actinometer solution (Bolton and Stefan, 2002; Jin et al., 2006) and did capture changes for the increased path length due to the reflections. Nevertheless, as it could be shown, the actinometry depicts the fluence rate within the water solution at the given absorbance of the actinometer and other water matrix compounds. To get the fluence rate without any absorption effects, the path length of the light is needed.

In recent research, it was observed that the photoproduct of uridine shows absorbance in the irradiated and measured wavelengths (Pousty et al., 2022), the new actinometric procedure (U2) was developed based on a semi-empirical model (Maafi and Maafi, 2013; Maafi and Maafi, 2015). Thereby path length was determined by performing the experiment with several actinometer concentrations analogous to Roibu et al. (2018). With the developed equation, photon flux at the water surface could be well quantified as the comparison with the radiometer readings showed. Furthermore, when the irradiated reactor volume was transformed using the calculated path length $V_{eff} = A \cdot l_{irr}$ the average fluence rate in the reactor volume could be calculated without any needed information on the irradiated surface, as surface area and volume are crossing out in equation (5-12). The calculated fluence rate of the new actinometric procedure could be validated with biodosimetry.

Basically, the described transformation with the effective volume leads to an increase of the fluence rate with the factor $\frac{V_{eff}}{V} = \frac{l_{irr}\,A}{V} = \frac{l_{irr}}{l_\perp}$ relative to the irradiance, with $l_\perp$ representing the water depth perpendicular to the irradiated surface/cross section. It is valid to use the calculated fluence rate and path length together and directly to determine the average fluence rate within a water body as the following example shows. Hereby a petri dish is being irradiated with parallel light and a specular reflection is occurring at the bottom. This would lead to twice the path length. Neglecting reflectance at the water surface, the fluence rate E_1' caused by the first pass of the light beam can be calculated based on the calculation for WF (Bolton and Linden, 2003; Morowitz, 1950) as following:

$$E_1' \ [mW\ cm^{-2}] = E_0' \cdot \frac{1 - 10^{-a^\lambda \cdot l_\perp}}{a^\lambda \cdot l_\perp \cdot \ln(10)} \tag{9-1}$$

With a^λ being the decadic absorption/attenuation coefficient at the wavelength of irradiation [cm⁻¹]. The fluence rate added during the second pass of the light beam after the specular reflection is calculated as

$$E_2' \ [mW\ cm^{-2}] = E_0' \cdot \frac{1 - 10^{-a^\lambda \cdot l_\perp}}{a^\lambda \cdot l_\perp \cdot \ln(10)} 10^{-a^\lambda \cdot l_\perp} \tag{9-2}$$

The total fluence rate in the water body then is equal to

$$E_{total}' \ [mW\ cm^{-2}] = E_1' + E_2' = E_0' \cdot \frac{1 - 10^{-a^\lambda \cdot l_\perp}}{a^\lambda \cdot l_\perp \cdot \ln(10)} \cdot \left(1 + 10^{-a^\lambda \cdot l_\perp}\right)$$
$$= E_0' \cdot \frac{1 - 10^{-a^\lambda \cdot 2 \cdot l_\perp}}{a^\lambda \cdot l_\perp \cdot \ln(10)} \tag{9-3}$$

Using the factor of path length ($f_l=2$) increase directly as a factor leads to the same results (equation (9-4)).

$$E_{total}' \ [mW\ cm^{-2}] = f_l \cdot E_0' \cdot \frac{1 - 10^{-a^\lambda \cdot f_l \cdot l_\perp}}{a^\lambda \cdot f_l \cdot l_\perp \cdot \ln(10)} = E_0' \frac{1 - 10^{-a^\lambda \cdot 2 \cdot l_\perp}}{a^\lambda \cdot l_\perp \cdot \ln(10)} \tag{9-4}$$

In summary, it was determined that the commonly used KI/KIO₃ actinometry is able to quantify irradiance in a system, and with the developed uridine actinometry, not only irradiance but also fluence rate can be calculated. As an increase in reflection basically leads to an increase of the path length of the light in the water body, **hypothesis 3 can be accepted** as the ratio fluence rate determined using uridine divided by the fluence rate (actually irradiance) with KI/KIO₃ gives the increase in path length and hence the quantified effect of reflection. Actually, the developed uridine actinometry could be used to also calculate irradiance as well and therefore KI/KIO₃ would not be needed. In the case of the experiments performed in Chapter 5, the increase of path light was 2.4-fold for the petri dish with the whole botting being reflecting and only 1.8-fold when half of the bottom was covered with PTFE foil.

Approximately the same increases were observed and validated by biodosimetry for the fluence rate.

Hypothesis 3	✓ **Accepted**

As discussed in Chapter 5, even though the developed actinometry method gives no information about fluence distribution, it has several potential applications. It might be used to validate the optical field in reactor models. Besides, coupled with results of biodosimetry, it can be used to assess the reactor performance through mixing efficiency and the equalness of the fluence distribution. Furthermore, it might be used to characterize alternative (non CBA) laboratory reactors or be useful if high fluence is employed and biodosimetry might be too sensitive. Perhaps with further development, the actinometric procedure using uridine or a non-toxic alternative actinometer in trace concentrations could be used to determine changes in the performance of reactors with reflective housings, hence meeting the standards for DIN 19294-1:2020-08 (DIN e.V., 2020). Finally, it can be used for a fluence determination for non-parallel light. Due to the limited power output of current LEDs, developing a CBA with LEDs could be difficult. There exists a LED CBA model on the market, but actually reflections in the collimator were suspected of causing a low Petri factor (TZW, 2020). Besides, non-parallel beams might cause problems for irradiance estimation with standard radiometers without diffusers (Bolton and Linden, 2003), which can be avoided through this actinometry.

The application of the actinometry to flow-through has been shown in Chapter 7 with promising results. Nevertheless, for a broad application of the uridine actinometer, the behavior of quantum yield over a broad range of concentrations, temperatures, wavelengths, fluence rates, and fluence should be additionally checked. Besides, application and validation on an industrial-scale reactor would be interesting.

Finally, the results of actinometry and path length determination should be further proven by a comparison with a validated UV reactor model. This is currently done and might be published in another study (see Chapter 12.8). In short, the reactor used in Chapter 7, was modeled and model results were validated by the biodosimetry results. As preliminary results show, at a flow of 4.25 L h^{-1}, the modeled LRV of MS2 was 1.99, whereas experimental results showed a LRV of 1.96. The average fluence rate in the reactor volume in this model was 25.6 mW cm^{-2}, whereas experimental results of actinometry showed a fluence rate of 29.2 mW cm^{-2}. Hence the validated model shows a deviation of less than 15% for the average fluence rate of the reactor body, compared to the actinometrical calculated values.

9.3. The limited effects of pulsed UV disinfection

The third objective of this dissertation was to "*Elucidate the effect of fluence rate in pulsed UVC-LED irradiation on disinfection efficiency*". Within this objective, hypothesis 4 was examined, "*With raising fluence rates (in the range of ~1 – 100 mW cm⁻²), the disinfection efficiency of pulsed UVC-LEDs is increasing significantly by more than 30% for bacteria*".

As it was elucidated in detail in Chapter 2.1.5, the effects of pulsed UV irradiation using LEDs are conversely discussed. Whereas some studies observed enhanced inactivation, others did not (Li et al., 2010; Nyangaresi et al., 2019; Sholtes and Linden, 2019; Song et al., 2018; Tran et al., 2014; Wengraitis et al., 2013; Zou et al., 2019). Song et al. (2018) proposed that the differences observed for water disinfection might be caused by an error in the fluence determination and it might be critical to normalize the log inactivation by UV fluence if a different fluence was applied. Additionally, they outlined that a too low energy output could be the reason for neither seeing an effect by photochemical nor photophysical damage. A deviation from Bunsen-Roscoe with a higher fluence rate leading to higher inactivation was observed for 254 nm irradiation by Sommer et al. (1998), whereas the opposite effects were observed by Pousty et al. (2021) for higher wavelengths.

To investigate the effects of pulsed UVC irradiation on microbial inactivation in flow-through systems, as described in Chapter 7, biodosimetry experiments with higher fluence rate during pulsation, but same fluence as the reference continuous irradiation setting were conducted. After developing a procedure for reproducible biodosimetry experiments (Chapter 6), biodosimetry for MS2 phage was performed with a fluence rate in continuous mode of 29.24 mW cm⁻² and 31.27 mW cm⁻² in pulsed equivalent (141.26 mW cm⁻² during the pulses) with a duty cycle of 22%. As no effects for increased fluence rate or pulsation per se were suspected for MS2 (Sommer et al., 1998; Song et al., 2018), this experiment could be used to investigate whether pulsed irradiation is changing the fluence distribution received of the microorganisms. However, as no significant differences for the inactivation of MS2 were observed, it is assumed the pulsed irradiation with 10 Hz had no considerable effects on fluence distribution at the achieved LRVs. As the average HRT (Volume/Flow) varied between approximately 1 to 4 s, for the lowest HRT, on average, the microorganisms should receive ten pulses. At the maximum flow (8.5 L h⁻¹), the flow is still in laminar regime with Reynolds number less than 2,300. Even when assuming maximal velocity u_{max} in the laminar pipe (relative to the average velocity u_{avg}) according to equation (9-5) (Nakayama, 2018), the microorganisms should at least receive five pulses. Considering this, a frequency of less than 2 Hz probably would be critical as some microorganism could pass unirradiated at the highest flow setting.

$$u_{avg} = \frac{1}{2}\ u_{max} \qquad\qquad (9\text{-}5)$$

Aside from biodosimetry using MS2, biodosimetry was performed using the biofilm forming bacteria *A. citratiphilum*. Thereby, the fluence rate in continuous mode was 2.02 mW cm^{-2} and 1.90 mW cm^{-2} for pulsed disinfection (141.26 mW cm^{-2} during the pulses) with a duty cycle of 1.4%. Hence, the difference in fluence rate was more than one order of magnitude (roughly two orders). HRTs investigated here were slightly higher (2-5 s). Here again, no significant difference in inactivation between pulsed and continuous irradiation was observed. This is in accordance with the findings of Song et al. (2018), who did not observe an enhanced inactivation for pulsed disinfection than for continuous setting with precisely determined fluence. According to the study of Pousty et al. (2021), the difference in time dose reciprocity present at the used wavelength (273 nm) might be rather little. Besides, it should be noted that time dose reciprocity was investigated at that wavelength for lower fluence rates (0.005-0.4 mW cm^{-2}) in the study of Pousty et al. (2021). In conclusion, this leads to the **rejection of hypothesis 4** as the pulsed irradiation with a difference in fluence rate during the pulses of 141 mW cm^{-2} in comparison to 2 mW cm^{-2} during the continuous equivalent showed no significantly enhanced disinfection.

Hypothesis 4	✕ **Rejected**

As suspected by Song et al. (2018), for achieving the same enhanced inactivation though photothermal and photophysical effects or even multiphoton absorption (Bolton and Cotton, 2022; Elmnasser et al., 2007), see Chapter 2.1.5 for a detailed review, by using LEDs in pulsed mode, the fluence rate of LEDs needs to be increased further. Whereas the light output of UV-LEDs is still in the range of mW, Xenon lamps have higher peak/pulse output in the order of MW (Oms-Oliu et al., 2010; Song et al., 2018).

In addition to the biodosimetry experiments, biofouling experiments with three pairs of pulsed and continuous settings were performed (Chapter 7). Interesting to note here is that for the pulsed settings, a significantly higher delay in subsequent biofilm formation was observed. Assuming that the inactivation of incoming cells is mainly causing the delay, it was hypothesized that the higher fluence rate might penetrate further into cell clusters leading to their inactivation. The hypothesis was supported by the study of Vitzilaiou et al. (2021), who also suspected that lower intensities at longer times might decrease the inactivation of cell aggregates. Further, for directly irradiated biofilms, biofilm control depended rather on light intensity than on total fluence (Torkzadeh et al., 2021; Torkzadeh and Cates, 2021). Nevertheless, the hypothesis of enhanced inactivation of cell aggregates could not be investigated and further research in this regard is advised. In case it should turn out that the higher fluence rate during pulsed irradiation should lead to an enhanced inactivation of cell clusters, this could indeed be a great advantage of pulsed disinfection.

With or without enhanced inactivation efficiency of pulsed UV disinfection, objective 4 of this study was to "*Investigate the potential of pulsed UV as an operational*

strategy for efficient control of biofouling". Thereby, not only the efficiency of pulsed inactivation but also general impacts on OPEX should be investigated. As a better thermal management of UV-LEDs under pulsed operation was observed (Nyangaresi et al., 2019; Song et al., 2018), hypothesis 5 tested if "*Applying pulsed UVC-irradiation as an operational strategy for biofouling control leads to 30% higher energy efficiency compared to continuous irradiation*".

As the biofouling experiments in Chapter 7 revealed, for the used setting, UV pre-treatment was predicted to save up to 24% of OPEX (here not considering OPEX of UV pre-treatment itself). Overall, a higher delay for pulsed operation was found, however, a higher hydraulic resistance for pulsed operations was observed, too. Over the fluence applied, a trend of higher savings with higher fluence could be proven. Nevertheless, the highest savings per applied fluence were around 4 mJ cm^{-2}. Overall, no significant difference for OPEX savings (including delay of biofilm formation, CIP and membrane replacement) between pulsed and continuous operation was detected. Therefore, it is assumed that overall, pulsed and continuous operation is not increasing energy efficiency on a fluence basis.

When measuring the power at the socket of the LED-Pulse-Controller, differences in electrical efficiency for light generation can be seen (Table 9-1). The performance indicator here was calculated as fluence rate at a certain setting, divided by the measured power at the socket. On average, an increased efficiency of 13% for pulsed disinfection can be seen. Nevertheless, this comparison is highly depending on the applied electricity supply of the LEDs. In this case, the LED-Pulse-Controller as a constant current source was used, supplied with a 24 V power supply. Thereby considerable power losses might occur, especially if the voltage needed by the LEDs is lower than the one supplied for the pulse generator.

Table 9-1:   *Comparison of the power demand using a performance indicator during continuous and pulsed irradiation using the power measured at the socket of the LED-pulse-controller.*

Setting continuous	Performance indicator continuous [10^{-3} cm^{-2}]	Setting pulsed	Performance indicator pulsed [10^{-3} cm^{-2}]	Performance indicator pulsed / continuous UV [%]
-	-	0.5%	0.8	-
16 mA	1.6	1.4%	1.7	111
48 mA	6.1	9.3%	7.1	116
96 mA	8.0	22%	8.9	112
400 mA	11.4	-	-	-

To further investigate the efficiency of UV light generation of the LEDs in pulsed and continuous modes, measurement of the voltage over time was conducted using an oscilloscope (Chapter 12.9), as done by Song et al. (2018). The voltage measured at the outlet of the LED-Pulse-Generator fitted to the ones indicated in the data sheet of the

array (around 15 V for 400 mA and 13 V for 100 mA) (Laser Components GmbH, 2019b). Within the measurements of pulsed irradiation, a voltage overshoot during pulsed irradiation similar to Song et al. (2018) was observed. This overshoot leads to increased average peak voltage demand during the pulsation.

The results for the performance indicator (fluence divided by the calculated power demand of the LEDs based on the oscilloscope measurements) are summarized in Table 9-2. Here it can be seen that the performance indicator based on the oscilloscope measurements is higher than the performance indicator based on the power demand measured at the socket. Especially for the low current and small duty cycles, the differences are higher (e.g., 35-fold for 0.5% duty cycle or 8-fold for 16 mA vs. 2-fold for 400 mA). Using a two-sided paired t-test, no significant differences of the performance indicator between the continuous and equivalent pulsed settings (p-value = 0.463, df = 2 and t-statistic = -0.901) were discovered. Besides, it can be seen that the performance indicator is rather constant around $25.6 \cdot 10^{-3}$ cm^{-2}, except for the 16 mA setting. The lower performance indicator at 16 mA might be caused by the LED running under unfavorable conditions at such small driving currents. In addition, the provided UV-LED rector used a 2P2S-S6060 UVC Quad SMD Module (Bolb Inc., United States). On this LED array, not only two LEDs in series are installed in two parallel lines, but also two LED drivers (type BCR421 (Bolb Inc., 2023)) are implemented on the printed circuit board. Each driver is connected over a 3R60 resistor for setting maximum current. Using the oscilloscope and the attached spectrophotometer (Chapter 7.3 and 12.9), it was observed that till 400 mA, the light intensity increased, but over 400 mA, somewhere around 450 mA the maximum was achieved. When using a constant current power supply like the utilized LED-Pulse-Controller, LEDs in series might be powered without any driver. Indeed, adding a driver together with a constant current supply might lead to unfavorable behavior or losses, e.g. a voltage drop might occur over the LED and an enabling current might pass through the driver but not to the LEDs. The current passing the driver and not the LEDs might be rather low, but may be relevant, especially for the 16 mA setting with two LED drivers. The behavior of the driver, in general, is influenced by the voltage supplied (Infineon Technologies AG, 2022). Nevertheless, powering LEDs in parallel by a single constant current might become problematic if one of the LED trains fails. Ideally, the reactor should have been powered by just the constant current supply and using a single output of the pulse controller for each LED string.

Table 9-2:   *Comparison of the power demand using a performance indicator during continuous and pulsed irradiation using the calculated power based on the measured voltages with the oscilloscope at the LED-Pulse-Controller outlet.*

Setting continuous	Performance indicator continuous [$10^{-3}\,cm^{-2}$]	Setting pulsed	Performance indicator pulsed [$10^{-3}\,cm^{-2}$]	Performance indicator pulsed / continuous UV [%]
-	-	0.5%	26.6	-
16 mA	12.8	1.4%	23.1	180
48 mA	26.9	9.3%	26.3	98
96 mA	25.9	22%	25.8	100
400 mA	25.0	-	-	-

The interplay of the constant current supply with the LED drives makes it difficult to judge the losses of voltage/currents passing not through the LEDs. To at least exclude the voltage drop by the LED drivers, a wire was soldered to the outlet of one driver, and the oscilloscope was connected there, as well as at the electricity connection of the printed circuit board (Chapter 12.9). With this configuration, it should be possible to measure the voltage powering the LEDs directly. Performance indicators calculated this way are summarized in Table 9-4. In general, the performance indicator additionally increased by 6% on average. Again, performance indicator of the 16 mA setting is lower than for the other settings that showed an average value of $27.6 \cdot 10^{-3}\,cm^{-2}$. As before, a two-sided paired t-test could not reveal significant differences for the paired settings of pulsed and continuous irradiation (p-value = 0.376, df = 2 and t-statistic = -1.130). Besides, the performance indicator of 400 mA in the continuous setting is comparable to the performance indicators of the pulsed modes. Still, within the measurements, non-explainable oscillations in the negative voltage regions after the pulses were observed (Chapter 12.9) and were not considered in the calculation, as current flow in LEDs is restricted in one direction.

Table 9-3:   *Comparison of the power demand using a performance indicator during continuous and pulsed irradiation using the calculated power based on the measured voltages with the oscilloscope at the LED driver outlet and electricity connection of the printed circuit board.*

Setting continuous	Performance indicator continuous [$10^{-3}\,cm^{-2}$]	Setting pulsed	Performance indicator pulsed [$10^{-3}\,cm^{-2}$]	Performance indicator pulsed / continuous UV [%]
-	-	0.5%	28.4	-
16 mA	12.9	1.4%	25.3	195
48 mA	27.7	9.3%	29.0	105
96 mA	27.1	22%	26.9	99
400 mA	27.8	-	-	-

In general, Song et al. (2018) and Nyangaresi et al. (2019) observed an increased effect of the duty cycle on the thermal management of the LEDs, hence for validating hypothesis 5, a higher performance indicator by better thermal management was expected. Just comparing the performance indicators for the pulsed settings, this should lead to an increasing performance indicator with reducing duty cycle. This trend could not be observed when comparing the performance indicator of 400 mA continuous to its pulsed settings with 400 mA and various duty cycles. Assuming that not captured artifacts of the LED driver behave similarly for the 400 mA as they do in the pulsed settings with 400 mA (e.g., any current loss), this lead to the conclusion that no enhanced electrical efficiency due to pulsed operation is present.

A possible explanation for not seeing enhanced efficiency through better thermal management during the pulsed irradiation could be reasoned with efficient heat dissipation. In the study of Song et al. (2018), the temperature of the LED with heat sink was actually maintained below 25 °C, but heating and the beneficial effects for the pulsed operation were observed without a heat sink attached. Here heating effects could be seen within a couple of seconds. It is difficult to compare the heat sink of Nyangaresi et al. (2019) (aluminum board) to the one used, but maybe by maintaining the ambient air temperature in the temperature cabinet at 15°C with the fan attached to the aluminum body at the backside of the LEDs, likely efficiently cooled the LEDs, limiting any positive effects of reduced LED temperature in pulsed irradiation settings. Effects of lower ambient temperature on LED solder temperature were observed by Nyangaresi et al. (2019). Besides, it is not clear to what extent, a better thermal management during pulsation in the end would affect the overall energy efficiency. Another explanation might be that when performing the oscilloscope measurements, only a few seconds passed after the LEDs were turned. Even though temperature changes of the LEDs were observed within seconds (Song et al., 2018), it cannot be excluded that the time was too short.

To conclude, for the used setting and UV-reactor, no significantly enhanced energy efficiency gain (neither comparing the OPEX of the membrane system nor in the electrical efficiency of the LEDs) could be proven and hence **hypotheses 5** (*"Applying pulsed UVC-irradiation as an operational strategy for biofouling control leads to 30% higher energy efficiency compared to continuous irradiation"*) **is rejected.** Still, two major limitations need to be stated. A detailed examination of the electrical efficiency of the LEDs without possible artifacts/power losses caused by the LED driver was not possible. Also, the unexplained oscillations in the negative region, as shown in Chapter 12.9, need to be kept in mind. Besides, during the power calculation, the set current was assumed to completely arrive at the LEDs. Actually, this current might differ, e.g. during the overshoot of the pulses, and due to a potential enabling current of the LED driver. Nevertheless, no trend of performance indicator could be observed between 400 mA and the pulsed settings, which were assumed to be similarly impacted by the driver.

| **Hypothesis 5** | ✕ **Rejected** |

Nevertheless, the observed better thermal management of LEDs in pulsed mode without a heat sink attached, as observed by Song et al. (2018), might be especially interesting when LEDs gained efficiency and less electrical energy is converted to heat. Still, the effects of better thermal management of pulsed operation in comparison to a reduced driving current without heat sink are not clear (e.g., 48 mA vs. 9.3% pulsed at 400 mA). Perhaps the same temperature management effects are also achieved with a lower current, making efforts for pulsed irradiation obsolete. Nonetheless, the study of Nyangaresi et al. (2019) indicates better thermal management by pulsation than by reduced current, but this topic could be investigated further in future studies.

9.4. UV pre-treatment as a promising technology for biofouling control

In Chapter 7, savings of OPEX (including a simple estimate OPEX from CIP and membrane replacement) due to UV pre-treatment were estimated to be up to 24% for a fluence of 57 mJ cm^{-2} (here not considering OPEX of UV pre-treatment itself). Further, it was hypothesized that the effects of the UV treatment might depend on the nutrient concentration of the feed water, the number of microorganisms, and the community diversity of microbial community. Whereas positive effects of UV pre-treatment were stated to rise with the number of microorganisms present in the feed, the effects might decline with nutrient concentrations. Actually, the used accelerated biofouling experiments might rather depict worst-case conditions of the UV pre-treatment as easily degradable nutrients were added. Depending on the community present in the feed water, it was hypothesized that positive or negative effects for the biofilm resistance might develop. Concerning the savings of OPEX by a changed biofilm resistance in the laboratory experiments, it was concluded that the effects of OPEX savings by changed biofilm resistance might have been over represented as only a short membrane specimen was used in the laboratory experiments, and biofouling might have been especially prominent here (Vrouwenvelder et al., 2009d).

Whereas energy costs by the LEDs in the current state and the utilized reactor were unable to compete with the OPEX savings, comparing the energy demand for conventional UV irradiation systems, some interesting observations were made (Chapter 7). For this comparison, it was assumed that the effects are not depending on wavelength, transfer directly to full-scale sites and energy demand for UV disinfection behaves linearly with fluence. In general, the OPEX for UV disinfection (only considering energy demand, excluding e.g., lamp replacement), were estimated to be small in comparison to the RO membrane treatment itself, e.g., ~1–2% for seawater and ~2–5% for brackish water desalination at a fluence of 40 mJ cm^{-2} and a UVT of 98 and 91%. On a fluence basis, the highest savings were found around 4 mJ cm^{-2}, but the saltier the water the less might the OPEX of UV compare to the overall OPEX from the membrane

filtration. For seawater desalination, full 40 mJ cm^{-2} or higher might be optimal, whereas for brackish water also lower fluence, e.g. 28 mJ cm^{-2} could be preferable.

When comparing total OPEX savings to OPEX savings by a changed biofilm resistance and FCPD increase curve, it was identified that a considerable proportion of OPEX savings are probably depending on the delay of biofouling and the resulting savings of CIP procedures and avoided membrane replacements. For those OPEX savings to occur in practice, it is essential that the delay of biofouling is still present after several CIP cycles and that cleanability is better or equal than for biofilms without UV pre-treatment. Whereas in the laboratory experiments, no difference in the biofilm cleanability concerning the restoration of FCPD was observed, the delay in biofouling was still present in two out of three cases.

For judging the potential of UV pre-treatment for biofouling control, it is of major importance that the benefits translate to real and up-scalded applications and over several CIP cycles. Therefore, objective 5 of this dissertation was to "*Validate the effect of in situ UV treatment for biofouling control under real feed water conditions in an up-scaled system*". Within this objective, hypothesis 6 shall be tested "*In situ UVC treatment of the feed stream in the pressure vessel of RO membrane systems is reducing the impacts of long-term biofouling under real conditions*".

9.4.1. UV pre-treatment in low nutrient conditions

As a first step, a commercial point-of-use UV-LED system was integrated into a lab-scale skid using three small SWM elements in series (Chapter 8.1). The feed water used was similar to the one utilized during the bench-scale experiments, but without the addition of easily degradable nutrients. The UV fluence delivered by the UV system was 15 mJ cm^{-2} (AquiSense Technologies, 2022). The measured electric power demand of 5.7 W fitted to the one stated in the data sheet (AquiSense Technologies, 2022). For a flow of 3.2 L min^{-1} this would lead to an energy demand of 29.7 Wh m^{-3}. This energy demand is higher than for conventional low-pressure systems (17 Wh m^{-3} for 40 mJ cm^{-2} at a UVT of ~91% (Schmalwieser et al., 2017)), but given the currently limited efficiency of LEDs (0.2-9.5% vs. 30-40% (Koutchma et al., 2019)), it looks promising.

Within the laboratory experiments, two interesting observations were made. First, whereas for the experiment without UV, biofouling was observed, indicated by an increase of FCPD, but the permeability of the membranes remained constant. Overall, the hydraulic resistance of the membrane was comparable to the ones observed in Chapter 7 ($9.0 \cdot 10^{13}$ m^{-1} vs. $7.5 \pm 1.9 \cdot 10^{13}$ m^{-1}). When opening the first membrane element after the termination of the experiment (Figure 8-3a), biofilm growth was only detected in the first cm of the element and in an area where the membrane was glued and hence not permeable. This demonstrates that the impact of biofilm in general, but also for UV pre-treatment, on the hydraulic resistance will be different from case to case. Besides, as discussed in Chapter 7, biofouling forms mainly in the lead elements (Vrouwenvelder et al., 2009d). As in the lab-scale experiments, only a short membrane

specimen was used, biofilm effects on hydraulic resistance might be over represented and lower in practice. The second observation made is that for the experiment with UV no biofouling could be observed at all, even though the system was operated for 100 days without UV at the end. Unfortunately, the feed water composition was not monitored frequently, but as the water originates from groundwater, it is assumed that its composition stays rather constant. A grap sample taken during the experiment without UV had a TOC of 1.22 mg L$^{-1,}$ whereas TOC for a sample taken during the experiment with UV was 1.79 mg L^{-1}. This would rather indicate a higher fouling propensity for the experiment with UV, but as sampling was not done regularly, a detailed comparison is not possible. Rather than a changed feed water composition, it is hypothesized that the biofilm formation was successfully inhibited by the UV pre-treatment on the membranes. However, likely biofilm formation might have occurred in the pipes before the membrane elements (Figure 8-3b). When switching off the UV system, the biofilm grown in the pipes might lower the already low amount of nutrients available in the feed water (PO$_4^{3-}$ concentrations below the detection limit). This might have led to reduced biofouling propensity even after the UV light was switched off. Nevertheless, this is just a hypothesis that would require further validation. To do so, it would be possible to quantify the nutrient concentration at the inlet of the skid and directly before the membrane module for both experiments. In case the effects should be proven, this would be an advantage of a possible integration of the UV-LEDs in the pressure vessel of the RO system, to not only reduce active microorganisms by regrowth after the UV reactor but also to maximize nutrient removal before the membrane elements. However, this effect might be limited to waters with very low nutrient concentrations in the feed, which likely tend to lower biofouling propensity in the first place.

9.4.2. Proof of technology at pilot-scale

Probably the most relevant results for investigating the transfer of the positive results of (pulsed) UV for biofouling control are the pilot-scale experiments summarized in Chapter 8.2. The feed water used showed a higher biofouling propensity than the well water used for the 1.8'' SWM experiments (Chapter 8.1). Without the addition of nutrients an increase of FCPD of 0.5 bar (an increase of 125% compared to the pressure drop without fouling of the reference line) was observed within 30 days without UV or biocide dosing (Figure 8-10). Comparing both the increase of FCPD2 (FCPD divided by the squared feed flow to encounter effects of feed flow variation) and FCPD3 (FCPD2 with the second value of each cycle subtracted in order to compare the increase in each cycle) for the first cycle (Figure 8-10), a lower FCPD increase by the UV and the biocide line than for the reference line was observed. Thereby the UV and biocide lines performed comparable (FCPD2), but biofilm formation was still observed. After a CIP and ten days still in continuous mode, irradiation was switched to pulsed operation. After approximately 31 days of operation, another CIP was initiated, and the system continued operation under pulsed conditions. Looking at cycle 2 and 3 (Figure 8-10) for

FCPD2, it could be seen that after the cleaning, FCPD2 for the biocide and reference line was below the starting point. For the UV line FCPD2 was "only" recovered back to the initial FCPD2. Looking at the increase of FCPD after CIP (FCPD3) in pulsed operation, biocide and UV performed equally, and again a delay in FCPD was observed. For the last cycle of operation (continuous mode), FCPD2 after CIP recovered fully below the starting point for all three lines (UV line still showing higher values than the others). This time, however, the biofilm growth for the UV line was slightly slower than for the biocide and the reference line (FCPD3). Overall, no clear benefit for the biofilm resistance due to UV pre-treatment can be seen. Delay of continuous irradiations, on the contrary, seems to perform equally or even better as the dosage of biocides does (comparing FCPD3). Pulsed irradiation performed better than the reference line and was equal to the biocide line.

Judging the effect of UV pre-treatment on the biofilm resistance is challenging as experiments were not terminated at the same FCPD. To enable a fair comparison, FCPD2 is plotted in Figure 9-2 against the resistance of biofilm (including other kinds of fouling and concentration polarization effects). As it can be seen, especially during the first and second cycles, the resistance of biofilm seems to be similar in all trains for a given FCPD/degree of fouling. For the third and fourth cycles, the resistance of UV biofilm seemed to be increased, even though that seemed to be the caused by a rather worse cleanability in the CIP between cycles 2 and 3 (can be also seen in the resistance graphs in Figure 8-10). It is interesting to note whereas the resistance in biofilm increased in the first cycle, it stayed rather constant over FCPD for the following cycles. This phenomenon could be similarly seen in the laboratory experiments (Figure 7-5).
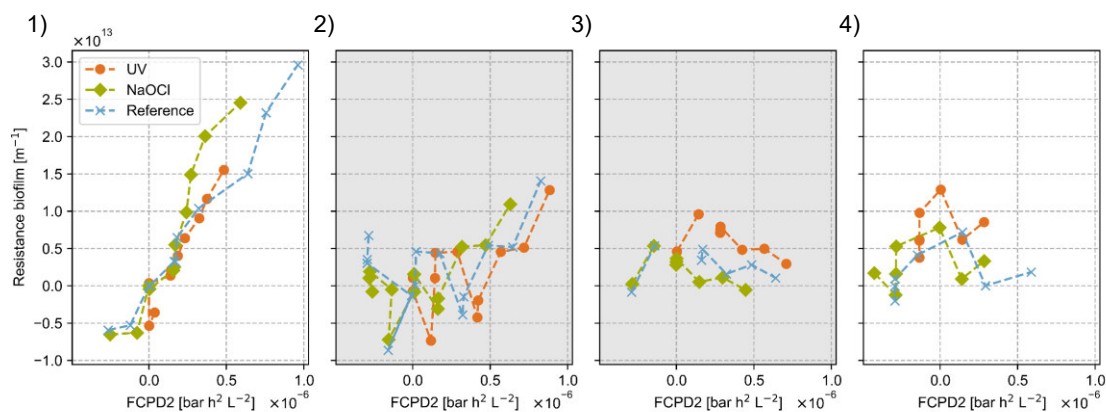
Figure 9-2:   Feed channel pressure drop (FCPD) increase divided by the squared feed flow - FCPD2 plotted against the biofilm resistance. The grey background color indicates pulsed UV irradiation.

The fluence rate in the membrane system was estimated with 0.91 mW cm^{-2}, excluding divergence, absorbance or reflectance effects, but might be lower in reality. At the utilized flow, this might result in 4.7 mJ cm^{-2}. Nevertheless, with the measured absorption coefficient of 0.066 cm^{-1} at 275 nm, with an assumed path length of approximately 3.6 cm (assumed distance between silica glass and pressure vessel wall),

the water factor would be equal to 0.77. Assuming the light diverges equally from the estimated surface area of the silica glass (131 cm^2) to the wall of the pressure vessel, including the PTFE (543 cm^2) fluence at the pressure vessel wall would be reduced by a factor of approximately 543/131 ≈ 4.1. After a distance of 1.82 cm, being approximately in the middle between silica glass and pressure vessel wall, due to divergence, the fluence rate might be reduced by a factor of 337/131 ≈ 2.6. Hence, following this very simplified estimation, the fluence in the reactor might only be around 1.4 mJ cm^{-2}. As during pulsed mode fluence rate was not increased, fluence might actually be only 0.7 mJ cm^{-2} (50% duty cycle). Even though this fluence estimation is very simplified, the effects of UV, delaying the biofilm formation at such small fluence looks promising.

In order to calculate the OPEX of the pilot-scale experiments, equations analogous to Chapter 7.3.7 were used. Thereby one modification was done according to equation (9-6). FCPD$_{initial}$ was calculated as the average FCPD of all three lines on day 5 of cycle 1. Q is equal to 850 L h^{-1} as feed flow and FCPD2, as described in Chapter 8.2.4, is the FCPD divided by the squared feed flow and the value at day 5 being subtracted. Besides, in cycles 1 and 4, only data for the reference line was considered till the first value of FCPD exceeded the FCPD of the UV line at the end of the cycle. The permeability at each time point was calculated from the average resistance of the membranes at the start of cycle 1 (day 5) and the added biofilm resistance. The calculated FCPD and membrane permeability are shown in Figure 9-3. For estimating the delay due to UV pre-treatment or NaOCl dosing, values were interpolated to get the same calculated FCPD as the UV line before initiating the CIP. For the first cycle, UV showed a delay of 22.4%, whereas biocide dosing led to a delay of 18.6%. For cycle 4, both UV and NaOCl showed a delay of around 16.7%. Interestingly, the delay due to UV pre-treatment got lower over the cycles, but it was still present in the last cycle. Calculated OPEX for both cycles are summarized in Table 9-4 and Table 9-5. As it can be seen in the results for the first cycle, total OPEX reduced by UV treatment might account for approximately 8%. Converting this back to energy demand, this would allow 11.4 W power for UV disinfection or 13.4 Wh m^{-3} that may be used by UV in order to still save OPEX (only including energy, excluding, e.g., lamp replacements). The median energy demand for a conventional UV disinfection for 40 mJ cm^{-2} for a UVT around 80% at 254 nm is 34 Wh m^{-3} (Schmalwieser et al., 2017). Assuming this reduces linearly to the utilized fluence of 1.4 mJ cm^{-2}, this would equal approximately 1.2 Wh m^{-3}. Assuming the same effects for UV irradiation at 254 nm would occur, this could save OPEX expressed in Wh m^{-3} of around 12.2 Wh m^{-3}, equal to approximately 7%. For the fourth cycle, no OPEX savings due to UV could be observed, likely caused by the higher resistance of the fouling layer formed, but also the higher starting FCPD could have influenced the results.

$$FCPD\ [bar] = FCPD_{initial} + Q^2 \cdot FCPD2$$

(9-6)
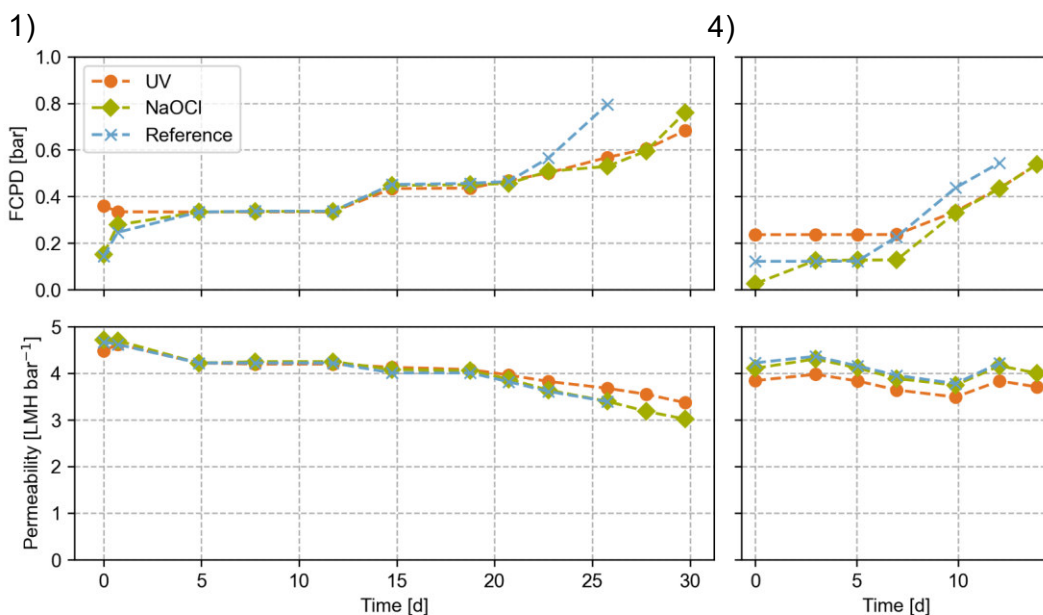
Figure 9-3: *Feed channel pressure drop (FCPD) calculated using equation (9-6) and permeability calculated using the biofilm and average membrane resistance for cycle 1 and 4.*

Table 9-4: *Estimated operational expenditures (OPEX) pilot-scale experiments, fist cycle, continuous UV pre-treatment, power describing the power demand of the pump.*

	Average Feed pressure [bar]	Power [W]	OPEX$_{FCPD\&Perm}$ [%]	OPEX$_{Total}$ [%]
UV	5.17	149	105	125
NaOCl	5.29	152	108	128
Reference	5.35	154	109	133
Without fouling	4.90	141	100	100

Table 9-5: *Estimated operational expenditures (OPEX) pilot-scale experiments, fourth cycle, continuous UV pre-treatment, power describing the power demand of the pump.*

	Average Feed pressure [bar]	Power [W]	OPEX$_{FCPD\&Perm}$ [%]	OPEX$_{Total}$ [%]
UV	5.48	158	112	117
NaOCl	5.07	146	103	109
Reference	5.02	145	102	108
Without fouling	4.90	141	100	100

Overall, the saved OPEX in the first cycle fit with the results observed in the laboratory experiments for the estimated fluence (Table 7-2). For the last run, no saved OPEX were seen, likely caused by the higher fouling layer resistance and FCPD[7]. However, the FCPD might only play a minor role as its contribution to the average feed pressure needed was calculated with 0.15 bar for the UV line and 0.12 bar for the reference. The effect of FCPD might be more pronounced for several elements in series. When looking at the development of resistance, it can be seen that the resistance after CIP after cycle 2 was only poorly restored and stayed rather high for the following cycles. This might be caused by the CIP procedure (acidic) which is not optimized for organic or biofouling (DuPont, 2022a). For organic and biofouling, alkaline CIP followed by acidic CIP is recommended (DuPont, 2022a). Perhaps with an enhanced CIP procedure, starting resistance and FCPD in cycle 4 might be lower, which could lead to OPEX savings still being present in the last cycle, as biofilm delay was still observed in the last cycle. In the laboratory experiments conducted in Chapter 7, when the resistance of the biofilm for UV was lower before the CIP, it was still lower after CIP. Nevertheless, due to different starting points of the resistance before the CIP a detailed comparison of biofilm resistance removal by CIP is difficult. In summary, for a final estimation of OPEX saved by UV pre-treatment, more repetitions would be needed with optimized CIPs. Besides, the effects of UV might get higher for a higher fluence. Fluence applied in the pilot-scale experiments was rather in the low range.

To compare the cost of conventional UV pre-treatment to the dosage of NaOCl, a cost of 159 € is assumed for 25 L[8] of 12% NaOCl (Carl Roth GmbH + Co. KG, n.d.). For a concentration of 0.1 ppm cost of chemicals would be around 0.005 € m^{-3}. In comparison, with an assumed energy cost of 0.32 € (kWh)$^{-1}$, this would result in less than 0.001 € m^{-3} for the UV pre-treatment. This comparison neglects investment costs, energy costs of dosing and other cost than energy for the UV disinfection (e.g., lamp replacement), but with comparable effects, UV pre-treatment might show lower OPEX than dosing of NaOCl. Overall, this stresses the potential of UV pre-treatment as an environmentally friendly pre-treatment technology. Besides, in comparison to biocide dosing, UV pre-treatment likely extends membrane live time through delayed biofouling and has no adverse effects on the membrane itself like NaOCl potentially has.

In conclusion, the delay of biofouling seems to transfer to pilot-scale applications for real feed waters. On the contrary, no change in biofilm resistance was observed for biofilms formed under UV irradiation. The resistance of the biofilm was likely less efficiently reduced during the last two CIPs for the UV line. This might be caused by either a less cleanable biofilm or the CIP procedure using acid is not optimal

---

[7] Costs of fouling in cycle 4 were also estimated to be low, limiting potential OPEX savings in general.

[8] Please note that the price is just a guess and might change, especially if bigger volumes are purchased.

for the biofilm. Nevertheless, the effect of delaying biofouling was still present after several cleaning cycles. Therefore, **hypothesis 6,** "*In situ UVC treatment of the feed stream in the pressure vessel of RO membrane systems is reducing the impacts of long-term biofouling under real conditions*", **is partially accepted**. Delay was retained after CIP, whereas especially the behavior of the biofilm resistance remains unclear and needs further evaluation. Overall, this is in accordance with other studies (Harif et al., 2011; Marconnet et al., 2011), which reported positive effects of UV pre-treatment on biofouling control in up-scaled applications for a single cycle.

Hypothesis 6	(✓) **Partially accepted**

Even though the *in situ* integration of UV-LEDs in the pressure vessel of RO systems showed promising results, considering the effort of such an integration, the approach is questionable. Overall, it is not clear what benefits an *in situ* integration has compared to a simple UV reactor before the entrance into the membrane pressure vessel. One possible benefit is that a biofilm formed for the UV treatment in the pipes might take up some nutrients (9.4.1), but this hypothesis needs further validation. It is probably limited to low nutrient conditions and might appear with a normal UV reactor as well, even though likely to a lesser extent. It is not clear how long the effect of UV disinfection holds, but if the distance between the UV reactor and the membrane system is kept short, HRT between the UV reactor and the membrane system might account for only a couple of seconds. Within this HRT it is assumed that the effects of UV are still present, but it is proposed for future research to investigate this, e.g., by inserting differently sized pipes between the UV treatment and the membrane module. Actually, placing a UV reactor before the high pressure pumps of the RO system would have the advantage of the LED system not needing to withstand high-pressures (especially for seawater desalination systems). When pressure is no problem, the UV reactor could be placed on different positions, e.g., recycling streams, as shown in Figure 2-5, even though the effects of such a position are not clear. The efficiency of LEDs is currently still limited, but in general, research using LEDs is promising, especially when considering the potential increase of LED efficiency in the future and considering that LEDs are free of mercury (Würtele et al., 2011). Another possible advantage of UV-LEDs could be that the heat is transferred to the backside of the LEDs, whereas for conventional lamps, it is transferred to the water. Nevertheless, assuming an energy demand of 34 Wh m^{-3} for a 80% UVT water (Schmalwieser et al., 2017) that gets 100% transferred to the water would still not result in any considerable warm-up of the water. To increase the fluence in an *in situ* integrated system, higher power output LEDs could be used. Currently, there are LEDs available with 100 mW (Laser Components GmbH, 2019a) for a single LED which would equal to almost the complete power of all 28 LEDs used in the current system. Still, with the currently limited efficiency of LEDs, a lot of energy will be dissipated as heat. This heat has to be diverted away from the LEDs, probably making higher power *in situ* systems more challenging. Here, pulsed operation could be interesting again. A great advantage that LEDs already have is their

applications in, for instance, point-of-use systems, as they can be switched on when needed and immediately disinfect the water, whereas this is not possible with conventional lamps (Chatterley and Linden, 2010). Hence, the combination of UV-LEDs with point-of-use or point-of-entry sized membrane modules could have a great potential. As LEDs can be turned on and off very quickly, their application might reduce biofouling, especially if water is stagnant for a certain time in the membrane modules.

10. Overall conclusion and outlook

Within the first part of this dissertation, the effects of UV disinfection using LEDs were validated (Chapter 4). It could be shown that already a low fluence has great impacts on the formation of biofilms. Not only was the biofilm formation delayed, but also the composition of the formed biofilms differed at the same degree of biofouling. This might likely be caused by changes in the microbial community, but also other effects might play a role.

Besides, it was recognized that quantifying the fluence in complex reactor geometries is challenging and biodosimetry might not always be practicable. Therefore, in Chapter 5, a new actinometric method was developed under controlled conditions and validated using MS2 phage. In Chapter 7, the method was adapted for a flow-through reactor to quantify the fluence rate in continuous and pulsed UV irradiation settings without potential biological effects. The proposed method was further validated in an additional study (Chapter 12.8) by using an optical model coupled with computational fluid dynamics. Thereby the model could be validated using the performed biodosimetry experiments. A comparison of the average fluence rate in the reactor with the results from actinometry does look promising. The actinometric method has a variety of possible applications, from validating non-standard laboratory setups (with or without reflections and non-parallel light beams) or reactor models, UV quantification for a combination of treatments, fluence estimation for UV based AOPs or qualitatively evaluating reactor design by a comparison with biodosimetry and calculating the mixing efficiency. The method might be used for fluence calculation, incorporating changes in the fluence rate by reflective reactor housings (as perquisite for the new DIN 19294-1:2020-08 (DIN e.V., 2020)). Nevertheless, this needs further investigation.

After developing a reliable biodosimetry procedure for the (challenging) biofilm forming *A. citratiphilum* (Chapter 6), pulsed and continuous irradiation were checked for enhanced disinfection performance for bacteria, while keeping the overall fluence equal, but increasing the fluence rate during the pulses (Chapter 7). No enhanced effects could be proven, but when applying the pulsed UV disinfection for biofouling control experiments, a higher delay for the biofilm formation was observed. This was explained as the light during the pulses with higher fluence rate might penetrate further into cell aggregates and hence leads to a more efficient disinfection. Nevertheless, this could not be proven and should be tested in further studies.

Overall, pulsed disinfection showed no increased OPEX savings in biofouling experiments compared to continuous irradiation (Chapter 7). In addition, when comparing the electrical efficiency between pulsed and continuous irradiation, no benefits from pulsed irradiation were seen in the used setting (Chapters 0, 9.4 and 12.9). Perhaps the LED cooling was efficient enough, so a potential better thermal management of LEDs as reported before (Nyangaresi et al., 2019; Song et al., 2018) could not be seen as all heat got dissipated. An alternative explanation would be that

the better thermal management did not influence the light generation efficiency considerably.

A general trend for increased OPEX savings with applied fluence could be confirmed (Chapter 7). Besides, especially for seawater desalination, the OPEX caused by UV disinfection might only account for a small percentage of the cost of the desalination itself. The cleanability of biofilms seemed not to be impacted by the UV pre-treatment as it was investigated in laboratory CIP experiments and comparing the restored FCPD.

In lab-scale experiments using feed water without the addition of nutrients (Chapter 8.1), biofouling seemed to be avoided by the UV pre-treatment even though quantification of the effects was not possible as no biofouling occurred after turning the irradiation off. This might be caused by a biofilm that formed before the UV reactor removing the already low amount of nutrients. Nevertheless, this could not be proven and needs further examination.

During pilot-scale experiments, *in situ* UV disinfection successfully delayed the biofilm formation (Chapter 8.2). Whereas the effects for biofouling delay got weaker in the last experimental cycle, around 7% OPEX were calculated to be saved by UV treatment at low fluence in the first cycle. With higher fluence, the positive effects are expected to rise and should be investigated during additional experiments. In the pilot-scale experiments, the resistance of the fouling layer for the UV train could not be restored as well as for the other trains, and hence comparing the last cycle of pilot operation did not lead to saved OPEX in the performed calculations and assumptions. Nevertheless, switching the CIP for enhanced biofilm removal could change this (e.g., using caustic cleaning as applied in Chapter 7).

The application of an *in situ* integration of the UV disinfection into the pressure vessel of membrane systems was not assumed to show other benefits than simply positioning a UV reactor in close vicinity of the membrane systems. However, for future studies, it would be interesting to compare different positions directly. The usage of UV-LEDs as biofouling control might be promising for point-of-use or point-of-entry applications, but in the current state, LEDs might not be comparable to conventional systems regarding OPEX. Nevertheless, this might change in the future due to the development of more efficient LEDs and therefore research to gain more experience with LEDs in general is encouraged and necessary.

Within this dissertation, two of the derived hypotheses were accepted, two were rejected, and two were partially accepted as effects did only partially occur or more research is needed. A summary of the hypotheses with the key points leading to their acceptance or rejection are summarized in Figure 10-1.

Hypothesis	Key observations
Hypothesis 1: UV treatment using UVC-LEDs with a fluence **lower** than **10 mJ cm⁻²** is capable of **delaying** severe biofouling (FCPD of 67 mbar cm⁻¹) of RO membranes by **more** than **10%**.	✓ **Less** than **10 mJ cm⁻²** ✓ **More** than **10% delay** **✓ Accepted**
Hypothesis 2: Due to a change of the microbial community structure, UV treatment using UVC-LEDs with a fluence **lower** than **10 mJ cm⁻²** is resulting in **15% less** hydraulic biofilm **resistance** at a severe biofouling state.	✓ **Less** than **10 mJ cm⁻²** ✓ **15% less hydraulic resistance** ✓ **Changed microbial community** ▪ Other effects also possible **(✓) Partially accepted**
Hypothesis 3: The **ratio** of **fluence rate** determined with **uridine** and **KI/KIO₃ actinometry** can be used to **quantitatively** characterize the **reflection** in UV reactors.	✓ **Irradiance** quantified with **KI/KIO₃** ✓ **Fluence rate** quantified with **uridine** ✓ **Reflections** correlate to **ratio fluence rate to irradiance** **✓ Accepted**
Hypothesis 4: With **raising fluence rates** (in the range of **~1 – 100 mW cm⁻²**), the disinfection efficiency of pulsed UVC-LEDs is increasing significantly by **more** than **30%** for **bacteria**.	▪ Fluence rate in peaks increased from **29** to **141 mW cm⁻²** ▪ **Same disinfection** of MS2 **virus** ✓ Fluence rate in peaks increased from **2** to **141 mW cm⁻²** ▪ **Same disinfection** for the tested **bacterium** **✕ Rejected**
Hypothesis 5: Applying pulsed UVC-irradiation as an operational strategy for biofouling control leads to **30% higher energy efficiency** compared to continuous irradiation**.**	▪ **No** significant **difference total OPEX** ▪ **No** significant **difference** based on the **power demand** in the **used setting** ✓ **Effects** likely **not seen due** to efficient **heat dissipation** **✕ Rejected**
Hypothesis 6: *In situ* **UVC treatment** of the feed stream in the pressure vessel of RO membrane systems **is reducing the impacts of long-term biofouling** under **real conditions.**	✓ **Delay** still visible **after multiple CIP cycles** ▪ **No reduced hydraulic resistance** of the biofilm over the experimental cycles ▪ **Cleanability** of the biofilm? ✓ **Saving of OPEX** in the **first** filtration **cycle comparable** **(✓) Partially accepted**

Figure 10-1:   Overview of the research hypotheses with the key observations leading to their acceptance or rejection.

Biofouling cannot be completely avoided by using UV pre-treatment, but it might be combined with other technologies. As described by Vrouwenvelder et al. (2010c) and Flemming (2020), the combination of several approaches might enhance effects as an integrated and holistic approach for biofouling control. In future studies, it should be investigated if the combination of for instance, nutrient removal by biological treatment or flocculation with UV disinfection might show symbiotic effects. A combination of reduced nutrients, e.g., biological pre-treatment or phosphorus removal (Griebe and Flemming, 1998; Vrouwenvelder et al., 2010c; Vrouwenvelder et al., 2010a) and controlled active biomass in the feed by the UV pre-treatment might effectively tackle biofouling. Besides, the utilization of membranes and spacers with low fouling properties, like Yang et al. (2009), would add an additional approach reducing the fouling caused by microorganisms that passed the UV pre-treatment. Next, the combination with easy to clean membranes, like applied by Son et al. (2018) or enhanced cleaning protocols as used by Sanawar et al. (2021) with early warning systems (Vrouwenvelder et al., 2010c) might be essential. When the formed biofilm is (more or less) completely removed from the membrane, followed by, e.g., a sanitizing CIP, the full potential of UV disinfection in the next filtration cycle might be seen. Other measures for biofouling control like UF (Vrouwenvelder et al., 2009d), applying more lead modules in parallel or feed flow reversal (Vrouwenvelder et al., 2010c) can be easily combined with UV pre-treatment, too. Aside from other approaches described by Vrouwenvelder et al. (2010c) or Desmond et al. (2022), in the future, UV pre-treatment might represent an additional tool for biofilm morphology engineering and reducing the negative impacts of formed biofilms.

To conclude, citing Hans-Curt Flemming (2020), biofilms are the oldest and most successful form of life and hence a simple and sustainable way to completely avoid them is unrealistic. Instead, we should rather learn to live with them as "teeth cannot be cleaned once and forever" (Flemming, 2020). "The key in anti-fouling strategies is only to extend the time until the organism wins" (Flemming, 2020).

Within this dissertation, the potentials of using UV irradiation as pre-treatment for biofouling control were investigated. For this application, not necessarily LEDs need to be used, but also conventional UV reactors might be employed. As UV reactors are a mature technology, I hope that I was able to elucidate the great potential for UV pre-treatment. Considering its great potentials, UV as a pre-treatment in membrane filtrations systems seems to be a rarely used and still an underrated technology. It might be readily applied and represents an easy solution for retrofitting existing plants suffering from biofouling. Using UV hopefully can save costs, energy, as well as chemicals for CIP procedures. It might be applied in combination with existing technologies to access challenging water resources more economically. Overall, it is contributing to a more sustainable water supply in a world where water stress is expected to rise.

11. References

Ajon, M., Fröls, S., van Wolferen, M., Stoecker, K., Teichmann, D., Driessen, A.J.M., Grogan, D.W., Albers, S.-V., Schleper, C., 2011. UV-inducible DNA exchange in hyperthermophilic archaea mediated by type IV pili. Molecular Microbiology 82 (4), 807–817. doi:10.1111/j.1365-2958.2011.07861.x.

Al-Amoudi, A., Lovitt, R.W., 2007. Fouling strategies and the cleaning system of NF membranes and factors affecting cleaning efficiency. Journal of Membrane Science 303 (1-2), 4–28. doi:10.1016/j.memsci.2007.06.002.

Allan, R.P., Barlow, M., Byrne, M.P., Cherchi, A., Douville, H., Fowler, H.J., Gan, T.Y., Pendergrass, A.G., Rosenfeld, D., Swann, A.L.S., Wilcox, L.J., Zolina, O., 2020. Advances in understanding large-scale responses of the water cycle to climate change. Ann. N.Y. Acad. Sci. 1472 (1), 49–75. doi:10.1111/nyas.14337.

Altschul, S.F., Gish, W., Miller, W., Myers, E.W., Lipman, D.J., 1990. Basic local alignment search tool. Journal of Molecular Biology 215 (3), 403–410. doi:10.1016/S0022-2836(05)80360-2.

Anderson, M.J., 2001. A new method for non-parametric multivariate analysis of variance. Austral Ecology 26 (1), 32–46. doi:10.1111/j.1442-9993.2001.01070.pp.x.

Appelmann, P., 2022. Methods for Correcting Inner Filter Effects Occurring when Measuring ATP Using a Bioluminescence Luciferase Assay. Study Project, Munich, Germany.

AquiSense Technologies, 2022. PearlAqua Micro Operations Manual, Erlanger, USA.

Ayache, C., Manes, C., Pidou, M., Croué, J.P., Gernjak, W., 2013. Microbial community analysis of fouled reverse osmosis membranes used in water recycling. Water Research 47 (10), 3291–3299. doi:10.1016/j.watres.2013.03.006.

Azimi, Y., Liu, Y., Tan, T.C., Allen, D.G., Farnood, R.R., 2017. The tail of two models: Impact of circularity and biomass non-homogeneity on UV disinfection of wastewater flocs. Water Research 126, 70–78. doi:10.1016/j.watres.2017.09.011.

Baghoth, S.A., Sharma, S.K., Amy, G.L., 2011. Tracking natural organic matter (NOM) in a drinking water treatment plant using fluorescence excitation-emission matrices and PARAFAC. Water Research 45 (2), 797–809. doi:10.1016/j.watres.2010.09.005.

Baker, J.S., Dudley, L.Y., 1998. Biofouling in membrane systems — A review. Desalination 118 (1-3), 81–89. doi:10.1016/S0011-9164(98)00091-5.

Beck, S.E., Wright, H.B., Hargy, T.M., Larason, T.C., Linden, K.G., 2015. Action spectra for validation of pathogen disinfection in medium-pressure ultraviolet (UV) systems. Water Research 70, 27–37. doi:10.1016/j.watres.2014.11.028.

Bel -Bel Composite Iberica S.L., 2020. Pressure vessels 8'' side port: Technical manual, Rev.6, Murcia, Spain. https://www.belvessels.com/sites/default/files/products_files/BEL8%27%27%20S.P.%20%26%20M.P.%20-%20TECHNICAL%20MANUAL%20-%20ENGLISH%20-%20rev%206.pdf (accessed 13.11.2022).

Bellona, C., Drewes, J.E., Xu, P., Amy, G., 2004. Factors affecting the rejection of organic solutes during NF/RO treatment--a literature review. Water Research 38 (12), 2795–2809. doi:10.1016/j.watres.2004.03.034.

Benjamini, Y., Hochberg, Y., 1995. Controlling the False Discovery Rate: A Practical and Powerful Approach to Multiple Testing. Journal of the Royal Statistical Society: Series B (Methodological) 57 (1), 289–300. doi:10.1111/j.2517-6161.1995.tb02031.x.

Bereschenko, L.A., Heilig, G.H.J., Nederlof, M.M., van Loosdrecht, M.C.M., Stams, A.J.M., Euverink, G.J.W., 2008. Molecular characterization of the bacterial communities in the different compartments of a full-scale reverse-osmosis water purification plant. Applied and Environmental Microbiology 74 (17), 5297–5304. doi:10.1128/AEM.00387-08.

Bereschenko, L.A., Prummel, H., Euverink, G.J.W., Stams, A.J.M., van Loosdrecht, M.C.M., 2011. Effect of conventional chemical treatment on the microbial population in a biofouling layer of reverse osmosis systems. Water Research 45 (2), 405–416. doi:10.1016/j.watres.2010.07.058.

Bereschenko, L.A., Stams, A.J.M., Euverink, G.J.W., van Loosdrecht, M.C.M., 2010. Biofilm formation on reverse osmosis membranes is initiated and dominated by Sphingomonas spp. Applied and Environmental Microbiology 76 (8), 2623–2632. doi:10.1128/AEM.01998-09.

Berghof Fluoroplastic Technology GmbH, n. d. Optopolymer®: The reference for light, Eningen, Germany. https://www.berghof-fluoroplastics.com/fileadmin/redaktion-bft/Downloads/03_Optisches_PTFE_-_Optopolymer_R_/BFT_Optopolymer_EN.pdf (accessed 6th June 2022).

Berney, M., Weilenmann, H.-U., Egli, T., 2006. Flow-cytometric study of vital cellular functions in Escherichia coli during solar disinfection (SODIS). Microbiology (Reading, England) 152 (Pt 6), 1719–1729. doi:10.1099/mic.0.28617-0.

Bhattacharjee, A.S., Choi, J., Motlagh, A.M., Mukherji, S.T., Goel, R., 2015. Bacteriophage therapy for membrane biofouling in membrane bioreactors and antibiotic-resistant bacterial biofilms. Biotechnology and bioengineering 112 (8), 1644–1654. doi:10.1002/bit.25574.

Bhattacharyya, D., Williams, M.E., 1992. Theory, in: Ho, W.S.W., Sirkar, K.K. (Eds.), Membrane Handbook. Springer US, Boston, MA, pp. 269–280.

Bhattacharyya, D., Williams, M.E., Ray, R.J., McCray, S.B., 1992. Design, in: Ho, W.S.W., Sirkar, K.K. (Eds.), Membrane Handbook. Springer US, Boston, MA, pp. 281–311.

Bierkens, M.F.P., Wada, Y., 2019. Non-renewable groundwater use and groundwater depletion: a review. Environ. Res. Lett. 14 (6), 63002. doi:10.1088/1748-9326/ab1a5f.

Blatchley, E.R., Shen, C., Naunovic, Z., Lin, L.-S., Lyn, D.A., Robinson, J.P., Ragheb, K., Grégori, G., Bergstrom, D.E., Fang, S., Guan, Y., Jennings, K., Gunaratna, N., 2006. Dyed Microspheres for Quantification of UV Dose Distributions:

Photochemical Reactor Characterization by Lagrangian Actinometry. J. Environ. Eng. 132 (11), 1390–1403. doi:10.1061/(ASCE)0733-9372(2006)132:11(1390).

Blatchley, E.R., Shen, C., Scheible, O.K., Robinson, J.P., Ragheb, K., Bergstrom, D.E., Rokjer, D., 2008. Validation of large-scale, monochromatic UV disinfection systems for drinking water using dyed microspheres. Water Research 42 (3), 677–688. doi:10.1016/j.watres.2007.08.019.

Bohrerova, Z., Shemer, H., Lantis, R., Impellitteri, C.A., Linden, K.G., 2008. Comparative disinfection efficiency of pulsed and continuous-wave UV irradiation technologies. Water Research 42 (12), 2975–2982. doi:10.1016/j.watres.2008.04.001.

Bolb Inc., 2021. High Power UV-C LED: SMD Modules and Arrays V1.7, Livermore, United States. https://bolb.co/wp-content/uploads/2021/08/BOLB-UVC-SMD-Modules-and-Arrays-V-1.7-March-2021.pdf.

Bolb Inc. -Blanc, Paul, 2023. E-Mail.

Bolton, J., 2000. Calculation of ultraviolet fluence rate distributions in an annular reactor: significance of refraction and reflection. Water Research 34 (13), 3315–3324. doi:10.1016/S0043-1354(00)00087-7.

Bolton, J.R., Beck, S., Linden, K.G., 2015. Protocol for the determination of fluence (UV dose) using a low-pressure or low-pressure high-output UV lamp in benchscale collimated beam ultraviolet experiments. International Ultraviolet Association (IUVA) (accessed 3.03.2023). https://iuva.org/resources/Resource%20Documents/Bolton-Protocol%20for%20the%20Determination%20of%20Fluence.pdf.

Bolton, J.R., Cotton, C.A., 2022. Ultraviolet disinfection handbook, Second edition ed. American Water Works Association, Denver, CO.

Bolton, J.R., Linden, K.G., 2003. Standardization of Methods for Fluence (UV Dose) Determination in Bench-Scale UV Experiments. J. Environ. Eng. 129 (3), 209–215. doi:10.1061/(ASCE)0733-9372(2003)129:3(209).

Bolton, J.R., Stefan, M.I., 2002. Fundamental photochemical approach to the concepts of fluence (UV dose) and electrical energy efficiency in photochemical degradation reactions. Res. Chem. Intermed. 28 (7-9), 857–870. doi:10.1163/15685670260469474.

Bolton, J.R., Stefan, M.I., Shaw, P.-S., Lykke, K.R., 2011. Determination of the quantum yields of the potassium ferrioxalate and potassium iodide–iodate actinometers and a method for the calibration of radiometer detectors. Journal of Photochemistry and Photobiology A: Chemistry 222 (1), 166–169. doi:10.1016/j.jphotochem.2011.05.017.

Bosshard, F., Bucheli, M., Meur, Y., Egli, T., 2010a. The respiratory chain is the cell's Achilles' heel during UVA inactivation in Escherichia coli. Microbiology (Reading, England) 156 (Pt 7), 2006–2015. doi:10.1099/mic.0.038471-0.

Bosshard, F., Riedel, K., Schneider, T., Geiser, C., Bucheli, M., Egli, T., 2010b. Protein oxidation and aggregation in UVA-irradiated Escherichia coli cells as signs of accelerated cellular senescence. Environmental Microbiology 12 (11), 2931–2945. doi:10.1111/j.1462-2920.2010.02268.x.

Boulos, L., Prévost, M., Barbeau, B., Coallier, J., Desjardins, R., 1999. LIVE/DEAD® BacLight™: application of a new rapid staining method for direct enumeration of viable and total bacteria in drinking water. Journal of Microbiological Methods 37 (1), 77–86. doi:10.1016/s0167-7012(99)00048-2.

Braslavsky, S.E., 2007. Glossary of terms used in photochemistry, 3rd edition (IUPAC Recommendations 2006). Pure and Applied Chemistry 79 (3), 293–465. doi:10.1351/pac200779030293.

Braun, J., 2022. Eine Literaturstudie zu den Effekten von ultravioletter Strahlung auf Mikroorganismen mit Fokus auf Inaktivierungs- und Reparaturmechanismen für LED spezifische Anwendungen. Bachelor's Thesis, Munich, Germany.

Bro, R., Kiers, H.A.L., 2003. A new efficient method for determining the number of components in PARAFAC models. J. Chemometrics 17 (5), 274–286. doi:10.1002/cem.801.

Bucheli-Witschel, M., Bassin, C., Egli, T., 2010. UV-C inactivation in Escherichia coli is affected by growth conditions preceding irradiation, in particular by the specific growth rate. Journal of Applied Microbiology 109 (5), 1733–1744. doi:10.1111/j.1365-2672.2010.04802.x.

Bucs, S.S., Farhat, N., Kruithof, J.C., Picioreanu, C., van Loosdrecht, M.C., Vrouwenvelder, J.S., 2018. Review on strategies for biofouling mitigation in spiral wound membrane systems. Desalination 434, 189–197. doi:10.1016/j.desal.2018.01.023.

Bucs, S.S., Valladares Linares, R., van Loosdrecht, M.C.M., Kruithof, J.C., Vrouwenvelder, J.S., 2014. Impact of organic nutrient load on biomass accumulation, feed channel pressure drop increase and permeate flux decline in membrane systems. Water Research 67, 227–242. doi:10.1016/j.watres.2014.09.005.

Callahan, B.J., McMurdie, P.J., Rosen, M.J., Han, A.W., Johnson, A.J.A., Holmes, S.P., 2016. DADA2: High-resolution sample inference from Illumina amplicon data. Nature Methods 13 (7), 581–583. doi:10.1038/nmeth.3869.

Carl Roth GmbH + Co. KG, n.d. Natriumhypochloritlösung, 25 l. Carl Roth GmbH + Co. KG (accessed 9.06.2023). https://www.carlroth.com/de/de/flaechen-desinfektionsmittel/natriumhypochloritloesung/p/0078.4.

Chae, H.-R., Lee, J., Lee, C.-H., Kim, I.-C., Park, P.-K., 2015. Graphene oxide-embedded thin-film composite reverse osmosis membrane with high flux, anti-biofouling, and chlorine resistance. Journal of Membrane Science 483, 128–135. doi:10.1016/j.memsci.2015.02.045.

Characklis, W.G., Marshall, K.C. (Eds.), 1990. Biofilms. Wiley series in ecological and applied microbiology. John Wiley & Sons, New York, New York, USA.

Chatterjee, N., Walker, G.C., 2017. Mechanisms of DNA damage, repair, and mutagenesis. Environmental and Molecular Mutagenesis 58 (5), 235–263. doi:10.1002/em.22087.

Chatterley, C., Linden, K., 2010. Demonstration and evaluation of germicidal UV-LEDs for point-of-use water disinfection. Journal of Water and Health 8 (3), 479–486. doi:10.2166/wh.2010.124.

Chen, J., Loeb, S., Kim, J.-H., 2017. LED revolution: fundamentals and prospects for UV disinfection applications. Environ. Sci.: Water Res. Technol. 3 (2), 188–202. doi:10.1039/c6ew00241b.

Chen, J.P., Mou, H., Wang, L.K., Matsuura, T., 2006. Membrane Filtration, in: Wang, L.K., Hung, Y.-T., Shammas, N.K. (Eds.), Advanced Physicochemical Treatment Processes. Humana Press, Totowa, NJ, pp. 203–259.

Chong, T.H., Fane, A.G., 2021. Nanofiltration Module Design and Operation, in: Schäfer, A.I., Fane, A.G. (Eds.), Nanofiltration. Principles, Applications, and New Materials, 2nd ed. ed. John Wiley & Sons, Incorporated, Newark.

Coble, P.G., 1996. Characterization of marine and terrestrial DOM in seawater using excitation-emission matrix spectroscopy. Marine Chemistry 51 (4), 325–346. doi:10.1016/0304-4203(95)00062-3.

CodeLine -CodeLine Division Pentair Water India Pvt. Ltd., 2009. User Guide 80A Series: Side Ported Pressure Vessels. https://codeline.pentair.com/~/media/websites/codeline/downloads/user%20guid es/codeline%20user%20guide%2080a%20series.pdf (accessed 13.11.2022).

Compound Semiconductor Magazine, 2012. SETi Breaks Barriers With UV-C LED Efficiencies Of Over 10%. Compound Semiconductor Magazine (accessed 22.01.2023). https://compoundsemiconductor.net/article/89383/SETi_breaks_barriers_with_UV-C_LED_efficiencies_of_over_10_.

Compound Semiconductor Magazine, 2018. Bolb Announces Single Chip UVC LED Breakthrough. Compound Semiconductor Magazine (accessed 22.01.2023). https://compoundsemiconductor.net/article/104558/Bolb_Announces_Single_Chip _UVC_LED_Breakthrough%7BfeatureExtra%7D.

COMSOL Support -Andersson, Linus, 2022. Mesh volume in state variable. Comsol support case 5561161.

Côté, P., Liu, M., Siverns, S., 2008. Water Reclamation and Desalination by Membranes, in: Li, N.N., Fane, A.G., Ho, W.S.W., Matsuura, T. (Eds.), Advanced Membrane Technology and Applications. John Wiley & Sons, Inc, Hoboken, NJ, USA, pp. 171–188.

Côté, P., Siverns, S., Monti, S., 2005. Comparison of Membrane-based Solutions for Water Reclamation and Desalination. Desalination 182 (1-3), 251–257. doi:10.1016/j.desal.2005.04.015.

Cover, W.H., Holloway, J.M., Xue, H., Busby, T.F., 2001. Inactivation of lipid enveloped and non-enveloped viruses in human plasma proteins with broad spectrum pulsed light: Plasma Product Biotechnology Meeting, 42–45.

Curtin, A.M., Thibodeau, M.C., Buckley, H.L., 2020. The Best-Practice Organism for Single-Species Studies of Antimicrobial Efficacy against Biofilms Is Pseudomonas aeruginosa. Membranes 10 (9). doi:10.3390/membranes10090211.

d'Angelo-Picard, C., Faure, D., Penot, I., Dessaux, Y., 2005. Diversity of N-acyl homoserine lactone-producing and -degrading bacteria in soil and tobacco rhizosphere. Environmental Science & Technology 7 (11), 1796–1808. doi:10.1111/j.1462-2920.2005.00886.x.

Darre, N.C., Toor, G.S., 2018. Desalination of Water: a Review. Curr Pollution Rep 4 (2), 104–111. doi:10.1007/s40726-018-0085-9.

Davies, D.G., Parsek, M.R., Pearson, J.P., Iglewski, B.H., Costerton, J.W., Greenberg, E.P., 1998. The involvement of cell-to-cell signals in the development of a bacterial biofilm. Science 280 (5361), 295–298. doi:10.1126/science.280.5361.295.

de Vries, H.J., Stams, A.J.M., Plugge, C.M., 2020. Biodiversity and ecology of microorganisms in high pressure membrane filtration systems. Water Research 172, 115511. doi:10.1016/j.watres.2020.115511.

Desmond, P., Best, J.P., Morgenroth, E., Derlon, N., 2018. Linking composition of extracellular polymeric substances (EPS) to the physical structure and hydraulic resistance of membrane biofilms. Water Research 132, 211–221. doi:10.1016/j.watres.2017.12.058.

Desmond, P., Huisman, K.T., Sanawar, H., Farhat, N.M., Traber, J., Fridjonsson, E.O., Johns, M.L., Flemming, H.-C., Picioreanu, C., Vrouwenvelder, J.S., 2022. Controlling the hydraulic resistance of membrane biofilms by engineering biofilm physical structure. Water Research 210, 118031. doi:10.1016/j.watres.2021.118031.

DIN e.V. -Deutsches Institut für Normung e.V. DIN 38405-9:2011-09, Deutsche Einheitsverfahren zur Wasser-, Abwasser- und Schlammuntersuchung_- Anionen (Gruppe_D)_- Teil_9: Photometrische Bestimmung von Nitrat_(D_9). Beuth Verlag GmbH, Berlin. doi:10.31030/1812578. 2011.

DIN e.V. -Deutsches Institut für Normung e.V. DIN 38406-6:1998-07, Deutsche Einheitsverfahren zur Wasser-, Abwasser- und Schlammuntersuchung_- Kationen (Gruppe_E)_- Teil_6: Bestimmung von Blei mittels Atomabsorptionsspektrometrie (AAS) (E_6). Beuth Verlag GmbH, Berlin. doi:10.31030/7500183. 1998.

DIN e.V. -Deutsches Institut für Normung e.V. DIN EN 1484:2019-04, Wasseranalytik_- Anleitungen zur Bestimmung des gesamten organischen Kohlenstoffs_(TOC) und des gelösten organischen Kohlenstoffs_(DOC); Deutsche Fassung EN_1484:1997. Beuth Verlag GmbH, Berlin. doi:10.31030/3042067. 2019.

DIN e.V. -Deutsches Institut für Normung e.V. DIN EN ISO 10304-1:2009-07, Wasserbeschaffenheit_- Bestimmung von gelösten Anionen mittels Flüssigkeits-Ionenchromatographie_- Teil_1: Bestimmung von Bromid, Chlorid, Fluorid, Nitrat, Nitrit, Phosphat und Sulfat (ISO_10304-1:2007); Deutsche Fassung EN_ISO_10304-1:2009. Beuth Verlag GmbH, Berlin. doi:10.31030/1518948. 2009.

DIN e.V. -Deutsches Institut für Normung e.V. DIN EN ISO 6878:2004-09, Wasserbeschaffenheit_- Bestimmung von Phosphor_- Photometrisches Verfahren

mittels Ammoniummolybdat (ISO_6878:2004); Deutsche Fassung EN_ISO_6878:2004. Beuth Verlag GmbH, Berlin. doi:10.31030/9552789. 2004.

DIN e.V. -Deutsches Institut für Normung e.V. DIN EN ISO 7980:2000-07, Wasserbeschaffenheit_- Bestimmung von Calcium und Magnesium_- Verfahren mittels Atomabsorptionsspektrometrie (ISO_7980:1986); Deutsche Fassung EN_ISO_7980:2000. Beuth Verlag GmbH, Berlin. doi:10.31030/8946736. 2000.

DIN e.V. -Deutsches Institut für Normung e.V., 2020. DIN 19294-1:2020-08, Geräte zur Desinfektion von Wasser mittels Ultraviolettstrahlung_- Teil_1: Geräte mit UV-Niederdrucklampen_- Anforderungen und Prüfung. Beuth Verlag GmbH, Berlin. doi:10.31030/3146809.

Dolnicar, S., Schäfer, A.I., 2009. Desalinated versus recycled water: public perceptions and profiles of the accepters. Journal of Environmental Management 90 (2), 888–900. doi:10.1016/j.jenvman.2008.02.003.

Dorel, C., Lejeune, P., Rodrigue, A., 2006. The Cpx system of Escherichia coli, a strategic signaling pathway for confronting adverse conditions and for settling biofilm communities? Research in Microbiology 157 (4), 306–314. doi:10.1016/j.resmic.2005.12.003.

Dow, n.d. FILMTEC™ Reverse Osmosis Membranes: Technical Manual Form No. 609-00071-0416. https://www.rainmandesal.com/wp-content/uploads/2018/09/dow-filmtec-sw30-manual.pdf (accessed 9.12.2020).

Dreszer, C., Vrouwenvelder, J.S., Paulitsch-Fuchs, A.H., Zwijnenburg, A., Kruithof, J.C., Flemming, H.-C., 2013. Hydraulic resistance of biofilms. Journal of Membrane Science 429, 436–447. doi:10.1016/j.memsci.2012.11.030.

Drewes, J.E., Horstmeyer, N., Michel, P., Khan, S., 2017. Producing high-quality recycled water, in: Lema, J.M., Suarez Martinez, S. (Eds.), Innovative Wastewater Treatment & Resource Recovery Technologies. Impacts on Energy, Economy and Environment. IWA Publishing, London, pp. 285–295.

Drewes, J.E., Khan, S., 2011. Water Reuse for Drinking Water Augmentation, in: Edzwald, J.K. (Ed.), Water quality & treatment. A handbook on drinking water, 6. ed. ed. McGraw-Hill, New York, 16.1-16.48.

DSMZ GmbH, 2007. 830a. MEDIUM R2A MODIFIED. DSMZ GmbH (accessed 26.07.2022). https://www.dsmz.de/microorganisms/medium/pdf/DSMZ_Medium830a.pdf.

DSMZ GmbH, 2012. 830. R2A MEDIUM. DSMZ GmbH (accessed 26.07.2022). https://www.dsmz.de/microorganisms/medium/pdf/DSMZ_Medium830.pdf.

Dunn, J., Ott, T., Clark, W., 1995. Pulsed-light treatment of food and packaging. Food Technology 1995 (Vol 49, Num 9), 95–98.

DuPont, 2020. FilmTec™ Reverse Osmosis Membranes: TechnicalManual Form No. 45-D01504-en, Rev. 2. https://www.dupont.com/content/dam/dupont/amer/us/en/water-solutions/public/documents/en/45-D01504-en.pdf (accessed 3.04.2020).

DuPont, 2022a. FilmTec™ Reverse Osmosis Membranes Technical Manual: Form No. 45-D01504-en, Rev. 12. https://www.dupont.com/content/dam/dupont/amer/us/en/water-solutions/public/documents/en/RO-NF-FilmTec-Manual-45-D01504-en.pdf (accessed 15.08.2022).

DuPont, 2022b. System Design: System Performance Projection Form No. 45-D01591-en, Rev. 10.

DVGW-Technologiezentrum Wasser (TZW), 2020. Charakterisierung von LED-basierten UV-Desinfektionsmodulen. Veröffentlichungen aus dem DVGW-Technologiezentrum Wasser Band 91, Eggenstein.

El Khodary, K., 2020. Impact of in-situ UVC Feed Stream Disinfection on the Microbial Diversity of Biofilms Formed in Reverse Osmosis (RO) processes. Bachelor's Thesis, Munich, Germany.

Elhadidy, A.M., van Dyke, M.I., Chen, F., Peldszus, S., Huck, P.M., 2017. Development and application of an improved protocol to characterize biofilms in biologically active drinking water filters. Environ. Sci.: Water Res. Technol. 3 (2), 249–261. doi:10.1039/C6EW00279J.

Elmnasser, N., Guillou, S., Leroi, F., Orange, N., Bakhrouf, A., Federighi, M., 2007. Pulsed-light system as a novel food decontamination technology: a review. Canadian Journal of Microbiology 53 (7), 813–821. doi:10.1139/W07-042.

Emerick, R.W., Loge, F.J., Ginn, T., Darby, J.L., 2000. Modeling the Inactivation of Particle-Associated Coliform Bacteria. Water Environment Research 72 (4), 432–438. doi:10.2175/106143000X137969.

Erental, A., Kalderon, Z., Saada, A., Smith, Y., Engelberg-Kulka, H., 2014. Apoptosis-like death, an extreme SOS response in Escherichia coli. mBio 5 (4), e01426-14. doi:10.1128/mBio.01426-14.

Erental, A., Sharon, I., Engelberg-Kulka, H., 2012. Two programmed cell death systems in Escherichia coli: an apoptotic-like death is inhibited by the mazEF-mediated death pathway. PLoS biology 10 (3), e1001281. doi:10.1371/journal.pbio.1001281.

Errol C. Friedberg, G.C.W.W.S.R.D.W., 2006. DNA Repair and Mutagenesis (2nd Edition). American Society for Microbiology.

EU -European Parliament and Council of the Eurpoean Union, 2012. Regulation (EU) No 528/2012 of the european parliament and of the council of 22 May 2021 concerning the making availability on the market and use of biocidal products: EU No 528/2012.

Fane, A.G., Tang, C.Y., Wang, R., 2011. Membrane Technology for Water: Microfiltration, Ultrafiltration, Nanofiltration, and Reverse Osmosis, in: , Treatise on Water Science. Elsevier, pp. 301–335.

Farhat, N.M., Vrouwenvelder, J.S., van Loosdrecht, M.C.M., Bucs, S.S., Staal, M., 2016. Effect of water temperature on biofouling development in reverse osmosis membrane systems. Water Research 103, 149–159. doi:10.1016/j.watres.2016.07.015.

Ferguson, G., Gleeson, T., 2012. Vulnerability of coastal aquifers to groundwater use and climate change. Nature Clim Change 2 (5), 342–345. doi:10.1038/nclimate1413.

Ferrera, I., Mas, J., Taberna, E., Sanz, J., Sánchez, O., 2015. Biological support media influence the bacterial biofouling community in reverse osmosis water reclamation demonstration plants. Biofouling 31 (2), 173–180. doi:10.1080/08927014.2015.1012640.

Fitzhenry, K., Clifford, E., Rowan, N., Del Val Rio, A., 2021. Bacterial inactivation, photoreactivation and dark repair post flow-through pulsed UV disinfection. Journal of Water Process Engineering 41, 102070. doi:10.1016/j.jwpe.2021.102070.

Flemming, H.-C., 1997. Reverse osmosis membrane biofouling. Experimental Thermal and Fluid Science 14 (4), 382–391. doi:10.1016/S0894-1777(96)00140-9.

Flemming, H.-C., 2011. Microbial Biofouling: Unsolved Problems, Insufficient Approaches, and Possible Solutions, in: Flemming, H.-C., Wingender, J., Szewzyk, U. (Eds.), Biofilm Highlights. Springer Series on Biofilms 5. Springer Berlin Heidelberg, Berlin/Heidelberg.

Flemming, H.-C., 2017. The perfect slime – and the "dark matter" of biofilms, in: Flemming, H.-C., Neu, T.R., Wingender, J. (Eds.), The perfect slime. Microbial extracellular polymeric substances (EPS). IWA Publishing, London.

Flemming, H.-C., 2020. Biofouling and me: My Stockholm syndrome with biofilms. Water Research 173, 115576. doi:10.1016/j.watres.2020.115576.

Flemming, H.-C., Neu, T.R., Wingender, J. (Eds.), 2017. The perfect slime: Microbial extracellular polymeric substances (EPS). IWA Publishing, London.

Flemming, H.-C., Schaule, G., Griebe, T., Schmitt, J., Tamachkiarowa, A., 1997. Biofouling—the Achilles heel of membrane processes. Desalination 113 (2-3), 215–225. doi:10.1016/S0011-9164(97)00132-X.

Flemming, H.-C., Wingender, J., 2010. The biofilm matrix. Nature Reviews. Microbiology 8 (9), 623–633. doi:10.1038/nrmicro2415.

Flemming, H.-C., Wingender, J., Szewzyk, U. (Eds.), 2011. Biofilm Highlights. Springer Series on Biofilms 5. Springer Berlin Heidelberg, Berlin/Heidelberg.

Fogler, H.S., 2016. Elements of chemical reaction engineering, 5. ed. ed. Prentice Hall, Boston.

Frederick, M.R., Kuttler, C., Hense, B.A., Eberl, H.J., 2011. A mathematical model of quorum sensing regulated EPS production in biofilm communities. Theoretical Biology & Medical Modelling 8, 8. doi:10.1186/1742-4682-8-8.

Friedberg, E.C., 2003. DNA damage and repair. Nature 421 (6921), 436–440. doi:10.1038/nature01408.

Friedman, L., Harif, T., Herzberg, M., Mamane, H., 2016. Mitigation of Biofilm Colonization on Various Surfaces in a Model Water Flow System by Use of UV Treatment. Water Air Soil Pollut 227 (2). doi:10.1007/s11270-015-2732-8.

Fröls, S., Ajon, M., Wagner, M., Teichmann, D., Zolghadr, B., Folea, M., Boekema, E.J., Driessen, A.J.M., Schleper, C., Albers, S.-V., 2008. UV-inducible cellular aggregation of the hyperthermophilic archaeon Sulfolobus solfataricus is mediated by pili

formation. Molecular Microbiology 70 (4), 938–952. doi:10.1111/j.1365-2958.2008.06459.x.

Gangal, A., 2023. Modelling the Inactivation Performance of a UVC-LED Flow-Through Reactor using COMSOL Multiphysics. Study Project, Munich, Germany.

Gao, D.-W., Wen, Z.-D., Li, B., Liang, H., 2013. Membrane fouling related to microbial community and extracellular polymeric substances at different temperatures. Bioresource Technology 143, 172–177. doi:10.1016/j.biortech.2013.05.127.

Garwood, F., 1936. (i) Fiducial Limits for the Poisson Distribution. Biometrika 28 (3-4), 437–442. doi:10.1093/biomet/28.3-4.437.

Giese, N., Darby, J., 2000. Sensitivity of microorganisms to different wavelengths of UV light: implications on modeling of medium pressure UV systems. Water Research 34 (16), 4007–4013. doi:10.1016/S0043-1354(00)00172-X.

Gillani, S.M.A., 2019. The Potential of UV Disinfection for Biofouling Mitigation in Spiral Wound Reverse Osmosis Membrane Modules. Master's Thesis, Munich, Germany.

Gillespie, J.B., Maclean, M., Given, M.J., Wilson, M.P., Judd, M.D., Timoshkin, I.V., MacGregor, S.J., 2017. Efficacy of Pulsed 405-nm Light-Emitting Diodes for Antimicrobial Photodynamic Inactivation: Effects of Intensity, Frequency, and Duty Cycle. Photomedicine and Laser Surgery 35 (3), 150–156. doi:10.1089/pho.2016.4179.

Gleeson, T., Befus, K.M., Jasechko, S., Luijendijk, E., Cardenas, M.B., 2016. The global volume and distribution of modern groundwater. Nature Geosci 9 (2), 161–167. doi:10.1038/ngeo2590.

Google LLC, n.d. Christuskirche - Pfarrsprengel Berlin-Oberspree-West. Google LLC (accessed 18.05.2023). https://www.google.com/maps/place/Christuskirche+-+Pfarrsprengel+Berlin-Oberspree-West/@52.4679252,13.4638873,12.38z/data=!4m6!3m5!1s0x47a8497873e7be59:0xe6b2b0ac711209f1!8m2!3d52.4636006!4d13.5244449!16s%2Fg%2F120pnbyq.

Griebe, T., Flemming, H.-C., 1998. Biocide-free antifouling strategy to protect RO membranes from biofouling. Desalination 118 (1-3), 153-IN9. doi:10.1016/S0011-9164(98)00113-1.

Guo, W., Ngo, H.-H., Li, J., 2012. A mini-review on membrane fouling. Bioresource Technology 122, 27–34. doi:10.1016/j.biortech.2012.04.089.

Gutman, J., Herzberg, M., Walker, S.L., 2014. Biofouling of reverse osmosis membranes: positively contributing factors of Sphingomonas. Environ. Sci. Technol. 48 (23), 13941–13950. doi:10.1021/es503680s.

Hamamoto, A., Mori, M., Takahashi, A., Nakano, M., Wakikawa, N., Akutagawa, M., Ikehara, T., Nakaya, Y., Kinouchi, Y., 2007. New water disinfection system using UVA light-emitting diodes. Journal of Applied Microbiology 103 (6), 2291–2298. doi:10.1111/j.1365-2672.2007.03464.x.

Han, X., Wang, Z., Zhu, C., Wu, Z., 2013. Effect of ultrasonic power density on extracting loosely bound and tightly bound extracellular polymeric substances. Desalination 329, 35–40. doi:10.1016/j.desal.2013.09.002.

Harif, T., Elifantz, H., Margalit, E., Herzberg, M., Lichi, T., Minz, D., 2011. The effect of UV pre-treatment on biofouling of BWRO membranes: A field study. Desalination and Water Treatment 31 (1-3), 151–163. doi:10.5004/dwt.2011.2377.

Harm, W., 1980. Biological effects of ultraviolet radiation. IUPAB biophysics series 1. Cambridge University Press, Cambridge.

Harris, G.D., Adams, V., Sorensen, D.L., Curtis, M.S., 1987. Ultraviolet inactivation of selected bacteria and viruses with photoreactivation of the bacteria. Water Research 21 (6), 687–692. doi:10.1016/0043-1354(87)90080-7.

He, Y.-Y., Häder, D., 2002. Reactive oxygen species and UV-B: effect on cyanobacteria. Photochemical & Photobiological Sciences : Official journal of the European Photochemistry Association and the European Society for Photobiology 1 (10), 729–736. doi:10.1039/b110365m.

Hecht, E., 2002. Optics, 4. ed., internat. ed. ed. Addison-Wesley, Reading, Mass.

Heck, K.L., van Belle, G., Simberloff, D., 1975. Explicit Calculation of the Rarefaction Diversity Measurement and the Determination of Sufficient Sample Size. Ecology 56 (6), 1459–1461. doi:10.2307/1934716.

Heidarinejad, G., Bozorgmehr, N., Safarzadeh, M., 2020. Effect of highly reflective material on the performance of water ultraviolet disinfection reactor. Journal of Water Process Engineering 36, 101375. doi:10.1016/j.jwpe.2020.101375.

Heisler, J., Glibert, P., Burkholder, J., Anderson, D., Cochlan, W., Dennison, W., Gobler, C., Dortch, Q., Heil, C., Humphries, E., Lewitus, A., Magnien, R., Marshall, H., Sellner, K., Stockwell, D., Stoecker, D., Suddleson, M., 2008. Eutrophication and Harmful Algal Blooms: A Scientific Consensus. Harmful Algae 8 (1), 3–13. doi:10.1016/j.hal.2008.08.006.

Herzberg, M., Elimelech, M., 2007. Biofouling of reverse osmosis membranes: Role of biofilm-enhanced osmotic pressure. Journal of Membrane Science 295 (1-2), 11–20. doi:10.1016/j.memsci.2007.02.024.

Herzberg, M., Elimelech, M., 2008. Physiology and genetic traits of reverse osmosis membrane biofilms: a case study with Pseudomonas aeruginosa. The R Journal 2 (2), 180–194. doi:10.1038/ismej.2007.108.

Hijnen, W.A.M., Beerendonk, E.F., Medema, G.J., 2006. Inactivation credit of UV radiation for viruses, bacteria and protozoan (oo)cysts in water: a review. Water Research 40 (1), 3–22. doi:10.1016/j.watres.2005.10.030.

Holm-Hansen, O., Booth, C.R., 1966. THE MEASUREMENT OF ADENOSINE TRIPHOSPHATE IN THE OCEAN AND ITS ECOLOGICAL SIGNIFICANCE1. Limnol. Oceanogr. 11 (4), 510–519. doi:10.4319/lo.1966.11.4.0510.

Howe, K.J., Hand, D.W., Crittenden, J.C., Trussell, R.R., Tchobanoglous, G., 2012. Principles of Water Treatment. Wiley, Hoboken.

Hu, H., Lu, Z., Wang, H., Yin, H., Hao, H., Ma, B., Shi, B., 2023. Microbial interaction energy and EPS composition influenced ultrafiltration membrane biofouling and the role of UV pretreatment. Desalination 548, 116304. doi:10.1016/j.desal.2022.116304.

Huang, H., Spinette, R., O'Melia, C.R., 2008a. Direct-flow microfiltration of aquasols. Journal of Membrane Science 314 (1-2), 90–100. doi:10.1016/j.memsci.2008.01.040.

Huang, L.-N., Wever, H. de, Diels, L., 2008b. Diverse and distinct bacterial communities induced biofilm fouling in membrane bioreactors operated under different conditions. Environ. Sci. Technol. 42 (22), 8360–8366. doi:10.1021/es801283q.

Hurlbert, S.H., 1971. The Nonconcept of Species Diversity: A Critique and Alternative Parameters. Ecology 52 (4), 577–586. doi:10.2307/1934145.

Hurwitz, G., Guillen, G.R., Hoek, E.M., 2010. Probing polyamide membrane surface charge, zeta potential, wettability, and hydrophilicity with contact angle measurements. Journal of Membrane Science 349 (1-2), 349–357. doi:10.1016/j.memsci.2009.11.063.

Hwang, K.-J., Hsueh, C.-L., 2003. Dynamic analysis of cake properties in microfiltration of soft colloids. Journal of Membrane Science 214 (2), 259–273. doi:10.1016/S0376-7388(02)00556-2.

Ibrahim, M.A.S., MacAdam, J., Autin, O., Jefferson, B., 2014. Evaluating the impact of LED bulb development on the economic viability of ultraviolet technology for disinfection. Environmental Technology 35 (1-4), 400–406. doi:10.1080/09593330.2013.829858.

Infineon Technologies AG, 2022. LED Driver: BCR 420U E6327 / BCR 421U E6327. https://www.google.com/url?sa=t&rct=j&q=&esrc=s&source=web&cd=&ved=2ahU KEwifiYejy7GBAxWG_rsIHcEXDwMQFnoECBMQAQ&url=https%3A%2F%2Fwww. infineon.com%2Fdgdl%2FInfineon-BCR420U-BCR421U-DataSheet-v02_02- EN.pdf%3FfileId%3D5546d4626102d35a01617524f09e061d&usg=AOvVaw0Qz8a myMdCDs7aygplkr08&opi=89978449 (accessed 17.09.2023).

Iqbal, T., Lee, K., Lee, C.-H., Choo, K.-H., 2018. Effective quorum quenching bacteria dose for anti-fouling strategy in membrane bioreactors utilizing fixed-sheet media. Journal of Membrane Science 562, 18–25. doi:10.1016/j.memsci.2018.05.031.

Ivanova, E.P., Alexeeva, Y.V., Pham, D.K., Wright, J.P., Nicolau, D.V., 2006. ATP level variations in heterotrophic bacteria during attachment on hydrophilic and hydrophobic surfaces. International Microbiology : The Official Journal of The Spanish Society for Microbiology 9 (1), 37–46.

Ivnitsky, H., Katz, I., Minz, D., Shimoni, E., Chen, Y., Tarchitzky, J., Semiat, R., Dosoretz, C.G., 2005. Characterization of membrane biofouling in nanofiltration processes of wastewater treatment. Desalination 185 (1-3), 255–268. doi:10.1016/j.desal.2005.03.081.

Jafari, M., D'haese, A., Zlopasa, J., Cornelissen, E.R., Vrouwenvelder, J.S., Verbeken, K., Verliefde, A., van Loosdrecht, M., Picioreanu, C., 2020. A comparison between chemical cleaning efficiency in lab-scale and full-scale reverse osmosis membranes: Role of extracellular polymeric substances (EPS). Journal of Membrane Science 609, 118189. doi:10.1016/j.memsci.2020.118189.

Jafari, M., Vanoppen, M., van Agtmaal, J., Cornelissen, E.R., Vrouwenvelder, J.S., Verliefde, A., van Loosdrecht, M., Picioreanu, C., 2021. Cost of fouling in full-scale reverse osmosis and nanofiltration installations in the Netherlands. Desalination 500, 114865. doi:10.1016/j.desal.2020.114865.

Jafra, S., Przysowa, J., Czajkowski, R., Michta, A., Garbeva, P., van der Wolf, J.M., 2006. Detection and characterization of bacteria from the potato rhizosphere degrading N-acyl-homoserine lactone. Canadian Journal of Microbiology 52 (10), 1006–1015. doi:10.1139/w06-062.

Jager, T.L. de, Cockrell, A.E., Du Plessis, S.S., 2017. Ultraviolet Light Induced Generation of Reactive Oxygen Species, in: Ahmad, S.I. (Ed.), Ultraviolet Light in Human Health, Diseases and Environment. Springer International Publishing, Cham, pp. 15–23.

Jarvis, Autin, Goslan, Hassard, 2019. Application of Ultraviolet Light-Emitting Diodes (UV-LED) to Full-Scale Drinking-Water Disinfection. Water 11 (9), 1894. doi:10.3390/w11091894.

Javier, L., Farhat, N.M., Vrouwenvelder, J.S., 2021a. Enhanced hydraulic cleanability of biofilms developed under a low phosphorus concentration in reverse osmosis membrane systems. Water Research X 10, 100085. doi:10.1016/j.wroa.2020.100085.

Javier, L., Pulido-Beltran, L., Kruithof, J., Vrouwenvelder, J.S., Farhat, N.M., 2021b. Phosphorus Concentration in Water Affects the Biofilm Community and the Produced Amount of Extracellular Polymeric Substances in Reverse Osmosis Membrane Systems. Membranes 11 (12). doi:10.3390/membranes11120928.

Jenny, R.M., Simmons, O.D., Shatalov, M., Ducoste, J.J., 2014. Modeling a continuous flow ultraviolet Light Emitting Diode reactor using computational fluid dynamics. Chemical Engineering Science 116 (2), 524–535. doi:10.1016/j.ces.2014.05.020.

Jiang, B., Liu, Y., 2013. Dependence of structure stability and integrity of aerobic granules on ATP and cell communication. Applied Microbiology and Biotechnology 97 (11), 5105–5112. doi:10.1007/s00253-012-4315-6.

Jiang, S., Li, Y., Ladewig, B.P., 2017. A review of reverse osmosis membrane fouling and control strategies. The Science of The Total Environment 595, 567–583. doi:10.1016/j.scitotenv.2017.03.235.

Jin, S., Linden, K.G., Ducoste, J., Liu, D., 2005. Impact of lamp shadowing and reflection on the fluence rate distribution in a multiple low-pressure UV lamp array. Water Research 39 (12), 2711–2721. doi:10.1016/j.watres.2005.04.071.

Jin, S., Mofidi, A.A., Linden, K.G., 2006. Polychromatic UV Fluence Measurement Using Chemical Actinometry, Biodosimetry, and Mathematical Techniques. J. Environ. Eng. 132 (8), 831–841. doi:10.1061/(ASCE)0733-9372(2006)132:8(831).

Joss, A., Keller, E., Alder, A.C., Göbel, A., McArdell, C.S., Ternes, T., Siegrist, H., 2005. Removal of pharmaceuticals and fragrances in biological wastewater treatment. Water Research 39 (14), 3139–3152. doi:10.1016/j.watres.2005.05.031.

Judd, S. (Ed.), 2010. The MBR book: Principles and applications of membrane bioreactors for water and wastewater treatment, 2nd ed. ed. Butterworth-Heinemann, Oxford.

Judd, S., Jefferson, B., 2003. Membranes for industrial wastewater recovery and re-use. Elsevier Science, Kidlington, Oxford, UK, New York, NY, USA.

Kalmbach, S., 2000. In situ probing reveals Aquabacterium commune as a widespread and highly abundant bacterial species in drinking water biofilms. Water Research 34 (2), 575–581. doi:10.1016/S0043-1354(99)00179-7.

Kalmbach, S., Manz, W., Wecke, J., Szewzyk, U., 1999. Aquabacterium gen. nov., with description of Aquabacterium citratiphilum sp. nov., Aquabacterium parvum sp. nov. and Aquabacterium commune sp. nov., three in situ dominant bacterial species from the Berlin drinking water system. International Journal of Systematic Bacteriology 49 Pt 2, 769–777. doi:10.1099/00207713-49-2-769.

Kampouris, I.D., Karayannakidis, P.D., Banti, D.C., Sakoula, D., Konstantinidis, D., Yiangou, M., Samaras, P.E., 2018. Evaluation of a novel quorum quenching strain for MBR biofouling mitigation. Water Research 143, 56–65. doi:10.1016/j.watres.2018.06.030.

Karsch-Mizrachi, I., Takagi, T., Cochrane, G., 2018. The international nucleotide sequence database collaboration. Nucleic Acids Research 46 (D1), D48-D51. doi:10.1093/nar/gkx1097.

Kayahan, E., Jacobs, M., Braeken, L., Thomassen, L.C., Kuhn, S., van Gerven, T., Leblebici, M.E., 2020. Dawn of a new era in industrial photochemistry: the scale-up of micro- and mesostructured photoreactors. Beilstein Journal of Organic Chemistry 16, 2484–2504. doi:10.3762/bjoc.16.202.

Khan, M.S., 2022a. Development and validation of a cultivation and flow-through biodosimetry procedure for Aquabacterium citratiphilum. Study Project, Munich, Germany.

Khan, M.S., 2022b. Optimization of UVC-LED pre-treatment integrated in spiral-wound elements for biofouling control in membrane desalination processes. Master's Thesis, Munich, Germany.

Khan, M.T., Hong, P.-Y., Nada, N., Croue, J.P., 2015. Does chlorination of seawater reverse osmosis membranes control biofouling? Water Research 78, 84–97. doi:10.1016/j.watres.2015.03.029.

Khan, M.T., O Manes, C.-L. de, Aubry, C., Gutierrez, L., Croue, J.P., 2013. Kinetic study of seawater reverse osmosis membrane fouling. Environ. Sci. Technol. 47 (19), 10884–10894. doi:10.1021/es402138e.

Kim, I.S., Lee, J., Kima, S.-J., Yu, H.-W., Am Jang, 2014. Comparative pyrosequencing analysis of bacterial community change in biofilm formed on seawater reverse osmosis membrane. Environmental Technology 35 (1-4), 125–136. doi:10.1080/09593330.2013.817445.

Kim, J., Park, K., Yang, D.R., Hong, S., 2019. A comprehensive review of energy consumption of seawater reverse osmosis desalination plants. Applied Energy 254, 113652. doi:10.1016/j.apenergy.2019.113652.

Kim, J.E., Phuntsho, S., Shon, H.K., 2013. Pilot-scale nanofiltration system as post-treatment for fertilizer-drawn forward osmosis desalination for direct fertigation. Desalination and Water Treatment 51 (31-33), 6265–6273. doi:10.1080/19443994.2013.780804.

Kolappan, A., Satheesh, S., 2011. Efficacy of UV Treatment in the Management of Bacterial Adhesion on Hard Surfaces. Polish Journal of Microbiology (Vol. 60, No 2), 119–123.

Koros, W.J., Ma, Y.H., Shimidzu, T., 1996. Terminology for membranes and membrane processes (IUPAC Recommendations 1996). Pure and Applied Chemistry 68 (7), 1479–1489. doi:10.1351/pac199668071479.

Koutchma, T., Popović, V., Green, A., 2019. Overview of Ultraviolet (UV) LEDs Technology for Applications in Food Production, in: , Ultraviolet LED Technology for Food Applications. Elsevier, pp. 1–23.

Kowalski, W.J., Bahnfleth, W.P., Raguse, M., Moeller, R., 2020. The cluster model of ultraviolet disinfection explains tailing kinetics. Journal of Applied Microbiology 128 (4), 1003–1014. doi:10.1111/jam.14527.

Koyama, K., Hokunan, H., Hasegawa, M., Kawamura, S., Koseki, S., 2016. Do bacterial cell numbers follow a theoretical Poisson distribution? Comparison of experimentally obtained numbers of single cells with random number generation via computer simulation. Food Microbiology 60, 49–53. doi:10.1016/j.fm.2016.05.019.

Krishnamurthy, K., Tewari, J.C., Irudayaraj, J., Demirci, A., 2010. Microscopic and Spectroscopic Evaluation of Inactivation of Staphylococcus aureus by Pulsed UV Light and Infrared Heating. Food Bioprocess Technol 3 (1), 93–104. doi:10.1007/s11947-008-0084-8.

Kucera, J., 2019. Biofouling of Polyamide Membranes: Fouling Mechanisms, Current Mitigation and Cleaning Strategies, and Future Prospects. Membranes 9 (9). doi:10.3390/membranes9090111.

Kuhn, H.J., Braslavsky, S.E., Schmidt, R., 2004. Chemical actinometry (IUPAC Technical Report). Pure and Applied Chemistry 76 (12), 2105–2146. doi:10.1351/pac200476122105.

Kurwadkar, S., Dane, J., Kanel, S.R., Nadagouda, M.N., Cawdrey, R.W., Ambade, B., Struckhoff, G.C., Wilkin, R., 2022. Per- and polyfluoroalkyl substances in water and wastewater: A critical review of their global occurrence and distribution. The Science of The Total Environment 809, 151003. doi:10.1016/j.scitotenv.2021.151003.

La Torre, A. de, 2008. Efficiency optimization in SWRO plant: high efficiency & low maintenance pumps. Desalination 221 (1-3), 151–157. doi:10.1016/j.desal.2007.02.052.

Labas, M., Brandi, R., Martin, C., Cassano, A., 2006. Kinetics of bacteria inactivation employing UV radiation under clear water conditions. Chemical Engineering Journal 121 (2-3), 135–145. doi:10.1016/j.cej.2006.05.012.

Lagkouvardos, I., Fischer, S., Kumar, N., Clavel, T., 2017. Rhea: a transparent and modular R pipeline for microbial profiling based on 16S rRNA gene amplicons. PeerJ 5, e2836. doi:10.7717/peerj.2836.

Lakretz, A., Mamane, H., Asa, E., Harif, T., Herzberg, M., 2018. Biofouling control by UV/H$_2$O$_2$ pretreatment for brackish water reverse osmosis process. Environ. Sci.: Water Res. Technol. 4 (9), 1331–1344. doi:10.1039/C8EW00183A.

Lakretz, A., Ron, E.Z., Mamane, H., 2010. Biofouling control in water by various UVC wavelengths and doses. Biofouling 26 (3), 257–267. doi:10.1080/08927010903484154.

Landini, P., 2009. Cross-talk mechanisms in biofilm formation and responses to environmental and physiological stress in Escherichia coli. Research in Microbiology 160 (4), 259–266. doi:10.1016/j.resmic.2009.03.001.

Larasser, M., 2017. Design, Construction and Commissioning of a Partially Automated Multi-Optional Membrane Test-Skid (NF/RO). Study Project, Munich, Germany.

Laser Components GmbH, 2018. 278 nm 100mW 6060 1in1 Flat LED PKG Rev. 0.1. https://www.google.com/url?sa=t&rct=j&q=&esrc=s&source=web&cd=1&ved=2ah UKEwj7toXy_tPoAhXusaQKHbluDOsQFjAAegQIBhAB&url=https%3A%2F%2Fww w.lasercomponents.com%2Ffileadmin%2Fuser_upload%2Fhome%2FDatasheets %2Flg%2Fleuva66h70hf00_278nm_high_power.pdf&usg=AOvVaw0lro6w8EigE-S1HTUS-UCV (accessed 6.04.2020).

Laser Components GmbH, 2019a. High Power UV-C LED Product Specifications 6060 SMD Packaged LED V1.3.

Laser Components GmbH, 2019b. High Power UV-C LED: SMD Modules and Arrays V0.9. https://www.lasercomponents.com/de/produkt/uvb-uvc-leds-260-315-nm/ (accessed 6.04.2020).

Legendre, P., Anderson, M.J., 1999. DISTANCE-BASED REDUNDANCY ANALYSIS: TESTING MULTISPECIES RESPONSES IN MULTIFACTORIAL ECOLOGICAL EXPERIMENTS. Ecological Monographs 69 (1), 1–24. doi:10.1890/0012-9615(1999)069[0001:DBRATM]2.0.CO;2.

Levenspiel, O., 2012. Tracer Technology 96. Springer New York, New York, NY.

Li, G.-Q., Wang, W.-L., Huo, Z.-Y., Lu, Y., Hu, H.-Y., 2017a. Comparison of UV-LED and low pressure UV for water disinfection: Photoreactivation and dark repair of Escherichia coli. Water Research 126, 134–143. doi:10.1016/j.watres.2017.09.030.

Li, J., Hirota, K., Yumoto, H., Matsuo, T., Miyake, Y., Ichikawa, T., 2010. Enhanced germicidal effects of pulsed UV-LED irradiation on biofilms. Journal of Applied Microbiology 109 (6), 2183–2190. doi:10.1111/j.1365-2672.2010.04850.x.

Li, K., Li, S., Huang, T., Dong, C., Li, J., Zhao, B., Zhang, S., 2019a. Chemical Cleaning of Ultrafiltration Membrane Fouled by Humic Substances: Comparison between

Hydrogen Peroxide and Sodium Hypochlorite. International journal of Environmental Research and Public Health 16 (14). doi:10.3390/ijerph16142568.

Li, M., Li, W., Qiang, Z., Blatchley, E.R., 2017b. On-Site Determination and Monitoring of Real-Time Fluence Delivery for an Operating UV Reactor Based on a True Fluence Rate Detector. Environmental Science & Technology 51 (14), 8094–8100. doi:10.1021/acs.est.7b01241.

Li, M., Qiang, Z., Li, T., Bolton, J.R., Liu, C., 2011. In situ measurement of UV fluence rate distribution by use of a micro fluorescent silica detector. Environmental Science & Technology 45 (7), 3034–3039. doi:10.1021/es103796v.

Li, W., Li, M., Bolton, J.R., Qu, J., Qiang, Z., 2017c. Impact of inner-wall reflection on UV reactor performance as evaluated by using computational fluid dynamics: The role of diffuse reflection. Water Research 109, 382–388. doi:10.1016/j.watres.2016.11.068.

Li, X., Cai, M., Wang, L., Niu, F., Yang, D., Zhang, G., 2019b. Evaluation survey of microbial disinfection methods in UV-LED water treatment systems. The Science of The Total Environment 659, 1415–1427. doi:10.1016/j.scitotenv.2018.12.344.

Liberti, L., Notarnicola, M., Petruzzelli, D., 2003. Advanced treatment for municipal wastewater reuse in agriculture. UV disinfection: parasite removal and by-product formation. Desalination 152 (1-3), 315–324. doi:10.1016/S0011-9164(02)01079-2.

Lin, Y.-H., Xu, J.-L., Hu, J., Wang, L.-H., Ong, S.L., Leadbetter, J.R., Zhang, L.-H., 2003. Acyl-homoserine lactone acylase from Ralstonia strain XJ12B represents a novel and potent class of quorum-quenching enzymes. Molecular Microbiology 47 (3), 849–860. doi:10.1046/j.1365-2958.2003.03351.x.

Linden, K.G., Darby, J.L., 1997. Estimating Effective Germicidal Dose from Medium Pressure UV Lamps. J. Environ. Eng. 123 (11), 1142–1149. doi:10.1061/(ASCE)0733-9372(1997)123:11(1142).

Ling, R., Yu, L., Pham, T.P.T., Shao, J., Chen, J.P., Reinhard, M., 2017. The tolerance of a thin-film composite polyamide reverse osmosis membrane to hydrogen peroxide exposure. Journal of Membrane Science 524, 529–536. doi:10.1016/j.memsci.2016.11.041.

Lonsdale, H.K., Merten, U., Riley, R.L., 1965. Transport properties of cellulose acetate osmotic membranes. J. Appl. Polym. Sci. 9 (4), 1341–1362. doi:10.1002/app.1965.070090413.

Love, M.I., Huber, W., Anders, S., 2014. Moderated estimation of fold change and dispersion for RNA-seq data with DESeq2. Genome Biology 15 (12), 550. doi:10.1186/s13059-014-0550-8.

Ma, H., Wang, X., Zhang, Y., Hu, H., Ren, H., Geng, J., Ding, L., 2018a. The diversity, distribution and function of N-acyl-homoserine lactone (AHL) in industrial anaerobic granular sludge. Bioresource Technology 247, 116–124. doi:10.1016/j.biortech.2017.09.043.

Ma, W., Panecka, M., Tufenkji, N., Rahaman, M.S., 2018b. Bacteriophage-based strategies for biofouling control in ultrafiltration: In situ biofouling mitigation, biocidal

additives and biofilm cleanser. Journal of Colloid and Interface Science 523, 254–265. doi:10.1016/j.jcis.2018.03.105.

Maafi, M., Maafi, W., 2015. Quantification of Unimolecular Photoreaction Kinetics: Determination of Quantum Yields and Development of Actinometers—The Photodegradation Case of Cardiovascular Drug Nisoldipine. International Journal of Photoenergy 2015, 1–12. doi:10.1155/2015/454895.

Maafi, W., Maafi, M., 2013. Modelling nifedipine photodegradation, photostability and actinometric properties. International Journal of Pharmaceutics 456 (1), 153–164. doi:10.1016/j.ijpharm.2013.07.075.

Mahesh, R.B., 2019. Development and Validation of a Procedure for Development and Validation of a Procedure for Accelerated Biofouling Studies Under Fully Controlled and Reproducible Conditions. Study Project, Munich, Germany.

Marconnet, C., Houari, A., Seyer, D., Djafer, M., Coriton, G., Heim, V., Di Martino, P., 2011. Membrane biofouling control by UV irradiation. Desalination 276 (1-3), 75–81. doi:10.1016/j.desal.2011.03.016.

Martino, D., Ahmed, H., Veronique, H., Cyril, M., 2011. Assessment of UV Pre-Treatment to Reduce Fouling of NF Membranes, in: Ning, R.Y. (Ed.), Expanding Issues in Desalination. IntechOpen, London, UK.

Maslowska, K.H., Makiela-Dzbenska, K., Fijalkowska, I.J., 2019. The SOS system: A complex and tightly regulated response to DNA damage. Environmental and Molecular Mutagenesis 60 (4), 368–384. doi:10.1002/em.22267.

Mason, J.M., Setlow, P., 1986. Essential role of small, acid-soluble spore proteins in resistance of Bacillus subtilis spores to UV light. Journal of Bacteriology 167 (1), 174–178. doi:10.1128/jb.167.1.174-178.1986.

Masuko, T., Minami, A., Iwasaki, N., Majima, T., Nishimura, S.-I., Lee, Y.C., 2005. Carbohydrate analysis by a phenol-sulfuric acid method in microplate format. Analytical Biochemistry 339 (1), 69–72. doi:10.1016/j.ab.2004.12.001.

Matallana-Surget, S., Wattiez, R., 2013. Impact of Solar Radiation on Gene Expression in Bacteria. Proteomes 1 (2), 70–86. doi:10.3390/proteomes1020070.

Matar, G., Gonzalez-Gil, G., Maab, H., Nunes, S., Le-Clech, P., Vrouwenvelder, J., Saikaly, P.E., 2016. Temporal changes in extracellular polymeric substances on hydrophobic and hydrophilic membrane surfaces in a submerged membrane bioreactor. Water Research 95, 27–38. doi:10.1016/j.watres.2016.02.064.

Matin, A., Khan, Z., Zaidi, S., Boyce, M.C., 2011. Biofouling in reverse osmosis membranes for seawater desalination: Phenomena and prevention. Desalination 281, 1–16. doi:10.1016/j.desal.2011.06.063.

McArdle, B.H., Anderson, M.J., 2001. Fitting Multivariate Models to Communuty Data: A Comment on Distance-Based Redundancy Analysis. Ecology 82 (1), 290–297. doi:10.1890/0012-9658(2001)082[0290:FMMTCD]2.0.CO;2.

McDonald, K.F., Curry, R.D., Clevenger, T.E., Unklesbay, K., Eisenstark, A., Golden, J., Morgan, R.D., 2000. A comparison of pulsed and continuous ultraviolet light sources

for the decontamination of surfaces. IEEE Trans. Plasma Sci. 28 (5), 1581–1587. doi:10.1109/27.901237.

McKinney, C.W., Pruden, A., 2012. Ultraviolet disinfection of antibiotic resistant bacteria and their antibiotic resistance genes in water and wastewater. Environ. Sci. Technol. 46 (24), 13393–13400. doi:10.1021/es303652q.

Mekonnen, M.M., Hoekstra, A.Y., 2016. Four billion people facing severe water scarcity. Science Advances 2 (2), e1500323. doi:10.1126/sciadv.1500323.

Merino, N., Qu, Y., Deeb, R.A., Hawley, E.L., Hoffmann, M.R., Mahendra, S., 2016. Degradation and Removal Methods for Perfluoroalkyl and Polyfluoroalkyl Substances in Water. Environmental Engineering Science 33 (9), 615–649. doi:10.1089/ees.2016.0233.

Mirlach, A., 2021. Establishing a characterization procedure for reflecting UVC reactors using actinometry and biodosimetry. Master's Thesis, Munich, Germany.

Mitchell, D.L., Jen, J., Cleaver, J.E., 1992. Sequence specificity of cyclobutane pyrimidine dimers in DNA treated with solar (ultraviolet B) radiation. Nucleic Acids Research 20 (2), 225–229. doi:10.1093/nar/20.2.225.

Mkandawire, T., 2008. Quality of groundwater from shallow wells of selected villages in Blantyre District, Malawi. Physics and Chemistry of the Earth, Parts A/B/C 33 (8-13), 807–811. doi:10.1016/j.pce.2008.06.023.

Mohaghegh Montazeri, M., Taghipour, F., 2023. Virtual prototyping and characterization of a point-of-entry UV-LED water disinfection reactor with the synergic effect of radiation, hydrodynamics, and inactivation kinetics. Water Research 230, 119581. doi:10.1016/j.watres.2023.119581.

Mondal, R.K., Adhikari, S., Chatterjee, V., Pal, S., 2021. Recent advances and challenges in AlGaN-based ultra-violet light emitting diode technologies. Materials Research Bulletin 140, 111258. doi:10.1016/j.materresbull.2021.111258.

Morowitz, H.J., 1950. Absorption effects in volume irradiation of microorganisms. Science 111 (2879), 229. doi:10.1126/science.111.2879.229-a.

Mukherjee, M., Hu, Y., Tan, C.H., Rice, S.A., Cao, B., 2018. Engineering a light-responsive, quorum quenching biofilm to mitigate biofouling on water purification membranes. Science Advances 4 (12), eaau1459. doi:10.1126/sciadv.aau1459.

Mulder, M., 1996. Basic Principles of Membrane Technology. Springer Netherlands, Dordrecht.

Müller, A., Orlowska, M., Knörr, M., Stahl, M.R., Greiner, R., Koutchma, T., 2017. Actinometric and biosimetric evaluation of UV-C dose delivery in annular, Taylor-Coutte and coiled tube continuous systems. Food Science and Technology International 23 (3), 222–234. doi:10.1177/1082013216679010.

Murphy, A., Moody, C., Riley, R., Lin, S., Murugaverl, B., Rusin, P., 2001. Microbiological damage of cellulose acetate RO membranes. Journal of Membrane Science 193 (1), 111–121. doi:10.1016/S0376-7388(01)00506-3.

Murphy, K.R., Stedmon, C.A., Graeber, D., Bro, R., 2013. Fluorescence spectroscopy and multi-way techniques. PARAFAC. Anal. Methods 5 (23), 6557. doi:10.1039/C3AY41160E.

Murphy, K.R., Stedmon, C.A., Wenig, P., Bro, R., 2014. OpenFluor– an online spectral library of auto-fluorescence by organic compounds in the environment. Anal. Methods 6 (3), 658–661. doi:10.1039/C3AY41935E.

Najid, N., Hakizimana, J.N., Kouzbour, S., Gourich, B., Ruiz-García, A., Vial, C., Stiriba, Y., Semiat, R., 2022. Fouling control and modeling in reverse osmosis for seawater desalination: A review. Computers & Chemical Engineering 162, 107794. doi:10.1016/j.compchemeng.2022.107794.

Nakayama, Y., 2018. Introduction to fluid mechanics, 2nd ed. ed. Butterworth-Heinemann, Oxford.

Nay, V., 2020. Sustainability study for drinking water ultrafiltration in rural deployment. Study Project, Munich, Germany.

NCBI -National Library of Medicine, National Center for Biotechnology Information, n.d. Standard Nucleotide BLAST: blastn. National Library of Medicine, National Center for Biotechnology Information (NCBI) (accessed 1.08.2022). https://blast.ncbi.nlm.nih.gov/Blast.cgi?PROGRAM=blastn&PAGE_TYPE=BlastSearch&LINK_LOC=blasthome.

Nguyen, T., Roddick, F.A., Fan, L., 2012. Biofouling of water treatment membranes: a review of the underlying causes, monitoring techniques and control measures. Membranes 2 (4), 804–840. doi:10.3390/membranes2040804.

Nguyen, X.Q., 2021. UV light modeling of a steady-state water reactor using COMSOL Multiphysics. Study Project, Munich, Germany.

Noguera-Oviedo, K., Aga, D.S., 2016. Lessons learned from more than two decades of research on emerging contaminants in the environment. Journal of Hazardous Materials 316, 242–251. doi:10.1016/j.jhazmat.2016.04.058.

NSF/ANSI -NSF International, American National Standards Institute, 2019. NSF/ANSI 55 Ultraviolet Microbiological Water Treatment Systems. NSF International, Michigan (USA).

Nyangaresi, P.O., Qin, Y., Chen, G., Zhang, B., Lu, Y., Shen, L., 2019. Comparison of the performance of pulsed and continuous UVC-LED irradiation in the inactivation of bacteria. Water Research 157, 218–227. doi:10.1016/j.watres.2019.03.080.

Oguma, K., Katayama, H., Ohgaki, S., 2002. Photoreactivation of Escherichia coli after low- or medium-pressure UV disinfection determined by an endonuclease sensitive site assay. Applied and Environmental Microbiology 68 (12), 6029–6035. doi:10.1128/AEM.68.12.6029-6035.2002.

Oguma, K., Kita, R., Sakai, H., Murakami, M., Takizawa, S., 2013. Application of UV light emitting diodes to batch and flow-through water disinfection systems. Desalination 328, 24–30. doi:10.1016/j.desal.2013.08.014.

Oguma, K., Kita, R., Takizawa, S., 2016. Effects of Arrangement of UV Light-Emitting Diodes on the Inactivation Efficiency of Microorganisms in Water. Photochem Photobiol 92 (2), 314–317. doi:10.1111/php.12571.

Oksanen, J., Blanchet, F.G., Friendly, M., Kindt, R., Legendre, P., McGlinn, D., Minchin, P.R., O'Hara, R.B., Simpson, G.L., Solymos, P., Stevens, M.H.H., Szoecs, E., Wagner, H., 2019. vegan: Community Ecology Package, 2nd ed. https://CRAN.R-project.org/package=vegan. accessed on 25.09.2020.

Olago, D., Marshall, M., Wandiga, S.O., Opondo, M., Yanda, P.Z., Kangalawe, R., Githeko, A., Downs, T., Opere, A., Kabumbuli, R., Kirumira, E., Ogallo, L., Mugambi, P., Apindi, E., Githui, F., Kathuri, J., Olaka, L., Sigalla, R., Nanyunja, R., Baguma, T., Achola, P., 2007. Climatic, Socio-economic, and Health Factors Affecting Human Vulnerability to Cholera in the Lake Victoria Basin, East Africa. AMBIO: A Journal of the Human Environment 36 (4), 350–358. doi:10.1579/0044-7447(2007)36[350:CSAHFA]2.0.CO;2.

Oms-Oliu, G., Martín-Belloso, O., Soliva-Fortuny, R., 2010. Pulsed Light Treatments for Food Preservation. A Review. Food Bioprocess Technol 3 (1). doi:10.1007/s11947-008-0147-x.

Ortuño, F., Molinero, J., Garrido, T., Custodio, E., 2012. Seawater injection barrier recharge with advanced reclaimed water at Llobregat delta aquifer (Spain). Water Science and Technology 66 (10), 2083–2089. doi:10.2166/wst.2012.423.

Otaki, M., Takizawa, S., Ohgaki, S., 1998. Control and modeling of membrane fouling due to microorganism growth by UV pretreatment. Water Science and Technology : A Journal of The International Association on Water Pollution Research 38 (4-5). doi:10.1016/S0273-1223(98)00539-3.

Otto, K., Silhavy, T.J., 2002. Surface sensing and adhesion of Escherichia coli controlled by the Cpx-signaling pathway. Proceedings of the National Academy of Sciences of the United States of America 99 (4), 2287–2292. doi:10.1073/pnas.042521699.

Painter, S.C., Lapworth, D.J., Woodward, E.M.S., Kroeger, S., Evans, C.D., Mayor, D.J., Sanders, R.J., 2018. Terrestrial dissolved organic matter distribution in the North Sea. The Science of The Total Environment 630, 630–647. doi:10.1016/j.scitotenv.2018.02.237.

Palma, D., Richard, C., Minella, M., 2022. State of the art and perspectives about non-thermal plasma applications for the removal of PFAS in water. Chemical Engineering Journal Advances 10, 100253. doi:10.1016/j.ceja.2022.100253.

Pan, H., Xia, Y., Qin, M., Cao, Y., Wang, W., 2015. A simple procedure to improve the surface passivation for single molecule fluorescence studies. Physical Biology 12 (4), 45006. doi:10.1088/1478-3975/12/4/045006.

Pang, C.M., Liu, W.-T., 2007. Community structure analysis of reverse osmosis membrane biofilms and the significance of Rhizobiales bacteria in biofouling. Environ. Sci. Technol. 41 (13), 4728–4734. doi:10.1021/es0701614.

Parks, D.H., Chuvochina, M., Waite, D.W., Rinke, C., Skarshewski, A., Chaumeil, P.-A., Hugenholtz, P., 2018. A standardized bacterial taxonomy based on genome

phylogeny substantially revises the tree of life. Nature Biotechnology 36 (10), 996–1004. doi:10.1038/nbt.4229.

Petersen, R.J., 1993. Composite reverse osmosis and nanofiltration membranes. Journal of Membrane Science 83 (1), 81–150. doi:10.1016/0376-7388(93)80014-O.

Pousty, D., Hofmann, R., Gerchman, Y., Mamane, H., 2021. Wavelength-dependent time-dose reciprocity and stress mechanism for UV-LED disinfection of Escherichia coli. Journal of Photochemistry and Photobiology. B, Biology 217, 112129. doi:10.1016/j.jphotobiol.2021.112129.

Pousty, D., Mamane, H., Cohen-Yaniv, V., Bolton, J.R., 2022. Ultraviolet actinometry – Determination of the incident photon flux and quantum yields for photochemical systems using low-pressure and ultraviolet light-emitting diode light sources. Journal of Environmental Chemical Engineering 10 (3), 107947. doi:10.1016/j.jece.2022.107947.

Promega Corporation, 2016. BacTiter-Glo™ Microbial Cell Viability Assay, Madison, WI, USA.

Pullerits, K., Ahlinder, J., Holmer, L., Salomonsson, E., Öhrman, C., Jacobsson, K., Dryselius, R., Forsman, M., Paul, C.J., Rådström, P., 2020. Impact of UV irradiation at full scale on bacterial communities in drinking water. npj Clean Water 3 (1), 3. doi:10.1038/s41545-020-0057-7.

QSIL GmbH, 2013. Materialspezifikation Quarzglas imasil(R) PN, 101st ed. https://www.qsil.com/fileadmin/user_upload/pdf_Dateien/Materialien_und_Produkte/QSILilmasilPN_d.pdf (accessed 12.03.2023).

Qualls, R.G., Johnson, J.D., 1983. Bioassay and dose measurement in UV disinfection. Applied and Environmental Microbiology 45 (3), 872–877. doi:10.1128/aem.45.3.872-877.1983.

Rabani, J., Mamane, H., Pousty, D., Bolton, J.R., 2021. Practical Chemical Actinometry-A Review. Photochem Photobiol 97 (5), 873–902. doi:10.1111/php.13429.

Radu, A.I., Vrouwenvelder, J.S., van Loosdrecht, M., Picioreanu, C., 2010. Modeling the effect of biofilm formation on reverse osmosis performance: Flux, feed channel pressure drop and solute passage. Journal of Membrane Science 365 (1-2), 1–15. doi:10.1016/j.memsci.2010.07.036.

Rahn, R.O., 1997. Potassium Iodide as a Chemical Actinometer for 254 nm Radiation: Use of Iodate as an Electron Scavenger. Photochem Photobiol 66 (4), 450–455. doi:10.1111/j.1751-1097.1997.tb03172.x.

Rahn, R.O., Stefan, M.I., Bolton, J.R., Goren, E., Shaw, P.-S., Lykke, K.R., 2003. Quantum Yield of the Iodide-Iodate Chemical Actinometer: Dependence on Wavelength and Concentration. Photochem Photobiol 78 (2), 146–152. doi:10.1562/0031-8655(2003)0780146QYOTIC2.0.CO2.

Ranga Suri, N.N.R., Murty M, N., Athithan, G., 2019. Outlier Detection, in: Ranga Suri, N.N.R., Murty M, N., Athithan, G. (Eds.), Outlier Detection: Techniques and Applications, vol. 155. Intelligent Systems Reference Library. Springer International Publishing, Cham, pp. 13–27.

Rastogi, R.P., Richa, Kumar, A., Tyagi, M.B., Sinha, R.P., 2010. Molecular mechanisms of ultraviolet radiation-induced DNA damage and repair. Journal of Nucleic Acids 2010, 592980. doi:10.4061/2010/592980.

Reed, R.H., 2004. The Inactivation of Microbes by Sunlight: Solar Disinfection as a Water Treatment Process. Adv. Appl. Microbiol. 54, 333–365. doi:10.1016/S0065-2164(04)54012-1.

Rehlen, L.F., 2017. Determination of a reliable method to identify the irradiance of LED array systems: For drinking water disinfection. Study Project, Munich, Germany.

Reichenberger, E.R., Rosen, G., Hershberg, U., Hershberg, R., 2015. Prokaryotic nucleotide composition is shaped by both phylogeny and the environment. Genome Biology and Evolution 7 (5), 1380–1389. doi:10.1093/gbe/evv063.

Rho, H., Yu, P., Zhao, Z., Lee, C.-S., Chon, K., Perreault, F., Alvarez, P.J.J., Amy, G., Westerhoff, P., 2022. Inhibition of biofouling on reverse osmosis membrane surfaces by germicidal ultraviolet light side-emitting optical fibers. Water Research 224, 119094. doi:10.1016/j.watres.2022.119094.

Richey, A.S., Thomas, B.F., Lo, M.-H., Famiglietti, J.S., Swenson, S., Rodell, M., 2015. Uncertainty in global groundwater storage estimates in a Total Groundwater Stress framework. Water Resources Research 51 (7), 5198–5216. doi:10.1002/2015WR017351.

Richter, Ł., Księżarczyk, K., Paszkowska, K., Janczuk-Richter, M., Niedziółka-Jönsson, J., Gapiński, J., Łoś, M., Hołyst, R., Paczesny, J., 2021. Adsorption of bacteriophages on polypropylene labware affects the reproducibility of phage research. Scientific Reports 11 (1), 7387. doi:10.1038/s41598-021-86571-x.

Ridgway, H.F., Kelly, A., Justice, C., Olson, B.H., 1983. Microbial fouling of reverse-osmosis membranes used in advanced wastewater treatment technology: chemical, bacteriological, and ultrastructural analyses. Applied and Environmental Microbiology 45 (3), 1066–1084. doi:10.1128/aem.45.3.1066-1084.1983.

Ridgway, H.F., Safarik J., 1991. Biofouling of reverse osmosis membranes, in: Flemming, H.-C., Geesey, G.G. (Eds.), Biofouling and Biocorrosion in Industrial Water Systems. Springer Berlin Heidelberg, Berlin, Heidelberg, pp. 81–111.

Riesenman, P.J., Nicholson, W.L., 2000. Role of the spore coat layers in Bacillus subtilis spore resistance to hydrogen peroxide, artificial UV-C, UV-B, and solar UV radiation. Applied and Environmental Microbiology 66 (2), 620–626. doi:10.1128/aem.66.2.620-626.2000.

Ritchie, H., Roser, M., 2017. Water Use and Stress (accessed 18.10.2022). https://ourworldindata.org/water-use-stress.

Roback, S.L., Ishida, K.P., Chuang, Y.-H., Zhang, Z., Mitch, W.A., Plumlee, M.H., 2021. Pilot UV-AOP Comparison of UV/Hydrogen Peroxide, UV/Free Chlorine, and UV/Monochloramine for the Removal of N -Nitrosodimethylamine (NDMA) and NDMA Precursors. ACS ES&T Water 1 (2), 396–406. doi:10.1021/acsestwater.0c00155.

Roibu, A., Fransen, S., Leblebici, M.E., Meir, G., van Gerven, T., Kuhn, S., 2018. An accessible visible-light actinometer for the determination of photon flux and optical pathlength in flow photo microreactors. Scientific Reports 8 (1), 5421. doi:10.1038/s41598-018-23735-2.

Romero-Martínez, L., Duque-Sarango, P., Acevedo-Merino, A., Nebot, E., 2019. Comparing the inactivating efficacy of enteric bacteria in seawater treated with different configurations of continuous flow-through ultraviolet devices: single-pass and recirculation. J. Chem. Technol. Biotechnol. 94 (9), 2980–2989. doi:10.1002/jctb.6108.

Saad, M.A., 1992. Biofouling prevention in RO polymeric membrane systems. Desalination 88 (1-3), 85–105. doi:10.1016/0011-9164(92)80107-K.

Sahai, H., Khurshid, A., 1993. Confidence Intervals for the Mean of a Poisson Distribution: A Review. Biom. J. 35 (7), 857–867. doi:10.1002/bimj.4710350716.

Sanawar, H., Kim, L.H., Farhat, N.M., van Loosdrecht, M.C.M., Vrouwenvelder, J.S., 2021. Periodic chemical cleaning with urea: disintegration of biofilms and reduction of key biofilm-forming bacteria from reverse osmosis membranes. Water Research X 13, 100117. doi:10.1016/j.wroa.2021.100117.

Sánchez, O., 2018. Microbial diversity in biofilms from reverse osmosis membranes: A short review. Journal of Membrane Science 545, 240–249. doi:10.1016/j.memsci.2017.09.082.

Schmalwieser, A.W., Hirschmann, G., Cabaj, A., Sommer, R., 2017. Method to determine the power efficiency of UV disinfection plants and its application to low pressure plants for drinking water. Water Supply 17 (4), 947–957. doi:10.2166/ws.2016.185.

Schwarzenbach, R.P., Egli, T., Hofstetter, T.B., Gunten, U. von, Wehrli, B., 2010. Global Water Pollution and Human Health. Annu. Rev. Environ. Resour. 35 (1), 109–136. doi:10.1146/annurev-environ-100809-125342.

Schwarzenbach, R.P., Escher, B.I., Fenner, K., Hofstetter, T.B., Johnson, C.A., Gunten, U. von, Wehrli, B., 2006. The challenge of micropollutants in aquatic systems. Science 313 (5790), 1072–1077. doi:10.1126/science.1127291.

Selinummi, J., Seppälä, J., Yli-Harja, O., Puhakka, J.A., 2005. Software for quantification of labeled bacteria from digital microscope images by automated image analysis. BioTechniques 39 (6), 859–863. doi:10.2144/000112018.

Seoul Viosys, 2017. UV CA3535 series (CUD7GF1B): Deep UV LED - 275nm, Rev. 2.0.

Severin, B.F., Suidan, M.T., Engelbrecht, R.S., 1983. Kinetic modeling of U.V. disinfection of water. Water Research 17 (11), 1669–1678. doi:10.1016/0043-1354(83)90027-1.

Shehata, O., 2020. Characterization of a pulsed flow through UVC-LED reactor and the impact of fluence rate on microbial disinfection. Master's Thesis, Munich, Germany.

Shiklomanoc, I.A., 1993. World fresh water resources, in: , Water in Crisis. A Guide to the World's Fresh Water Resources, New York, USA, pp. 13–24.

Sholtes, K., Linden, K.G., 2019. Pulsed and continuous light UV LED: microbial inactivation, electrical, and time efficiency. Water Research 165, 114965. doi:10.1016/j.watres.2019.114965.

Shrivastava, A., Rosenberg, S., Peery, M., 2015. Energy efficiency breakdown of reverse osmosis and its implications on future innovation roadmap for desalination. Desalination 368, 181–192. doi:10.1016/j.desal.2015.01.005.

Siddiqui, A., Lehmann, S., Bucs, S.S., Fresquet, M., Fel, L., Prest, E.I.E.C., Ogier, J., Schellenberg, C., van Loosdrecht, M.C.M., Kruithof, J.C., Vrouwenvelder, J.S., 2017. Predicting the impact of feed spacer modification on biofouling by hydraulic characterization and biofouling studies in membrane fouling simulators. Water Research 110, 281–287. doi:10.1016/j.watres.2016.12.034.

Silva, C., Pinto da Cunha, J., Pereira, A., Chepel, V., Lopes, M.I., Solovov, V., Neves, F., 2010. Reflectance of polytetrafluoroethylene for xenon scintillation light. Journal of Applied Physics 107 (6), 64902. doi:10.1063/1.3318681.

Simons, R., Gabbai, U.E., Moram, M.A., 2014. Optical fluence modelling for ultraviolet light emitting diode-based water treatment systems. Water Research 66, 338–349. doi:10.1016/j.watres.2014.08.031.

Sinha, R.P., Häder, D.P., 2002. UV-induced DNA damage and repair: a review. Photochemical & Photobiological Sciences : Official journal of the European Photochemistry Association and the European Society for Photobiology 1 (4), 225–236. doi:10.1039/b201230h.

Smith, J.A., Hurrell, J., Leach, S.J., 1978. Elimination of nonspecific adsorption of serum proteins by Sepharose-bound antigens. Analytical Biochemistry 87 (2), 299–305. doi:10.1016/0003-2697(78)90679-6.

Smith, W.L., Lagunas-Solar, M.C., Cullor, J.S., 2002. Use of pulsed ultraviolet laser light for the cold pasteurization of bovine milk. Journal of Food Protection 65 (9), 1480–1482. doi:10.4315/0362-028X-65.9.1480.

Solano, C., Echeverz, M., Lasa, I., 2014. Biofilm dispersion and quorum sensing. Current Opinion in Microbiology 18, 96–104. doi:10.1016/j.mib.2014.02.008.

Soloshenko, I.A., Bazhenov, V.Y., Khomich, V.A., Tsiolko, V.V., Potapchenko, N.G., 2006. Comparative Research of Efficiency of Water Decontamination by UV Radiation of Cold Hollow Cathode Discharge Plasma Versus That of Low- and Medium-Pressure Mercury Lamps. IEEE Trans. Plasma Sci. 34 (4), 1365–1369. doi:10.1109/TPS.2006.878997.

Sommer, R., Cabaj, A., Haider, T., 1996. Microbicidal effect of reflected uv radiation in devices for water disinfection. Water Science and Technology 34 (7-8). doi:10.1016/S0273-1223(96)00742-1.

Sommer, R., Haider, T., Cabaj, A., Pribil, W., Lhotsky, M., 1998. Time dose reciprocity in UV disinfection of water. Water Science and Technology : A Journal of The International Association on Water Pollution Research 38 (12). doi:10.1016/S0273-1223(98)00816-6.

Son, M., Yang, W., Bucs, S.S., Nava-Ocampo, M.F., Vrouwenvelder, J.S., Logan, B.E., 2018. Polyelectrolyte-Based Sacrificial Protective Layer for Fouling Control in Reverse Osmosis Desalination. Environ. Sci. Technol. Lett. 5 (9), 584–590. doi:10.1021/acs.estlett.8b00400.

Song, K., Mohseni, M., Taghipour, F., 2016. Application of ultraviolet light-emitting diodes (UV-LEDs) for water disinfection: A review. Water Research 94, 341–349. doi:10.1016/j.watres.2016.03.003.

Song, K., Mohseni, M., Taghipour, F., 2019a. Mechanisms investigation on bacterial inactivation through combinations of UV wavelengths. Water Research 163, 114875. doi:10.1016/j.watres.2019.114875.

Song, K., Taghipour, F., Mohseni, M., 2018. Microorganisms inactivation by continuous and pulsed irradiation of ultraviolet light-emitting diodes (UV-LEDs). Chemical Engineering Journal 343, 362–370. doi:10.1016/j.cej.2018.03.020.

Song, K., Taghipour, F., Mohseni, M., 2019b. Microorganisms inactivation by wavelength combinations of ultraviolet light-emitting diodes (UV-LEDs). The Science of The Total Environment 665, 1103–1110. doi:10.1016/j.scitotenv.2019.02.041.

Song, L., Elimelech, M., 1995. Theory of concentration polarization in crossflow filtration. Faraday Trans. 91 (19), 3389. doi:10.1039/ft9959103389.

Sperle, P., Khan, M.S., Drewes, J.E., Wurzbacher, C., 2023a. A Practical Bacterial Biodosimetry Procedure to Assess Performance of Lab-Scale Flow-through Ultraviolet Water Disinfection Reactors. ACS ES&T Water 3 (8), 2130–2139. doi:10.1021/acsestwater.2c00648.

Sperle, P., Khan, M.S., Skibinski, B., Wurzbacher, C., Drewes, J.E., 2023b. Optimizing UVC-disinfection using LEDs as an energy efficient pre-treatment for biofouling control in spiral-wound membrane systems. Desalination 557, 116589. doi:10.1016/j.desal.2023.116589.

Sperle, P., Mirlach, A., Linden, K., Hübner, U., Drewes, J.E., 2023c. An actinometric method to characterize performance of reflecting UVC reactors used for water treatment. Water Research 230, 119543. doi:10.1016/j.watres.2022.119543.

Sperle, P., Wurzbacher, C., Drewes, J.E., Skibinski, B., 2020a. Reducing the Impacts of Biofouling in RO Membrane Systems through In Situ Low Fluence Irradiation Employing UVC-LEDs. Membranes 10 (12). doi:10.3390/membranes10120415.

Sperle, P., Wurzbacher, C., Drewes, J.E., Skibinski, B. [Dataset], Mendeley Data, V1, 2020b. Supplementary Materials: Reducing the Impacts of Biofouling in RO Membrane Systems through in-situ Low Fluence Irradiation Employing UVC-LEDs. doi:10.17632/rcpkdzzx7s.1. https://data.mendeley.com/datasets/rcpkdzzx7s. accessed on 09.12.2020.

SphereOptics, 2021. Calibration Certificate: Report-No. 21060406, Herrsching am Ammersee, Germany.

Stedmon, C.A., Bro, R., 2008. Characterizing dissolved organic matter fluorescence with parallel factor analysis: a tutorial. Limnol. Oceanogr. Methods 6 (11), 572–579. doi:10.4319/lom.2008.6.572.

Stephens, M., 2017. False discovery rates: a new deal. Biostatistics (Oxford, England) 18 (2), 275–294. doi:10.1093/biostatistics/kxw041.

Subramani, A., Hoek, E.M., 2010. Biofilm formation, cleaning, re-formation on polyamide composite membranes. Desalination 257 (1-3), 73–79. doi:10.1016/j.desal.2010.03.003.

Suhalim, N.S., Kasim, N., Mahmoudi, E., Shamsudin, I.J., Mohammad, A.W., Mohamed Zuki, F., Jamari, N.L.-A., 2022. Rejection Mechanism of Ionic Solute Removal by Nanofiltration Membranes: An Overview. Nanomaterials (Basel, Switzerland) 12 (3). doi:10.3390/nano12030437.

Sultana, H., 2022. UVC-pretreatment using LEDs for biofouling control in reverse osmosis membrane systems. Study Project, Munich, Germany.

Sun, L., Chen, W., Huang, K., Lyu, W., Gao, X., 2021. Aquabacterium soli sp. nov., a novel bacterium isolated from soil under the long-term application of bifenthrin. International Journal of Systematic and Evolutionary Microbiology 71 (9). doi:10.1099/ijsem.0.004768.

Sun, Z., Li, M., Li, W., Qiang, Z., 2022. A review of the fluence determination methods for UV reactors: Ensuring the reliability of UV disinfection. Chemosphere 286 (Pt 1), 131488. doi:10.1016/j.chemosphere.2021.131488.

Takeshita, K., 2003. Damage of yeast cells induced by pulsed light irradiation. International Journal of Food Microbiology 85 (1-2), 151–158. doi:10.1016/S0168-1605(02)00509-3.

Tan, Y.-J., Sun, L.-J., Li, B.-T., Zhao, X.-H., Yu, T., Ikuno, N., Ishii, K., Hu, H.-Y., 2017. Fouling characteristics and fouling control of reverse osmosis membranes for desalination of dyeing wastewater with high chemical oxygen demand. Desalination 419, 1–7. doi:10.1016/j.desal.2017.04.029.

Tang, C.Y., Fu, Q.S., Robertson, A.P., Criddle, C.S., Leckie, J.O., 2006. Use of reverse osmosis membranes to remove perfluorooctane sulfonate (PFOS) from semiconductor wastewater. Environ. Sci. Technol. 40 (23), 7343–7349. doi:10.1021/es060831q.

Tang, C.Y., Kwon, Y.-N., Leckie, J.O., 2007. Probing the nano- and micro-scales of reverse osmosis membranes—A comprehensive characterization of physiochemical properties of uncoated and coated membranes by XPS, TEM, ATR-FTIR, and streaming potential measurements. Journal of Membrane Science 287 (1), 146–156. doi:10.1016/j.memsci.2006.10.038.

Tang, L., Livi, K.J.T., Chen, K.L., 2015. Polysulfone Membranes Modified with Bioinspired Polydopamine and Silver Nanoparticles Formed in Situ To Mitigate Biofouling. Environ. Sci. Technol. Lett. 2 (3), 59–65. doi:10.1021/acs.estlett.5b00008.

Taylor, R.G., Scanlon, B., Döll, P., Rodell, M., van Beek, R., Wada, Y., Longuevergne, L., Leblanc, M., Famiglietti, J.S., Edmunds, M., Konikow, L., Green, T.R., Chen, J., Taniguchi, M., Bierkens, M.F.P., MacDonald, A., Fan, Y., Maxwell, R.M., Yechieli, Y., Gurdak, J.J., Allen, D.M., Shamsudduha, M., Hiscock, K., Yeh, P.J.-F., Holman, I.,

Treidel, H., 2013. Ground water and climate change. Nature Clim Change 3 (4), 322–329. doi:10.1038/nclimate1744.

Ternes, T.A., Giger, W., Joss, A., 2006. Introduction, in: Ternes, T., Joss, A. (Eds.), Human Pharmaceuticals, Hormones and Fragrances. The Challenge of Micropollutants in Urban Water Management 5. IWA Publishing, London, UK.

The SILVA ribosomal RNA database project, n. d. The SILVA Taxonomy. The SILVA ribosomal RNA database project (accessed 13.10.2020). https://www.arb-silva.de/documentation/silva-taxonomy/.

Thoma, F., 1999. Light and dark in chromatin repair: repair of UV-induced DNA lesions by photolyase and nucleotide excision repair. The EMBO Journal 18 (23), 6585–6598. doi:10.1093/emboj/18.23.6585.

Tiwari, K., 2022. Effect of oxygen partial pressure on MBBR treatment of Produced Water. Master's Thesis, Munich, Germany, Copenhagen, Denmark.

Tomaszewska, M., 2007. Industrial wastewater treatment by means of membrane techniques. Polish Journal of Chemical Technology 9 (3), 149. doi:10.2478/v10026-007-0074-z.

Torkzadeh, H., Cates, E.L., 2021. Biofilm growth under continuous UVC irradiation: Quantitative effects of growth conditions and growth time on intensity response parameters. Water Research 206, 117747. doi:10.1016/j.watres.2021.117747.

Torkzadeh, H., Zodrow, K.R., Bridges, W.C., Cates, E.L., 2021. Quantification and modeling of the response of surface biofilm growth to continuous low intensity UVC irradiation. Water Research 193, 116895. doi:10.1016/j.watres.2021.116895.

Tran, T., Racz, L., Grimaila, M.R., Miller, M., Harper, W.F., 2014. Comparison of continuous versus pulsed ultraviolet light emitting diode use for the inactivation of Bacillus globigii spores. Water Science and Technology : A Journal of The International Association on Water Pollution Research 70 (9), 1473–1480. doi:10.2166/wst.2014.395.

U.S. Environmental Protection Agency (U.S. EPA), 2003. Ultraviolet Disindection Guidance Manual, Washington DC, USA. https://nepis.epa.gov/Exe/ZyNET.exe/901T0000.TXT?ZyActionD=ZyDocument&Client=EPA&Index=2000+Thru+2005&Docs=&Query=&Time=&EndTime=&SearchMethod=1&TocRestrict=n&Toc=&TocEntry=&QField=&QFieldYear=&QFieldMonth=&QFieldDay=&IntQFieldOp=0&ExtQFieldOp=0&XmlQuery=&File=D%3A%5Czyfiles%5CIndex%20Data%5C00thru05%5CTxt%5C00000011%5C901T0000.txt&User=ANONYMOUS&Password=anonymous&SortMethod=h%7C-&MaximumDocuments=1&FuzzyDegree=0&ImageQuality=r75g8/r75g8/x150y150g16/i425&Display=hpfr&DefSeekPage=x&SearchBack=ZyActionL&Back=ZyActionS&BackDesc=Results%20page&MaximumPages=1&ZyEntry=1&SeekPage=x&ZyPURL#.

U.S. Environmental Protection Agency (U.S. EPA); CDM Smith, 2017. Potable Reuse Compendium. https://www.epa.gov/sites/production/files/2018-01/documents/potablereusecompendium_3.pdf.

U.S. EPA, 2006. Ultraviolet disinfection guidance manual for the final long term 2 enhanced surface water treatment rule, Washington DC. https://www.epa.gov/dwreginfo/long-term-2-enhanced-surface-water-treatment-rule-documents (accessed 11.12.2022).

Ulm, K., 1990. A simple method to calculate the confidence interval of a standardized mortality ratio (SMR). American Journal of Epidemiology 131 (2), 373–375. doi:10.1093/oxfordjournals.aje.a115507.

United Nations Educational, Scientific and Cultural Organization (UNESCO). Wastewater: The untapped resource. The United Nations World Water Development Report, Paris, 180 pp. http://www.unesco.org/ulis/cgi-bin/ulis.pl?catno=247153.

United Nations Educational, Scientific and Cultural Organization (UNESCO), 2020. Water and climate change: The united Nations World water development report 2020, Paris, France. https://unesdoc.unesco.org/ark:/48223/pf0000372985.locale=en (accessed 18.10.2022).

United Nations Educational, Scientific and Cultural Organization (UNESCO), 2022. Groundwater making the invisible visible: The United Nations World Water Development Report 2022, Paris, France. https://www.unesco.org/reports/wwdr/2022/en (accessed 18.10.2022).

Uroz, S., Dessaux, Y., Oger, P., 2009. Quorum sensing and quorum quenching: the yin and yang of bacterial communication. Chembiochem : A European Journal of Chemical Biology 10 (2), 205–216. doi:10.1002/cbic.200800521.

van der Bruggen, B., 2018. Microfiltration, ultrafiltration, nanofiltration, reverse osmosis, and forward osmosis, in: , Fundamental Modelling of Membrane Systems. Elsevier, pp. 25–70.

van der Bruggen, B., Vandecasteele, C., van Gestel, T., Doyen, W., Leysen, R., 2003. A review of pressure-driven membrane processes in wastewater treatment and drinking water production. Environ. Prog. 22 (1), 46–56. doi:10.1002/ep.670220116.

van Houtte, E., Verbauwhede, J., 2013. Long-time membrane experience at Torreele's water re-use facility in Belgium. Desalination and Water Treatment 51 (22-24), 4253–4262. doi:10.1080/19443994.2013.769487.

van Weert, F., van der Gun, J., Reckmann, J., 2009. Global Overview of Saline Groundwater Occurrence and Genesis. International Groundwater Resources Assessment Centre (igrac), Utrecht, Netherlands.

Velten, S., Hammes, F., Boller, M., Egli, T., 2007. Rapid and direct estimation of active biomass on granular activated carbon through adenosine tri-phosphate (ATP) determination. Water Research 41 (9), 1973–1983. doi:10.1016/j.watres.2007.01.021.

Vilhunen, S., Särkkä, H., Sillanpää, M., 2009. Ultraviolet light-emitting diodes in water disinfection. Environmental Science and Pollution Research International 16 (4), 439–442. doi:10.1007/s11356-009-0103-y.

Vitzilaiou, E., Kuria, A.M., Siegumfeldt, H., Rasmussen, M.A., Knøchel, S., 2021. The impact of bacterial cell aggregation on UV inactivation kinetics. Water Research 204, 117593. doi:10.1016/j.watres.2021.117593.

von Sonntag, C., Schuchmann, H.-P., 1992. UV disinfection of drinkingwater and by-product formation-some basic considerations. J. Water SRT-Aqua (Vol. 41), 67–74.

Vonderheide, A.P., Mueller, K.E., Meija, J., Welsh, G.L., 2008. Polybrominated diphenyl ethers: causes for concern and knowledge gaps regarding environmental distribution, fate and toxicity. The Science of The Total Environment 400 (1-3), 425–436. doi:10.1016/j.scitotenv.2008.05.003.

Voutchkov, N., Semanti, R., 2008. Seawater Desalination, in: Li, N.N., Fane, A.G., Ho, W.S.W., Matsuura, T. (Eds.), Advanced Membrane Technology and Applications. John Wiley & Sons, Inc, Hoboken, NJ, USA, pp. 47–86.

Vrouwenvelder, J., Vanpaassen, J., Wessels, L., Vandam, A., Bakker, S., 2006. The Membrane Fouling Simulator: A practical tool for fouling prediction and control. Journal of Membrane Science 281 (1-2), 316–324. doi:10.1016/j.memsci.2006.03.046.

Vrouwenvelder, J.S., Beyer, F., Dahmani, K., Hasan, N., Galjaard, G., Kruithof, J.C., van Loosdrecht, M.C.M., 2010a. Phosphate limitation to control biofouling. Water Research 44 (11), 3454–3466. doi:10.1016/j.watres.2010.03.026.

Vrouwenvelder, J.S., Buiter, J., Riviere, M., van der Meer, W.G.J., van Loosdrecht, M.C.M., Kruithof, J.C., 2010b. Impact of flow regime on pressure drop increase and biomass accumulation and morphology in membrane systems. Water Research 44 (3), 689–702. doi:10.1016/j.watres.2009.09.054.

Vrouwenvelder, J.S., Graf von der Schulenburg, D.A., Kruithof, J.C., Johns, M.L., van Loosdrecht, M.C.M., 2009a. Biofouling of spiral-wound nanofiltration and reverse osmosis membranes: a feed spacer problem. Water Research 43 (3), 583–594. doi:10.1016/j.watres.2008.11.019.

Vrouwenvelder, J.S., Hinrichs, C., van der Meer, W.G.J., van Loosdrecht, M.C.M., Kruithof, J.C., 2009b. Pressure drop increase by biofilm accumulation in spiral wound RO and NF membrane systems: role of substrate concentration, flow velocity, substrate load and flow direction. Biofouling 25 (6), 543–555. doi:10.1080/08927010902972225.

Vrouwenvelder, J.S., Kruithof, J., van Loosdrecht, M., 2009c. Biofouling of spiral wound membrane systems. IWA Publishing, London, UK.

Vrouwenvelder, J.S., Kruithof, J.C., van Loosdrecht, M.C.M., 2010c. Integrated approach for biofouling control. Water Science and Technology : A Journal of The International Association on Water Pollution Research 62 (11), 2477–2490. doi:10.2166/wst.2010.747.

Vrouwenvelder, J.S., van der Kooij, D., 2001. Diagnosis, prediction and prevention of biofouling of NF and RO membranes. Desalination 139 (1-3), 65–71. doi:10.1016/S0011-9164(01)00295-8.

Vrouwenvelder, J.S., van Loosdrecht, M., Kruithof, J.C., 2011. Early warning of biofouling in spiral wound nanofiltration and reverse osmosis membranes. Desalination 265 (1-3), 206–212. doi:10.1016/j.desal.2010.07.053.

Vrouwenvelder, J.S., van Paassen, J., Kruithof, J.C., van Loosdrecht, M., 2009d. Sensitive pressure drop measurements of individual lead membrane elements for accurate early biofouling detection. Journal of Membrane Science 338 (1-2), 92–99. doi:10.1016/j.memsci.2009.04.016.

Wang, C.-P., Chang, C.-S., Lin, W.-C., 2021. Efficiency improvement of a flow-through water disinfection reactor using UV-C light emitting diodes. Journal of Water Process Engineering 40, 101819. doi:10.1016/j.jwpe.2020.101819.

Wang, H., Hu, H., Chen, S., Schwarz, C., Yin, H., Hu, C., Li, G., Shi, B., Huang, J., 2023a. UV pretreatment reduced biofouling of ultrafiltration and controlled opportunistic pathogens in secondary water supply systems. Desalination 548, 116282. doi:10.1016/j.desal.2022.116282.

Wang, L., He, J., Heiranian, M., Fan, H., Song, L., Li, Y., Elimelech, M., 2023b. Water transport in reverse osmosis membranes is governed by pore flow, not a solution-diffusion mechanism. Science Advances 9 (15), eadf8488. doi:10.1126/sciadv.adf8488.

Wang, T., MacGregor, S.J., Anderson, J.G., Woolsey, G.A., 2005. Pulsed ultra-violet inactivation spectrum of Escherichia coli. Water Research 39 (13), 2921–2925. doi:10.1016/j.watres.2005.04.067.

Wang, W.-L., Wu, Q.-Y., Li, Z.-M., Lu, Y., Du, Y., Wang, T., Huang, N., Hu, H.-Y., 2017. Light-emitting diodes as an emerging UV source for UV/chlorine oxidation: Carbamazepine degradation and toxicity changes. Chemical Engineering Journal 310, 148–156. doi:10.1016/j.cej.2016.10.097.

Warnecke, F., Sommaruga, R., Sekar, R., Hofer, J.S., Pernthaler, J., 2005. Abundances, identity, and growth state of actinobacteria in mountain lakes of different UV transparency. Applied and Environmental Microbiology 71 (9), 5551–5559. doi:10.1128/AEM.71.9.5551-5559.2005.

Warsinger, D.M., Chakraborty, S., Tow, E.W., Plumlee, M.H., Bellona, C., Loutatidou, S., Karimi, L., Mikelonis, A.M., Achilli, A., Ghassemi, A., Padhye, L.P., Snyder, S.A., Curcio, S., Vecitis, C.D., Arafat, H.A., Lienhard, J.H., 2018. A review of polymeric membranes and processes for potable water reuse. Progress in Polymer Science 81, 209–237. doi:10.1016/j.progpolymsci.2018.01.004.

Webb, J.S., Thompson, L.S., James, S., Charlton, T., Tolker-Nielsen, T., Koch, B., Givskov, M., Kjelleberg, S., 2003. Cell death in Pseudomonas aeruginosa biofilm development. Journal of Bacteriology 185 (15), 4585–4592. doi:10.1128/JB.185.15.4585-4592.2003.

Weidner, V.R., Hsia, J.J., 1981. Reflection properties of pressed polytetrafluoroethylene powder. J. Opt. Soc. Am. 71 (7), 856. doi:10.1364/JOSA.71.000856.

Weidner, V.R., Hsia, J.J., Adams, B., 1985. Laboratory intercomparison study of pressed polytetrafluoroethylene powder reflectance standards. Applied Optics 24 (14), 2225. doi:10.1364/ao.24.002225.

Wekhof, A., 2000. Disinfection with Flash Lamps. PDA Journal of Pharmaceutical Science & Technology 2000 (Vol. 54, No. 3), 264–276.

Wekhof, A., Trompeter, F.-J., Franken Oliver (Eds.), 2001. Pulsed UV Disintegration (PUVD): a new sterilisation mechanism for packaging and broad medical-hospital applications.

Wengraitis, S., McCubbin, P., Wade, M.M., Biggs, T.D., Hall, S., Williams, L.I., Zulich, A.W., 2013. Pulsed UV-C disinfection of Escherichia coli with light-emitting diodes, emitted at various repetition rates and duty cycles. Photochem Photobiol 89 (1), 127–131. doi:10.1111/j.1751-1097.2012.01203.x.

Wenjun, S., Wenjun, L., 2009. A pilot-scale study on ultraviolet disinfection system for drinking water. Journal of Water Supply: Research and Technology—AQUA 58 (5), 346. doi:10.2166/aqua.2009.086.

WHO -World Health Organization, 2017. Potable reuse: Guidance for producing safe drinking-water, Geneva, Switzerland.

Wilbert, M.C., 1997. Enhancement of Membrane Fouling Resistance through Surface Modification. A Study Using the Principle of Membrane Fouling and Cleaning To Develop Ways to Enhance Membrane Fouling Resistance. Water Treatment Technology Program Report 22. US Department of the Interior, Bureau of Reclamation, Denver, CO, USA.

Williams, P.M., 2015. Membrane Roughness, in: Drioli, E., Giorno, L. (Eds.), Encyclopedia of Membranes. Springer Berlin Heidelberg, Berlin, Heidelberg, pp. 1–2.

Wingender, J., Neu, T.R., Flemming, H.-C., 1999. Microbial Extracellular Polymeric Substances. Springer Berlin Heidelberg, Berlin, Heidelberg.

Wols, B.A., Hofman-Caris, C., Harmsen, D.J., Beerendonk, E.F., van Dijk, J.C., Chan, P.-S., Blatchley, E.R., 2012. Comparison of CFD, Biodosimetry and Lagrangian Actinometry to Assess UV Reactor Performance. Ozone: Science & Engineering 34 (2), 81–91. doi:10.1080/01919512.2012.651398.

Wood, T.L., Guha, R., Tang, L., Geitner, M., Kumar, M., Wood, T.K., 2016. Living biofouling-resistant membranes as a model for the beneficial use of engineered biofilms. Proceedings of the National Academy of Sciences of the United States of America 113 (20), E2802-11. doi:10.1073/pnas.1521731113.

World Health Organization (WHO), 2018. Chemical releases caused by natural hazard events and disasters: Information for public health authorities. https://www.who.int/publications/i/item/9789241513395.

Wright, E.S., 2016. Using DECIPHER v2.0 to Analyze Big Biological Sequence Data in R. The R Journal (8(1)), 352–359.

Wu, Y.-H., Chen, Z., Li, X., Wang, Y.-H., Liu, B., Chen, G.-Q., Luo, L.-W., Wang, H.-B., Tong, X., Bai, Y., Xu, Y.-Q., Ikuno, N., Li, C.-F., Zhang, H.-Y., Hu, H.-Y., 2021a. Effect

of ultraviolet disinfection on the fouling of reverse osmosis membranes for municipal wastewater reclamation. Water Research 195, 116995. doi:10.1016/j.watres.2021.116995.

Wu, Z., Barua, H., Rylski, J.R., Taylor, J.B., Kim, J., 2021b. A multiple regression model framework for designing a UVC LED reactor for point-of-use water treatment. Environ. Sci.: Water Res. Technol. 7 (8), 1516–1529. doi:10.1039/D1EW00215E.

Würtele, M.A., Kolbe, T., Lipsz, M., Külberg, A., Weyers, M., Kneissl, M., Jekel, M., 2011. Application of GaN-based ultraviolet-C light emitting diodes--UV LEDs--for water disinfection. Water Research 45 (3), 1481–1489. doi:10.1016/j.watres.2010.11.015.

Xiao, Y., Chu, X.N., He, M., Liu, X.C., Hu, J.Y., 2018. Impact of UVA pre-radiation on UVC disinfection performance: Inactivation, repair and mechanism study. Water Research 141, 279–288. doi:10.1016/j.watres.2018.05.021.

Yamashita, Y., Boyer, J.N., Jaffé, R., 2013. Evaluating the distribution of terrestrial dissolved organic matter in a complex coastal ecosystem using fluorescence spectroscopy. Continental Shelf Research 66, 136–144. doi:10.1016/j.csr.2013.06.010.

Yamashita, Y., Panton, A., Mahaffey, C., Jaffé, R., 2011. Assessing the spatial and temporal variability of dissolved organic matter in Liverpool Bay using excitation–emission matrix fluorescence and parallel factor analysis. Ocean Dynamics 61 (5), 569–579. doi:10.1007/s10236-010-0365-4.

Yamashita, Y., Tanoue, E., 2004. Chemical characteristics of amino acid-containing dissolved organic matter in seawater. Organic Geochemistry 35 (6), 679–692. doi:10.1016/j.orggeochem.2004.02.007.

Yang, C., Sun, W., Ao, X., 2020. Bacterial inactivation, DNA damage, and faster ATP degradation induced by ultraviolet disinfection. Front. Environ. Sci. Eng. 14 (1), 135. doi:10.1007/s11783-019-1192-6.

Yang, H.-L., Lin, J.C.-T., Huang, C., 2009. Application of nanosilver surface modification to RO membrane and spacer for mitigating biofouling in seawater desalination. Water Research 43 (15), 3777–3786. doi:10.1016/j.watres.2009.06.002.

Younas, H., Fei, Y., Shao, J., He, Y., 2016. Developing an antibacterial super-hydrophilic barrier between bacteria and membranes to mitigate the severe impacts of biofouling. Biofouling 32 (9), 1089–1102. doi:10.1080/08927014.2016.1229775.

Zalazar, C.S., Labas, M.D., Martín, C.A., Brandi, R.J., Alfano, O.M., Cassano, A.E., 2005. The extended use of actinometry in the interpretation of photochemical reaction engineering data. Chemical Engineering Journal 109 (1-3), 67–81. doi:10.1016/j.cej.2005.03.011.

Zhang, Z., Cao, R., Jin, L., Zhu, W., Ji, Y., Xu, X., Zhu, L., 2019. The regulation of N-acyl-homoserine lactones (AHLs)-based quorum sensing on EPS secretion via ATP synthetic for the stability of aerobic granular sludge. The Science of The Total Environment 673, 83–91. doi:10.1016/j.scitotenv.2019.04.052.

Zhang, Z., Schwartz, S., Wagner, L., Miller, W., 2000. A greedy algorithm for aligning DNA sequences. Journal of Computational Biology : A Journal of Computational Molecular Cell Biology 7 (1-2), 203–214. doi:10.1089/10665270050081478.

Zhu, X., Elimelech, M., 1997. Colloidal Fouling of Reverse Osmosis Membranes: Measurements and Fouling Mechanisms. Environ. Sci. Technol. 31 (12), 3654–3662. doi:10.1021/es970400v.

Zodrow, K.R., Bar-Zeev, E., Giannetto, M.J., Elimelech, M., 2014. Biofouling and microbial communities in membrane distillation and reverse osmosis. Environ. Sci. Technol. 48 (22), 13155–13164. doi:10.1021/es503051t.

Zou, X.-Y., Lin, Y.-L., Xu, B., Cao, T.-C., Tang, Y.-L., Pan, Y., Gao, Z.-C., Gao, N.-Y., 2019. Enhanced inactivation of E. coli by pulsed UV-LED irradiation during water disinfection. The Science of The Total Environment 650 (Pt 1), 210–215. doi:10.1016/j.scitotenv.2018.08.367.

12. Appendix

12.1. List of publications and conferences

12.1.1. Research articles (peer-reviewed)

1. Sperle, P., Wurzbacher, C., Drewes, J.E., Skibinski, B., 2020. Reducing the Impacts of Biofouling in RO Membrane Systems through In Situ Low Fluence Irradiation Employing UVC-LEDs. Membranes 10 (12). doi:10.3390/membranes10120415.
   This publication is included in Chapter 4.

2. Sperle, P., Mirlach, A., Linden, K., Hübner, U., Drewes, J.E., 2023. An actinometric method to characterize performance of reflecting UVC reactors used for water treatment. Water research 230, 119543. doi:10.1016/j.watres.2022.119543.
   This publication is included in Chapter 5.

3. Sperle, P., Khan, M.S., Drewes, J.E., Wurzbacher, C., 2023. A Practical Bacterial Biodosimetry Procedure to Assess Performance of Lab-Scale Flow-through Ultraviolet Water Disinfection Reactors. *ACS ES&T Water* 3 (8), 2130–2139.. doi:10.1021/acsestwater.2c00648.
   This publication is included in Chapter 6.

4. Sperle, P., Khan, M.S., Skibinski, B., Wurzbacher, C., Drewes, J.E., 2023. Optimizing UVC-disinfection using LEDs as an energy efficient pre-treatment for biofouling control in spiral-wound membrane systems. Desalination 557, 116589. doi:10.1016/j.desal.2023.116589.
   This publication is included in Chapter 7.

12.1.2. Research reports

Drewes, J.E., Sperle, P., 2022. Entwicklung eines neuartigen UV-Bestrahlungssystems zur Steigerung der Ressourceneffizienz von Umkehrosmoseanlagen in der Wasseraufbereitung, Teilprojekt 3 (TUM) : Sachbericht zum Verwendungsnachweis : Laufzeit: 10.2018-12.2021 02WQ1467C, 01184175. Technical University of Munich.

12.1.3. Conference talks

- Sperle P.; Wurzbacher C.; Skibinski B.; Drewes J.E.: Reducing the impacts of biofouling in reverse osmosis membrane systems through low fluence pretreatment employing UVC-LED irradiation. International Water Association (IWA) Biofilms Virtual Conference – Emerging Trends and Developments in Biofilm Processes, virtual conference / Notre Dame, USA, 2020

- Sperle, P.; Wurzbacher, C.; Drewes, J.E; Skibinski, B.; UVC-LED based pretreatment for biofouling control in desalination processes with thin-film composite membranes. The International Conference on UV LED Technologies & Application (ICULTA), virtual conference / Berlin, Germany, 2021

- Sperle, P.; Wurzbacher, C.; Drewes, J.E; Optimization of UVC-LED pre-treatment embedded in spiral-wound elements for biofouling control in membrane desalination processes. 17th International Water Association (IWA) Leading Edge Conference on Water and Wastewater Technologies (LET), Reno, USA, 2022

12.1.4. Conference posters

Skibinski B.; Sperle P.; Drewes J. E.: *UV-LED based pre-treatment for biofouling control in desalination processes with thin film composite membranes*. The 9th International Water Association (IWA) Membrane Technology Conference & Exhibition for Water and Wastewater Treatment and Reuse, Toulouse, France, 2019

12.2. List of supervised student works

12.2.1. Study projects

- Appelmann, P., 2022. Methods for Correcting Inner Filter Effects Occurring when Measuring ATP Using a Bioluminescence Luciferase Assay. Study Project, Munich, Germany.

- Gangal, A., 2023. Modelling the Inactivation Performance of a UVC-LED Flow-Through Reactor using COMSOL Multiphysics. Study Project, Munich, Germany.

- Khan, M.S., 2022a. Development and validation of a cultivation and flow-through biodosimetry procedure for Aquabacterium citratiphilum. Study Project, Munich, Germany.

- Mahesh, R.B., 2019. Development and Validation of a Procedure for Development and Validation of a Procedure for Accelerated Biofouling Studies Under Fully Controlled and Reproducible Conditions. Study Project, Munich, Germany.

- Nay, V., 2020. Sustainability study for drinking water ultrafiltration in rural deployment. Study Project, Munich, Germany.
- Nguyen, X.Q., 2021. UV light modeling of a steady-state water reactor using COMSOL Multiphysics. Study Project, Munich, Germany.
- Sultana, H., 2022. UVC-pretreatment using LEDs for biofouling control in reverse osmosis membrane systems. Study Project, Munich, Germany.

12.2.2. Bachelor's theses

- El Khodary, K., 2020. Impact of in-situ UVC Feed Stream Disinfection on the Microbial Diversity of Biofilms Formed in Reverse Osmosis (RO) processes. Bachelor's Thesis, Munich, Germany.
- Braun, J., 2022. Eine Literaturstudie zu den Effekten von ultravioletter Strahlung auf Mikroorganismen mit Fokus auf Inaktivierungs- und Reparaturmechanismen für LED spezifische Anwendungen. Bachelor's Thesis, Munich, Germany.

12.2.3. Master's theses

- Gillani, S.M.A., 2019. The Potential of UV Disinfection for Biofouling Mitigation in Spiral Wound Reverse Osmosis Membrane Modules. Master's Thesis, Munich, Germany.
- Khan, M.S., 2022b. Optimization of UVC-LED pre-treatment integrated in spiral-wound elements for biofouling control in membrane desalination processes. Master's Thesis, Munich, Germany.
- Mirlach, A., 2021. Establishing a characterization procedure for reflecting UVC reactors using actinometry and biodosimetry. Master's Thesis, Munich, Germany.
- Shehata, O., 2020. Characterization of a pulsed flow through UVC-LED reactor and the impact of fluence rate on microbial disinfection. Master's Thesis, Munich, Germany.
- Tiwari, K., 2022. Effect of oxygen partial pressure on MBBR treatment of Produced Water. Master's Thesis, Munich, Germany, Copenhagen, Denmark.

12.3. Supplementary information Chapter 4

This chapter has been published with some editorial changes as "*Supplementary Materials: Reducing the Impacts of Biofouling in RO Membrane Systems through in situ Low Fluence Irradiation Employing UVC-LEDs*", representing the supplementary information of Sperle et al. (2020a). It can be also found on Mendeley Database (Sperle et al., 2020b).

12.3.1. Local tap water analysis

Table S12-1: Summary of the local tab water analysis.

Parameter	Mean	Standard deviation
TOC [mg·L^{-1}]	1.08	0.79
NO$_3$-N [mg·L^{-1}]	0.31	0.16
PO$_4$-P [mg·L^{-1}]	-[1]	-[1]
pH [-]	7.62	0.26
Electrical conductivity [µS·cm^{-1}]	572.49	24.64
TDC [1·mL^{-1}]	4.21 x10^4	1.49 x10^4
Ca [mg·L^{-1}]	60.83	3.2
Cl [mg·L^{-1}]	14.13	2.65
F [mg·L^{-1}]	0.137	0.005
Fe [µg·L^{-1}]	26.80	16.2
K [mg·L^{-1}]	0.98	0.01
Cu [µg·L^{-1}]	18.75	2.22
Mg [mg·L^{-1}]	23.75	0.64
Mn [µg·L^{-1}]	-[1]	-[1]
Na [mg·L^{-1}]	31.65	0.84
SO$_4$ [mg·L^{-1}]	38.38	5.09

[1] Lower than limit of detection

Anion and cation analysis was performed according to Standard Methods (DIN e.V. (DIN 38405-9:2011-09); DIN e.V. (DIN 38406-6:1998-07); DIN e.V. (DIN EN ISO 10304-1:2009-07); DIN e.V. (DIN EN ISO 6878:2004-09); DIN e.V. (DIN EN ISO 7980:2000-07)). NO$_3$ and PO$_4$ were analyzed using cuvette tests (LCK339 and LCK349, Hach, Germany). The remaining anions and cations were analyzed using ion chromatography (Metrohm 930 Compact IC Flex and Metrosep A Supp 7 250 mm, Metrohm, Germany) or atomic absorption spectroscopy (240FS AA and 240Z AA, Agilent, USA).

12.3.2. Laboratory skid for biofouling experiments

The laboratory skid for biofouling experiments consists of 2 parallel treatment trains, on with and one without UVC-LEDs (Figure S12-1). As feed, either deionized (DI) or tap water can be used. Tap water is filtered twice, DI water only once, through a 10 µm PE filter (F) to remove any particulate matter. Next, the water is brought to the desired temperature in a feed tank, submerged in a water bath (TW). The level within the feed tank is controlled by a level sensor (L) connected to a magnetic valve (MV). A magnetic stirrer is mixing the feed water (X2) and the temperature is recorded online (T). Feed water is pumped out of the bottle with the two frequency regulated gear pumps (P2). Shortly after the feed bottle, a nutrient or salt solution can be injected using a dosing pump (P1). The pump speed is measured gravimetrically (S1). Following the dosing, a self-made static mixer ensures that nutrient or salt solutions are equally distributed in the flow. After the mixer, the feed flow splits into 2 parallel treatment trains. In immediate vicinity of the MFS, the in- and outlet pressures are measured (P). Upstream of the MFS, the UV-LED reactor can be attached to one of the trains (within 10 cm distance of the membrane). A "UV-reactor dummy", simply a silica glass pipe with the same dimensions as used in the UV reactor, can be attached to the other train to ensure the same hydraulic retention times in the system. Below the membranes, permeate is collected in a beaker. The flux through the membranes is measured gravimetrically (S2) and recorded online. When the beaker is filled, it is emptied by a suction pump (P3). During the emptying process, the conductivity is recorded (EC2). The MFS, pressure sensors, scales and LED reactors are placed in a temperature-controlled cabinet (TC). Following the MFS, the flow of the concentrate stream is measured using magnetic-inductive flow meters (FM1 and FM2), after which the pressure of the system is regulated by automated needle valves (NV1 and NV2). Using a PI control, the computer aided control system is regulating the flow (measured in the flowmeters) by changing the frequencies of the gear pumps. Finally, after the needle valves, the conductivity of the concentrate is measured (EC1). Data is saved in 5 min intervals. Manufacturer of the parts are summarized in Table S12-2.
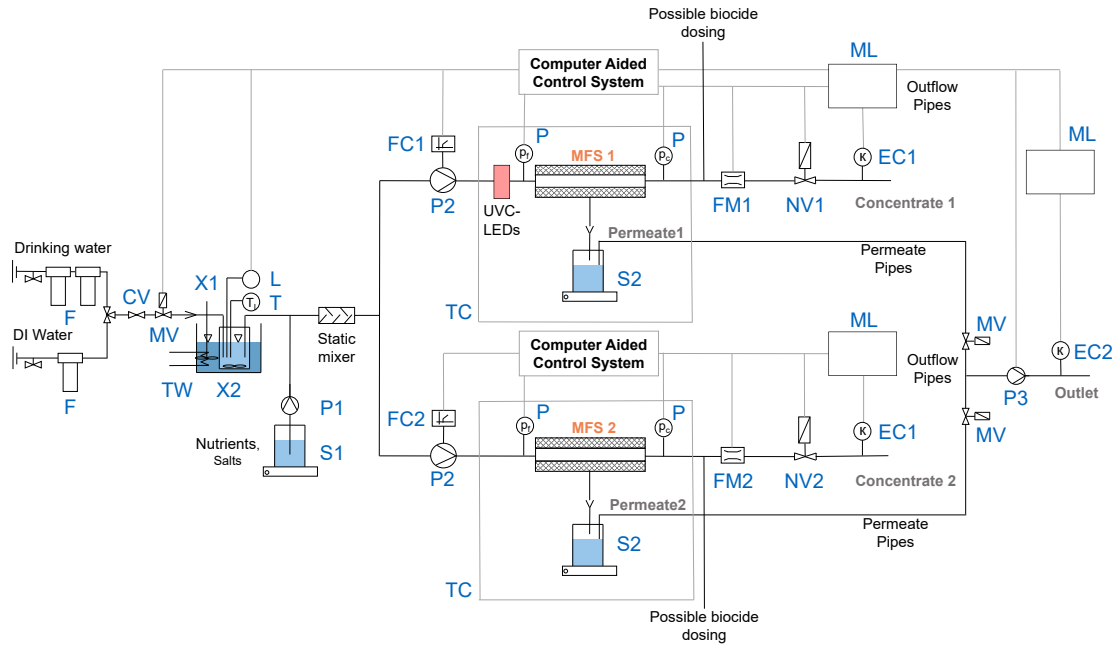
Figure S12-1: Schematic drawing of the laboratory-scale skid for biofouling experiments.

Table S12-2: Summary of the used material in the laboratory skid for the biofouling experiments.

Symbol	Function	Model	Manufacturer
F	10 µm PE filter	F20 housing and 10 PE filter	MTS & APIC Filter GmbH & Co.KG (Germany)
CV	Control valve	5A111G0414PV	EM-Technik GmbH (Germany)
MV	Magnetic valve	8208066.8050.02400	Buschjost GmbH (Germany)
X1	Stirrer	RZR 2000/D	Heidolph GmbH & Co. KG (Germany)
X2	Magnetic stirrer	17995	Reichelt Chemietechnik GmbH + Co. (Germany)
TW	Water bath and recirculation cooler	UWK 140	Gebrüder HAAKE GmbH (Germany)
L	Level meter	CPA03A2P550A	Schmidt Mess- und Regeltechnik (Germany)
T	Temperature sensor	Pt100 (Biostat)	Sartorius AG (Germany)
P1	Peristaltic pump	DULCO®flex	ProMinent GmbH
S1	Scale	572-49	KERN & SOHN GmbH (Germany)
P2	Gear pump	DGS.38PPPV2NN00000	Tuthill Alsip (United States)
FC1	Frequency converter	FU-E2/370W/IP65	GATHER Industrie GmbH (Germany)

Symbol	Function	Model	Manufacturer
FC2	Frequency converter	FUS 150/EV/IP65	PETER electronic GmbH & Co. KG, (Germany)
TC	Temperature cabinet	Innova 4230	New Brunswick Scientific (United States)
P	Pressure sensor	SML-10	ADZ NAGANO GmbH (Germany)
S2	Scale	572-45	KERN & SOHN GmbH (Germany)
FM1	Magnetic-inductive flow meter	COPA-XM DM23	ABB Automation Products GmbH (Germany)
FM2	Magnetic-inductive flow meter	Proline Promag 10 HART DN02	Endress+Hauser Messtechnik GmbH+Co.KG (Germany)
NV1	Motorized needle valve	Motor: MCL-000AI Valve: SS-4MG2	Motor: Hanbay Inc (United States) Valve: Swagelok (United States)

12.3.3. Detailed description of the steps for the accelerated biofouling experiments

The workflow for the biofouling experiments consisted of 4 basic steps:

1. **Cleaning and sterilization:** First, the system (without membrane) was flushed with 0.1% NaOH (Merck, Germany) to remove organic matter (DuPont, 2020). NaOH was recycled for 10 min and afterward soaked for > 12 h, followed by DI water flushing. Next, the disassembled MFS was cleaned using DI water and soap (pure, Baktolin, Germany). The pipe system until the flowmeters was disassembled and autoclaved at 121 °C for 20 min. Membranes were stored at 4 °C in 1% $NaHSO_3$ (Acros Organics, Belgium) till usage (DuPont, 2020). Parts not suitable for autoclaving, including feed and permeate spacer, membrane, MFS, sealing, silica glass pipe, magnetic valve, 10 µm cartridge filters, pressure, temperature and level sensors, were flushed with MilliQ and soaked in 0.25% H_2O_2 solution (Merck, Germany) for at least 24 h to achieve sufficient disinfection (analogous to analogous to Dow (n.d.), DuPont (2020), Kucera (2019), Li et al. (2019a) and Ling et al. (2017).

2. **Reassembling of the skid:** After the cleaning and sterilization, the skid was reassembled under sterile conditions.

3. **Compaction:** To ensure steady-state conditions for every experiment a compaction of 16 h was performed. Therefore, as feed, DI water was used and a sterile NaCl (Appli Chem, Germany) solution was dosed, resulting in a final concentration of 5.25 mmol·L^{-1} NaCl. The water flow in both lines was set to 4.25

L·h^{-1} and within the first 2 h, a pressure of 8 bar was maintained. The remaining 14 h were used to set a flux of 20 L·m^{-2}·h^{-1} (LMH). The temperature of the feed water was maintained at 15 °C.

4. **Accelerated biofouling phase:** For starting the biofouling experiment, the feed was switched from DI to tap water. UV-LEDs were turned on and nutrients instead of a salt solution were added. Nutrients were sterilized and the pH was set to 10.5 to avoid microbial growth (Vrouwenvelder et al., 2009c). Nutrient dosing speed was set to reach the aimed concentration of 1,000:200:100 µg·L^{-1}of C:N:P (Dreszer et al., 2013). Roughly every 3 days NaOCl (Merck, Germany) in a 3% solution was dosed for 5 min behind the MFS to avoid clogging of the needle valve. The NaOCl concentration in the concentrate stream was roughly 500 to 1,500 ppm. Throughout the experiment, the feed pressure was kept constant. When a feed channel pressure drop (FCPD) of 0.8 bar was reached, the experiments were terminated.

12.3.4. Biofilm extraction

For biofilm extraction, first, the fouled membrane and feed spacer were cut, into approximately 1 cm² pieces and placed in a falcon tube containing 30 mL of 0.1 M NaCl. Next, the membrane and spacers were vortexed for 1 h similar as described Matar et al. (2016). After vortexing, samples for ATP, total direct cell count (TDC) and microbial diversity analysis using 16S rRNA sequencing were taken. ATP and TDC analysis were performed within 5 h after the experiment stopped. 16S rRNA samples were frozen at – 80 °C till analysis. To separate the EPS from the cells, ultrasonic treatment for 2 min, using 20 W at 20 kHz and the GM 70 HD (Bandelin electronics, Germany) with the UW 70 probe (Bandelin electronics, Germany) and an immersed area of 0.28 cm², was applied. Those settings were adapted from Han et al. (2013) and kept rather conservative to ensure as low cell lysis as possible. After the ultrasonic treatment, the remaining membrane and spacer pieces were disposed. At this point samples for TOC and fluorescence measurements were taken. The final step consists of a centrifugation at 12,000 rcf and 4 °C for 20 min to separate the cells and the EPS (Matar et al., 2016). After cell separation, the EPS was analyzed for its TOC, protein and polysaccharide content. Within 24 h, fluorescence spectroscopy was performed of both, the total biofilm and EPS sample. Samples for protein and polysaccharides analysis were stored at -20 °C. Every analysis except for 16S rRNA amplicon sequencing and fluorescence spectroscopy was performed in triplicates.

12.3.5. Aqualog settings

Integration time for fluorescence spectroscopy using the Aqualog (HORIBA Jobin Yvon, Germany) was set to 1 s and the CCD gain to medium. The samples were excited in a 3 nm step from 230 to 599 nm, while recording emission from 211 to 621 nm, each 4 nm. The fluorescence signal was normalized to a daily measure Raman peak (using MilliQ) and corrected for inner filter effects using the HORIBA Scientific and

Aqualog V 3.6 software. Besides, a blank was subtracted to account for Raman scattering and Rayleigh scattering areas were set to 0.

12.3.6. Actinometry

During the KI/KIO$_3$ actinometry in a photochemical process I$_3^-$ is formed (Rahn, 1997; Rahn et al., 2003):

$$8KI + KIO_3 + 3H_2O + h\nu \rightarrow 3I_3^- + 6OH^- + 9K^+,$$
(S12-1)
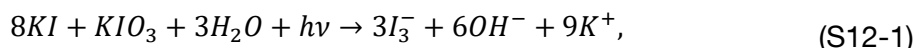
the concentration of the produced I$_3^-$ can now be calculated, by measuring the absorbance at 352 nm and dividing this value through the molar absorption coefficient of 27 600 M^{-1}·cm^{-1} (Rahn et al., 2003). Combining the kinetic of the I$_3^-$ formation over several irradiation times and the wavelength depending quantum yield, the irradiance of the LED can be calculated over the whole spectrum based on the following equation (Zou et al., 2019):

$$I\left[\frac{mW}{cm^2}\right] = \frac{[I_3^-] \cdot V \cdot h\nu \cdot N_A}{S \cdot t \cdot \Phi},$$
(S12-2)

with [I$_3^-$] being the concentration of I$_3^-$ (mol·L^{-1}), V the solution volume (mL), N the quantity of photons absorbed by the solution (Einstein), Φ the quantum yield of I$_3^-$ (mol·Einstein^{-1}), I the UV irradiance/fluence rate (mW·cm^{-2}), S the irradiated surface area, t is the irradiation time (s), h is the Planck constant (6.626×10^{-34} J·s), ν the frequency of the wave (s^{-1}) and N$_A$ the Avogadro constant (6.022 × 10^{23}). As Φ is wavelength dependent, a linear interpolation was used over the whole spectrum as described by (Wang et al., 2017; Zou et al., 2019). [I_3^-]/t was estimated as the slope of the several flow steps with hydraulic retention times in the reactor between 0.7 to 6 s. This was seen more appropriate than using a single step as the fitted regression line showed an offset for t=0 (Figure S12-2). The skid used for actinometry experiments is shown in Figure S12-3, the parts are described in Table S12-3.
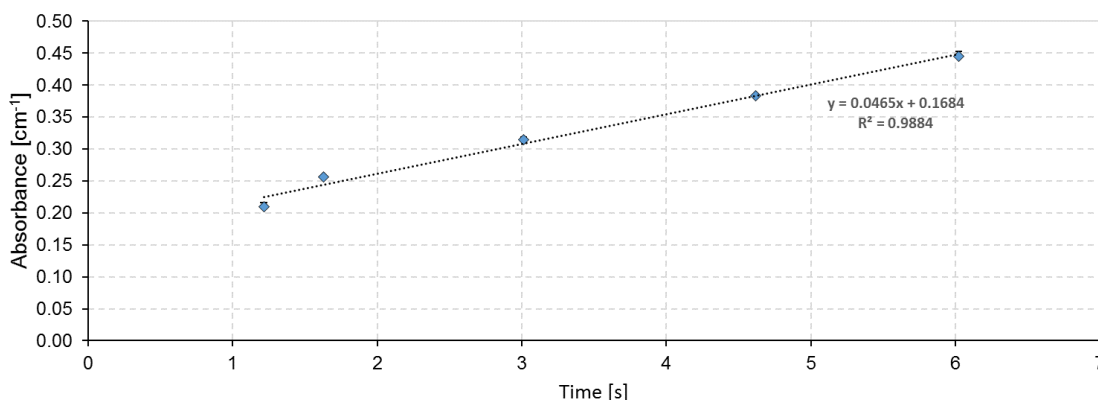

Figure S12-2:   *Change of absorbance at 352 nm over hydraulic retention time.*
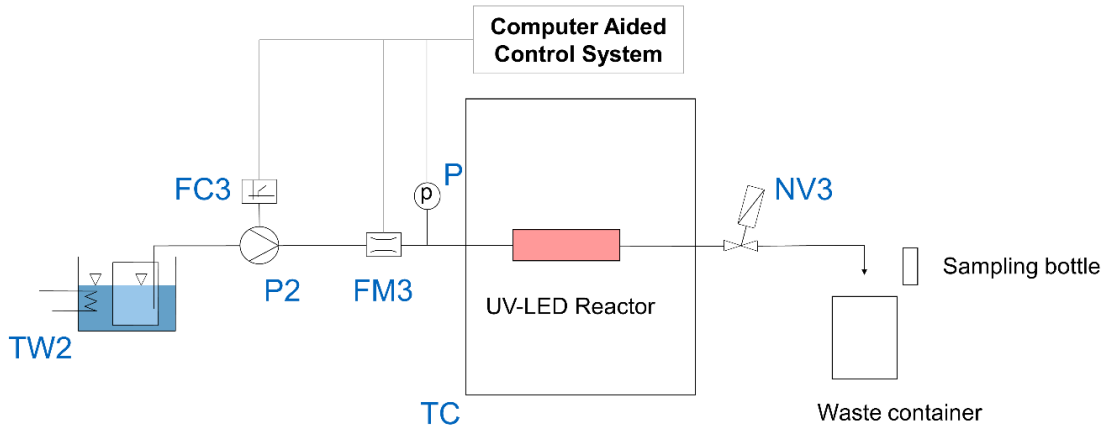
Figure S12-3:   *Laboratory skid for actinometry experiments.*

Table S12-3:   *Summary of the used material in the laboratory skid for the actinometry experiments.*

Symbol	Function	Model	Manufacturer
TW2	Water bath		
P2	Gear pump	DGS.38PPPV2NN00000	Tuthill Alsip (United States)
FC2	Frequency converter	FUS 037/E2	PETER electronic GmbH & Co. KG, (Germany)
FM3	Magnetic-inductive flow meter	MIK-6FC08AC34P	KOBOLD Messring GmbH (Germany
P	Pressure sensor	SML-10	ADZ NAGANO GmbH (Germany)
TC	Temperature cabinet	Innova 4230	New Brunswick Scientific (United States)
NV3	Needle valve	SS-4MG2	Swagelok (United States)

12.3.7. Calculation of feed channel pressure drop (FCPD), permeability und hydraulic resistance

Outlier analysis for pressure data and calculated permeability (e.g. caused by an emptying of the beaker collecting the permeate) was done based on the interquartile range (Ranga Suri et al., 2019) (p. 14) of a 3 h interval. FCPD and permeability were calculated as moving average for 1.5 h intervals and at least 5 elements:

$$\text{FCPD [bar]} = \frac{\sum_{i=t-0.75}^{t+0.75} p_{in,i}}{n_{p_{in}}} - \frac{\sum_{i=t-0.75}^{t+0.75} p_{out,i}}{n_{p_{out}}} \qquad \text{(S12-3)}$$

with t being the time point in h, p_{in} and p_{out} the in- and outlet pressure and n the number of data points in the interval,

$$\text{Permeability } \left[\frac{\text{LMH}}{\text{bar}}\right] = \frac{\Delta W}{\Delta t\, A} / \left(\frac{\sum_{i=t-0.75}^{t+0.75} p_{in,i}}{2n_{p_{in}}} + \frac{\sum_{i=t-0.75}^{t+0.75} p_{out,i}}{2n_{p_{out}}}\right), \qquad (S12\text{-}4)$$

With ΔW being the difference in weight [g] measured in the beaker collecting the permeate within the time interval Δt [h] (difference of the first and last value in the 1.5 h interval) and A the membrane area [m²]. Within calculating the 95% confidence intervals, propagation of uncertainty was considered. The relative permeability is the permeability, normalized to the maximum value found in the first 5 days of the experiment. This value is also used to calculate the hydraulic resistance of the membrane. In general, the total hydraulic resistance can be calculated, adopted from Dreszer et al. (2013):

$$\text{R }\left[\frac{1}{\text{m}}\right] = \frac{1}{\eta\, Permeability}, \qquad (S12\text{-}5)$$

With R being the total resistance [m⁻¹] and η the dynamic viscosity of water [Pa s] at 15 °C. Further, according to Dreszer et al. (2013), the biofilm/fouling layer resistances can be calculated

$$\text{R}_{biofilm}\left[\frac{1}{\text{m}}\right] = R_{total} - R_{membrane}. \qquad (S12\text{-}6)$$

12.3.8. Parallel factor (PARAFAC) modeling

A three component PARAFAC model was built using 24 samples (Figure S12-4). For each biofilm sample, an analysis for the EPS and the filtered sample was done. The model was built by first setting areas of Raman and Rayleigh scattering to missing. As a high noise in the UV region was monitored, excitation < 250 and emission < 299 nm was removed. Besides the higher wavelength part for emission > 550 nm was excluded. The model was build out of 10 randomly initialized models using a non-negativity constrain with a convergence of 10^{-8}. For modeling 3 outliers needed to be removed and each EEM was normalized to total intensity.

The PARAFAC model was validated by the variance explained, core consistency and split half analysis. On the one hand, the model showed an explained variance of 98.8% and a core consistency of 86.0%. On the other hand, some limitations for the split-half analysis need to be mentioned. To reduce inner filter effects caused by the high absorbance of the samples, they were diluted 1:20. Whereas in the EEMs pronounced peaks in the protein regions are visible, the signal in the humic substance region was low and prone to measurement noise. This noise can be found in the spectra of the components, as well. This noise and the low sample number is subjected to cause a not stable validation with the split-half analysis in random split mode. Anyway, in a randomized $S_4C_6T_3$ split, two of the three comparisons could be validated with a Tucker correlation coefficient of > 95% (Murphy et al., 2013). The other comparison showed a similarity of 94.6, 89.5 and 89.9% for the three components.
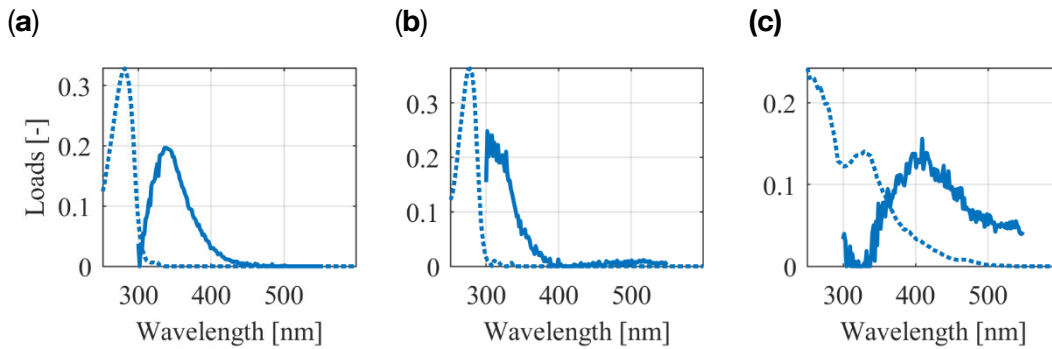
Figure S12-4: *Excitation (dashed line) and emission spectrum (solid line) of the three parallel factors (PARAFAC) model components: (a) Component 1 (C1); (b) Component 2 (C2); (c) Component 3 (C3).*

12.3.9. Distance-based redundancy analysis
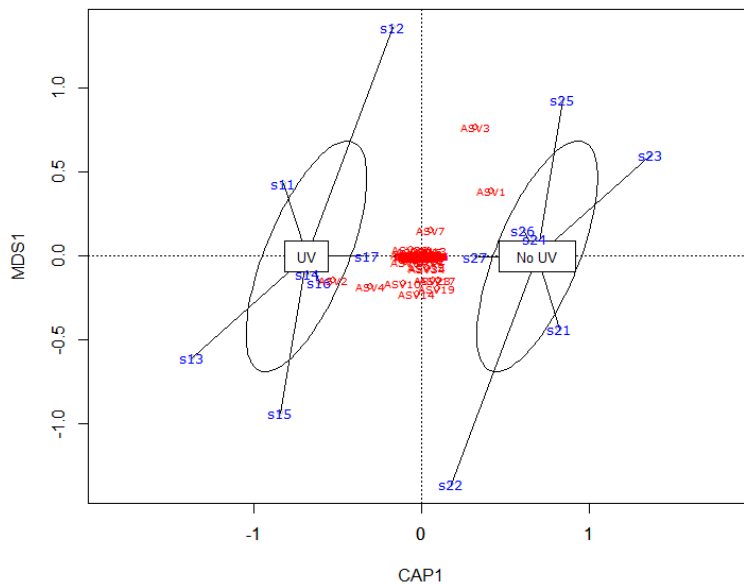
Figure S12-5: *Plot of the distance based redundancy analysis using Bray-Curtis dissimilarity, differentiating for the treatment condition in each experiment. The first number in the sample name represents the treatment condition (2 = untreated, 1 = treated), whereas the second number represents the experimental run.*

12.4. Supplementary information Chapter 5

This chapter has been published with some editorial changes as "*Supplementary materials: An actinometric method to characterize performance of reflecting UVC reactors used for water treatment*", representing the supplementary information of Sperle et al. (2023c).

12.4.1. List of abbreviations and acronyms

|			
AOPs	advanced oxidation processes	R0	standard case without reflection
CBA	collimated beam apparatus	R05	half of the bottom of the Petri dish covered with polytetrafluoroethylene
HA	humic acids sodium salt	R1	whole bottom of the Petri dish covered with polytetrafluoroethylene
LHS	left-hand side	REF	reduction equivalent fluence
LRV	logarithmic removal value	T100	transmittance not adjusted with humic acids sodium salt
LVRPA	local volumetric rate of photon absorption	T70	transmittance of 70% adjusted with humic acids sodium salt
PBS	phosphate buffer	T85	transmittance of 85% adjusted with humic acids sodium salt
PTFE	polytetrafluoroethylene	U1	conventional uridine actinometry
QC	quality control	U2	optimized uridine actinometry

12.4.2. List of symbols

Symbol	Meaning	Unit	Symbol	Meaning	Unit
A	surface area	cm^2	H'$_{U1}$	average fluence estimated with conventional uridine actinometry within the water body	mJ cm^{-2}
a^{254}	decadic absorption coefficient at 254 nm	cm^{-1}	H'$_{U2}$	average fluence estimated with optimized uridine actinometry within the water body	mJ cm^{-2}
$A^{254}(t)$	absorbance readings at 254 nm at time t	-	k$_{MS2}$	slope of logarithmic removal values over time	s^{-1}
$A^{262}(t)$	absorbance readings at 262 nm at time t	-	L	distance of the lamps to the water surface	cm
$a^{352}(t)$	decadic absorption coefficient at 352 nm at time t	cm^{-1}	l	path length perpendicular to the lamp in the cell suspension	cm

Symbol	Meaning	Unit	Symbol	Meaning	Unit
$C_U(0)$	initial uridine concentration	mol L^{-1}	l_{irr}	path length of the light within the solution	cm
DF	divergence factor	-	l_{obs}	thickness of the cuvette used for absorbance measurements	cm
E	irradiance	mW cm^{-2}	PF	petri factor	-
E'	fluence rate	mW cm^{-2}	q_0^{254}	photon flux at the sample surface	Einstein s^{-1}
$E'_{0,U1}$	fluence rate calculated with conventional uridine actinometry above water surface in the middle of the petri dish	mW cm^{-2}	RF	reflection factor	-
E'_0	fluence rate above water surface in the middle of the petri dish	mW cm^{-2}	U	photon energy at 254 nm	mJ Einstein^{-1}
E'_{U1}	average fluence rate calculated with conventional uridine actinometry within the water body	mW cm^{-2}	V	volume	L
$E'_{0,KI/KIO_3}$	fluence rate calculated with KI/KIO$_3$ actinometry above water surface in the middle of the petri dish	mW cm^{-2}	V$_{eff}$	effective volume	L
$E_{0,U2}$	irradiance calculated with optimized uridine actinometry above water surface in the middle of the petri dish	mW cm^{-2}	WF	water factor	-
$E'_{0,U2}$	fluence rate calculated with optimized uridine actinometry above water surface in the middle of the petri dish	mW cm^{-2}	ε^{352}	molar absorption coefficient of I$_3^-$	M^{-1} cm^{-1}
E'_{KI/KIO_3}	average fluence rate calculated with KI/KIO$_3$ actinometry within the water body	mW cm^{-2}	ε_H^{254}	molar absorption coefficient of uridine photoproduct at 254 nm	M^{-1} cm^{-1}
E_{U2}	average irradiance calculated with optimized uridine actinometry within the water body	mW cm^{-2}	ε_H^{262}	molar absorption coefficient of uridine photoproduct at 262 nm	M^{-1} cm^{-1}
E'_{U2}	average fluence rate calculated with optimized uridine actinometry within the water body	mW cm^{-2}	ε_U^{254}	molar absorption coefficient of uridine at 254 nm	M^{-1} cm^{-1}
F_H	photokinetic factor of at t = ∞	-	ε_U^{262}	molar absorption coefficient of uridine at 262 nm	M^{-1} cm^{-1}
H'	fluence	mJ cm^{-2}	$\eta_{H'}$	mixing efficiency at fluence H'	-

Symbol	Meaning	Unit	Symbol	Meaning	Unit
H'$_{0,radio}$	fluence measured with the radiometer	mJ cm^{-2}	Φ^{254}	quantum yield at 254 nm	mol Einstein^{-1} / -
H'$_{KI/KIO3}$	average fluence estimated with KI/KIO3 actinometry within the water body	mJ cm^{-2}			

12.4.3. Details on the reflection measurement of the polytetrafluoroethylene (PTFE) foil

According to the received calibration certificate, the reflectance was determined as following: "The 8°/Hemispherical spectral reflectance was measured for the sample listed above. The calibration was performed with a Perkin-Elmer Lambda 950 UV-VIS-NIR spectrometer (serial number 950L1211082) equipped with a 150 mm integrating sphere. The reflectance was determined by using a standard from SphereOptics GmbH, part number SG3051, which has been calibrated by the National Metrology Institute of the Federal Republic of Germany (Physikalisch-Technische Bundesanstalt, calibration certificate: PTB 44154/20)" (SphereOptics, 2021). The measurement uncertainty (95% confidence) in the range of 250 to 300 nm was estimated with 1.11% (SphereOptics, 2021).

12.4.4. Photoproduct of uridine

To investigate the formed photoproduct of uridine, 0.012 mM uridine solution was irradiated using the short collimator beam with average irradiance at measured with the radiometer of ~0.55 mW cm^{-2} for 212 min in the petri dish without reflection and every 30 min analyzed for absorbance using a 5 cm cuvette and the DR 6000 (Hach Lange, Germany). The measured absorbance over fluence became steady at around 4,950 mJ cm^{-2} (Figure S12-6(S12-6)). The molar absorption coefficients of the photoproduct at 254 and 262 nm were calculated analogous as described by Pousty et al. (2022) with $\varepsilon_H^{262} = 0.06 \cdot \varepsilon_U^{262}$ and $\varepsilon_H^{254} = 0.08 \cdot \varepsilon_U^{254}$. Spectrum scan of the uridine and its photoproduct, measured with the 5 cm cuvette and at H'$_{0,radio}$ of 6,985 mJ cm^{-2} is depicted in Figure S12-7.
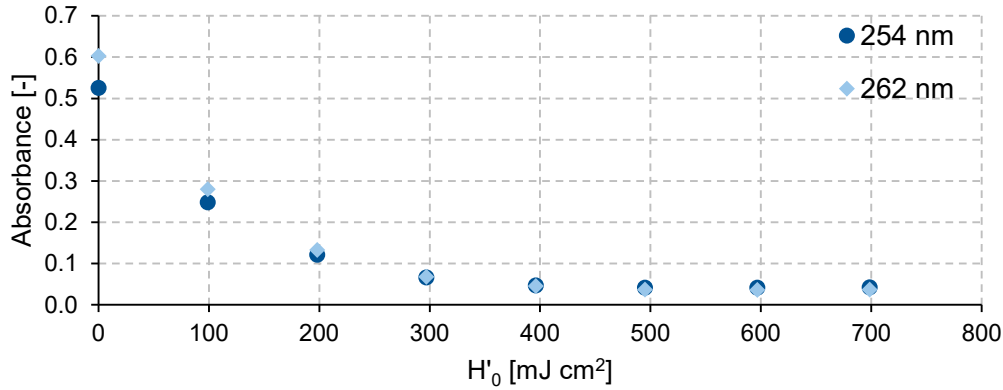
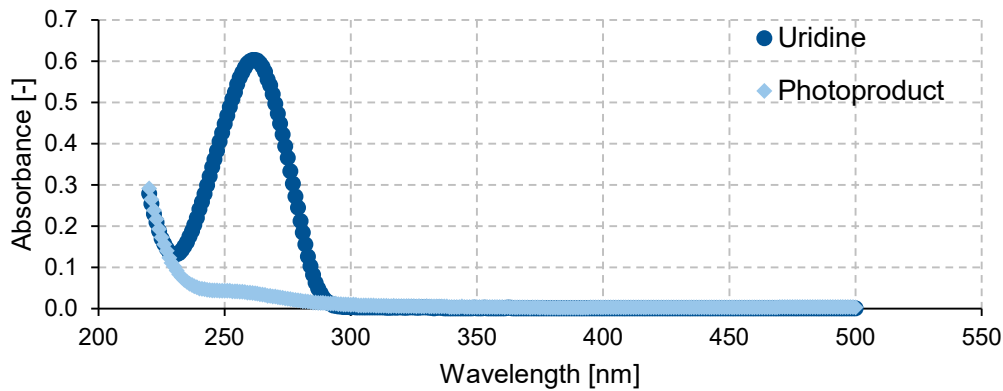*Figure S12-6:   Absorbance uridine over fluence.*

Figure S12-7:   Spectrum scan of uridine (0.012 mM) and the photoproduct irradiated with $H'_{0,radio}$ = 6,985 mJ cm^{-2}.

12.4.5. Deduction of equation 7

The semi-empirical equation (Maafi and Maafi, 2013; Maafi and Maafi, 2015) to model an a photodegradation where the photoproduct shows an absorbance relates in the case of uridine to equation (S12-7).

$$A^{262}(t) = A^{262}(\infty) + \frac{A^{262}(0) - A^{262}(\infty)}{A^{254}(0) - A^{254}(\infty)} \cdot \frac{l_{obs}}{l_{irr}}$$
$$\cdot \log\left[1 + \left(10^{\left[\left(A^{254}(0) - A^{254}(\infty)\right) \cdot \frac{l_{irr}}{l_{obs}}\right]} - 1\right)\right.$$
$$\left. \cdot e^{-\Phi^{254} \cdot \varepsilon_U^{254} \cdot l_{irr} \cdot \frac{q_0^{254}}{V} \cdot t \cdot F_H}\right] \tag{S12-7}$$

Hereby $A^{262}(t)$ represents the total absorbance measured with the cuvette at 262 nm and time point t. $A^{254}(t)$ represents the total absorbance measured in the same cuvette but with irradiation wavelength 254 nm. t = 0 represents starting point of the experiment, t = ∞ represents the time after irradiation when all of uridine was converted to the resulting photoproduct. l_{obs} represents the thickness of the measuring cuvette and l_{irr} path length of the light through the solution. Φ^{254} is the quantum yield, q_0^{254} is the photon

flux at the sample surface, V the reactor volume, ε_U^{254} the molar absorption coefficient of uridine at 254 nm. F_H equals to the photokinetic factor at t = ∞.

$$F_H = \frac{1 - 10^{-\left(A^{254}(\infty)\cdot\frac{l_{irr}}{l_{obs}}\right)}}{A^{254}(\infty)\cdot\frac{l_{irr}}{l_{obs}}} \tag{S12-8}$$

Further the following equations need to be considered:

$$A^{262}(0) = C_U(0)\cdot \varepsilon_U^{262}\cdot l_{obs} \tag{S12-9}$$

$$A^{262}(\infty) = C_U(0)\cdot \varepsilon_H^{262}\cdot l_{obs} = \frac{A^{262}(0)\,\varepsilon_H^{262}}{\varepsilon_U^{262}} \tag{S12-10}$$

$$A^{254}(0) = C_U(0)\cdot \varepsilon_U^{254}\cdot l_{obs} = \frac{A^{262}(0)\,\varepsilon_U^{254}}{\varepsilon_U^{262}} \tag{S12-11}$$

$$A^{254}(\infty) = C_U(0)\cdot \varepsilon_H^{254}\cdot l_{obs} = \frac{A^{262}(0)\,\varepsilon_H^{254}}{\varepsilon_U^{262}} \tag{S12-12}$$

$C_U(0)$ equals the initial concentration of uridine, ε_U^{262} molar absorption coefficient of uridine at 262nm, ε_H^{262} ε_H^{252} the respective molar absorption coefficient of the photoproduct of the given wavelength. Following equation (S12-13) holds true

$$
\begin{aligned}
A^{262}(t) = {} & A^{262}(\infty) + \frac{\varepsilon_U^{262} - \varepsilon_H^{262}}{\varepsilon_U^{254} - \varepsilon_H^{254}}\cdot\frac{l_{obs}}{l_{irr}} \\
& \cdot \log\left[1 + \left(10^{\left[\left(A^{254}(0) - A^{254}(\infty)\right)\cdot\frac{l_{irr}}{l_{obs}}\right]} - 1\right)\right. \\
& \left. \cdot e^{-\Phi^{254}\cdot\varepsilon_U^{254}\cdot l_{irr}\cdot\frac{q_0^{254}}{V}\cdot t\cdot F_H}\right]
\end{aligned}
\tag{S12-13}
$$

$$
\begin{aligned}
\left(A^{262}(t) - A^{262}(\infty)\right) & \cdot \frac{\varepsilon_U^{254} - \varepsilon_H^{254}}{\varepsilon_U^{262} - \varepsilon_H^{262}}\cdot\frac{l_{irr}}{l_{obs}} \\
= {} & \log\left[1 + \left(10^{\left[\left(A^{254}(0) - A^{254}(\infty)\right)\cdot\frac{l_{irr}}{l_{obs}}\right]} - 1\right)\right. \\
& \left. \cdot e^{-\Phi^{254}\cdot\varepsilon_U^{254}\cdot l_{irr}\cdot\frac{q_0^{254}}{V}\cdot t\cdot F_H}\right]
\end{aligned}
\tag{S12-14}
$$

$\frac{\varepsilon_U^{254} - \varepsilon_H^{254}}{\varepsilon_U^{262} - \varepsilon_H^{262}}$ will be further referred to as D.

$$
\begin{aligned}
10^{\left(A^{262}(t) - A^{262}(\infty)\right)\cdot D\cdot\frac{l_{irr}}{l_{obs}}} & - 1 \\
= {} & \left(10^{\left[\left(A^{254}(0) - A^{254}(\infty)\right)\cdot\frac{l_{irr}}{l_{obs}}\right]} - 1\right) \\
& \cdot e^{-\Phi^{254}\cdot\varepsilon_U^{254}\cdot l_{irr}\cdot\frac{q_0^{254}}{V}\cdot t\cdot F_H}
\end{aligned}
\tag{S12-15}
$$

$$\ln\left(10^{\left(A^{262}(t)-A^{262}(\infty)\right)\cdot D\cdot\frac{l_{irr}}{l_{obs}}}-1\right) \tag{S12-16}$$

$$-\ln\left(10^{\left[\left(A^{254}(0)-A^{254}(\infty)\right)\cdot\frac{l_{irr}}{l_{obs}}\right]}-1\right)$$

$$=-\Phi^{254}\cdot\varepsilon_U^{254}\cdot l_{irr}\cdot\frac{q_0^{254}}{V}\cdot t\cdot F_H$$

$$\frac{\ln\left(10^{\left[\left(A^{254}(0)-A^{254}(\infty)\right)\cdot\frac{l_{irr}}{l_{obs}}\right]}-1\right)}{F_H} \tag{S12-17}$$

$$-\frac{\ln\left(10^{\left(A^{262}(t)-A^{262}(\infty)\right)\cdot D\cdot\frac{l_{irr}}{l_{obs}}}-1\right)}{F_H}$$

$$=\Phi^{254}\cdot\varepsilon_U^{254}\cdot l_{irr}\cdot\frac{q_0^{254}}{V}\cdot t$$

12.4.6. Behavior of left-hand side (LHS) of equation 7 over path lengths
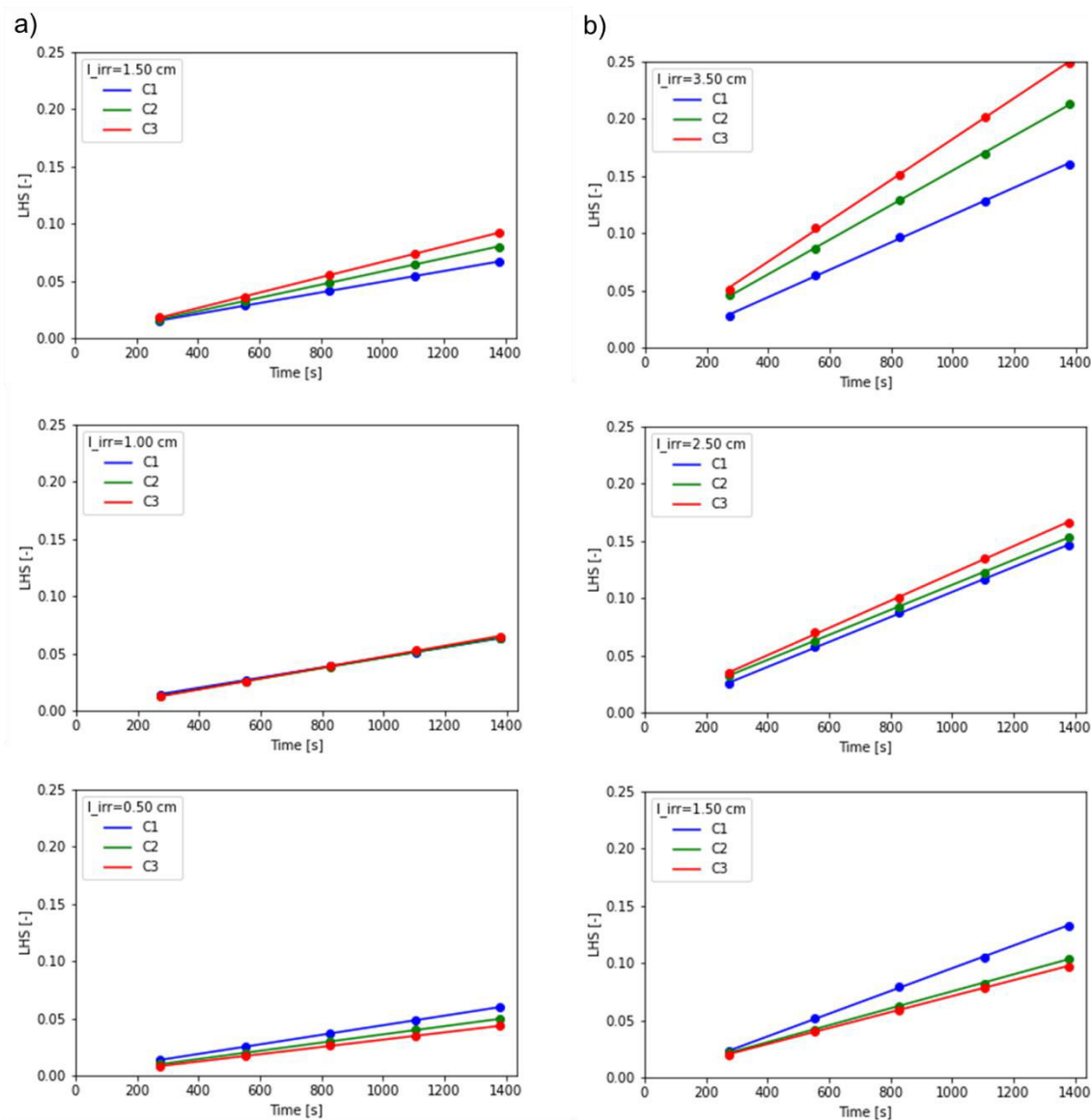
a)

b)

Figure S12-8: Behavior of left-hand side (LHS) of equation *(5-7)* for different l_{irr}; C1=0.012 mM, C2=0.06 mM, C3=0.108 mM uridine; a) No reflection (R0); b) Full reflection (R1); Associated gifs are found as separate files in the supplementary materials.
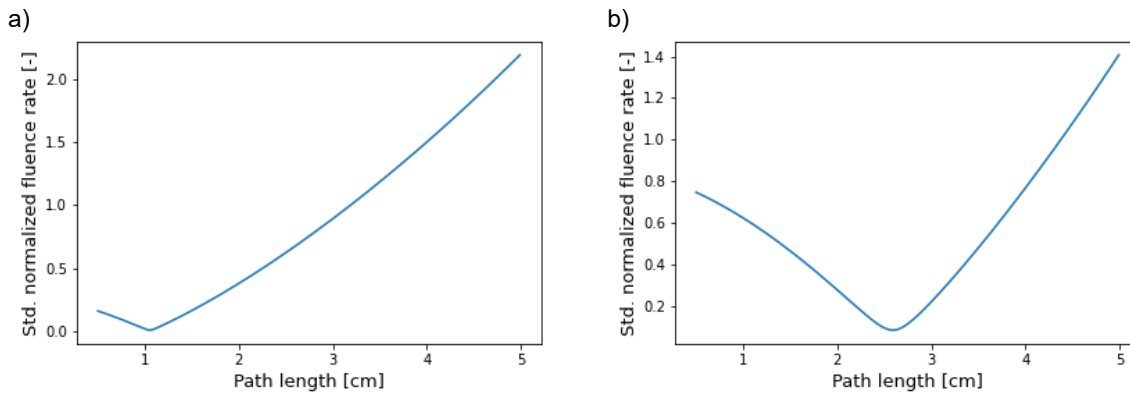
Figure S12-9:   Standard deviation of normalized $E'_{0,U2}$ of the three different concentrations over path length; a) No reflection (R0); b) Full reflection (R1)

12.4.7. Test with increased water depth

To additionally validate that the calculated path lengths are influenced by the real path length of the light through the solution, another test with a higher water depth was performed. Therefore, the long collimator tube and a beaker of 3.3 cm inner diameter were used. The beaker was filled with 0.0155 L of solution resulting in ~1.8 cm water table. The three uridine solutions were irradiated with $H'_{0,radio}$ ~590 mJ cm^{-2}. Using the quantum yields of 0.0185, 0.0201 and 0,0208 mol Einstein^{-1} for the concentrations of 0.012, 0.06 and 0.108 mM, path length was estimated with 1.74. Calculated normalized irradiance $E_{0,U2}$ and fluence rate $E'_{0,U2}$ were 0.99 and 0.95.

12.5.   Supplementary information Chapter 6

This chapter has been published with some editorial changes as "*Supporting information: A Practical Bacterial Biodosimetry Procedure to Assess Performance of Lab-Scale Flow-through Ultraviolet Water Disinfection Reactors*", representing the supplementary information of Sperle et al. (2023a).

12.5.1. Schematic drawing of the utilized UV-LED reactor
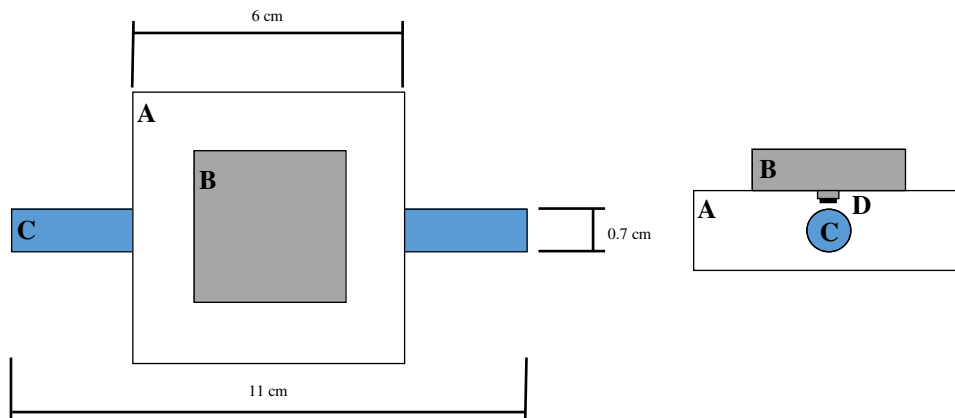

*Figure S12-10:   Simple schematic of the used UV-LED reactor; **A** reflective PTFE block, **B** LED cooling, **C** silica glass pipe, **D** LEDs; left: Top view, right: Sectional view.*

12.5.2. Optimized cultivation

To monitor cell growth, absorbance readings at 600 nm (A_{600}) were checked over time for different cultivation approaches to find a practical procedure. With an iterative approach, nutrient concentrations and inoculation method was optimized. A single colony of a one-week-old streaked *Aquabacterium citratiphilum* plate was inoculated in 80 mL of bouillon in a 250 ml Erlenmeyer flask. By using twice the concentrated bouillon after an incubation of 48 h at 20 °C and shaking of 120 rpm, high cell concentrations in exponential growth phase were obtained.

12.5.3. Growth curve
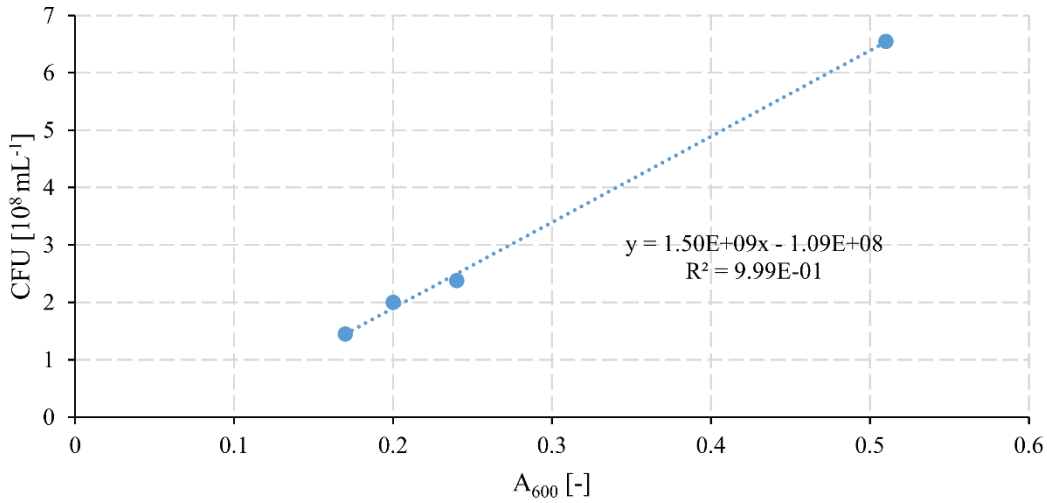
Figure S12-11:   Developed growth curve without low binding tubes and Tween20 using absorbance readings at 600 nm (A_{600}) measured with a 1 cm cuvette.

12.5.4. Results biodosimetry 96 mA, chronologically ordered with sampling

Figure S12-12:   Results biodosimetry 96 mA, chronologically ordered according to sampling; Red lines representing the time when a blank sample was taken; The numbers 1, 2 and 3 are referring to the repetitions of the experiment.

12.5.5. Sampling tubes 15 and 1.5 mL

Figure S12-13:   Comparison of 15 and 1.5 mL sample tubes.

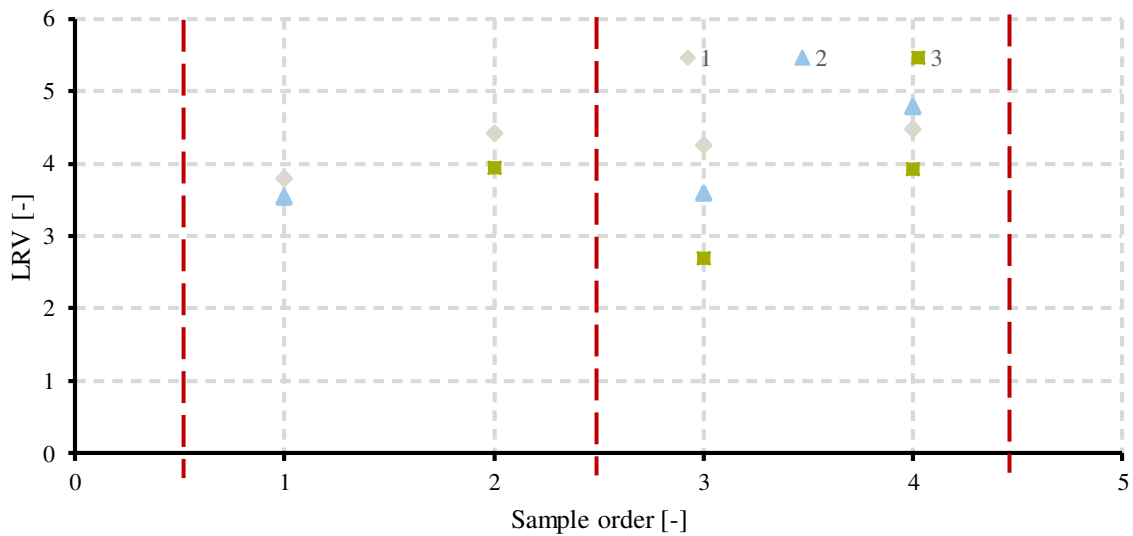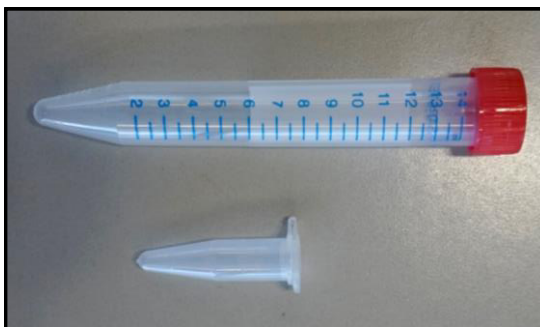### 12.5.6. Hands on protocol for simple tracer test and the developed biodosimetry procedure

The protocol shown here was developed according to the needs of the study and is based on standard methods for microbiology not further explained here. Depending on the needs, parts of the procedure might be adopted, bearing in mind the critical parts discussed. Please note that appropriate disposal of used chemicals is needed according to the local circumstances but not further described here.

Materials and Equipment

- Active *A. citratiphilum* (DSM 11900) streaked on an 830a agar plate

- Autoclave

- Bunsen-burner

- Cell density meter or apparatus to measure absorbance at 600 nm with disposable cuvette

- Centrifuge

- Colony counter

- Erlenmeyer flasks (250 mL)

- Incubator

- Inoculation loop

- Micropipettes with disposable, sterile (low retention) tips, at least 200 and 1.000 µL

- pH probe

- Pipette controller and disposable, sterile pipettes, e.g. 25 and 50 mL

- Portable electrical conductivity (EC) meter

- Spectrometer for measuring absorbance at irradiated wavelength with a silica glass cuvette

- Sterile (low binding) 1.5 mL Eppendorf tubes

- Sterile 830a agar plates prepared according to (DSMZ GmbH, 2007, 2012)

- Sterile 50 mL falcon tubes

- Three identical Drigalski spatulas

- Volumetric flasks, e.g. 250, 500, 1000 and 2000 mL

- Vortex mixer

Solutions

Solution A – Deionized (DI) water

Should show an (EC) < 10 µS cm^{-1}.

Solution B – Tab water or alternative tracer solution

Used for positive step tracer test, should show an (EC) > 500 µS cm^{-1}.

Solution C – Sterile modified 830a bouillon

Prepared according to medium plates prepared according to (1, 2), but in double concentration and without agar.

Solution D – Sterile phosphate buffered saline (PBS) plus Tween20

1x 2.5 L, 2x 0.5L prepared according to NSF/ANSI 55 (NSF/ANSI, 2019) added with 0.02 mL Tween20 per L, autoclaved and stored in a closed bottle. Add magnetic stirring bar for the 2.5 L before autoclaving.

Solution E – Ethanol

80% ethanol for disinfection.

Solution F – 1% H_2O_2 solution

2x 0.25 L 1% H_2O_2 prepared from concentrated, for room temperature stabilized H_2O_2 stock solution on the day of experiment.

Solution G – Sterile Milli-Q water

1 L autoclaved Milli-Q water stored in a closed bottle.

Solution H – Sterile phosphate buffered saline (PBS)

2x 1 L prepared according to NSF/ANSI 55 (NSF/ANSI, 2019), autoclaved and stored in a closed bottle.

Preparations and experiment

Determine the hydraulics of the system, steady state conditions, and the volume for flushing between samples. It should be performed at two flow rates covering the range of flow rates to be used in the biodosimetry experiments. The tracer test described below represents a simple solution that can be modified if needed with different tracer solutions.

224

1. Tracer test:

   o Determine space-time τ of the system by measuring and calculating void volume or alternatively first fill the system with DI water (solution A) and completely drain it again. Measure volume or weight of drained water to calculate space-time, e.g. 100 g of drained water at 20 °C represent ~100 mL, with a flow rate of 1 L h^{-1} $\tau \approx 360$ s.

   o Analyze EC tracer solutions (solutions A and B).

   o Connect conductivity meter to the outflow.

   o Fill system with DI water (solution A).

   o Stop pump and switch to tracer solution (tap water (solution B)).

   o Start pump at desired flow speed, e.g. 6 L h^{-1} and continuously monitor EC till it becomes steady.

   o Calculate mean residence time as described in Chapter 6.3.

   o Check cumulative residence time distribution for volume to be flushed to reach steady state, F(t) at least > 0.97, ideally > 0.99.

Next to the knowledge on the hydraulics, key parameters (growth conditions and growth curves) for the challenge organism has to be set up, i.e. here for *A. citratiphilum.*

2. Growth curve:

   o Inoculate an active distinct colony of *A. citratiphilum* (a colony grown at 20 °C on 830a agar plates after streaking seven days ago using three-phase streaking pattern or similarly) in desired amount (e.g. 80 mL) of bouillon (solution C) in a 250 mL Erlenmeyer flask and incubate at 20°C and 120 rpm. If time for cell growth needs to be increased, several colonies may be inoculated.

   o Take samples in regular (e.g. 8 h) or practical intervals and measure absorbance readings at 600 nm (A$_{600}$) using the cell density meter.

   o When taking A$_{600}$ reading first measure and then subtract blank reading of bouillon (solution C).

   o Equilibrate 830a agar plates to room temperature if stored at 4 °C.

   o Prepare 10-fold dilutions using PBS with Tween20 (solution D) in 1.5 mL Eppendorf vials and plate 0.1 mL of the vortexed 10-fold dilutions on the 830a agar plates.

   o Use the Drigalski spatulas for streaking till a resistance between spatula and plate can be felt. Disinfect spatula first with 80% ethanol (solution E) and then flame it using a Bunsen-burner. Let Drigalski spatula cool down and use other sterile Drigalski spatula meanwhile.

- o Count colonies after plates been inverted and stored in the dark for seven days at 20 °C.

- o Count colonies using a colony counter.

- o Build linear regression curve of A_{600} vs. CFU mL^{-1}, considering only plates with 25-250 colonies analogous to (NSF/ANSI, 2019).

- o Continue to check A_{600} till it reaches a maximum to investigate when stationary phase is reached (e.g. > 0.6 cm^{-1}).

To avoid contaminations and false positive signals, several precautious disinfections steps are required before and after every experiment.

3. Disinfection procedure:

- o Freshly prepare two times the 1% H_2O_2 solution F in a volume bigger than the systems void volume (e.g. 250 mL, when void volume around 120 mL).

- o Flush system with DI water (solution A).

- o Switch feed to H_2O_2 (solution F) and discard the first void volume.

- o Start recirculation for 10 min at flow speed similar as used in the experiments or slightly higher, e.g. 10 L h^{-1}.

- o Disinfect the outsides if influent and effluent pipes if necessary using surfactant, e.g. 80% ethanol (solution E) or heat.

- o Sterilely connect Milli-Q water (solution G) as feed and discard void volume.

- o Collect H_2O_2 and discard according to your local regulations.

Depending on the time *A. citratiphilum* need to be cultivated to reach the desired cell number, in our case around 1.25 10^{10} CFU (typically reached after ~48 h), starting time to prepare the feed solution needs to be adopted.

4. Preparing *A. citratiphilum* feed solution:

- o As described in section 2 (growth curve) inoculate an active colony in 80 mL bouillon in a 250 Erlenmeyer flask and inoculate at 20°C with 120 rpm. It can be practical to prepare two of this cell cultures, to avoid waiting periods on the day of experiment.

- o After approximately 48 h, check A_{600}.

- o Calculate cell number according to growth curve.

- o Check if sufficient total cell number in the bouillon (~1.25 10^{10} CFU) is reached (in our case within the A_{600} the range of 0.3 to 0.5 cm^{-1}).

- o When cell number is sufficient and cells are still in exponential growth phase e.g. $A_{600} < 0.6$, start washing procedure.

- o For washing fill cell suspension in sterile 50 mL falcon tubes and centrifuge at 5000 rpm at 4°C for 10 min.

- o Remove supernatant, resuspend cell pellet in sterile PBS (solution H) and vortex for 10 s.

- o Repeat washing so in total suspension was centrifuged three times.

- o For the last resuspension step use PBS plus Tween20 added (solution D) instead of only PBS.

- o Depending on cell density, add needed volume of washed cell suspension to the 2.5 L of sterile PBS plus Tween20 (solution D) that shall be used as feed and shake it. Make sure before the PBS was sterilized a magnetic stirring bar was added if needed.

- o It is important to start the experiment (5. Biodosimetry experiment) as soon as possible after the preparation to avoid cells adapting to new low nutrient condition (Bucheli-Witschel et al., 2010), in our case <1 h.

To safe time, it is recommended to prepare low binding vials with 0.9 mL of PBS + Tween20 (solution D) that can be used for preparing 10-fold dilutions the day before the experiment. Further if agar plates are stored at 4°C, these should be brought to room temperature a couple of hours before the processing of the samples starts.

5. Biodosimetry experiment:

- o Connect 1 L sterilized PBS (solution H) as feed to the system.

- o Take a negative control sample in the same vials used for sampling later (to prove that system is disinfected/ CFU free).

- o Turn UV source and let it heat up if needed (we used 10 minutes for our LED to reach steady conditions in the used temperature cabinet).

- o Set slowest flow rate through the reactor, e.g. 1.7 L h^{-1}.

- o Switch feed to *A. citratiphilum* solution prepared according to section 4.

- o Start with slowest flow rate/highest fluence, e.g. 1.7 L h^{-1} and 16 mA driving current for the LED.

- o As soon as flow stabilized, stop time to flush enough volume through the system to reach steady state (as calculated by tracer experiment, e.g. 0.2 L).

- o Take replicated samples in low binding tubes.

- o Immediately store samples cool and in dark (e.g. in a cooling box and on ice).

- o Switch to next flow step (descending with fluence) and repeat, e.g. 2.13 L h^{-1} after 1.7 etc.

- o As last sample type, take the blank control blank samples without UV (use different flow rates to ensure pumping speed is not affecting cell viability, e.g. 4.25 L h^{-1} and 1.7 L h^{-1}).

After the experiment is finished, samples should be processed as soon as possible. Please note that when e.g. the bacterial solution is transported over longer distances, a trip control as described by U.S. EPA (U.S. EPA, 2006) might be needed. Further, in case samples without UV are collected before the UV reactor, at least once a sample after the reactor without UV should be compared (reactor controls (U.S. EPA, 2006)).

6. Sample processing

- o All processing of the samples need to occur in a red light only laboratory to avoid photorepair effects.

- o Prepare 10-fold dilutions using low retention tips, low binding vials and PBS with Tween20 added (solution D).

- o Plate 0.1-0.15 mL on an agar plate, samples should to be processed in random order.

- o Use sterile Dirgalski spatula to spread sample on agar plate as stand procedures in microbiology till you feel a resistance (see section 2 for preparation of growth curve).

- o The following contamination controls are plated: Bouillon (solution C), PBS+Tween (solution D) used for dilution, PBS+Tween (solution D) used for solution (last washing step), PBS used for washing (solution H) and negative control taken before the start of experiment.

- o After plating, agar plates are inverted and stored in the dark for seven days at 20°C.

- o After seven days CFU can be counted using a cell counter (only consider 25-250 CFU per plate analogous to (NSF/ANSI, 2019)).

- o Check if inconsistencies among the sample dilutions are occurring (using equations (6-12) & (6-13).

- o Calculate LRV by using geometrical mean of replicate samples (NSF/ANSI, 2019).

12.6. Supplementary information Chapter 7

This chapter has been published with some editorial changes as "*Supporting Information: Optimizing UVC-disinfection using LEDs as an energy efficient pre-treatment for biofouling control in reverse osmosis membrane systems*", representing the supplementary information of Sperle et al. (2023b).

12.6.1. List of abbreviations and acronyms

CBA	collimated beam apparatus	OPEX	operational expenditures
CFU	colony forming units	PBS	phosphate buffer saline
CIP	cleaning-in-place	PFU	plug forming units
EPS	extracellular polymeric substances	RO	reverse osmosis
HRT	hydraulic retention time	ROS	reactive oxygen species
MFS	membrane fouling simulator	UV	ultraviolet
OD	optical density	PTFE	polytetrafluoroethylene

12.6.2. List of symbols

Symbol	Meaning	Unit	Symbol	Meaning	Unit
A^{262}	absorbance reading at 262 nm	-			
A^{irr}	absorbance reading at irradiated wavelength	-	P_{feed}	feed pressure	bar
C_e	costs of energy	kWh^{-1}	q_0^{irr}	photon flux at the sample surface	Einstein s^{-1}
$C_{uridine}$	concentration of uridine	mol L^{-1}	R	reaction rate of uridine	mol s^{-1}
D	delay of biofouling	%	$R_{avg\_biofilm}$	average resistance of the biofilm	m^{-1}
E'	fluence rate	mW cm^{-2}	$R_{biofilm}$	resistance of the biofilm	m^{-1}
E'_{rel}	normalized fluence rate	-	$R_{membrane}$	average membrane resistance	m^{-1}
$F_{CIP\&membrane}$	factor for saving cleaning in place and membrane replacement	-	t	time	s
FCPD	feed channel pressure drop	bar	T	total experimental runtime	s
$FCPD_{avg}$	average feed channel pressure drop	bar	TMP	transmembrane pressure	bar

Symbol	Meaning	Unit	Symbol	Meaning	Unit
g	weighting function	-	U	photon energy at irradiated wavelength	mJ Einstein^{-1}
GF	germicidal factor	-	U_{irr}	average photon energy at irradiated wavelength	mJ Einstein^{-1}
GF_{irr}	average germicidal factor at irradiated wavelength	-	V_R	volume reactor	L
H'$_{germicidal}$	germicidal fluence	mJ cm^{-2}	V_T	volume solution	L
HRT	hydraulic retention time	s	ε	molar absorption coefficient	M^{-1} cm^{-1}
J_{design}	aimed flux	L m^{-2} h^{-1}	ε_H^{262}	molar absorption coefficient of the photoproduct of uridine at 262 nm	M^{-1} cm^{-1}
l_{irr}	effective path length of the light	cm	ε_H^{irr}	molar absorption coefficient of the photoproduct of uridine at irradiated wavelength	M^{-1} cm^{-1}
l_{obs}	thickness of measurement cuvette	cm	ε_U^{262}	molar absorption coefficient of uridine at 262 nm	M^{-1} cm^{-1}
LRV	logarithmic removal value	-	ε_U^{irr}	molar absorption coefficient of uridine at irradiated wavelength	M^{-1} cm^{-1}
OPEX$_{CIP\&membrane}$	operational expenditures considering cleaning in place and membrane replacement	€ y^{-1}	η	dynamic viscosity	Pa s
OPEX$_{FCPD\&Perm}$	operational expenditures considering feed channel pressure drop and permeability	€ y^{-1}	η_{Pump}	efficiency of a pump	-
OPEX$_{no\ fouling}$	operational expenditures without fouling	€ y^{-1}	λ	wavelength	nm
OPEX$_{Total}$	total operational expenditure	€ y^{-1}	Φ^{irr}	quantum yield at irradiated wavelength	mol Einstein^{-1}
P	pumping power	W			

12.6.3. Recorded spectrum of the LED and weighting function for the calculation of ε_U^{irr}, ε_H^{irr} and GF_{irr}
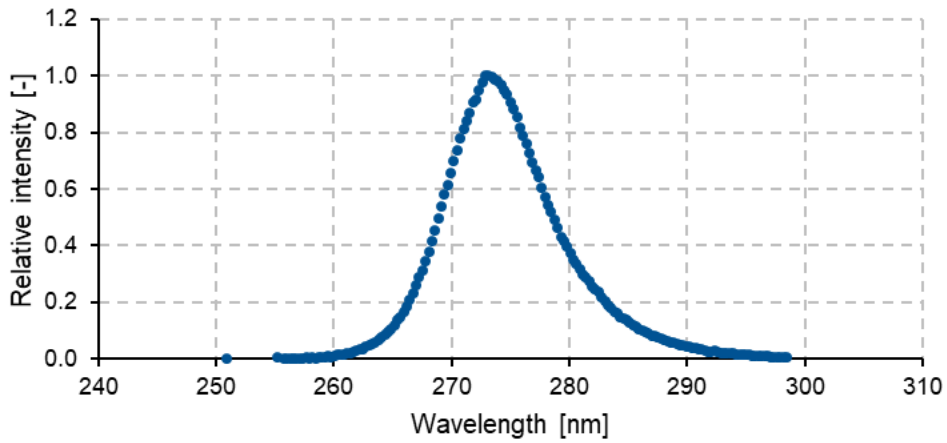

Figure S12-14:   Recorded spectrum of the used UVC-LED.

The used weighting function $g\,(\lambda_i)$ is given in equation (S12-18) with $E'_{rel}\,(\lambda_i)$ being the relative intensity of the spectrum at wavelength λ_i. Calculation of molar absorption coefficients ε_U^{irr} was done ε_H^{irr} using equation (S12-19). Here, $\varepsilon\,(\lambda)$ was measured as the relative absorbance in comparison to the peak absorbance at 262 nm measured at three different uridine concentrations and then multiplied with $\varepsilon\,(262)$ once for uridine and once for its photoproduct. During weighting, the measurement closest to $(\frac{\lambda_i+\lambda_{i-1}}{2})$ was used for $\varepsilon\,(\lambda)$. The calculation of photon energy U^{irr} and germicidal factor GF_{irr} was done analogous using equations (S12-20) and (S12-21). The germicidal factors closest to $(\frac{\lambda_i+\lambda_{i-1}}{2})$ were taken from Beck et al. (2015).

$$g\,(\lambda_i) = \frac{\frac{\{(E'_{rel}\,(\lambda_i) + E'_{rel}\,(\lambda_{i-1})\}\,(\lambda_i - \lambda_{i-1})}{2}}{\sum_{i=1}^{N} \frac{\{(E'_{rel}\,(\lambda_i) + E'_{rel}\,(\lambda_{i-1})\}\,(\lambda_i - \lambda_{i-1})}{2}} \tag{S12-18}$$

$$\varepsilon^{irr} = \sum_{i=1}^{N} g\,(\lambda_i)\,\varepsilon\,(\frac{\lambda_i + \lambda_{i-1}}{2}) \tag{S12-19}$$

$$U^{irr} = \sum_{i=1}^{N} g\,(\lambda_i)\,U(\frac{\lambda_i + \lambda_{i-1}}{2}) \tag{S12-20}$$

$$GF_{irr} = \sum_{i=1}^{N} g\,(\lambda_i)\,GF(\frac{\lambda_i + \lambda_{i-1}}{2}) \tag{S12-21}$$

12.6.4. Photographs of the used UVC-LED reactor
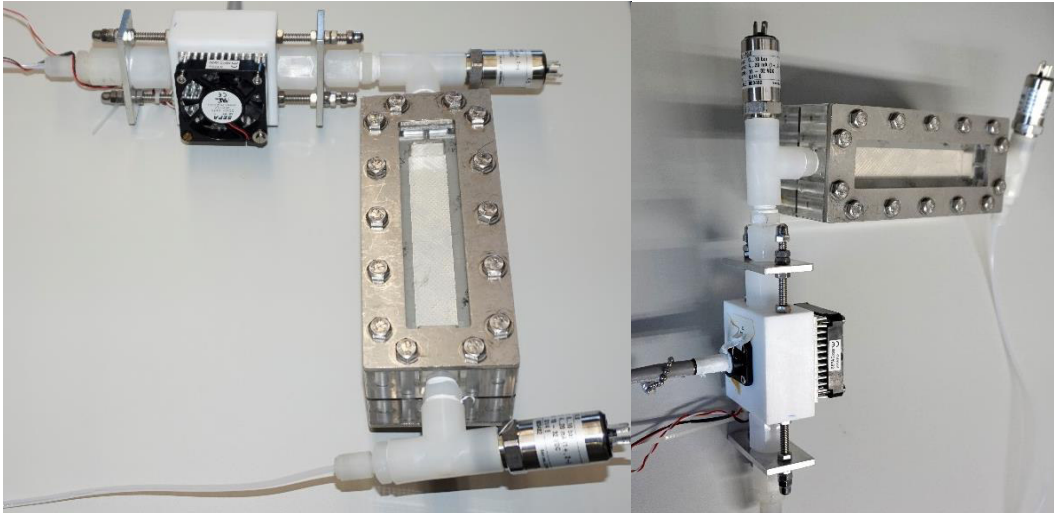

Figure S12-15:   *UVC-LED reactor attached to membrane fouling simulator (MFS) from two perspectives.*

12.6.5. Local tap water analysis

Table S12-4:   Analysis of the local tap water as shown in the study of Sperle et al. (Sperle et al., 2020a); Added values for total organic carbon (TOC) and for the (decadic) absorption coefficient at 273 nm, measured using the Aqualog (HORIBA Jobin Yvon, Germany).

Parameter	Mean	Standard deviation
TOC [mg·L^{-1}]	1.02	0.70
NO$_3$-N [mg·L^{-1}]	0.31	0.16
PO$_4$-P [mg·L^{-1}]	-[1]	-[1]
pH [-]	7.62	0.26
Electrical conductivity [µS·cm^{-1}]	572.5	24.6
Absorption coefficient at 273 nm [cm^{-1}]	0.0065	0.0008
Total direct cell count [1·mL^{-1}]	4.21 x10^4	1.49 x10^4
Ca [mg·L^{-1}]	60.83	3.2
Cl [mg·L^{-1}]	14.13	2.65
F [mg·L^{-1}]	0.137	0.005
Fe [µg·L^{-1}]	26.80	16.2
K [mg·L^{-1}]	0.98	0.01
Cu [µg·L^{-1}]	18.75	2.22
Mg [mg·L^{-1}]	23.75	0.64
Mn [µg·L^{-1}]	-[1]	-[1]

Parameter	Mean	Standard deviation
Na [mg·L^{-1}]	31.65	0.84
SO$_4$ [mg·L^{-1}]	38.38	5.09

[1] Lower than limit of detection

12.6.6. Simplified schematic of the adopted laboratory skid for biofouling experiments
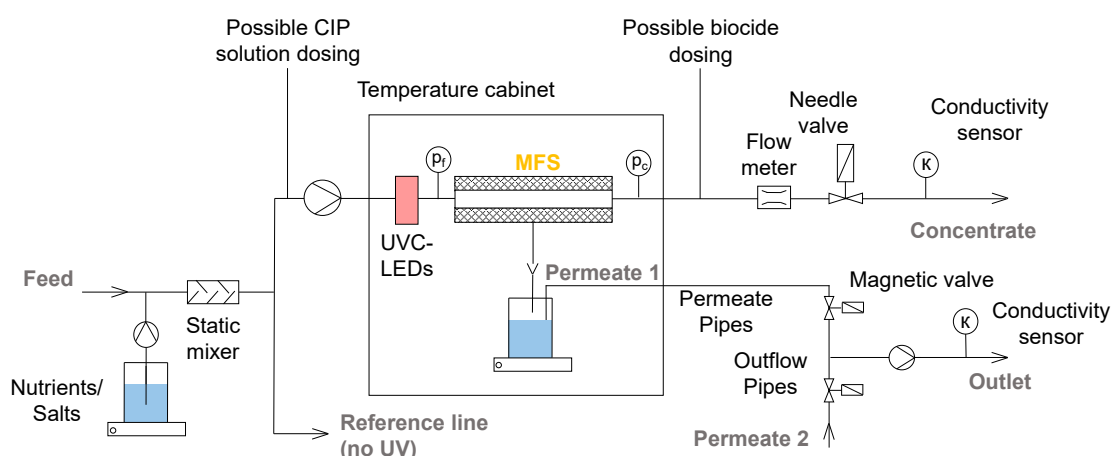

Figure S12-16: *Schematic of the laboratory skid for biofouling experiments; MFS represents the membrane fouling simulators; Modified from (Sperle et al., 2020a) with added possibility for dosing cleaning-in-place (CIP) solution*

12.6.7. Behavior fluence over driving current and duty cycle
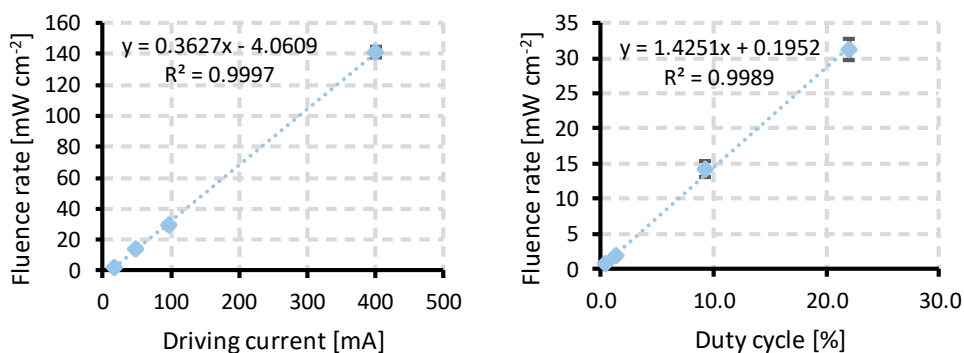
Figure S12-17: *Left:* Fluence rate over driving current; Right: Fluence rate over duty cycle at 400 mA and 10 Hz; Error bars are representing standard deviation.

12.6.8. The choice of *A. citratiphilum* as surrogate for biodosimetry with the link to biofouling control

In our previous study (Sperle et al., 2020a), we observed a correlation between the resistance of biofilm and an *Aquabacterium* species, a typical biofilm forming bacterium (Kalmbach et al., 1999). To further identify the species, the gene sequence of the amplicon sequence variant was analyzed with the blastn algorithm using the 16S_ribosomal_RNA database and excluding uncultured/environmental sample sequences (NCBI, n. d; Zhang et al., 2000). When doing so at the beginning of the study (end of 2020) the species with the highest score was *A. citratiphilum* (E-value 0.0 and 99.76% identity). Therefore, the species of *A. citratiphilum* was used as a surrogate to study the UV disinfection as an important biofilm bacterium. Nevertheless, it must be noted, that when now using the blastn algorithm, the highest score is obtained by *Aquabacterium soli* (E-value 0.0 and 100.00% identity) which was just recently discovered in the study of Sun et al. (2021). *A. soli* would probably have been the better choice of surrogate, but unfortunately, it was too late for its usage in this study.

12.7. Reproducibility of biofouling results for both lines of the laboratory skid used in the lab-scale experiments

With the built laboratory skid and the developed biofouling protocol (chapter 4 and 7), reproducible results could be obtained. Results of a biofouling experiment, both lines without UV are shown in Figure S12-18. The time for reaching the desired FCPD was 11.5 days for line 1 and 11.4 days for line 2, so there is less than 1% difference.
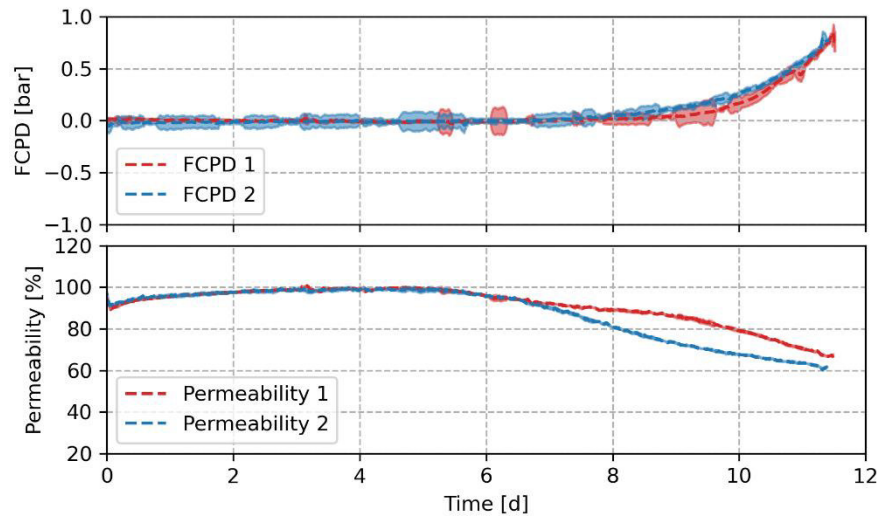

Figure S12-18: Experiment showing reproducibility between the two lines run in parallel in each biofouling experiment; shaded areas represent the standard deviation.

12.8.   Preliminary results on UV-LED reactor modeling

To further validate the actinometry procedure developed in Chapter 5, the results of the actinometry applied to a flow-through LED reactor (Chapter 7) shall be checked by a reactor model. The reactor model consists of a combination of a hydraulic model, including a Lagrangian particle tracing, with an optical field model. With such a model, the LRV of UV reactors used for water disinfection can be calculated (Mohaghegh Montazeri and Taghipour, 2023; Wu et al., 2021b). The modeled LRV shall be validated with the experimentally determined LRV of MS2. Finally, the average fluence rate of the model shall be compared to the actinometry results.

The results of this study shall be submitted to the Journal *Water Research* with the preliminary title "Validation of an actinometric procedure for flow-through reactors using uridine by a multiphysics model" by Advait Gangal and Philipp Sperle, Sibel Tas Köhler, André Lerch, and Jörg E. Drewes.

Preliminary author contributions: Philipp Sperle initiated and conceptualized the study. Philipp Sperle and Advait Gangal developed the methodology and did the investigations as well as the formal analysis. Advait Gangal was in charge of the modeling, data curation and visualization. Data was validated by all authors. Original draft was prepared by Advait Gangal and Philipp Sperle. Review and editing of the draft will be done by André Lech, Siebel Köhler and Jörg E. Drewes. Supervison of the study was done by Philipp Sperle, André Lerch and Jörg E. Drewes. Jörg E. Drewes was further in charge of project administration and funding acquisition.

The preliminary results shown here are based on and adapted from the Study Project of Advait Gangal (2023), which was supervised by Philipp Sperle, Sibel Tas Köhler and Jörg E. Drewes. Besides, general basics in the optical field modeling were outlined by Xuan Quyet Nguyen (2021).

Overall, it shall be emphasized that the presented results here are preliminary and the actual model needs to be revised before publication.

12.8.1. Multiphysic model development

A simple version of the used UV-LED reactor (Chapter 7) was implemented in COMSOL Multiphysics (Version 5.6), consisting of the silica glass pipe and the water body (Figure S12-19). Besides, small air pocket between the LEDs and the silica glass pipe was added. To mimic the reflectance of PTFE, the outer boundaries of silica glass pipe that were covered by PTFE were set to 96% diffuse reflection. Unfortunately, due to the limited computation power, only an extra coarse grid could be used. This will be changed as a machine with higher computational power was purchased. UVT of the water was set to 96%, being equal to a Napierian absorption coefficient of 4 m^{-1}. Within the future model development, the UVT should be adapted to the measured UVT of 99% at 273 nm during the biodosimetry experiments.
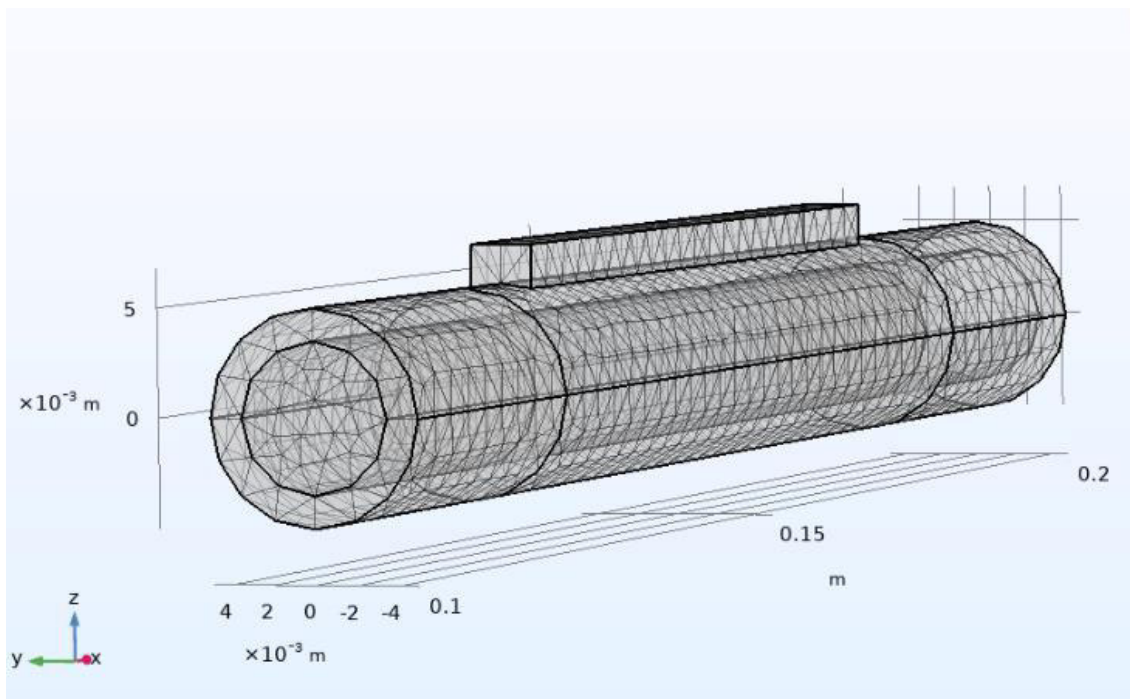
Figure S12-19:   Modeled and meshed reactor geometry.

COMSOL's laminar flow module with stationary conditions was used to model the hydrodynamic flow field, as the calculated Reynolds number (internal diameter of 0.7 cm) at a flow of 4.25 L h^{-1} is small. For the water flow, incompressibility was set. As boundary conditions, for the inlet, average water velocity was used, calculated as flow divided by cross section. For the effluent, the boundary condition was set to zero pressure. The silica glass walls were set as a non-slip boundary.

For modeling the flow of phages through the reactor, COMSOL's particle tracing module was used. The drag force of particles was modeled based on Schiller-Naumann law. The particle diameter was set to 0.1 um, which needs to be decreased in future to more accurate size of an MS2 virus. Besides density of the particles was assumed with 1400 kg m^{-3}. Drag force was mistakenly set in the negative z direction with gravity acceleration instead of the negative x direction. Nevertheless, drag force was found to only have a negligible influence on the model results. Overall, 5000 particles were released. The particle release in the inlet was weighted by the velocity of the fully developed laminar flow profile. This was reasoned as the concentration of particles is constant in the reactor, but particles flowing through each streamline would result by the multiplication of concentration with flow. Particles reaching the outlet of the reactor were set to freeze. Particles hitting a silica glass wall were set to freeze, as well, even though this might need to be changed to bouncing off. However, through the laminar flow, no particles were observed to stick on the walls. The runtime of particle tracing was set to 10 s. All except one particle reached the effluent with this stopping criterion.

The optical field in the UV reactor was modeled using the ray optics module. For simplification, the LEDs were assumed to emit monochromatically at 270 nm. Secondary rays were limited to 60,000, and the unmeshed domain was set to have a

refractive index of 1. Furthermore, the simulation was solved for intensity and power with a total run time of 2 ns, representing a theoretical path length for the light of 0.6 m. Real and imaginary parts for the refractive index were taken from the build in library. The attenuation of the light beams was calculated based on the extinction coefficient. The threshold power for reflected rays of the PTFE boundaries was set to 0.001 mW, whereas it was set to never for all other boundaries. For solving intensity, the threshold was set to 1 mW m^{-2}. The boundary condition on the PTFE interfaces was set to diffuse reflection. The light source of the LEDs was modeled as a hexapolar grid with 50 polar angles (N_Θ), resulting in 7651 rays emitted. The light sources were modeled with a conical emission spectrum having a cone angle of 90°. The emission spectrum of the 2P2S SMD LED module was read out from the data sheet (Bolb Inc., 2021). The relative intensity of the emission spectra was fitted from the datasheet using the curve fitting tool of Matlab (Version 2020b) analogous as done by Simons et al. (2014) and Oguma et al. (2016):

$$RI\ [-] = \frac{2.357 - 1.537 * \theta}{\theta^2 - 2.525 * \theta + 2.707} \tag{S12-22}$$

$$\theta\ [rad] = \arccos\left(\left|\frac{gop.vgz}{\sqrt{gop.vgx^2 + gop.vgy^2 + gop.vgz^2}}\right|\right) \tag{S12-23}$$

here gop.vgx, gop.vgy, and gop.vgz are the COMSOL's reference names for the x-, y-, and z-direction group velocities of a released ray. The relative intensity was used as a power weighting factor. According to the datasheet, the LEDs should emit around 360 mW with a driving current of around 600 mA. As only 96 mW were used in the laboratory experiments, and some aging of the LEDs was expected, the total emitted source power was set to 51 mW.

Within the model development, the biggest challenge was to calculate the fluence rate in each mesh element. A simple accumulation of the light beams passing the mesh element was not sufficient, as light beams might hit the mesh elements with different angles and hence also cross sections. To avoid this problem, the idea was to calculate the fluence rate in each mesh element as the power transported by the beam, multiplied by the path length through the mesh element and divided by the mesh element volume. Nevertheless, reading the path length through each mesh element was challenging. As advised by the COMSOL Support (2022), this could be archived by using COMSOL's deposited ray power node. This functionality calculates the absorbed power in each mesh element based on the imaginary part of the refractive index (k).

The imaginary part relates to the Napierian absorption coefficient $a_{\lambda,napierian}$ as following (COMSOL Support, 2022; Hecht, 2002):

$$a_{\lambda,napierian}\ [cm^{-1}] = \frac{4\pi k}{\lambda} \tag{S12-24}$$

Hence, from the UVT, the imaginary part of the refractive index was calculated. The average fluence rate E'_{avg} in each mesh element was then derived as:

$$E'_{avg}[mW\ cm^{-2}] = \frac{P_{abs}}{a_{\lambda,napierian}} = \frac{P_{abs}}{a_{\lambda,decadic}\ \ln(10)} \tag{S12-25}$$

Where $a_{\lambda,decadic}$ represent the decadic absorption coefficient at wavelength λ and P_{abs} is equal to the absorbed power per volume V, calculated over the deposited ray power node. The relation of equation (S12-25) is proven in the following:

$$E'_{avg} = \frac{\phi}{A}\ WF = \frac{\phi}{A}\ \frac{1-\ 10^{-a_{\lambda,decadic}\cdot\ l_{irr}}}{a_{\lambda,decadic}\cdot\ l_{irr}\ \cdot\ln(10)} \tag{S12-26}$$

With A being the effectively irradiated cross section [cm²], ϕ represent the radiant flux [mW] and WF is the Water factor according to Morowitz (1950), and Bolton and Linden (2003).

$$P_{abs}[W\ L^{-1}] = \frac{\phi}{V}\left(1-\ 10^{-a_{\lambda,decadic}\cdot\ l_{irr}}\right) \tag{S12-27}$$

$$\phi\ [W] = \frac{P_{abs}V}{\left(1-\ 10^{-a_{\lambda,decadic}\cdot\ l_{irr}}\right)} \tag{S12-28}$$

Inserting equation (S12-28) in equation (S12-26) leads to equation (S12-25) with V= A l_{irr}.

Fluence received by each particle was calculated as the integral of fluence rate over time along the particle trajectories. Therefore, first the optical model was solved, followed by the laminar flow, and finally by the particle tracing model. Analogous to Wu et al. (2021b) the LRV was calculated using equation (S12-29) with H'_i being the fluence received by each particle, multiplied with the germicidal factor of 0.94 determined in Chapter 7 (Sperle et al., 2023b), $f(H'_i)$ representing the linear model fitted to the standard case in a irradiated petri dish without reflection as measured for MS2 in Chapter 5 (Sperle et al., 2023c), and N_0 representing the number of particles released.

$$LRV = -\log\left(\frac{\sum_{i=1}^{N_0} 10^{-f(H'_i)}}{N_0}\right) \tag{S12-29}$$

12.8.2. Preliminary model results

Results for the model flow field are visualized in Figure S12-20. Shortly after the inlet, the flow becomes fully developed. For the developed flow, the typical velocity distribution of an ideal pipe flow can be seen, highest velocity in the middle and zero velocity at the walls due to the non-slip boundary condition.
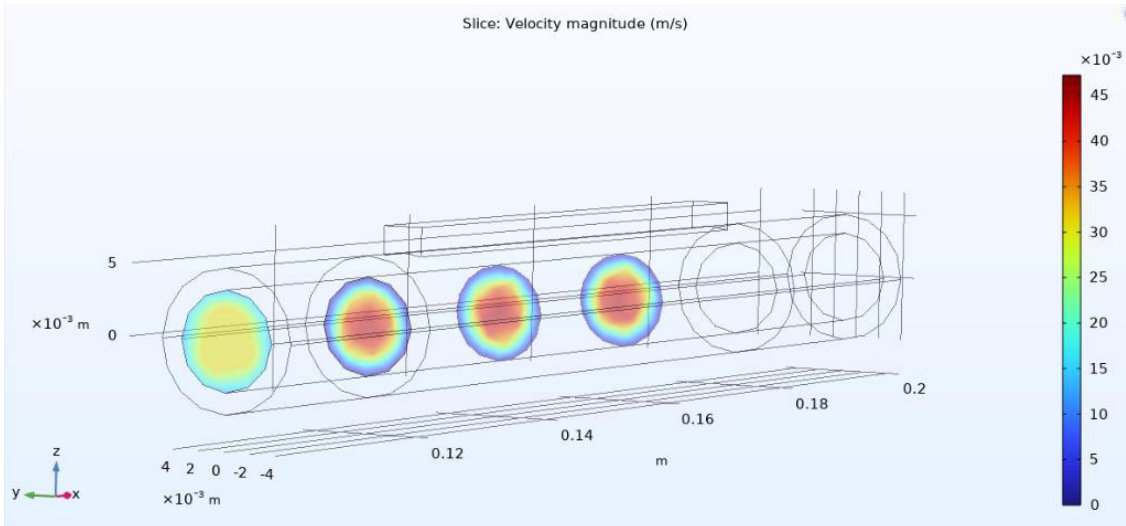
Figure S12-20:   Modeled laminar flow field.

The fluence rate within the reactor is shown in Figure S12-21 and Figure S12-22. Here, the highest fluence rates are observed below the LEDs and as expected fluence rate diverges through the reactor volume. At the opposite of the LEDs, an increased fluence rate is observed due to the reflection by the PTFE. The fluence rate within the water body seems relatively equally distributed, but a finer mesh with a higher number of rays is likely to enhance the results.
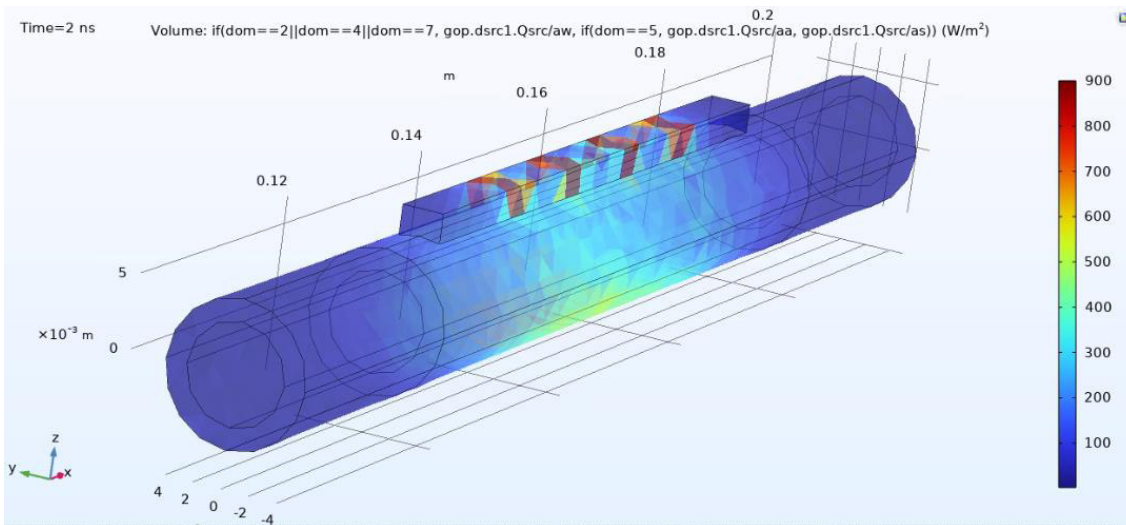

Figure S12-21:   Volume plot of the modeled fluence rate.
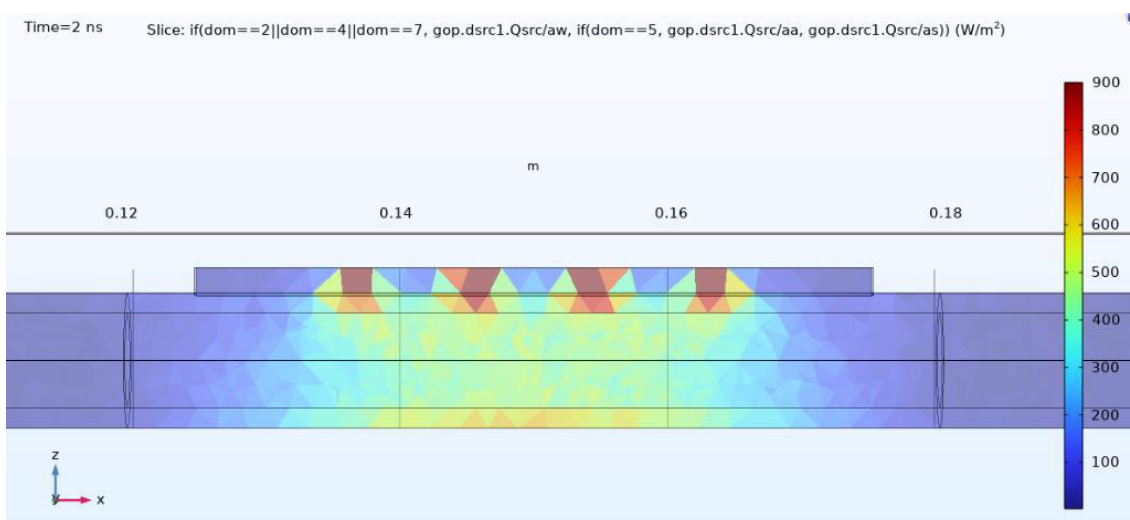
Figure S12-22:   Slice plot of the modeled fluence rate.

Particle trajectories are depicted in Figure S12-23 and the histogram of fluence received by the particles is shown in Figure S12-24. For the particles traced, a parabolic shape, fitting well to the flow velocities, can be seen. As the histogram indicates, there is no hydraulic shortcut in the reactor and most particles receive a fluence around 40-50 mJ cm^{-2}. This fluence range likely represents the particle trajectories in the middle of the reactor. For higher fluence, a long tail is observed, likely caused by particles flowing close to the UV-LEDs and wall of the silica glass pipe with a reduced velocity. Overall, at the modeled flow of 4.25 L h^{-1}, the LRV of MS2 was calculated with 1.99, whereas experimental results showed a LRV of 1.96. Hence, the calculated LRV is < 2% higher than the experimental results. The average fluence rate in the reactor volume in this model was 25.6 mW cm^{-2}, whereas experimental results of actinometry showed a fluence rate of 29.2 mW cm^{-2}. Here model results are < 13% smaller than the measured results. Overall, the modeled LRV matches the results from biodosimetry, and hence the model is regarded as validated. The lower value of modeled fluence rate than the experimental results could be caused by the too low set UVT or other modeling errors like a not very detailed geometry, coarse mesh or wrong absorbance by the silica glass pipe. Besides, an uncertainty of the quantum yield for the actinometry calculations, as described in Chapter 5, might cause the difference. Nevertheless, an uncertainty of less than 15% might be acceptable in this stage of modeling.
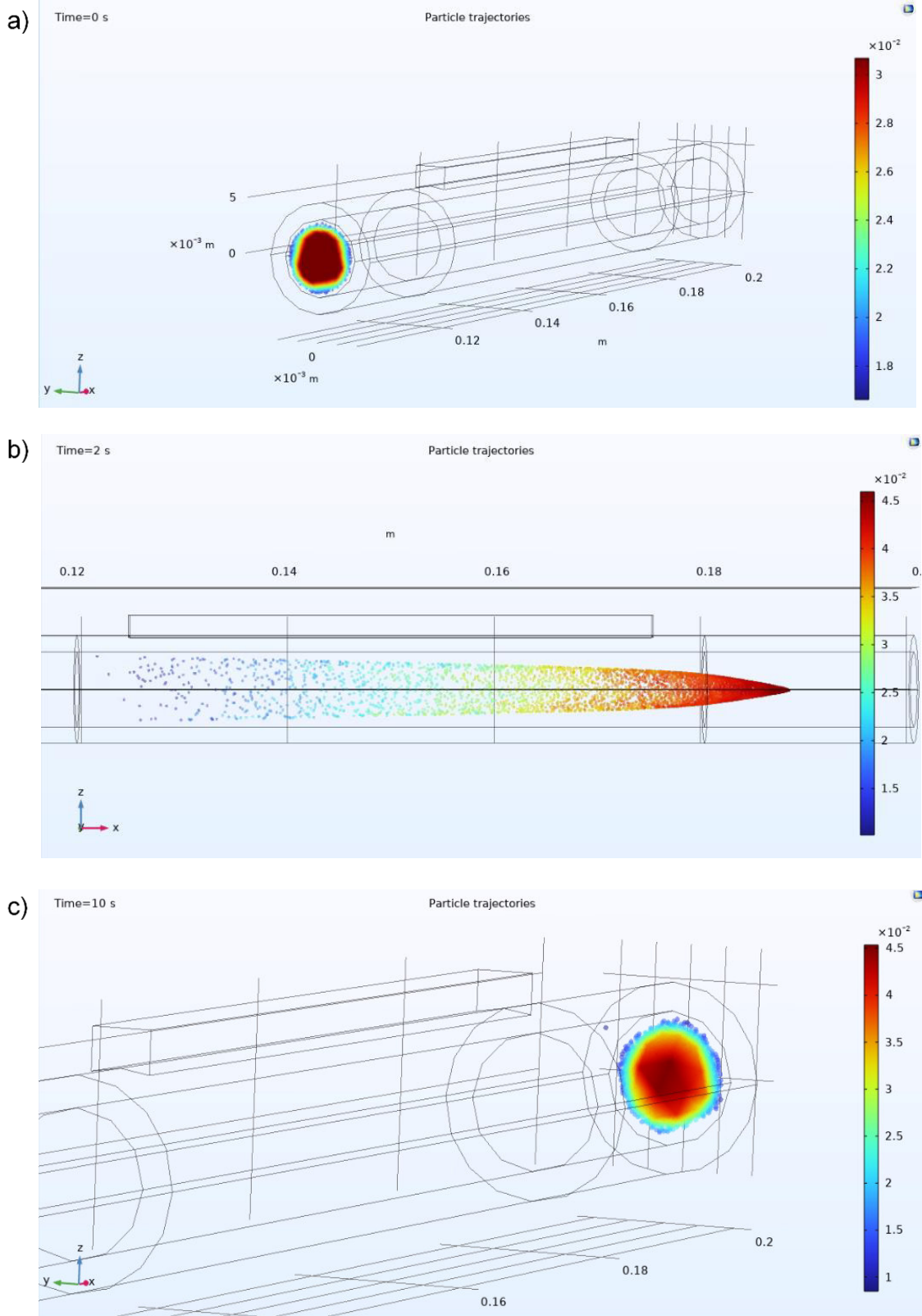
Figure S12-23:   Particle trajectories over time; a) Particle Positions at t = 0 s; b) Particle Positions at t = 2 s; c) Particle Positions at t = 10 s.
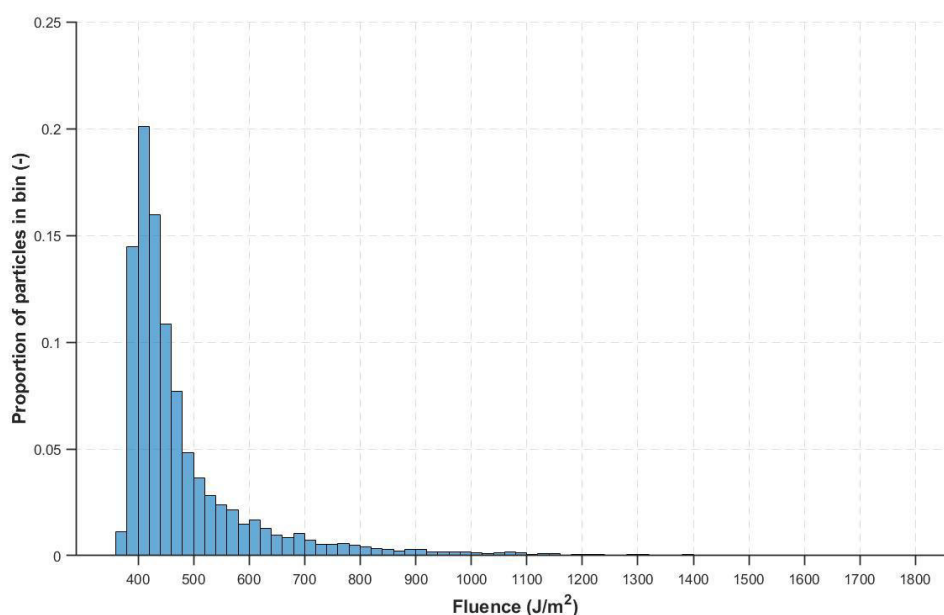
Figure S12-24:   *Histogram of fluence received by set of 5000 released particles*

Overall, the model still needs to be enhanced. Aside from the smaller modifications to the boundary conditions that were mentioned already, it seems essential to extend the model so the actual dimensions of the surrounding PTFE body with the distance of the LEDs to the silica glass pipes are implemented. Besides, the independence of the results to the mesh should be shown. Furthermore, showing the independence of results on the number of rays and experimental runtimes could be important. In addition, a method to extract the average path length of the rays within the water body is needed to validate the effective path length calculated within the actinometry experiments. Nevertheless, the preliminary results fit well with the experimental biodosimetry results. Besides, the deviation of less than 15% between the model and the actinometry results looks promising for a validation of the actinometric procedure.

12.9. Recoded voltage during pulsed UV-LED operation

To check the power demand, excluding losses due to the LED-Pulse-Controller (Leistungselektronik JENA GmbH, Germany), the behavior of voltage over time during the pulsed and continuous operation was recorded using a USB powered oscilloscope (6022BE, Hantek, China) with a sampling rate of approximately 48 MSa/s. Besides, to avoid any ground loop or similar electrical shortcut, the LED-Pulse-Controller, function generator, and LED fan were powered over an isolation transformer (MII 500, Bronson++, Germany). Furthermore, during the measurements with the oscilloscope, the LED-Pulse-Controller was disconnected from any laptop. Oscilloscope was connected once to the cables directly at the outlet of the LED-Pulse-Controller. The average voltages recorded for 16, 48, 96, and 400 mA were 9.82, 11.12, 11.78, and 14.12 V (Table S12-5). The curves for the pulsed operation are shown in Figure S12-25 to Figure S12-28. Unfortunately, the software of the oscilloscope does not enable a sampling time during data export. As the exact time steps between the readings exported are not know (but seem to be constant), the voltage was plotted over the sample number. During the live measurement, the set frequency of 10 Hz could be confirmed using the software integrated tool for frequency determination. For the pulsed operation, average voltage during peaks was calculated, ignoring values below 9.8 V. 9.8 V was used as threshold as this represents the average voltage for the 16 mA setting with already only low currents. For the 10 Hz operation with a driving current of 400 mA, for the duty cycles of 0.5, 1.4, 9.3, and 22% were 14.33, 14.58, 14.538, and 14.30 V. In addition, Table S12-6 shows the calculated power. For continuous mode, this power was simply calculated as average voltage multiplied by the driving current. For pulse mode, the power was calculated for the first nine cycles. Thereby an average was calculated from the voltage multiplied by the driving current. Below 9.8 V driving current was assumed to be 0 mA and above 400 mA. Finally, the theoretical power for pulsed operation is shown, calculated as the power of continuous irradiation at 400 mA multiplied by the duty cycle. Due to the overshoot of the voltage during pulsation, the power demand calculated directly is most of the time slightly higher than the theoretical power demand.
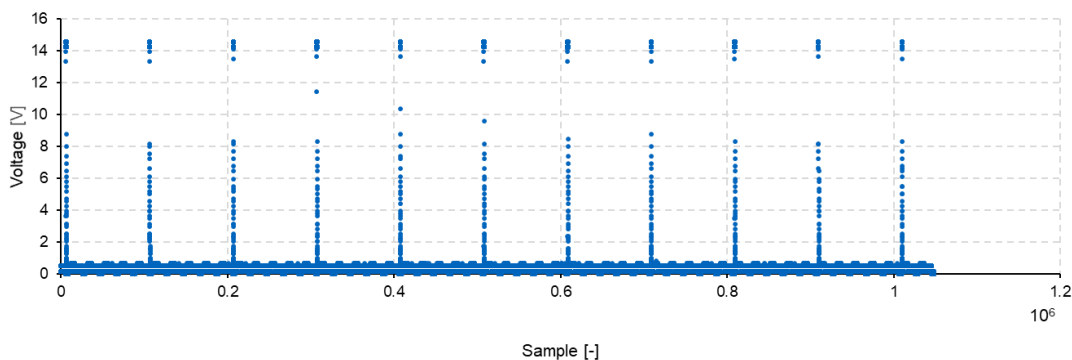

Figure S12-25:   Recoded voltage during pulsed operation with 10 Hz, 400 mA and 0.5% duty cycle.
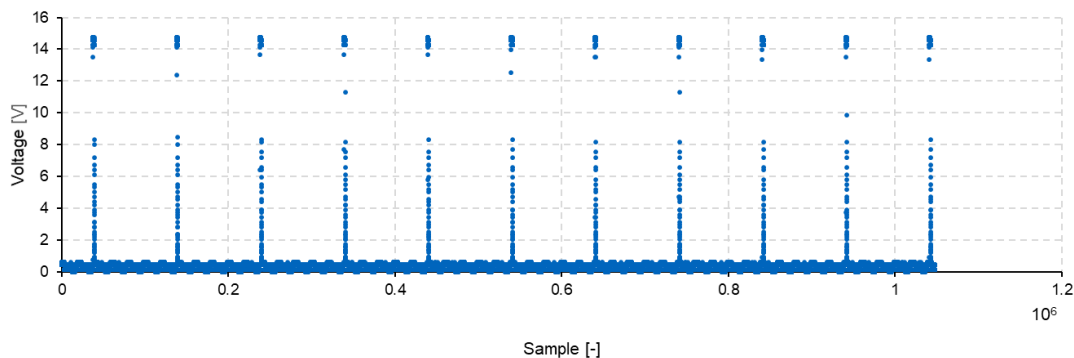
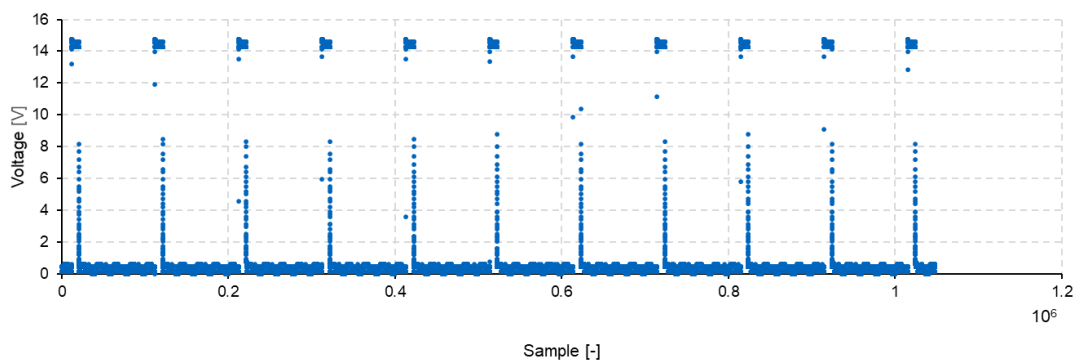*Figure S12-26:* Recoded voltage during pulsed operation with 10 Hz, 400 mA and 1.4% duty cycle.

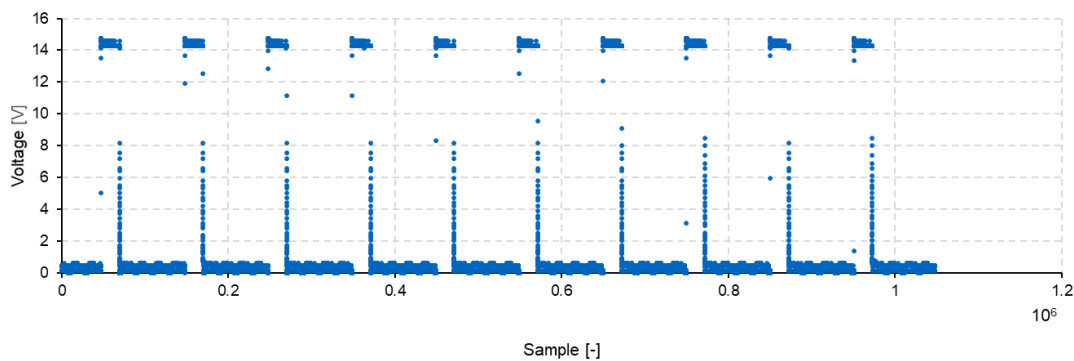*Figure S12-27:* Recoded voltage during pulsed operation with 10 Hz, 400 mA and 9.3% duty cycle.

Figure S12-28: Recoded voltage during pulsed operation with 10 Hz, 400 mA and 22% duty cycle.

Table S12-5: Measured voltage during the irradiation settings

Setting continuous	Voltage [V]	Setting pulsed	Voltage peak [V]
		0.50%	14.333
16 mA	9.818	1.40%	14.578
48 mA	11.120	9.30%	14.382
96 mA	11.781	22%	14.301
400 mA	14.116		

Table S12-6:   *Summary calculated power LEDs from voltage.*

Setting continuous	Power continuous [W]	Setting pulsed	Power pulsed [W]	Power pulsed theoretical [W]	Power pulsed/ power continuous [%]
		0.50%	0.029	0.028	
16 mA	0.157	1.40%	0.082	0.079	52
48 mA	0.534	9.30%	0.539	0.525	101
96 mA	1.131	22%	1.212	1.242	107
400 mA	5.646				

As on the printed circuit board, LED drivers were soldered in addition to the constant current supply by the LED-Pulse-Controller, the measurements were repeated, this time, the oscilloscope connected once to a wire connected to the probable outlet of the driver and once to the electricity connection at the entrance of the printed circuit board. Voltages recorded are similar, although slightly lower for the higher mA region and pulsed operation (Table S12-7). As this time, the average voltage for 16 mA operation was 9.7 V, this value was used as threshold for the power and voltage calculation in the pulsed settings (Table S12-8). When looking and the voltage curves over time, this time, some unexpected oscillations in the negative Voltage regions after the pulses was observed (Figure S12-29 till Figure S12-32). Unfortunately, no explanation for these oscillations can be given here.

Table S12-7:   *Measured voltage during the irradiation settings after the LED driver*

Setting continuous	Voltage [V]	Setting pulsed	Voltage peak [V]
		0.50%	13.406
16 mA	9.735	1.40%	13.320
48 mA	10.795	9.30%	13.029
96 mA	11.227	22%	13.101
400 mA	12.703		

Table S12-8:   *Summary calculated power LEDs from voltage after the LED driver.*

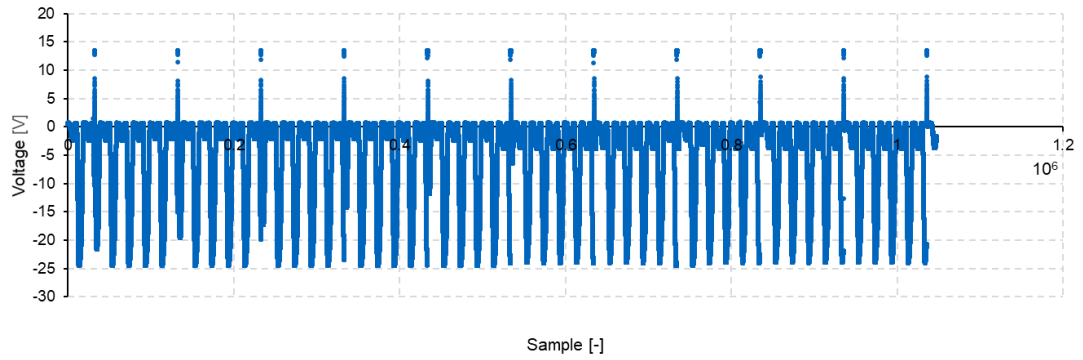| Setting continuous	Power continuous [W]	Setting pulsed	Power pulsed [W]	Power pulsed theoretical [W]	Power pulsed/ power continuous [%]
		0.50%	0.027	0.025	
16 mA	0.156	1.40%	0.075	0.071	48
48 mA	0.518	9.30%	0.488	0.473	94
96 mA	1.078	22%	1.161	1.118	108
400 mA	5.081				

Figure S12-29:   Recoded voltage during pulsed operation with 10 Hz, 400 mA and 0.5% duty cycle after the LED driver.
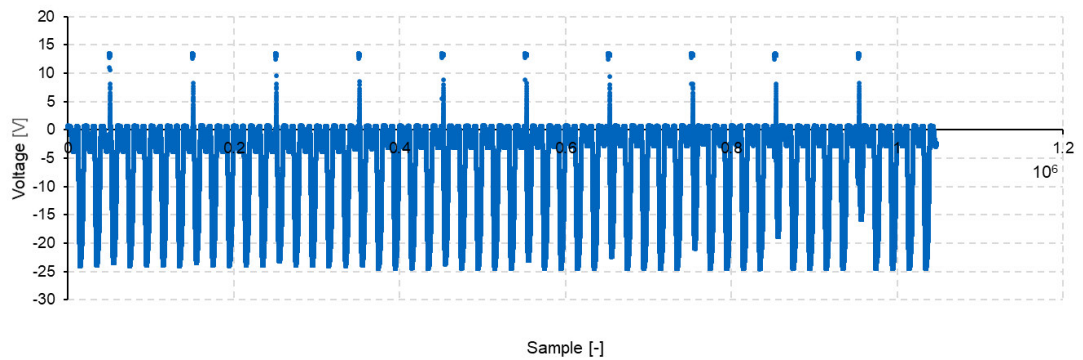

Figure S12-30:   Recoded voltage during pulsed operation with 10 Hz, 400 mA and 1.4% duty cycle after the LED driver.
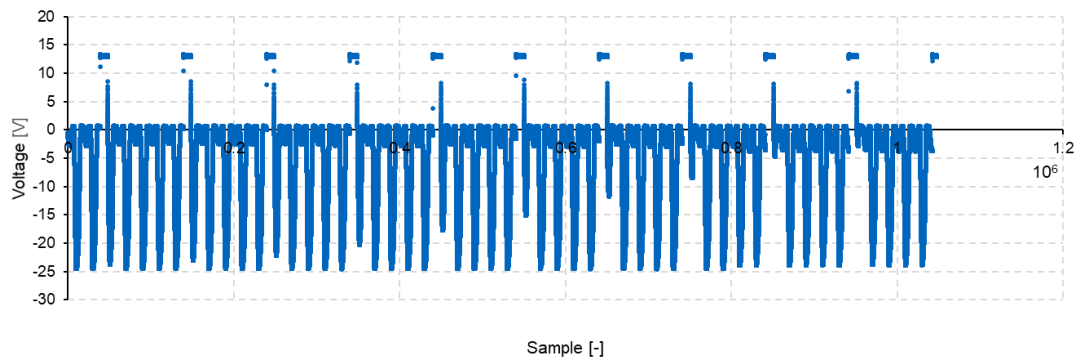

Figure S12-31:   Recoded voltage during pulsed operation with 10 Hz, 400 mA and 9.3% duty cycle after the LED driver.
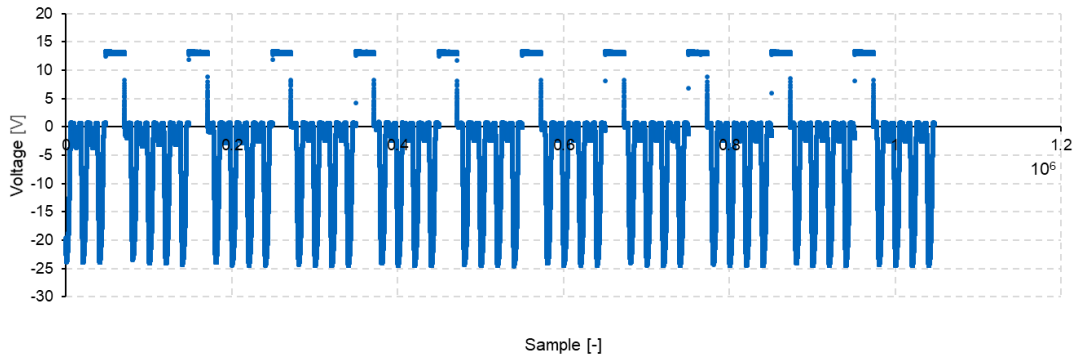
Figure S12-32:   Recoded voltage during pulsed operation with 10 Hz, 400 mA and 22% duty cycle after the LED driver.